MAGNETOTELLURIC IMAGING OF LITHOSPHERIC MODIFICATION IN THE RIO GRANDE RIFT, COLORADO AND NEW MEXICO, USA

by

DANIEL WESTON FEUCHT

B.A., University of California, Berkeley, 2010

A thesis submitted to the
Faculty of the Graduate School of the
University of Colorado in partial fulfillment
Of the requirement for the degree of
Doctor of Philosophy
Department of Geological Sciences
2017

This thesis entitled:
Magnetotelluric Imaging of Lithospheric Modification in the Rio Grande rift, Colorado and New Mexico, USA
written by Daniel Weston Feucht
has been approved for the Department of Geological Sciences

_____
Professor Anne Sheehan

_____
Dr. Paul Bedrosian

Date_____

The final copy of this thesis has been examined by the signatories, and we find that both the content and the form meet acceptable presentation standards of scholarly work in the above mentioned discipline.

Feucht, Daniel Weston (Ph.D., Geological Sciences)

Magnetotelluric Imaging of Lithospheric Modification in the Rio Grande Rift, Colorado and New Mexico, USA

Thesis directed by Professor Anne F. Sheehan and Dr. Paul A. Bedrosian

Knowledge of the physical and chemical properties of the lithosphere plays an important role in determining how deep geodynamic processes that drive plate tectonics are expressed at the surface of the Earth. Magnetotellurics (MT), an electromagnetic geophysical imaging technique, allows us to map variations in electric resistivity at great depth, providing a unique window into the modern-day condition of the crust and upper mantle. The Rio Grande rift is a mid- to late-Cenozoic age continental rift system in the southwestern United States that is located at the boundary between the actively deforming western U.S. and the stable continental interior. Previous work in the rift has revealed an apparent discrepancy in the vertical distribution of extensional rift structure in that an exceptionally broad low velocity zone in the upper mantle appears to underlie a series of narrow axial rift basins. I present the results of a wide-aperture, high-resolution, deep sensing magnetotelluric survey across the Rio Grande rift that was designed to reconcile this discrepancy through targeted imaging of the lower crust and uppermost mantle.

Two-dimensional modeling of broadband and long period magnetotelluric data along three ~450 km profile lines straddling the Rio Grande rift at latitudes of 39.2ºN, 36.2ºN and 32.0ºN reveals anisotropic electrical resistivity structure along

the rift axis to depths >150 km. A consistently broad (200 km wide) zone of high electrical conductivity is present within the lower crust along the entire length of the rift axis. This feature is interpreted to be the result of recent tectonic activity, including a recent supply of partial melt and/or saline fluids to the mid- to lower-crust from a broad zone of high-temperature upper mantle. Imaging of the upper mantle reveals a zone of hydrous modification within the sub-continental lithospheric mantle that extends east of the Rocky Mountain Front.

A focused magnetotelluric study of the Jemez Mountains Volcanic Field, a major volcanic center on the margin of the rift in northern New Mexico, reveals local perturbations to the regional scale resistivity structure with implications for the most recent episodes of magmatic activity in the Valles caldera.

ACKNOWLEDGEMENTS

First and foremost I would like to thank my thesis advisors, Anne Sheehan and Paul Bedrosian, and my committee members, Craig Jones, Lang Farmer and Shijie Zhong. I am grateful to have benefited from the knowledge and encouragement of such an accomplished and professional committee. Their patience and guidance throughout my graduate career has given me opportunities to succeed and grow as a scientist for which I cannot thank them enough.

I will forever be indebted to the small army of volunteers, including undergraduates, colleagues, friends, and professors, who sacrificed weekends and vacation time in exchange for long days of driving, digging holes, and hauling wire. This project would not have been possible without the monumental generosity and enthusiasm of these special individuals.

I have been incredibly fortunate throughout my early career as a geophysicist to participate in a number of field experiments, educational opportunities, and travel for the sake of scientific pursuits. I owe these experiences to G. Jiracek, L. Pellerin, L. Braile, J. Ferguson, S. Baldridge, K. Key, and P. Wannamaker.

I owe special thanks to Diana Brown. She has been there for me through all the highs and lows and she inspires me every day.

This thesis is dedicated to my parents, whose unconditional support and encouragement have made me the person I am today, and to my sisters, for inspiring me to follow my passion with a full heart and unwavering determination.

CONTENTS

TABLES

Table

FIGURES

Figure

CHAPTER 1

INTRODUCTION

The varied landscapes that we observe on the surface of continents (e.g. mountain ranges, plains, valleys) are the outward expression of physical processes occurring deep within the Earth over geologic time. Deciphering the detailed origins of these landscapes can be difficult based on surface observations alone. Geophysical imaging techniques provide a window into the modern-day physical and chemical conditions of the subsurface that, when placed in the context of geologic observations and a well constrained tectonic history, reveal details of the origin and ongoing evolution of the landscapes we see around us.

The focus of this dissertation is to image physical and chemical modification of the crust and uppermost mantle beneath the Rio Grande rift, the southern Rocky Mountains, and the Valles caldera in an effort to investigate the significance of that modification to the past and present evolution of those tectonic regimes. The tectonic history of the Rio Grande rift is intimately intertwined with the larger Cenozoic history of the western United States. The axial basins of the rift parallel the Rocky Mountain Front, a north-south trending line along the western margin of the Great Plains that is widely considered the demarcation boundary between stable lithosphere to the east and actively deforming lithosphere to the west. Also parallel to this boundary, and coincident with the northern rift, is the range crest of the southern Rocky Mountains, which achieves some of the highest elevations and

greatest relief of any mountain range in North America. The Valles caldera, the site of two massive rhyolitic eruptions in the Quaternary, resides at the intersection of the Rio Grande rift and the Jemez Lineament, a linear chain of volcanic centers that may represent a reactivation of a pre-existing structural weakness in the lithosphere. The variety of landscapes and tectonic regimes present within this relatively confined region of the North American continent can be attributed to regional tectonic forces acting upon a heterogeneous lithosphere with internal variations in temperature, composition, and stress regime.

To investigate lithospheric modification of the southwestern United States, I use new magnetotelluric data to image variations in electrical resistivity structure to >150 km depth. Images of electrical resistivity structure on their own have a limited utility in geologic and tectonic interpretation owing to the varied possible origins of low resistivity anomalies. In the brittle upper crust, electrical resistivity, or its inverse electrical conductivity, is primarily a function of mineral alteration (e.g. clay content, hydrothermal fluid-rock interactions) or the porosity of fluid bearing stratigraphic units. In the mid- to lower-crust, where deformation is often ductile and fracture networks are less likely to persist over geologic time, low resistivity anomalies are the result of highly conductive phases existing as interconnected networks along grain boundaries. These conductive phases include saline fluids, partial melt, and conductive mineralization, such as sulfides and graphite. In the uppermost mantle, variations in resistivity indicate elevated temperature, hydration of nominally anhydrous mineral phases, and/or the

presence of partial melt. Thus a crucial component of this dissertation is invoking laboratory derived empirical relationships, previous geophysical results, and a wealth of geological observations to place novel magnetotelluric results in the context required to arrive at a unique and defensible interpretation.

1.1 Thesis Outline

The three main chapters contained herein were prepared in the format of stand-alone journal articles intended for publication. Chapters 2 and 3 detail the modeling and interpretation of magnetotelluric data collected for the Deep Rift Electrical Resistivity (DRIFTER) experiment, a large-scale survey of the Rio Grande Rift and southern Rocky Mountains, while Chapter 4 is a more focused study of the resistivity structure beneath the Valles caldera and Jemez Mountains volcanic complex in northern New Mexico. The appendices provide supplementary information for the preceding chapters as well as a detailed catalog of the magnetotelluric data used in this dissertation.

Chapter 2 details the results of two-dimensional anisotropic inversion of the northern-most profile of DRIFTER magnetotelluric data spanning the southern Rocky Mountains, the Rio Grande Rift, the Rocky Mountain Front Range, and the western Great Plains. This chapter provides constraints on the isotropic and anisotropic modeling capabilities of MARE2DEM, a 2D MT inversion program, including both vertical and lateral resolution of features located beneath conductive features in the near surface. The interpretation focuses on quantifying conductivity

mechanisms that produce two low resistivity anomalies: one in the lower crust beneath the Rocky Mountains and another in the sub-continental lithospheric mantle beneath the western-most Great Plains. A variety of end-member interpretative scenarios that fit the MT data are presented with a discussion of which are more likely given a priori geologic and geophysical constraints.

Chapter 3 presents 2D electrical resistivity modeling of the central and southern DRIFTER profiles, collected in the central and southern Rio Grande rift in New Mexico. These two profiles were collected in similar but distinct tectonic environments with the central rift characterized by classic narrow rift half-graben structures bounded by rift flank uplifts, and the southern rift exhibiting features more akin to basin and range type extension. Emphasis is placed on comparing and contrasting resistivity structure along the rift axis and evaluating the strikingly similar features of the lower crust present beneath both profiles.

Chapter 4 is a more focused magnetotelluric study of the Valles caldera and the Jemez Mountains volcanic field. This study utilizes a diverse collection of modern and archival MT data acquired by both industry and the Summer of Geophysical Experience (SAGE) to image two- and three-dimensional electrical resistivity structure beneath a major volcanic center of the western U.S. The 2D modeling provides an investigation into the regional setting of the volcanic field, while the 3D models image the detailed near-surface structure of the caldera interior.

CHAPTER 2

MAGNETOTELLURIC IMAGING OF LOWER CRUSTAL MELT AND LITHOSPHERIC HYDRATION IN THE ROCKY MOUNTAIN FRONT TRANSITION ZONE, COLORADO, USA

2.1 Abstract

We present an electrical resistivity model of the crust and upper mantle from two-dimensional (2D) anisotropic inversion of magnetotelluric data collected along a 450 km transect of the Rio Grande Rift, southern Rocky Mountains, and High Plains in Colorado, USA. Our model provides a window into the modern-day lithosphere beneath the Rocky Mountain Front to depths in excess of 150 km. Two key features of the 2D resistivity model are (1) a broad zone (~200 km wide) of enhanced electrical conductivity (<20 Ωm) in the mid- to lower-crust that is centered beneath the highest elevations of the southern Rocky Mountains and (2) hydrated lithospheric mantle beneath the Great Plains with water content in excess of 100 ppm. We interpret the high conductivity region of the lower crust as a zone of partially-molten basalt and associated deep-crustal fluids that is the result of recent (less than 10 Ma) tectonic activity in the region. The recent supply of volatiles and/or heat to the base of the crust in the late Cenozoic implies that modern-day tectonic activity in the western United States extends to at least the western margin of the Great Plains. The transition from conductive to resistive upper mantle is caused by a gradient in lithospheric water content, with maximum

hydration occurring beneath the Rocky Mountain Front. This lithospheric "hydration front" has implications for the tectonic evolution of the continental interior and the mechanisms by which water infiltrates the lithosphere.

2.2 Introduction

The Rocky Mountain Front (RMF) is a north-south trending physiographic boundary in the west-central United States that separates the Great Plains to the east from the Rocky Mountains and Basin and Range to the west [Fenneman 1946]. The Great Plains are characterized by a low-relief landscape, broad flat sedimentary packages, and anomalously high topography (>1600 m) over a broad region east of the Rocky Mountain Front [Eaton 1987]. This topography slopes gently down to the east for nearly 900 km, finally reaching elevations <300 m at the Missouri River near Kansas City, Missouri. The absence of major faulting, structural dismemberment, and volcanism suggest that the high western plains immediately adjacent to the RMF have been largely undeformed since the Proterozoic assembly of the North American continent. Exceptions to this include (1) tilting, subsidence, and rebound in response to Farallon slab subduction, sedimentation, and subsequent slab removal [Mitrovica et al., 1989; Dickinson et al., 1988] and (2) anorogenic uplift related to lithospheric modification and de-densification caused by hydration of the lithosphere during Farallon slab subduction [Humphreys et al., 2003; Jones et al., 2015].

In contrast, the mountains to the west of the RMF are characterized by high relief and topography, with the southern Rocky Mountains in Colorado representing the most significant collection of high peaks on the North American plate [Eaton 2008]. The modern landscape of the southern Rocky Mountains is the result of a protracted tectonic history extending at least as far back in time as the formation of the Ancestral Rocky Mountains in the Pennsylvanian [Mallory 1958]. Since just the late Cretaceous, the region has been subjected to basement-cored thrust faulting associated with the Laramide orogeny [DeCelles 2004], high-volume silicic volcanism in the Paleogene [Lipman 1992], widespread landscape beveling during the Eocene [Epis and Chapin, 1975], and at least two distinct episodes of continental rifting along the Rio Grande Rift from the Oligocene to the modern day [Chapin and Cather, 1994; Landman and Flowers, 2013]. Quaternary fault scarps [Tweto 1979], geodetic observations [Berglund et al., 2012], seismicity [Nakai et al., 2017], and recent volcanism [Leat et al., 1989] suggest that the southern Rocky Mountains are tectonically active in the present day.

2.2.1 Previous Geophysical Results

Geophysical studies on both regional and continental scales suggest that the physiographic contrast observed across the Rocky Mountain Front is at least coincident with, if not indicative of, a more profound lithospheric discontinuity at depth [Pakiser and Zietz, 1965]. Investigations into seismic velocity of the crust and upper mantle and seismic attenuation suggest the Rocky Mountain Front delineates

the transition between younger, actively deforming lithosphere of western North America and older, more stable Proterozoic lithosphere to the east [Boyd and Sheehan, 2005; Phillips et al., 2014; Schmandt and Lin, 2014; Schmandt et al., 2015].

Teleseismic shear-wave travel time residuals recorded by the Rocky Mountain Front PASSCAL experiment show a distinct increase in residual delay times from east to west across the Rocky Mountain Front [Lee and Grand, 1996]. Subsequent tomographic inversions of those delay times reveal a low-velocity mantle (shear-wave velocity anomalies as low as -4.5% relative to PREM 1981 at depths of 50-100 km) beneath the southern Rocky Mountains in central Colorado [Lee and Grand, 1996]. Li et al. [2002] inverted Rayleigh-wave phase velocities from the same experiment to show that there is also a crustal low-velocity zone (shear-wave velocity anomaly as low as -4% relative to a modified version of AK135) beneath the highest topography in Colorado. Recent analysis of seismic data from the EarthScope USArray and co-deployed regional seismic networks (e.g. CREST [Hansen et al., 2013]) have produced a multitude of seismic-velocity models of the western United States and Rocky Mountain Front [e.g. Schmandt and Humphreys, 2010; Shen et al., 2013; Hansen et al. 2013, Porritt et al., 2014; Schmandt and Lin, 2014]. A broad low-velocity zone in the upper mantle beneath Colorado west of the RMF is a common feature of each of these models. Possible explanations for the anomaly include both thermal and compositional variations in the upper mantle, including both thinned and/or chemically modified lithosphere. Low velocity

anomalies in the lower crust are typically attributed to compositional variations, specifically an abundance of low-density felsic material in the crust west of the Rocky Mountain Front [Decker et al., 1988; Li et al., 2002; Schmandt et al., 2015]. The magnetotelluric (MT) method is particularly well suited for differentiating thermal and compositional origins of geophysical anomalies within the lithosphere. The method is sensitive to contrasts in electrical resistivity, and has resolution capabilities comparable to seismic tomography. Analysis of MT models in the context of independent geological constraints, geophysical models and petrologic data reduces the non-uniqueness associated with interpreting regions of anomalous conductivity.

In this paper we present results from a magnetotelluric survey in central Colorado that straddles the Rocky Mountain Front. Using a 2-D anisotropic inverse modeling approach for determining electrical resistivity structure beneath our profile, we confirm that the RMF is a geophysical boundary in both the shallow and deep lithosphere. In particular, we image (1) a zone of high conductivity in the lower crust beneath the southern Rocky Mountains and (2) distinct compositional modification of the lithospheric mantle beneath the western edge of the Great Plains. We attribute the elevated lower-crustal conductivity to a zone of partial melt and associated saline fluids, and infer modification of the crust to be the result of recent tectonic activity. High conductivity in the lithospheric mantle east of the Rocky Mountain Front is likely due to mantle hydration associated with passage of the Farallon slab.

2.3 Methods and Data

2.3.1 Magnetotellurics

Magnetotelluric data is collected by measuring spatial and temporal variations in the naturally occurring electric (E) and magnetic (H) fields at the surface of the earth. The magnetotelluric impedance tensor (Z) is a second-rank complex tensor that in the frequency domain relates horizontal magnetic fields to horizontal electric fields by

$$\begin{bmatrix} E_X \\ E_Y \end{bmatrix} = \begin{bmatrix} Z_{XX} & Z_{XY} \\ Z_{YX} & Z_{YY} \end{bmatrix} \cdot \begin{bmatrix} H_X \\ H_Y \end{bmatrix} \quad (1)$$

The four components of the complex, frequency-dependent impedance tensor can be represented as scaled amplitude (apparent resistivity, ρ_a, units of Ωm) and phase. The magnetic-field transfer function (T), or tipper, is a complex unitless vector quantity that relates the horizontal magnetic field to the vertical magnetic field by

$$H_Z = \begin{bmatrix} T_X & T_Y \end{bmatrix} \cdot \begin{bmatrix} H_X \\ H_Y \end{bmatrix} \quad (2)$$

These transfer functions vary both spatially according to the electrical resistivity structure of the subsurface and with frequency as a function of changes in subsurface resistivity with depth. A magnetotelluric sounding consists of estimates of impedance and tipper as a function of period, obtained via spectral analysis of

electromagnetic-field time series. The depth of investigation of each sounding depends on both the period (the inverse of frequency) and the local electrical resistivity structure, with longer periods and a more resistive subsurface allowing for a greater depth of investigation.

The magnetotelluric method is in particular sensitive to electrical resistivity, or its reciprocal conductivity, which is dependent upon mineralogy, fluid content, partial melting, and chemical alteration of the subsurface. Sources of high conductivity in sedimentary basins and within the brittle upper crust include clay minerals, fault gouge, and groundwater. The primary controls on electrical conductivity in the lower crust are the abundance and interconnectedness of aqueous fluid, small volumes of partial melt, and grain boundary mineralization. Electrical conductivity in the upper mantle is primarily controlled by the concentration of water in nominally-anhydrous minerals [Poe et al., 2010; Dai and Karato, 2009], the presence of partial melt, and to a lesser extent the bulk temperature of the rock [Constable et al., 1992].

2.3.2 Data

Twenty-three magnetotelluric soundings were collected in central Colorado along a 450 km profile located at 39.2°N latitude (Figure 2.1). Time series data at each MT site were recorded for two orthogonal components of the horizontal electric field and three orthogonal components of the magnetic field at each station location. Broadband magnetotelluric data (100 Hz - 1000 s) were collected using

Electromagnetic Instruments low-frequency MT24 data loggers and three orthogonal Schlumberger magnetic induction coils. Long period MT data (10 - 11,000 s) were collected using NIMS data loggers and three-component fluxgate magnetometers. Electric field measurements were collected using two orthogonal 100 m dipoles each consisting of two non-polarizing electrodes connected by copper wire. Broadband instruments were allowed to record for 24-48 hours while long period instruments recorded for three to six weeks. Of the 23 stations, six were instrumented with only broadband equipment, seven with only long-period equipment, and ten with both. Nominal station spacing was 5-10 km near the center of the profile and more distributed (up to 30 km spacing) on the eastern and western ends of the profile. Data were collected simultaneously at several (2-4) stations to permit multi-station remote-reference processing [Egbert, 1997; Gamble et al., 1979].

Time-series processing and transfer-function estimation was performed using the approach of Egbert [1997] for multi-station arrays with remote referencing [Gamble et al., 1979]. Some stations required additional pre-processing prior to transfer function estimation due to operator error, data logger malfunction, and/or station disturbance during recording. Pre-processing steps included trimming of data contaminated by cultural noise, scaling, and correction of layout errors (e.g. electric and magnetic channel flips). Figure 2.2 shows representative transfer function curves for two stations: stn016 located in the mountains and stn024 in the plains.

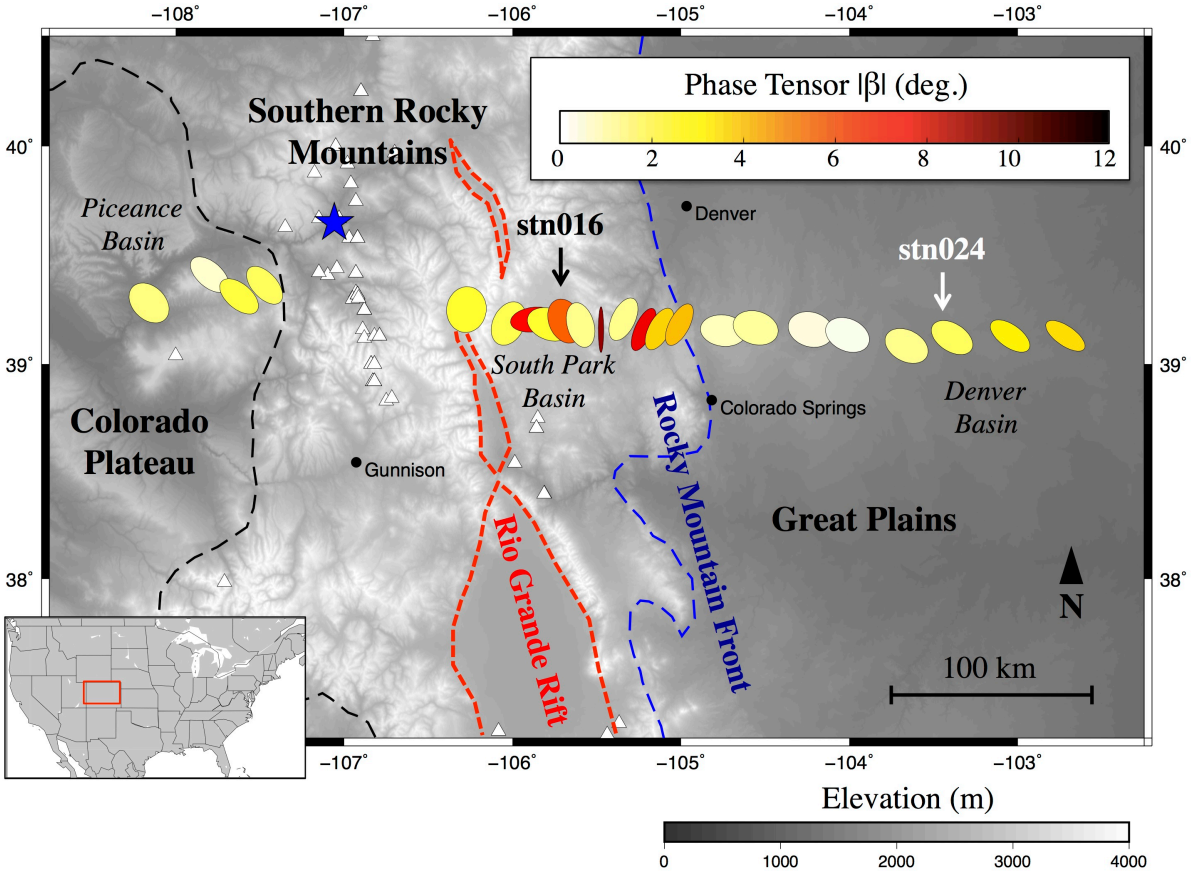

Figure 2.1. Map of magnetotelluric stations in central Colorado. Station locations represented by magnetotelluric phase tensor ellipses at period of 1000 s. Phase tensor ellipse fill color is scaled by $|\beta|$, with larger values indicating 3D structure. In the presence of 2-D electrical resistivity structure, the major axis of phase tensor ellipses will align parallel [perpendicular] to regional geoelectric strike for data collected on the resistive [conductive] side of a geoelectrical contact. Note the 90° rotation of the phase tensor ellipses across the Rocky Mountain Front [blue dashed line] that separates resistive basement-cored uplifts to the west from conductive sedimentary units of the Denver Basin to the east. Red dashed lines are approximate outlines of axial basins of the Rio Grande Rift. Black and blue dashed lines are physiographic province boundaries [Fenneman, 1946]. Blue star is location of Quaternary basalt flow near Dotsero, CO [see Section 4.2]. White triangles are young volcanic rocks [<10 Ma] from the NAVDAT database [Walker et al., 2006]. Location of MT data shown in Figure 2.2 indicated by arrows and station labels.

The magnetotelluric phase tensor [Caldwell et al., 2004], a mathematical transformation of the impedance tensor, is used to examine the dimensionality of MT data. Interpretation of the phase tensor is performed by examining maps of normalized phase tensor ellipses, the major and minor axes of which are proportional to the rotationally-invariant maximum and minimum principle values of the represented phase tensor. Circular phase tensors reflect a one-dimensional impedance (layer-cake subsurface resistivity structure) while non-circular ellipses indicate higher-order electrical resistivity structure (e.g. lateral variations in resistivity). In the two-dimensional (2D) case, the major axis of the ellipse will align either perpendicular or parallel to the predominant geo-electric strike for data collected on the conductive or resistive side, respectively, of a geo-electrical contact. Figure 2.1 shows normalized phase tensor ellipses for all 23 MT stations at a period of 1000 s. Note the major-axis orientation of the phase tensor ellipses changes from generally north-south to east-west moving west to east across the Rocky Mountain Front, indicating a major geo-electric contact coincident with the Rocky Mountains-Great Plains physiographic boundary. The scalar value β, another rotationally-invariant phase tensor parameter, is an indicator of three-dimensional (3D) geo-electric structure. Typically, $|\beta| > 3^{o}$ is considered an indication of 3D structure [Booker 2014]. The majority of the ellipses in Figure 2.1 exhibit low values of β (see fill color) with either major or minor axes trending sub-parallel to the profile, indicating that two-dimensional inversion of the measured data is justified. We note high β values are observed for several stations in the mountains (106ºW-105ºW) at

period of 1000 s. Given the high resistivity of the plutonic and metamorphic rocks of the Rocky Mountain Front Range that underlie these particular stations, the phase tensors at the displayed period may have sensitivity to mid- to lower crustal structure, indicating that the geoelectric structure is complex at depth. Quasi-3D electrical resistivity structure is also observed in the distribution of induction vector orientations. The ability of the 2D anisotropic inversion to fit these pseudo 3D data is shown in Figure 2.2a for stn016.

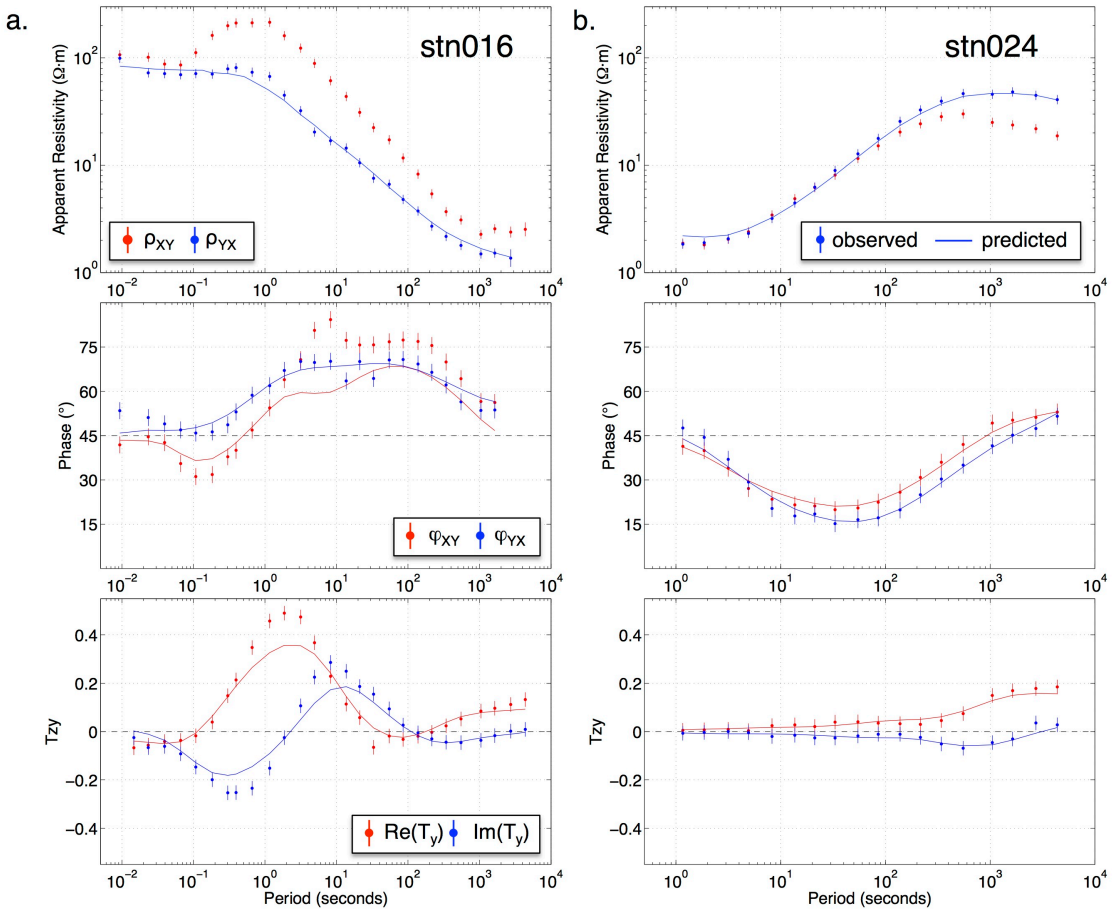

Figure 2.2. [previous page] MT apparent resistivity, phase, and tipper [T_Y] [data points with 1 sigma uncertainty] and 2D anisotropic model fits [solid lines] for stations [a] 016 in the mountains and [b] 024 in the plains. TE mode [Z_{XY}] apparent resistivity omitted from the inversion inputs to reduce influence of 3D electrical resistivity structure.

2.3.3 2-D Inversion

We invert for two-dimensional isotropic and anisotropic electrical resistivity structure along our profile using the finite-element inversion algorithm MARE2DEM [Key 2016]. The MARE2DEM algorithm utilizes an Occam's inversion approach [Constable et al., 1987], which seeks to iteratively determine the smoothest possible electrical resistivity structure that minimizes the functional

$$U = \| \boldsymbol{\partial}\mathbf{m} \|^2 + \mu^{-1}\left[\| \mathbf{W}\left(\mathbf{d} - F(\mathbf{m})\right) \|^2 - \chi^2 \right] \quad (3)$$

where **d** is the magnetotelluric data, F(**m**) is the forward MT response [Key and Ovall, 2011], **W** is a diagonal matrix of inverse data standard errors, μ is a regularization factor, χ^2 is a user-defined misfit tolerance, and **δm** is a model roughness term. The inversion progresses by first automatically sweeping through values of μ to find the best fitting model and iterating until the χ^2 target misfit is achieved. The second phase of the inversion involves searching for the smoothest model that also achieves the desired misfit. Model updates are performed at each iteration via linearizing the functional about a starting model. The inclusion of the χ^2 tolerance in the functional allows the inversion to avoid extreme local minima

based on select noisy or non-physical data. Data fit is assessed using a root mean square misfit that is normalized by data errors and the number of variables

$$\mathrm{RMS} = \sqrt{\frac{1}{n}\sum_{i=1}^{n}\left[\frac{d_i - F_i(\mathbf{m})}{s_i}\right]^2} \quad (4)$$

where d_i and $F_i(m)$ are individual and datum and corresponding forward response, s_i is data uncertainty and n is the total number of data points.

Anisotropy for the purposes of this study refers to strictly horizontal (or transverse) anisotropy, wherein the electrical resistivity of each grid cell is allowed to vary in two directions: parallel (ρ_{yy}) and perpendicular (ρ_{xx}) to the profile trace. It is expected that transverse anisotropic structure oriented at an oblique angle to the profile trace will partition into ρ_{xx} and ρ_{yy} components. Anisotropy is incorporated into the inversion through the model roughness term, which contains a measure of the difference between the ρ_{xx} and ρ_{yy} resistivity models, regularized by an anisotropy penalty factor, α. The value of α varies from 0 (completely anisotropic) to 1 (isotropic) and is defined by the user prior to inversion. For the anisotropic inverse models shown in this study we set α = 0.1 to allow for moderate anisotropy.

2.3.4 Data Preparation

Inputs into the inversion include apparent resistivity and phase of the principal impedances (Z_{XY} and Z_{YX}) and the complex 2D component of the tipper (T_Y). The apparent resistivity of the transverse electric (TE) mode, $\rho_{a,xy}$, was omitted

from the inversion input due to its sensitivity to off-profile (i.e. 3D) electrical resistivity structure [Wannamaker et al., 1984]. The remaining data were decimated to five periods per decade, yielding a total of 30 inverted periods distributed logarithmically over six decades (0.01 - 10,923 s). A subset of the decimated data (~13%) was manually culled via visual inspection of transfer function curves to eliminate obvious outliers. In total, 2496 data points distributed across all 23 stations were inverted for 2D isotropic and anisotropic resistivity structure. Prior to inversion, data errors for apparent resistivity and phase were increased to a minimum threshold, or error floor, of 10% $|Z_{ij}|$, corresponding to an error in phase of 2.8°, to reduce the likelihood of over-fitting data points with exceptionally small statistically-determined errors. An error floor of 0.03 was applied to all tipper components. Data inputs for the isotropic and anisotropic inversions were identical.

2.3.5 Mesh Preparation

Resistivity models for each inversion were parameterized as unstructured meshes using the graphical user interface Mamba2D (http://mare2dem.ucsd.edu/). Mamba2D is a MATLAB based program that uses Delaunay triangulation to automatically populate regions within the mesh with triangular grid cells of similar size, where size is defined by the nominal side length of each triangular grid cell. An "area of interest" extending from the surface to 150 km depth (approximately one-third of the survey aperture) and 25 km laterally beyond the first and last stations

along the profile was divided into three layers initially populated by triangles of similar size. The three horizontal layers are parameterized as follows: 2 km triangles for 0-10 km depth, 5 km triangles for 10-60 km depth, and 10 km triangles for 60-150 km depth. Outside the region of interest, triangles are allowed to grow exponentially in size towards the edges of the model domain that extends 1000 km in all directions. The atmosphere is parameterized as a 1000 km thick layer with a fixed resistivity value of $1x10^9$ Ωm. Topography is not incorporated into the model. The resistivity of the isotropic half-space starting model, 30 Ωm, was selected by determining which among a series of isotropic half-space models with varying resistivity values exhibited the smallest initial misfit to the data. Model grid parameterization and the starting model for each of the isotropic and anisotropic inversions were identical.

2.4 Results

Figure 2.3 shows the isotropic resistivity model obtained by inverting the magnetotelluric data along our profile. This model achieved an RMS of 1.3 given the applied errors, representing an 88% reduction in data residual relative to the starting model (initial RMS of 11.3). The horizontally alternating pattern of conductive and resistive anomalies visible in the mid-crust to upper mantle (25-100 km depth) is reminiscent of the modeling results of Heise and Pous [2001] on the isotropic inversion of anisotropic data. They observed that 2D isotropic inversions of azimuthally anisotropic magnetotelluric data produce characteristic artifacts in

modeled resistivity structure, including alternating regions of high and low resistivity. Motivated by these previous findings and the clear pattern seen in Figure 2.3, we performed a similar modeling study using MARE2DEM. The results of that study, which can be found in the Appendix, support the hypothesis that some of the structure observed in the isotropic model in Figure 2.3 is an artifact introduced by insufficient modeling of anisotropic data (Figure A.1). For the purposes of model analysis and interpretation going forward we will focus on the anisotropic inversion results.

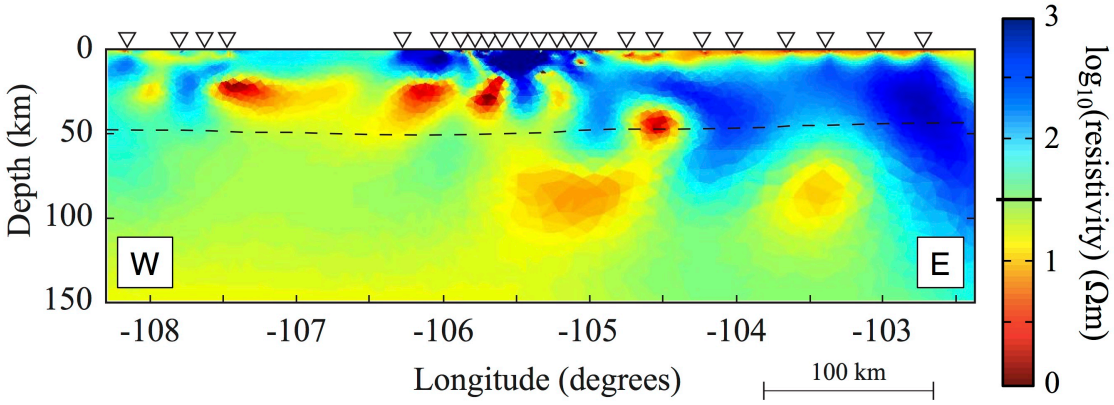

Figure 2.3. 2D isotropic electrical resistivity model. Black dashed line is Moho estimate from Shen et al. [2013]. Note alternating resistor-conductor-resistor pattern suggestive of anisotropic resistivity structure in the lower crust [Appendix, Figure A.1]. Inverted white triangles indicate MT station locations. Bold line on resistivity color bar indicates starting model resistivity of 30 Ωm.

Figure 2.4 shows our preferred 2D horizontally-anisotropic resistivity model. The models in Figures 2.4a and 2.4b show the electrical resistivity structure

perpendicular (ρ_{xx}) and parallel (ρ_{yy}) to profile, respectively. The ρ_{xx} model represents the resistivity structure parallel to inferred north-south geo-electric strike. After seven iterations, our preferred model achieved an RMS of 1.2 given the applied errors, representing an 89% variance reduction relative to the starting model (initial RMS of 11.3). The forward response of the final model and data fits for two representative stations are shown in Figure 2.2.

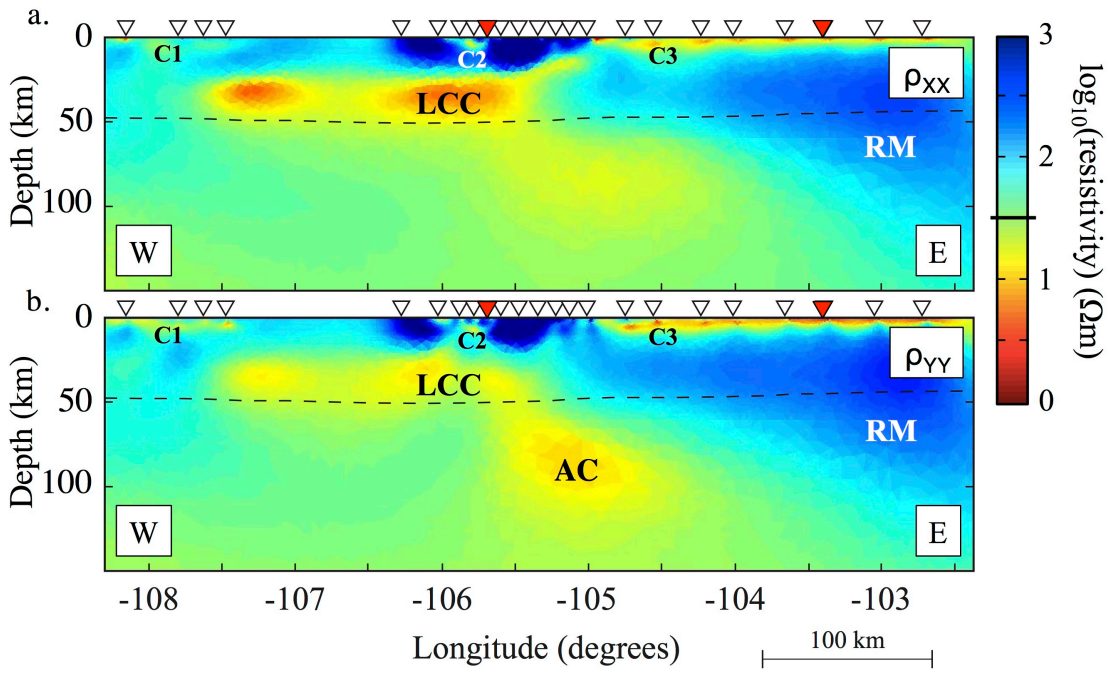

Figure 2.4. 2D anisotropic electrical resistivity models. Models for resistivity in [a] N-S [ρ_{xx}] and [b] E-W [ρ_{yy}] directions. Annotations as in Figure 2.3 plus red triangles denote along-profile location of stations shown in Figure 2.2. LCC = lower crustal conductor, RM = resistive mantle, AC, C1, C2, C3 = low resistivity anomalies [see text].

2.4.1 Upper Crust

The shallow crust (0-10 km depth) along the profile is resistive with the exception of three thin conductors at or near the surface. These conductors range in resistivity from 5-30 Ωm and correlate with the known sedimentary basins labeled in Figure 2.1. These basins and the corresponding labels in Figure 2.4 are, from east to west, the westward-thickening Denver Basin (C3), the South Park Basin (C2), and the Piceance Basin (C1). The upper crust (0-25 km) outside these conductors is generally resistive (>100 Ωm), reaching a maximum value of 1000 Ωm beneath the Rocky Mountain Front Range (105ºW-106.5ºW).

2.4.2 Lower Crust

The crust beneath the Rocky Mountains is electrically conductive (low resistivity) from mid-crustal depths of 25-35 km to the base of the crust at 45-50 km depth [Sheehan et al., 1995; Gilbert 2012, Shen et al., 2013]. Dense station coverage on the west and east ends of this lower crustal conductor (LCC) constrains its width to ~200 km, from western Colorado to just east of the South Park Basin. Model sensitivity testing (Appendix, Figure A.3) confirms that the data supports a laterally continuous LCC despite the ~100 km gap in station coverage (Figure 2.1). Magnetotellurics is primarily sensitive to the conductance (conductivity-thickness product) of conductors, and thus there is a trade off between the resolvable thickness and absolute conductivity of the LCC (see Appendix, Figure A.2). Figure 2.5 shows the vertically integrated conductance along the profile of both the ρ_{xx} and

ρ_{yy} models, divided into three layers of equal thickness: upper crust (0-25 km), lower crust (25-50 km), and upper mantle (50-75 km). The conductance of the lower crust beneath the Rocky Mountains is 1500-2000 Siemens (S). In comparison to other regions of our model, the LCC exhibits twice the conductance of the upper mantle directly beneath it, four times that of the Denver Basin (~500 Siemens), and an order of magnitude greater than that of the adjacent lower crust beneath the Great Plains. A lower-crustal conductance of 2000 S is extremely high for tectonically stable lower crust (averaging 40-400 S) [Jones 1992] but is modest compared to more tectonically active regions such as the Tibetan plateau (minimum 6000 S) [Li et al., 2003] and the East African Rift (~10 kS) [Desissa et al., 2013]. Given the well-resolved top of the LCC and assuming a uniform electrical resistivity for the entire lower crust yields a maximum average resistivity of 12-17 Ωm. Any vertically-varying distribution of lower crustal conductivity would thus require the existence of zones of much lower resistivity. Indeed if the observed lower-crustal conductance were confined to a layer 200 m thick within an otherwise resistive crust, the resistivity of that conductor would be ~0.1 Ωm. Additional petrologic, geologic, and geophysical data are required to reasonably constrain the total thickness and conductivity of this anomaly.

The lower-crustal conductor further exhibits the strongest degree of anisotropy (anisotropy factor of 2-3) of any feature in the top 75 km of the model (note separation of conductance curves in Figure 2.5b). Electrical resistivity in the lower crust appears to be enhanced in the x-direction (north-south, strike parallel)

relative to the y-direction (east-west, strike perpendicular) (see Figures 2.4 and 2.5). Thus the electrical conductivity in the lower crust is enhanced in a direction sub-parallel to both the Rocky Mountain Front and the Rio Grande rift.

The anisotropic behavior we observe could be an artifact of the inversion produced by a series of north-south oriented elongate conductors with finite along strike length (i.e. quasi 3D conductive bodies parallel to strike). In this scenario, the segmented LCC shown in the isotropic model would be closer to the real Earth structure. We advocate instead for a bulk anisotropy based on the behavior of the tipper functions over the top of the conductor. The wavelength of the segmented conductors in Figure 3 is on the order of ~20 km. With nominal station spacing over the LCC of 5-10 km we should be able to resolve variability in the tipper due to the presence of strong lateral resistivity contrasts in the lower crust. Pseudo sections of Parkinson-convention tipper, especially the along profile component (Tzy) show a binary distribution of induction vector orientations, with western stations pointing east and eastern stations pointing west, towards the interior of the LCC, as expected for a cohesive conductor.

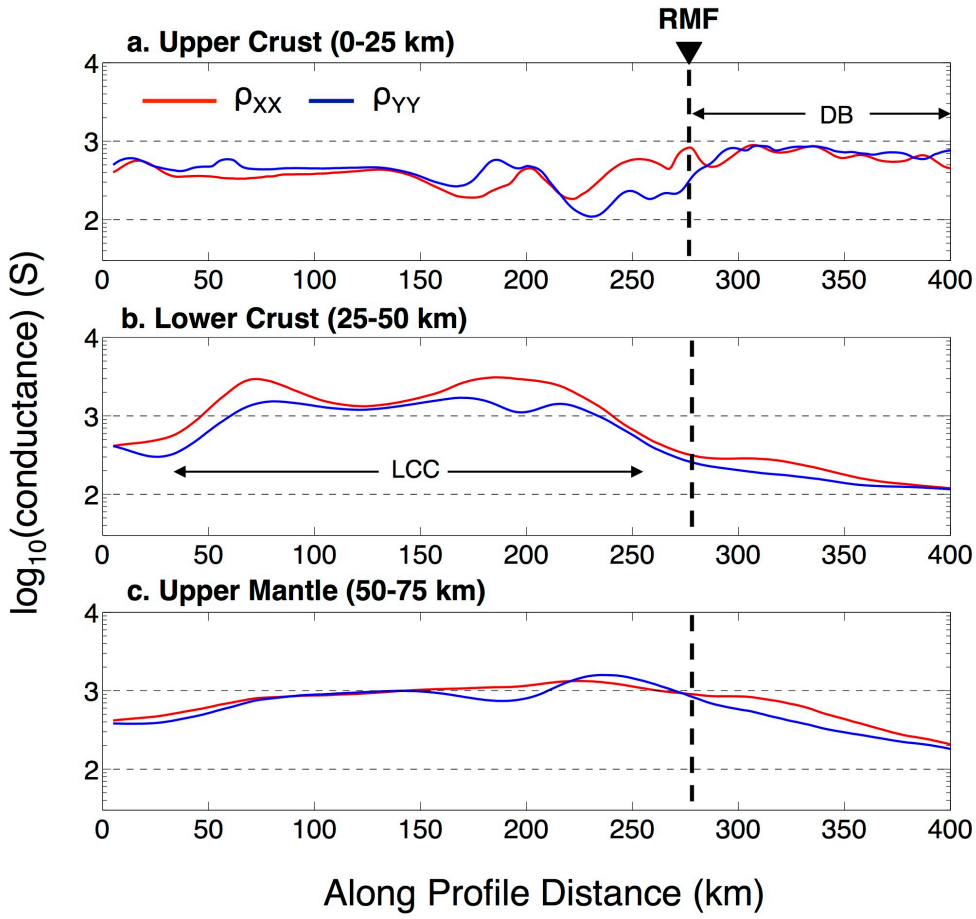

Figure 2.5. Vertically-integrated conductance [conductivity-thickness product] of final [ρ_{xx}] and [ρ_{yy}] resistivity models for [a] upper crust [0-25 km depth], [b] lower crust [25-50 km depth], and [c] upper mantle [50-75 km depth]. Bold dashed line indicates location of Rocky Mountain Front [RMF]. Conductance along profile shown as separate lines for ρ_{xx} and ρ_{yy} resistivity models. Along profile distance = 0 corresponds to location of westernmost station at approximately (39.2ºN, 108.2ºW). DB = Denver Basin, LCC = lower crustal conductor.

2.4.3 Upper Mantle

The upper mantle in our anisotropic model is electrically conductive (< 30 Ωm) beneath the Rocky Mountains and increasingly resistive east of the Rocky Mountain Front. An eastward thickening wedge of resistive material extending

from the base of the crust into the upper mantle (RM in Figure 2.4) characterizes the lateral transition from conductive to resistive mantle structure. This is in contrast to a similar lateral transition in the lower-crustal resistivity structure that is characterized by a sharp vertical contact located directly beneath the RMF. The gradual increase in upper-mantle resistivity to the east is also evident in Figure 2.5c, which shows gradually decreasing upper-mantle conductance east of the RMF. The maximum resistivity observed in the upper mantle lies near the base of the crust on the eastern edge of our profile.

The lowest resistivity in the upper mantle is observed in the ρ_{yy} model directly beneath the Rocky Mountain Front (AC in Figure 2.4). While this anomaly appears in the model as an isolated body of low resistivity beneath the Front Range, it is possible that enhanced conductivity in the upper mantle extends to the west, beneath the lower-crustal conductor, and/or vertically down into the mantle directly beneath AC. The masking effects of the LCC and limited data coverage west of 106.25ºW make the lateral extent of this conductive anomaly difficult to resolve. By ~150 km depth the upper mantle is conductive (< 30 Ωm) across the entire profile.

To first order, electrical resistivity structure below 150 km is characterized by subtle variations in resistivity, with a range of resistivity values spanning only half a decade in log-resistivity space (10-30 Ωm) over the entire model from 150-300 km depth. Lateral variations are practically non-existent and the overall trend is of decreasing resistivity with depth. If our data were sensitive to this type of resistivity structure, we would expect apparent resistivity of the off-diagonal

impedance elements to decrease at long periods and for the corresponding phase at those periods to be increasing toward 90º. We do not observe these trends at most stations (e.g. Figure 2.2a, also see Appendix) and where we do (e.g. Figure 2.2b) we prefer to attribute these effects to the large resistivity contrast in the uppermost mantle (i.e. 50-150 km depth) rather than a subtle resistivity gradient below 150 km. In an effort to limit our interpretation to the minimum structure required by the data, we therefore omit discussion of a possible vertical conductivity gradient in the mantle below 150 km.

2.5 Discussion

Important elements of the 2D anisotropic resistivity models shown in Figure 2.4 include: (1) a series of thin, near-surface conductors; (2) a crust that is broadly resistive with the exception of the LCC; (3) the lower-crustal conductor; and (4) the gradual transition from conductive to resistive upper mantle under the Great Plains. We will address the first two briefly before commenting on the lower-crustal conductor and mantle resistivity structure in greater detail. Figure 2.6 shows an interpretive view of the anisotropic resistivity model with labels corresponding to major features and subsequent interpretation.

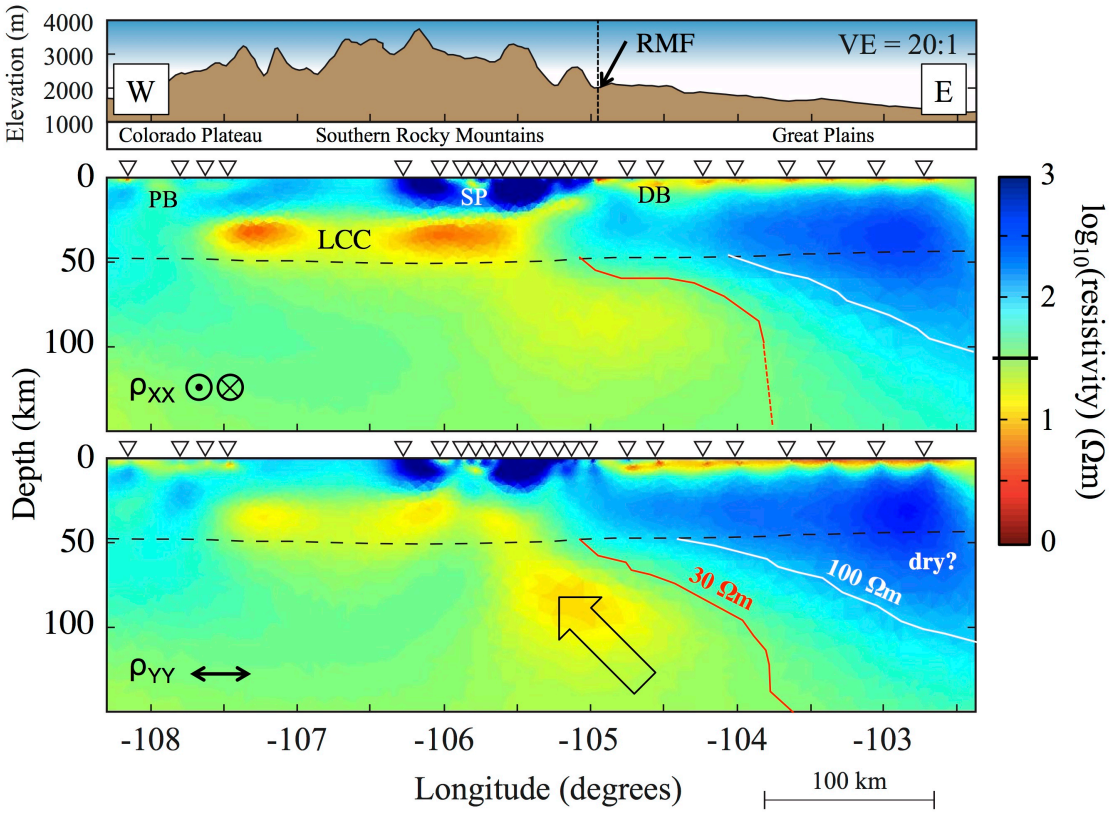

Figure 2.6. Interpretation of anisotropic electrical resistivity model. Models for resistivity in [top] N-S [ρ_{xx}] and [bottom] E-W [ρ_{yy}] directions. Includes topography and approximate physiographic province boundaries along profile. Annotations as in Figure 2.3 plus white and red lines are approximate resistivity contours for 30 and 100 Ωm, respectively. Arrow in ρ_{yy} model indicates supply of heat and/or volatiles to the lithospheric mantle. LCC = lower crustal conductor; DB = Denver Basin; SP = South Park Basin; PB = Piceance Basin; RMF = Rocky Mountain Front.

The three near-surface conductors (PB, SP, and DB in Figure 2.6) correlate with three deep sedimentary basins: the Piceance, South Park, and Denver Basins (Figure 2.1). The low resistivity observed in each of these basins is likely due to the presence of electrically conductive Mesozoic marine shales. These are the Mancos shale in the Piceance and South Park Basins and a correlating unit, the Pierre

shale, in the Denver Basin [Izett et al., 1971; Maughan 1988]. While the conductivity-thickness trade off discussed above prevents us from directly measuring the thickness of these sedimentary basins using our 2D resistivity model, we can derive an estimate for thickness using observed conductance and in situ measurements of electrical resistivity. For example, ground and airborne electromagnetic measurements of the Pierre shale in the Denver Basin show that it is electrically conductive, typically 3-8 Ωm [e.g. Ackermann 1974; Abraham et al., 2012]. Assuming that this unit is responsible for the majority of the upper-crustal conductance observed east of the Rocky Mountain Front (~500 S, see Figure 2.5), we calculate a thickness for the Pierre shale of 1500-4000 m, which is consistent with previously published estimates for that particular unit in the Denver Basin (e.g. 2420 m, [Porter and Weimar, 1982]).

Excluding the lower crustal conductor and the sedimentary basins discussed above, the top 50 km of our anisotropic resistivity model exhibits conductance values of stable tectonic crust [Jones 1992]. The upper crust to the west, beneath the Rocky Mountain Front Range, appears to exhibit substantially greater resistivity (>1000 Ωm) than that of the Great Plains (100-300 Ωm). This contrast is likely in part due to the screening effect of the conductive Denver Basin masking higher resistivity values in the upper crust beneath the Great Plains. The near-surface conductor associated with the Denver Basin is much thicker than estimated depth to resistive basement [Mooney and Kaban, 2010], indicating vertical smearing of this conductor. There is no such screening effect observed for the Rocky

Mountain Front Range, where resistive metamorphic and plutonic basement rocks often outcrop at the surface. Previous geophysical studies suggest that the bulk composition of the shallow crust in the southern Rocky Mountains has been altered by repeated intrusion of high-volume silicic magma bodies in the late Cenozoic [McCoy et al., 2005; Li et al., 2002; Decker et al., 1988]. Our results do not contradict this interpretation. However, our results do suggest that there is no significant volume of fluid or partial melt in the upper crust today. A large volume of interconnected melt fraction or aqueous fluid in the upper crust would significantly reduce bulk resistivity, which we do not observe.

2.5.1 Lower Crustal Conductor

2.5.1.1 Solid-state Conductivity Mechanisms in the Lower Crust

The presence of low resistivity in the lower crust and upper mantle is consistent with previous investigations into the electrical resistivity structure of the lithosphere in Colorado. Reitzal et al., [1970] present the results of a large scale geomagnetic deep-sounding (GDS) survey of the western United States and find two broad "ridges" of high conductivity in the uppermost mantle, one beneath the southern Rocky Mountains and Rio Grande Rift and the other along the Wasatch Front in Utah. Both anomalies are elongate in the north-south direction, parallel to the Rocky Mountain Front. Subsequent modeling of that same data by Porath [1970] yielded two quantitative models of upper mantle resistivity structure that confirmed that high conductivity shallows beneath the Rocky Mountains in

Colorado. Unfortunately, that study lacked the depth resolution to differentiate between models with high conductivities near the lithosphere-asthenosphere boundary at 150 km, and an alternate but equally well fitting model with high conductivity near the base of the crust at 45 km. Our results suggest that the model with a shallower conductor in the lower crust and uppermost mantle is the more likely scenario

The mechanisms most often invoked for explaining low resistivity in the lower crust are highly conductive phases that form interconnected conduction pathways along grain boundaries, including sulfide minerals, graphite films, and fluids such as partial melt or saline brines [Yang 2011]. Kariya and Shankland [1983] show that the resistivity of crustal rocks may also decrease with increasing temperature, e.g. dry basaltic rocks decrease in resistivity from 10^4 to 20 Ωm from 500-1000ºC. Low seismic velocities in the upper mantle [e.g. Hansen et al., 2015] and elevated crustal geotherms [Decker et al., 1988] suggest that upper-mantle and lower-crustal temperatures in some regions of the southern Rocky Mountains in Colorado may easily exceed 1000ºC. Could elevated crustal temperatures, essentially hot dry rock, produce the observed conductivity anomaly in the mid-to lower crust without the need for additional conductivity mechanisms?

Kariya and Shankland [1983] compile results from a multitude of laboratory studies to examine the effect of temperature on the bulk resistivity of dry, sub-solidus crustal rocks of both mafic and felsic composition. They show that dry rocks of felsic and intermediate compositions do not achieve resistivity values below

~2000 Ωm, even at elevated temperatures approaching the solidus (~1000ºC). Basaltic rocks can achieve the resistivity required to explain the lower crustal conductor ($\rho < 20$ Ωm), but only at or near the solidus. Adjusting for the effect of pressure on the basalt dry solidus would theoretically allow the lower crust to achieve higher temperatures (and thus lower resistivity) without melting (e.g. maximum temperature of 1200ºC at 50 km depth). However, in order for elevated bulk temperature to account for the observed lower crustal anomaly, the entire crust from 25 km depth to the crust-mantle interface would need to be comprised of basalt at or above 1000ºC. Not only are mid-crustal temperatures >1000ºC not supported by regional estimates of crustal geotherms [e.g. Decker et al., 1988], several seismic tomography studies argue in favor of a predominantly felsic composition of the lower crust west of the Rocky Mountain Front [e.g. Li et al., 2002; Schmandt et al., 2015]. We conclude that if the lower crust is dry, variations in bulk temperature and composition are insufficient to produce the observed conductivity anomaly without additional contributions from grain-boundary conduction mechanisms.

Sulfide mineralization and thin graphite films can be exceptionally conductive and produce significant low resistivity anomalies in otherwise cold and dry lower crust [e.g. Bedrosian and Box, 2016; Bedrosian 2016; Boerner et al., 1996]. Thin graphite films form when thick packages of carbon bearing sedimentary rocks, typically deposited in deep marine basins, are subjected to intense heat and pressure, leading to the formation of graphite films along metamorphic fabrics.

Sulfide mineralization occurs by a similar process, involving large volumes of sulfide-bearing sedimentary rocks, also typically sourced from deep marine depositional environments. The presence of graphite or sulfide mineralization in the deep crust requires both a geologic source of the appropriate minerals and a tectonic history that includes forces capable of emplacing those minerals in the deep crust. There is no evidence to suggest that central Colorado meets either of these requirements.

The most significant source of sulfide mineralization in Colorado is the "Colorado Mineral Belt" (CMB) [Tweto and Sims, 1963], a collection of sulfide-bearing hydrothermal, volcanic, and plutonic ore-bodies that form a northeast trending line from the southwest corner of the state to near Boulder, Colorado. The CMB crosses our profile near 106ºW longitude, well within the surface projection of the lower crustal conductor. However, the CMB is a relatively narrow feature (~50 km wide at most) and the presence of sulfides near the surface does not require the existence of large volumes of sulfide mineralization at depth. In terms of graphite mineralization, there is no geologic evidence to suggest a large source volume of carbon-bearing rocks exist in central Colorado.

2.5.1.2 Partial Melt

We consider saline fluids and partial melt the most likely sources of high conductivity in the lower crust of the southern Rocky Mountains. The inherent non-uniqueness of the magnetotelluric problem and the tendency for conductive bodies

to smear vertically in regularized inversion (e.g. Figure A.2) make it difficult to differentiate between fluids and melt with MT alone. We will use petrologic, geochemical, and additional geophysical evidence to investigate the likelihood that the imaged conductor is partial melt, saline fluid, or a combination of the two. Figure 2.7 provides a diagram of the various melt and fluid distributions described below.

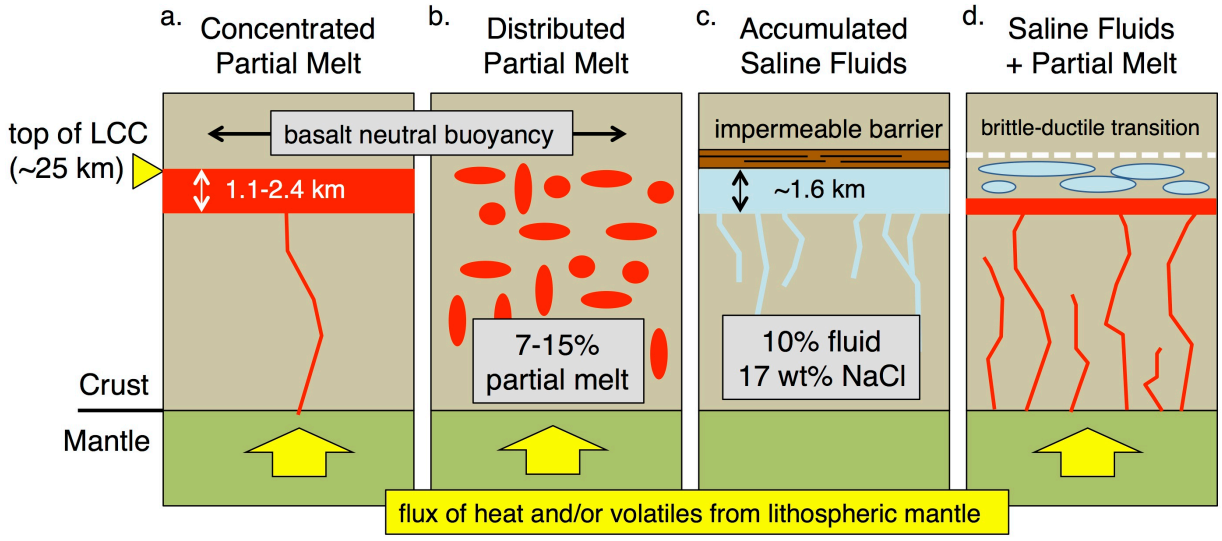

Figure 2.7. Collection of partial melt and/or fluid distributions that could produce the high conductivity observed in the lower crust beneath the Rocky Mountains. Including: a series of molten sills [a], distributed partial melt [b], saline fluid ponding beneath an impermeable barrier to upward fluid flow [c], and intermediate combinations of ponded fluid and distributed and/or ponded partial melt. Yellow arrow represents supply of heat and/or volatiles driving production of melt in lithospheric mantle. Preferred interpretation most closely resembles [d] [see text for details].

We first consider the end-member case in which the high conductivity of the lower crustal conductor is attributed solely to partial melt (Figures 2.7a and 2.7b). Annen et al. [2006] describe in detail the type of deep-crustal magma reservoir, or "lower crustal hot zone", that could produce the observed conductivity anomaly: Over a protracted period of time, basaltic magma is intermittently or continuously injected into the crust from the underlying mantle as horizontal sills. The basaltic melt then stalls in the mid- to lower crust either because it is of sufficient density to be neutrally buoyant or because it is sufficiently viscous due to a higher volatile content. The melt then cools and fractionates into more buoyant, andesitic melt that rises towards the surface, leaving behind a basalt residual. Small pipes of basaltic melt may also escape towards the surface [Jacob et al., 2015].

There is ample evidence to support the existence of this petrologic model at work in the southern Rocky Mountains in the present or the very recent past. As stated previously, seismic tomography reveals the upper mantle directly beneath the Rocky Mountains to be anomalously warm and may contain melt that could be supplied to the lower crust [e.g. Humphreys et al., 2003]. The presence of melt in the crust would increase seismic attenuation and Phillips et al. [2014] observe that seismic attenuation of Lg surface waves at frequencies corresponding to crustal depths (0.75-1.5 Hz) is high for most of Colorado west of the Rocky Mountain Front. Levandowski et al. [2014] found that mapping seismic shear-wave velocity to density structure overestimates the buoyancy of the crust in central Colorado. They conclude that the presence of crustal melt could produce the observed effect, as

partial melt would greatly reduce shear-wave speed without significantly altering bulk density. Geotherm estimates from Decker et al. [1988] suggest that the crust beneath the Rio Grande Rift in central Colorado (106.25ºW along our profile) resides above the basalt dry solidus at depths >36 km and above the alkali basalt saturated solidus at even shallower depths. Lastly, and perhaps most directly relevant, there is a collection of Quaternary age basalt flows in central Colorado, the youngest of which was erupted ~4,150 years before present [Rowe et al., 2015] near Dotsero, CO (blue star, Figure 2.1). Geochemical analysis performed by Leat et al. [1989] suggest that the Dotsero magmas did experience at least a limited amount of fractional crystallization at pressures appropriate for the lower crust.

Assuming that the elevated electrical conductivity observed in the mid- to lower-crust is the result of a distinct crustal zone containing some unknown melt fraction, we can constrain the physical and petrologic properties of that melt using the work of Waff [1974]. The bulk conductivity of a rock hosting partial melt is largely dependent on the electrical conductivity of the melt, the degree to which the melt is connected, and the fraction of the rock that contains partial melt. The contribution of the solid matrix resistivity to the bulk electrical properties of the rock is in most cases negligible. We will need to independently constrain most of these parameters if we are to extract a meaningful interpretation of the imaged MT anomaly.

We start by constraining the various parameters that control the conductivity of the melt. We utilize the online tool SIGMELTS [Pommier and Trong, 2011] which

uses a large database of experimental results and empirically-derived relationships to estimate the electrical conductivity of a melt based on a variety of physical and chemical parameters. More specifically, SIGMELTS provides a means for calculating silicate melt conductivity as a function of temperature, pressure, and melt composition (wt% H_2O, Na_2O, SiO_2). Partial melt is only electrically conductive so long as it is fluid, so presumably any melt observable by MT has a minimum temperature above the solidus. The basalt dry solidus for depths of 25-50 km is 1160º-1200ºC. The solidus for wet basalt in the mid-crust is much lower, ~800ºC [Decker et al., 1988], due to the effect of water lowering the melting point. In the high temperature extreme we assume the melt has recently been extracted from the upper mantle. Hansen et al. [2015] map surface-wave shear velocities to lithospheric temperature for most of the U.S. and find a maximum temperature of ~1300ºC beneath central Colorado at a depth of 82 km. Leat et al. [1989] performed major element geochemistry for 14 rock samples collected from four Quaternary basalt flows in central Colorado, including the Dotsero flow. They found basalts high in sodium (wt% Na_2O = 3.74±0.34%) with silica values typical for basalt (wt% SiO_2 = 49.51±0.84%). Estimates of wt% H_2O for in situ partial melt are difficult to obtain but can be estimated via analysis of the volatiles present in fluid inclusions. A recent study of late Cenozoic basalts erupted in northern New Mexico estimated the water content of the melt at 0.5-2.0 wt% H_2O [Rowe et al., 2015]. To our knowledge, no estimates of in situ water content exist for Quaternary magmas in Colorado, so we will consider the end-member cases of both dry and wet (2 wt%

H_2O) basalt. Depth to the top of the conductor (25 km) provides an estimate of the minimum pressure experienced by the melt (~1 GPa). Passing these constraints through the SIGMELTS program yields melt conductivities of 0.6-1.5 S/m for dry basalt and 0.3-3.5 S/m for wet basalt, with the range of melt conductivity values encompassing the range of permissible temperature. Assuming a melt temperature of 1200ºC yields melt conductivities of 0.83 S/m and 1.78 S/m for dry and wet basalt, respectively.

Figure 2.8 shows the relationship between bulk resistivity of a rock and melt fraction contained within that rock for a melt of a particular conductivity, in this case 0.83 S/m (dry basalt) and 1.78 S/m (wet basalt). The geometrical model that forms the basis for this relationship (equation (26) in Waff [1974]) assumes a small melt fraction (<15%), a solid rock matrix that is substantially more resistive than the melt, and a 100% interconnected melt. Owing to the latter assumption, melt fraction estimates from this analysis are minimum values, as a less interconnected melt would require higher melt concentrations to produce the same bulk resistivity values. Because the physical constraints of the magnetotelluric method prohibit the independent determination of the thickness or absolute conductivity of the conductor (Figure A.2), there is a tradeoff between bulk resistivity and melt fraction. In the extreme case that the melt is confined to a single tabular layer of molten rock, or a series of such layers containing nearly 100% melt (Figure 2.7a), the cumulative thickness of those melt layers would be 1.1 and 2.4 km for the wet and dry basalt, respectively. In the other extreme, where melt is distributed

uniformly from 25 km depth to the base of the crust (Figure 2.7b), the melt fraction in the lower crust would be 7-15% for wet and dry basalt, respectively. We consider this a substantial melt fraction for a relatively amagmatic region of the continental interior. For comparison, Desissa et al. [2013] use magnetotelluric data and a similar analysis to estimate a melt fraction >13% for the crust beneath an incipient mid-ocean ridge in the Afar region of the East African Rift.

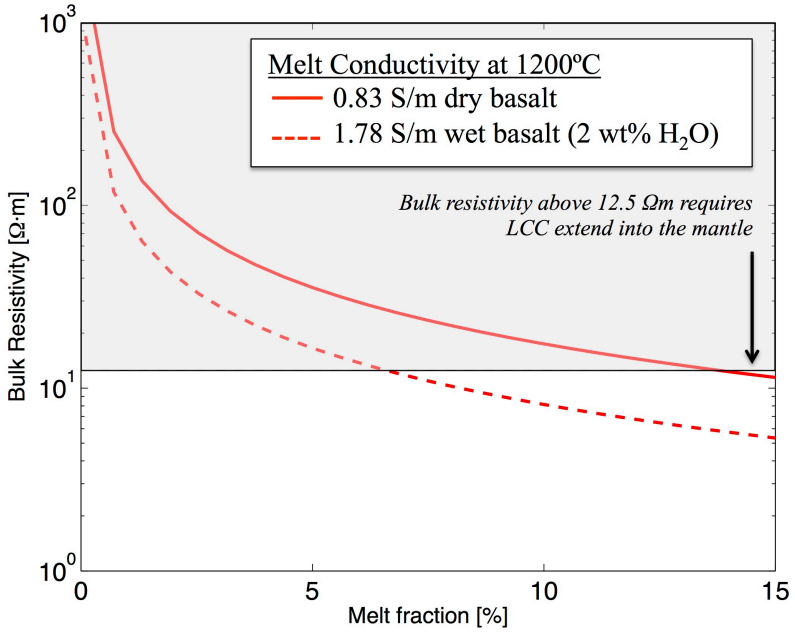

Figure 2.8. Trade-off between bulk resistivity of imaged MT anomaly and melt fraction for dry and wet basalt at 1200ºC. Based on equations from Waff [1974] assuming 100% interconnected melt, small melt fraction, and resistive mineral grains. Melt conductivity calculated using SIGMELTS [Pommier and Trong, 2011]. Melt parameters derived from petrologic and geophysical data [see references in text]. Dashed line represents minimum electrical conductivity of our lower crustal conductor, which corresponds to the end-member case of melt distributed uniformly from the Moho to 25 km depth.

Basaltic underplating and/or injection of molten basalt into the mid-crust are expected to result in at least a limited degree of crustal melting. Relatively low seismic velocities in the deep crust [e.g. Li et al., 2003] and a high magnitude density contrast across the crust-mantle boundary found by Schmandt et al. [2015] suggest that the deep crust beneath Colorado is of intermediate or felsic composition. If we alter the melt parameters in SIGMELTS to simulate the chemical composition of a typical rhyolite (~70% SiO_2, ~5% Na_2O) we find melt conductivities at 1200ºC of 0.09-0.44 S/m for dry and wet melts, respectively. Assuming a more felsic melt in our interpretation would require a thicker melt layer and/or a higher melt fraction within the melt zone. In interpreting the presence of melt in the lower crust we recognize that a spectrum of melt compositions is likely present, including a felsic component contributed by anatectic melts, especially given the inferred composition of the lower crust in Colorado. However, for the purposes of putting meaningful constraints on melt fraction and melt layer thickness, we restrict our interpretation to high conductivity melts (i.e. basaltic melts) as that assumption provides

2.5.1.3 Aqueous Fluid

Another likely source of high conductivity in the lower crust, especially in active tectonic environments, is aqueous fluid [e.g. Li et al., 2003; Wannamaker et al., 2008]. Saline fluids in the deep crust can easily exceed the conductivity of seawater (>3 S/m) and can produce high conductivity anomalies with far smaller

fluid volumes than required for anomalies of similar conductance comprised of partial melt. Where it is available, seismic reflection data can be helpful in differentiating aqueous fluid from partial melt in deep-crustal conductors. The concentration of fluids into lenses produces high impedance contrast "bright spots" in seismic reflection sections that are often coincident with lower-crustal conductors [Hyndman and Shearer, 1989]. The Continental Dynamics of the Rocky Mountains (CD-ROM) experiment included the acquisition of seismic refraction and reflection data along the crest of the southern Rocky Mountains. At the latitude of our MT profile in central Colorado, Rumpfhuber and Keller [2009] observe a mid-crustal reflector in the CD-ROM data at depths similar to the well-resolved top of the lower crustal conductor (22-23 km). However, they suggest the reflector is a product of the interwedging of crustal blocks from adjacent Proterozoic terranes, juxtaposed during the assembly of the North American continent, and do not consider the role of fluids in their interpretation.

Absent independent geologic and geophysical evidence for the presence of saline fluid in the deep crust we rely on the results of laboratory studies and estimates of fluid porosity to assess the likelihood that fluids contribute to the observed high conductivity. We do not consider the scenario in which aqueous fluids permeate the entire lower crust. Yardley and Valley [1997] argue that in stable tectonic regimes, high-grade metamorphic and igneous rocks of the lower crust will readily incorporate free fluids to produce hydrated retrograde minerals and that the lower crust in general behaves as a fluid-sink rather than a fluid-source. Even in

more active tectonic regimes it is difficult to maintain vertically distributed free fluids in the lower crust. The permeability required to produce observable volumes of interconnected free fluid in the lower crust would also facilitate the evacuation of that buoyant fluid to shallower depths.

Figure 2.7c shows a typical model of fluid distribution that is often invoked to explain low resistivity anomalies in the mid- to lower crust. In this model, saline fluids are typically interpreted as thin horizons of accumulated fluid ponding beneath impermeable barriers to upward fluid flow [e.g. Hyndman and Shearer, 1989; Jiracek et al., 1983; Eaton 1980]. Eaton [1980] suggests that ductile shear concentrated near the brittle-ductile transition during lithospheric extension may produce a pervasive physical barrier to fluid migration. Fluid flow at mid-crustal levels may also be impeded by fluid-rock interactions that reduce permeability, such as silicate precipitation and/or volume increasing hydration reactions [Hyndman and Shearer, 1989]. In the former scenario, the LCC indicates depth to the brittle-ductile transition and/or a pervasive mid-crustal decollement associated with regional-scale crustal extension. In the latter, the top of the LCC corresponds to the isotherm associated with silicate precipitation and retrograde metamorphism reactions (350-400ºC). These interpretations are not mutually exclusive.

Shimojuku et al. [2014] provide estimates of the bulk electrical conductivity of brine-bearing quartzite under mid-crustal conditions (T = 800-1100 K, P = 1 GPa). The most conductive sample tested (quartzite with 30% fluid fraction consisting of 17 wt% NaCl brine) exhibited a bulk conductivity of ~4 S/m, with little

variation due to temperature. A layer of brine-bearing quartzite with this porosity and salinity would need to be just 500 m thick in order to produce the observed lower crustal conductance of 2000 S. Extrapolating to a more modest fluid fraction of 10%, based on examination of mid-crustal "bright spots" in Tibet [Caldwell et al., 2009], yields a bulk conductivity of 1.25 S/m, which would require a layer of fluid-bearing rock 1.6 km thick to produced the observed conductance. We consider this the minimum thickness of a brine-bearing rock layer required to produce the observed high conductivity, as thinner layers would require salinity and/or fluid fractions that may not be reasonable for the depths at which high conductivity is observed. Lower salinity and/or porosity would require a thicker layer of fluid accumulation and an increasingly high aggregate volume of mid-crustal fluid.

2.5.1.4 Preferred Geologic Model for the Lower Crust

Figure 2.7d shows our preferred interpretation of the lower crustal conductor, in which both partial melt and saline fluids are present. The end-member cases presented in the previous sections and illustrated in Figure 2.7a-c are problematic in that they would not produce the observed strike-parallel anisotropy. We appeal instead to a model in which melt is supplied to the crust via melt-filled fractures, or vertical dikes, aligned parallel to strike. These melt-filled cracks would produce the observed anisotropy by providing a north-south aligned fabric that would preferentially channel electric currents into a strike-parallel direction. These fractures are either sufficiently thin or too closely spaced so as to prevent our model

from resolving individual cracks. The north-south orientation of the fractures is consistent with the inferred local stress regime. Geodetic observations suggest that much of Colorado is experiencing distributed east-west extension [Berglund et al., 2012], implying that the least principal stress direction is also oriented east-west. Injection of magma into this type of stress regime would produce north-south oriented dikes trending perpendicular to the least principal stress direction.

We cannot rule out the possibility that these strike-parallel fractures are alternatively or simultaneously occupied by transient pulses of aqueous fluid. However, we find it difficult to advocate for a model that does not include some fraction of partial melt. The fluid concentrations required to produce the observed anomaly (up to 10%, see above) would reduce the solidus to the point of melting the crust given the high temperatures modeled for the lower crust in the region [Decker et al., 1988]. Furthermore, the independent geophysical evidence for lower crustal melt and Quaternary volcanism in Colorado described above suggest that a "water only" model is unlikely.

Our preferred model includes melt and aqueous fluid ponding at mid-crustal levels. These features are added to explain the presence of the lower crustal conductor in the strike perpendicular resistivity model. These ponded fluids provide a component of isotropic high conductivity at the top of the LCC resolvable in both components of the anisotropic inversion results. Ponded melt is a straightforward consequence of supplying melt to the lower crust, while ponded fluids are expected to result from crust-melt interactions. Possible sources of fluid in this scenario

include magmatic fluid exsolving from the partial melt as it cools and metamorphic fluids released by heating of hydrous minerals in the surrounding crust.

2.5.2 Upper Mantle Resistivity Structure

Seismic tomography, teleseismic travel time residuals, and receiver function studies suggest a substantial increase in thickness of the sub-continental lithospheric mantle (SCLM) from west to east across the Rocky Mountain Front [e.g. Sheehan et al., 1995; Lee and Grand, 1996; Yuan et al., 2014; Hansen et al., 2015]. Sheehan et al., [1995], for example, advocate for a mantle density structure in which the high density lithospheric mantle lid is 60 km thicker under the Great Plains than it is under the adjacent Southern Rocky Mountains. Seismic tomography models image high seismic velocities extending into the upper mantle beneath the Great Plains in eastern Colorado to depths of >150 km [e.g. Schmandt and Humphreys, 2010; Shen and Ritzwoller, 2016] with generally much lower velocities beneath the Rocky Mountains. Our preferred anisotropic electrical resistivity model shows a moderately resistive (>50 Ωm) eastward-thickening feature in the Great Plains upper mantle extending from the base of the crust to depths of 125-150 km beneath the eastern edge of our profile (RM in Figure 2.4). Does this transition from conductive to resistive upper mantle represent the electrical lithosphere-asthenosphere boundary (LAB) shallowing to the west? Or is it simply an alteration and/or thermal boundary internal to the mantle lithosphere?

We first consider the scenario in which the resistivity structure beneath the Great Plains images the electrical LAB shallowing towards the range front from the east. We estimate a typical electrical resistivity of the asthenosphere and compare it to the values observed in our model. Dai and Karato [2009] estimate the water content of typical asthenosphere to be about 100 ppm. Using a unified electrical conductivity model for isotropic olivine hydrated to 100 ppm [Gardes et al., 2014] and assuming an adiabatic geotherm in the asthenosphere with a potential temperature of 1300ºC, we estimate a typical asthenospheric resistivity of ~30 Ωm. Figure 2.6 shows an approximate 30 Ωm resistivity contour for the upper mantle of our model east of the range front. If we assume that this contour represents the LAB, we would expect asthenospheric temperatures of >1200ºC, and consequently low seismic velocities, to be imaged east of the Rocky Mountain Front at depths <100 km.

Seismic tomography studies that utilize surface waves and/or ambient noise are in particular sensitive to seismic velocity structure over the depth range of the most pronounced features in our electrical resistivity models (near-surface to 150 km). A number of such studies have been performed across the RMF [Li et al., 2002; Shen et al., 2013; Hansen et al., 2015; Shen and Ritzwoller 2016]. Shen and Ritzwoller [2016], for example, provide a high-resolution image of upper mantle velocity perturbations along our profile that shows a sharp lateral contrast in upper mantle velocity structure across a vertical boundary that persists to depths >150 km. Interestingly, the steepest portion of this lateral gradient, which divides above

average mantle velocity to the east from below average mantle velocity to the west, is offset from the Rocky Mountain Front to the east by about three degrees of longitude (about 270 km east of the RMF at this latitude). The region of the upper mantle between the RMF and fast mantle of Shen and Ritzwoller [2016] is precisely where we image a ramp-like gradient in electrical resistivity. This implies that at least electrically, the transition from thick, cold, continental lithosphere to the east to thinner actively deforming lithosphere to the west occurs over a continuum rather than a step. We assume based on the arguments mentioned above that the 30 Ωm contour is the minimum depth to the electrical LAB. In reality, the depth to the LAB is likely much deeper than the 30 Ωm contour, especially near the range front where the contour impinges on the base of the crust. We expect that a buffer of lithospheric material of likely indeterminable thickness (in this study) is present at the base of the crust across our entire profile.

To further examine the possible distribution of lithospheric mantle material beneath the Great Plains, and to better characterize the physical and chemical state of said lithosphere, we examine typical resistivity values of continental lithospheric mantle. Electrical conductivity of the lithospheric mantle may be enhanced by the presence of partial melt, water in nominally anhydrous minerals, and to a lesser extent, elevated bulk temperature. Using the same olivine conductivity model as above [Gardes et al., 2014] and assuming dry conditions, we estimate that even at exceptionally high temperatures (>1300ºC), the resistivity of the mantle lithosphere cannot achieve resistivity values below ~100 Ωm without the addition of melt and/or

hydration. Figure 2.6 shows an approximate 100 Ωm contour for the upper mantle east of the RMF. This line represents the maximum depth to which the mantle may be dry and/or melt-free. The low resistivity values observed below the 100 Ωm contour are incompatible with unmodified SCLM. We note that the lithosphere above this line may also be modified given that 100 Ωm is the resistivity for dry mantle at extremely high temperatures in excess of 1300ºC. Hansen et al., [2015] provide a seismically-derived map of upper-mantle temperature for the western U.S. that indicates the upper mantle beneath eastern Colorado is closer to 1000ºC at 82 km depth, which would correspond to resistivity values closer to ~10^4 Ωm dry olivine [Constable et al., 1992] for, much higher than the observed values.

Figure 2.9 shows the analysis used to estimate the distribution of dissolved water content in the lithospheric mantle beneath the Great Plains. This figure was inspired by a similar analysis performed by Bedrosian [2016] to assess hydration of the SCLM beneath the Midwestern United States. Figure 2.9a shows several resistivity vs. depth profiles for the Great Plains upper mantle taken from the 2D ρ_{xx} model in Figure 2.4a. Vertical resistivity profiles are extracted from a region of the model extending laterally from the eastern edge of the profile to just east of the RMF, with a spacing of about 20 km between profiles. Overlain on that plot are three resistivity vs. depth profiles derived from an olivine electrical conductivity model that is primarily a function of water content and an assumed geotherm [Gardes et al., 2014]. We assume a conductive mantle geotherm for the region, accounting for variable heat production and a surface heat flow of 50 mW/m^2

[Hasterok and Chapman, 2011]. This geotherm (Figure 2.9b) is consistent with the limited available heat flow data for eastern Colorado as well as two independent estimates of upper-mantle temperature provided by regional seismic studies (green boxes in Figure 2.9b, [Schutt et al., 2011; Hansen et al., 2015]). Upon intersection with the mantle adiabat, the geotherm changes slope due to the transition from predominantly conductive to convective heat transfer that occurs at the thermally defined lithosphere-asthenosphere boundary. This produces a corresponding change in slope in the olivine conductivity profiles (located at ~120 km depth in Figure 2.9) below which resistivity is primarily a function of asthenospheric water content.

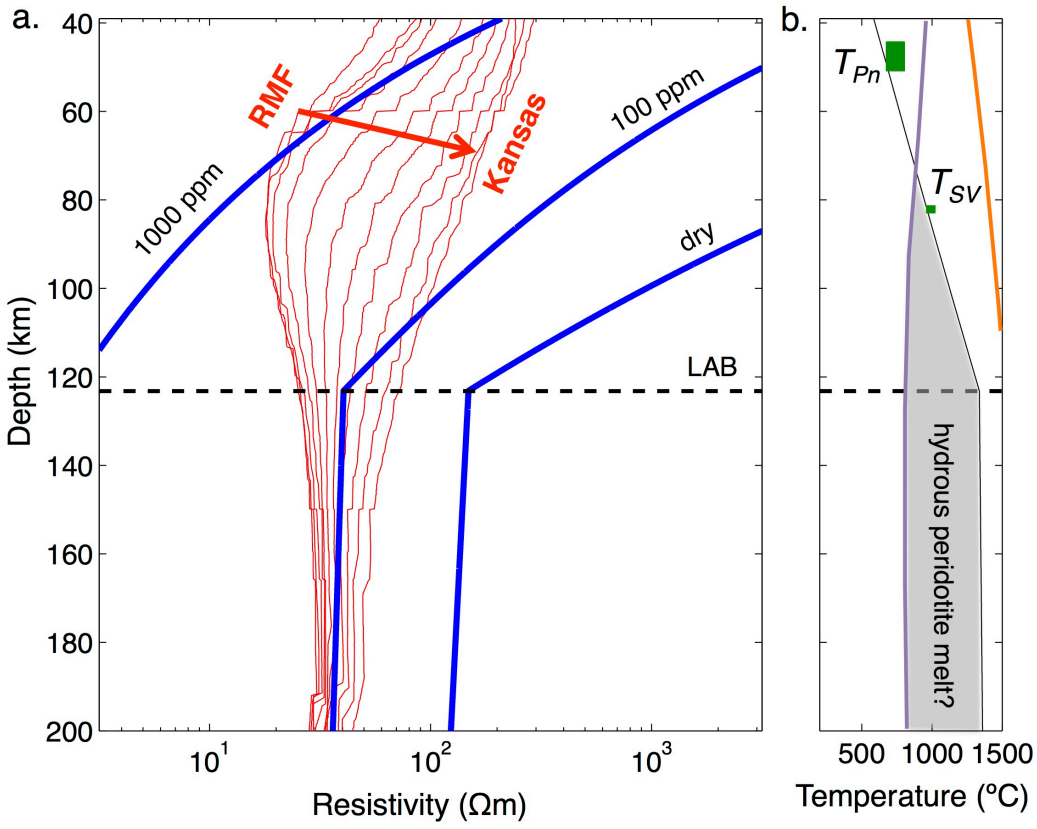

Figure 2.9. [previous page] Mantle resistivity vs. lithospheric hydration. Red lines in [a] are resistivity-depth profiles extracted from Great Plains region of ρ_{xx} model in Figure 2.4a. Red arrow indicates increasing upper-mantle resistivity with eastward progression of profile from the Rocky Mountain Front [RMF] to near the Colorado-Kansas border. Blue lines are electrical resistivity models [Gardes et al., 2014] for olivine with [0, 100, 1000 ppm] H_2O assuming geotherm shown. Geotherm [b] accounts for variable lithospheric heat production and surface flow of 50 mW/m^2 [Hasterok and Chapman, 2011]. Orange line is peridotite dry solidus [Hirschmann 2000] and purple line is peridotite saturated solidus [Till et al., 2010] with the shaded area representing the conditions for melting of hydrated peridotite. Green squares indicate seismically derived estimates of upper mantle temperature from Schutt et al., [2012] [T_{Pn}] and Hansen et al. [2015] [T_{SV}]. Dashed line is lithosphere-asthenosphere boundary [LAB] determined from change in slope of geotherm [i.e. depth of transition from conductive to convective geotherm].

We see from Figure 2.9 that the observed resistivity structure in the Great Plains lithospheric mantle cannot be controlled by temperature alone, as none of the resistivity profiles from the MT model approach the high resistivity values required for dry SLCM. This implies that the majority of the SLCM immediately east of the RMF is either hydrated, with estimated water contents ranging from 100 to 1000 ppm, or contains partial melt. The value of 1000 ppm is exceptionally high for olivine water content in the mantle and is only plotted in Figure 2.9a to provide a bracket for the water content required to approach the modeled resistivity values. More reasonable values for mantle olivine are several hundred ppm at most. We observe two clear patterns in resistivity profiles from our anisotropic model: (1) the average bulk resistivity of the upper mantle increases from west to east and (2) the depth to the minimum resistivity increases along the same trend, i.e. the profiles becomes steeper towards Kansas. The second trend, a steepening of the resistivity

profile, is consistent with the behavior observed for a decrease in geothermal gradient, or thickening of the lithosphere. That we observe steepening of the profiles from west to east suggests that the lithosphere may be thickening to the east. Figure 2.9 also suggests that there is a contribution to the transition from conductive to resistive upper mantle caused by a gradient in lithospheric water content, with maximum hydration occurring beneath the Rocky Mountain Front.

It is possible that partial melt contributes to the high conductivity beneath the westernmost Great Plains as well. There is no direct evidence from seismic tomography, body-wave attenuation [Boyd and Sheehan, 2005], seismicity [Nakai et al., 2017], surface geology, or heat flow to suggest that there are any active or recently active magmatic systems beneath the Great Plains in eastern Colorado at this latitude. However, projecting the peridotite solidus [both dry and saturated, Hirschmann 2000 and Till et al., 2010, respectively] onto the geotherm in Figure 2.9b shows that conditions may exist in the upper mantle that would be favorable to melting of hydrous peridotite. This same plot demonstrates that melting of dry peridotite would be difficult to achieve given the assumed geotherm and temperature regime of the upper mantle in eastern Colorado. Partial melt beneath the western plains may be the source melt for the lower crustal conductor, with the AC anomaly in Figure 2.4b representing a sub-horizontal transport pathway to the lower crust.

We limit our discussion of the upper-mantle resistivity structure west of the Rocky Mountain Front to a few broad observations, given that screening effects of

the lower-crustal conductor severely limit our ability to resolve mantle structure and the resistivity contrasts in the mantle below it are expected to be slight. The upper mantle beneath the southern Rocky Mountains appears to be generally conductive (~30 Ωm) and isotropic (Figure 2.5c). Seismic tomography and receiver function studies indicate that the lithosphere-asthenosphere boundary is relatively shallow beneath the southern Rocky Mountains, perhaps at depths <90 km [e.g. Sheehan et al., 1995]. The resistivity values observed beneath the LCC at those depths are consistent with modeled asthenospheric resistivity (30 Ωm for 100 ppm asthenosphere). However, lithospheric mantle that has been hydrated and/or infiltrated by partial melt, as suggested, for example, by Humphreys et al. [2003], is expected to exhibit similarly low resistivity values. This lithospheric stratigraphy is in contrast to that of the more energetic Snake River Plain magmatic region near Yellowstone, which exhibits resistivity values in the upper mantle consistent with dry lithosphere [Meqbel et al., 2014]. The low resistivity lithosphere beneath the southern Rocky Mountains suggests that melt and/or fluids persist in the upper mantle and remained to be fluxed through this less active magmatic system.

Thinned lithosphere beneath the SRM is a plausible explanation for the observed resistivity structure, although it is unlikely that we can independently constrain lithospheric thickness in this portion of the model. Petrologic and geophysical evidence suggests that lithospheric stratigraphy beneath the southern Rocky Mountains in Colorado consists of heavily modified lower crust [this study], hot and/or partially molten mantle lithosphere [e.g. Humphreys et al. 2003], and

hydrous asthenosphere, none of which is expected to be resistive. Determining lithospheric thickness in this type of tectonic environment (i.e. imaging the boundary between two conductive layers of the upper mantle) would be difficult even without the masking effects of the LCC. In terms of upper mantle structure beneath the LCC, we appeal to the existing interpretations from the seismic community (i.e. thinned lithosphere) and note that our data does nothing to refute that hypothesis.

2.5.3 Tectonic Implications

2.5.3.1 Partial Melt in the Lower Crust

In interpreting the lower crustal conductor we must consider the timing of fluid emplacement, the source of fluids, and the spatial scale of the anomaly. Partial melt emplaced in the mid-crust is not at thermal equilibrium with the surrounding rock and will freeze over several thousands to millions of years, depending on the volume and frequency of repeated injection and initial crustal temperature [Annen et al., 2006]. Yardley and Valley [2000] argue that saline brines in the lower crust can only persist as free fluids for a limited geologic time before the chemical, thermal, and pressure conditions of the lower crust that favor hydration reactions will consume those fluids in retrograde metamorphism. The width of the lower crustal resistivity anomaly dictates that any mechanism we invoke for supplying fluids to the lower crust must be capable of producing laterally pervasive crustal modification. The high conductivity that we image is therefore the result of recent

tectonic activity that has provided volatiles, heat, and/or magma across a broad area of the lower crust over the last few million years.

It is reasonable to assume that the partial melt that we interpret to exist in the mid- to lower crust is the result of melting of the lithosphere. Humphreys et al., [2003] argue that low seismic velocity in the upper mantle beneath the southern Rocky Mountains represents hot, dry, and perhaps partially molten lithospheric mantle. Leat et al. [1989] advocate for a lithospheric mantle source for the Quaternary lavas erupted in central Colorado. Lithospheric melting is achieved through three mechanisms: the addition of heat, the addition of volatiles, and/or decompression melting. The first two mechanisms may also supply free fluids to the lower crust, either as exsolved magmatic fluids or fluids released from high-temperature metamorphic reactions of previously hydrated minerals.

Small-scale convection of the upper mantle is one plausible mechanism for melting the mantle lithosphere. The advection of heat, volatiles, and/or partially molten asthenosphere to the base of the lithosphere could all contribute to partial melting of lithospheric mantle. Geodynamic modeling by van Wijk et al. [2010] suggests small-scale edge-driven convection can initiate at a step in lithospheric thickness. They suggest this process is in part responsible for initiation of the Rio Grande Rift at the boundary between the Colorado Plateau and Great Plains in New Mexico, where the Great Plains crust and lithosphere is much thicker than that of the Colorado Plateau today [Wilson et al., 2005]. Section 2.5.2 describes the evidence for a differential lithospheric thickness across the Rocky Mountain Front

in Colorado that could be responsible for the initiation of edge-driven convection in the sub-lithospheric mantle.

Determining the mechanism responsible for the initiation and continuation of small-scale convection beneath Colorado, or otherwise supplying melt to the lower crust, is left for future geodynamic modeling studies. We speculate, based on modest estimates of Cenozoic extension at the surface, that there are processes at work other than rifting, unless the mantle lithosphere has become substantially decoupled from the overlying crust. A mechanical destabilized lower crust could provide another means of initiating convection. The presence of water in the lower crust, especially at volumes suggested by the water rich end-member case discussed above (Figure 7c), could weaken and destabilize the crust [e.g. Jackson et al., 2004]. If the lower crust is also anti-buoyant, for example after basaltic underplating has densified the crust-mantle interface, one could imagine a scenario in which foundering of lithosphere into a shallow asthenosphere could generate decompression melting.

Electrical conductivity of the upper mantle is enhanced directly beneath the RMF (AC in Figure 2.4b, arrow in Figure 2.6). This anomaly appears to be anisotropic as well, with conductivity enhanced in the east-west direction, perpendicular to geoelectric strike (ρ_{yy} model in Figure 2.6). We speculate this resistivity structure to reflect a flux of partial melt and fluids into the mantle lithosphere from an east-west directed convection cell upwelling beneath the Rocky Mountain Front transition zone. The 200 km width of the lower-crustal conductor

may represent some characteristic length scale of this inferred convection cell, wherein melt and fluids flux out of the sub-lithospheric mantle as material moves from east to west, ultimately down welling beneath western Colorado.

2.5.3.2 Hydration of the Lithospheric Mantle

The possible identification of pervasive hydration of the lithospheric mantle east of the Rocky Mountain Front has implications for the tectonic evolution and modification history of the continental interior. An apparent eastward decrease in the degree of modification to the SCLM is consistent with progressive dewatering during subduction of the eastward-dipping Farallon slab. A similar mechanism for supplying water to the mantle has been proposed for more active tectonic regions to the west [e.g. Humphreys et al., 2003] and has been invoked to explain kimberlite eruptions in eastern Kansas in the late Cretaceous [Currie and Beaumont, 2011]. It is difficult to constrain the hydration state east of the range front due to (1) a low availability of extrusive volcanism east of the range front to provide direct sampling of lithospheric mineralogy and water content and (2) the minor H_2O concentration in nominally anhydrous minerals has a negligible effect on bulk density and seismic velocity. The penetration of hydrous phases into the uppermost mantle has implications for the ability of water to migrate through the lithosphere and may help explain the presence of hydrated mineral phases in lower-crustal rocks above relatively thick lithosphere [Jones et al., 2015]. One interpretation of the so-called "ignimbrite flare up" [Lipman 1992] is that pervasive mantle hydration and

refrigeration provided by the Farallon slab primed the lithospheric mantle for melting upon slab removal and exposure to high temperature asthenosphere. The reason the hydrated western plains did not follow a similar volcanic progression is unclear, although hydrous partial melt may reside in the Great Plains lithosphere today.

2.6 Conclusions

We present a 2D anisotropic electrical resistivity model of the crust and upper mantle beneath the southern Rocky Mountains and Great Plains. We identify two significant features that have implications for the tectonic evolution of the boundary between stable Proterozoic lithosphere of the western Great Plains and recently modified lithosphere of the southern Rocky Mountains: (1) a broad zone (200 km wide) of low resistivity (<20 Ωm) located at 25 km depth beneath the highest topography in Colorado and (2) lower than expected resistivity in the upper mantle east of the range front that we interpret as an eastward deepening "hydration front" extending into the lithospheric mantle beneath the Great Plains. Interpreting the lower-crustal conductor in the context of petrologic and geophysical constrains, we eliminate temperature, composition, graphite and sulfide mineralization as the primary source of high conductivity. End member petrologic models that may explain the high conductivity include ubiquitous basaltic melt in the mid- to lower crust (7-15% melt fraction), a several kilometer thick sequence of mafic sills recently injected into the mid-crust, and an accumulation of saline fluid

ponding at the brittle-ductile transition. The reality is likely some combination of these readily quantifiable end member scenarios involving both saline fluids and partial melt (Figure 2.7d). One such scenario is a series of north-south oriented magmatic dikes that periodically supply basaltic magma and exsolved magmatic fluids to mid-crustal levels. We speculate that basaltic magma in the lower crust beneath the Rocky Mountains is the result of partial melting of the lithospheric mantle driven by the addition of heat and/or volatiles from below. The existence of partial melt in the lower crust indicates that the southern Rocky Mountains remain tectonically active, and that edge-driven convection initiated along a step in lithospheric thickness may play a significant role in driving that tectonic activity. The increase in upper-mantle conductivity with depth beneath the Great Plains likely represents a modification gradient internal to the sub-continental lithospheric mantle, although a westward thinning lithosphere cannot be entirely ruled out. Hydration of the SCLM beneath the plains, possibly accomplished by dewatering of the shallowly subducting Farallon slab in the early Cenozoic, has implications for the tectonic evolution of the continental interior worthy of further investigation.

2.7 Acknowledgments

The authors thank Craig Jones, Lang Farmer, Peter Molnar, and Ned Sterne for valuable discussions. We thank Kerry Key and the Seafloor Electromagnetic Methods Consortium for the use of MARE2DEM and advice on its use. Our

magnetotelluric data were collected over two summer field campaigns through a joint effort by the United States Geological Survey and the University of Colorado Boulder. Daniel Zietlow and Benjamin Bloss provided significant contributions to the field effort. Instrumentation was provided by the United States Geological Survey in Denver, CO and by Martyn Unsworth at the University of Alberta. This work was supported by the University of Colorado Boulder Geological Sciences Department Spetzler and W.O. Thompson awards, the Rocky Mountain Association of Geologists Bolyard Scholarship, the Society of Exploration Geophysicists, the Geological Society of America, and National Science Foundation grants EAR-1249669 and EAR-1053596. Additional support was provided by EarthScope (EAR-0323309). This work would not have been possible without land access granted by the National Forest Service, the State of Colorado, James Mark Jones State Wildlife Area, Douglas County Colorado, and numerous private landowners. Various maps and graphics were created using Generic Mapping Tools [Wessel and Smith, 1991].

2.8 References

Abraham, J. D., Cannia, J. C., Bedrosian, P. A., Johnson, M. R., Ball, L. B., & Sibray, S. S. (2012), Airborne electromagnetic mapping of the base of aquifer in areas of western Nebraska: U.S. Geological Survey Scientific Investigations Report 2011-5219.

Ackermann, H. D. (1974), Shallow seismic compressional and shear wave refraction and electrical resistivity investigations at Rocky Flats, Jefferson County, Colorado. Journal of Research of the U.S. Geological Survey, 2(4), 421–430.

Annen, C., Blundy, J. D., & Sparks, R. S. J. (2005), The Genesis of Intermediate and Silicic Magmas in Deep Crustal Hot Zones. Journal of Petrology, 47(3), 505–539, doi:10.1093/petrology/egi084

Bedrosian, P. A. (2016), Making it and breaking it in the Midwest: Continental assembly and rifting from modeling of EarthScope magnetotelluric data. Precambrian Research, 278, 337–361, doi:10.1016/j.precamres.2016.03.009

Bedrosian, P. A., & Box, S. E. (2016), Highly conductive horizons in the Mesoproterozoic Belt-Purcell Basin: Sulfidic early basin strata as key markers of Cordilleran shortening and Eocene extension. In J. S. MacLean & J. W. Sears (Eds.), Belt Basin: Window to Mesoproterozoic Earth: Geological Society of America Special Paper 522 (pp. 305–339), doi:10.1130/2016.2522(12).

Berglund, H. T., Sheehan, A. F., Murray, M. H., Roy, M., Lowry, A. R., Nerem, R. S., & Blume, F. (2012), Distributed deformation across the Rio Grande Rift, Great Plains, and Colorado Plateau. Geology, 40(1), 23–26, doi:10.1130/G32418.1

Boerner, D. E., Kurtz, R. D., & Craven, J. A. (1996), Electrical conductivity and Paleo-Proterozoic foredeeps. Journal of Geophysical Research, 101(B6), 13775–13791, doi:10.1029/96JB00171.

Booker, J. R. (2014), The Magnetotelluric Phase Tensor : A Critical Review. Surveys in Geophysics, 35, 7–40, doi:10.1007/s10712-013-9234-2.

Boyd, O. S., & Sheehan, A. F. (2005), Attenuation Tomography Beneath the Rocky Mountain Front: Implications for the Physical State of the Upper Mantle. In The Rocky Mountain Region: An Evolving Lithosphere (pp. 361–377), Washington D.C.: American Geophysical Union.

Caldwell, T. G., Bibby, H. M., & Brown, C. (2004), The magnetotelluric phase tensor. Geophysical Journal International, 158, 457–469, doi:10.1111/j.1365-246X.2004.02281.x.

Caldwell, W. B., Klemperer, S. L., Rai, S. S., & Lawrence, J. F. (2009), Tectonophysics Partial melt in the upper-middle crust of the northwest Himalaya revealed by Rayleigh wave dispersion. Tectonophysics, 477, 58–65, doi:10.1016/j.tecto.2009.01.013.

Chapin, C. E., & Cather, S. M. (1994), Tectonic setting of the axial basins of the northern and central Rio Grande rift. In G. R. Keller & S. M. Cather (Eds.), Basins of the Rio Grande Rift: Structure, Stratigraphy, and Tectonic Setting: Geological Society of America Special Paper (Vol. 291, pp. 5–26), Boulder, Colorado, doi:10.1130/SPE291-p5.

Constable, S. C., Parker, R. L., & Constable, C. G. (1987), Occam's inversion: A practical algorithm for generating smooth models from electromagnetic sounding data. Geophysics, 52(3), 289–300.

Constable, S., Shankland, T. J., & Duba, A. (1992), The Electrical Conductivity of an Isotropic Olivine Mantle. Journal of Geophysical Research, 97(B3), 3397–3404, doi:10.1029/91JB02453.

Currie, C. A., & Beaumont, C. (2011), Are diamond-bearing Cretaceous kimberlites related to low-angle subduction beneath western North America?, Earth and Planetary Science Letters, 303, 59-70.

Dai, L., & Karato, S. (2009), Electrical conductivity of orthopyroxene: Implications for the water content of the asthenosphere. Proc. Jpn. Acad. Ser., 85, 466–475, doi:10.2183/pjab.85.466.

DeCelles, P. G. (2004), Late Jurassic to Eocene evolution of the Cordilleran thrust belt and foreland basin system, western U.S.A. American Journal of Science, 304, 105–168.

Decker, E. R., Heasler, H. P., Buelow, K. L., Baker, K. H., & Hallin, J. S. (1988), Significance of past and recent heat-flow and radioactivity studies in the Southern Rocky Mountains region. Geological Society of America Bulletin, 100, 1851–1885.

Desissa, M., Johnson, N. E., Whaler, K. A., Hautot, S., Fisseha, S., & Dawes, G. J. K. (2013), A mantle magma reservoir beneath an incipient mid-ocean ridge in Afar, Ethiopia. Nature Geoscience, 6, 861–865, doi:10.1038/ngeo1925.

Dickinson, W. R., Klute, M. A., Hayes, M. J., Janecke, S. U., Lundin, E. R., McKittrick, M. A., & Olivares, M. D. (1988), Paleogeographic and paleotectonic setting of Laramide sedimentary basins in the central Rocky Mountain region. Geological Society of America Bulletin, 100, 1023–1039.

Eaton, G. P. (1980), Geophysical and geological characteristics of the crust of the Basin and Range province. In Studies in Geophysics-Continental Tectonics (pp. 96–113), Washington D.C.: National Academy of Science.

Eaton, G. P. (1987), Topography and origin of the southern Rocky Mountains and Alvarado Ridge. In M. P. Coward, J. F. Dewey, & P. L. Hancock (Eds.), Continental Extensional Tectonics, Geological Society Special Publication (Vol. 28, pp. 355–369), Geological Society.

Eaton, G. P. (2008), Epeirogeny in the Southern Rocky Mountains region: Evidence and origin. Geosphere, 4(5), 764–784, doi:10.1130/GES00149.1.

Egbert, G. D. (1997), Robust multiple-station magnetotelluric data processing. Geophysical Journal International, 130, 475–496.

Epis, R. C., & Chapin, C. E. (1975), Geomorphic and Tectonic Implications of the Post-Laramide, Late Eocene Erosion Surface in the Southern Rocky Mountains. Geological Society of America Memoir, 144, 45–74.

Fenneman, N. M. (1946), Physical divisions of the United States.

Gamble, T. D., Goubau, W. M., & Clarke, J. (1979), Magnetotellurics with a remote magnetic reference. Geophysics, 44(1), 53–68.

Gardes, E., Gaillard, F., & Tarits, P. (2014), Toward a unified hydrous olivine electrical conductivity law. Geochemistry, Geophysics, Geosystems, 15, 4984–5000, doi:10.1002/2014GC005496.

Gilbert, H. (2012), Crustal structure and signatures of recent tectonism as influenced by ancient terranes in the western United States. Geopshere, 8(1), 141–157, doi:10.1130/GES00720.1.

Hansen, S. M., Dueker, K. G., Stachnik, J. C., Aster, R. C., & Karlstrom, K. E. (2013), A rootless rockies - Support and lithospheric structure of the Colorado Rocky Mountains inferred from CREST and TA seismic data. Geochemistry, Geophysics, Geosystems, 14(8), 2670–2695, doi:10.1002/ggge.20143.

Hansen, S. M., Dueker, K., & Schmandt, B. (2015), Thermal classification of lithospheric discontinuities beneath USArray. Earth and Planetary Science Letters, 431, 36–47, doi:10.1016/j.epsl.2015.09.009.

Hasterok, D., & Chapman, D. S. (2011), Heat production and geotherms for the continental lithosphere. Earth and Planetary Science Letters, 307, 59–70, doi:10.1016/j.epsl.2011.04.034.

Heise, W., & Pous, J. (2001), Effects of anisotropy on the two-dimensional inversion procedure. Geophysical Journal International, 147, 610–621.

Hirschmann, M. M. (2000), Mantle solidus: experimental constraints and the effects of peridotite composition. Geochem. Geophys, Geosyst. 1 (10).

Humphreys, E., Hessler, E., Dueker, K., Farmer, G. L., Erslev, E., & Atwater, T. (2003), How Laramide-Age Hydration of North American Lithosphere by the Farallon Slab Controlled Subsequent Activity in the Western United States. International Geology Review, 45(7), 575–595, doi:10.2747/0020-6814.45.7.575.

Hyndman, R. D., & Shearer, P. M. (1989), Water in the lower continental crust: modelling magnetotelluric and seismic reflection results. Geophysical Journal International, (98), 343–365.

Izett, G. A., Cobban, W. A., & Gill, J. R. (1971), The Pierre Shale Near Kremmling, Colorado, And Its Correlation to The East and the West: Geological Survey Professional Paper 684-A.

Jackson, J. A., Austrheim, H., McKenzie, D., & Priestley, K. (2004), Metastability, mechanical strength, and the support of mountain belts. Geology, 32, 625-628, doi:10.1130/G20397.1.

Jacob, K. H., Farmer, G. L., Buchwaldt, R., & Bowring, S. A. (2015), Deep crustal anatexis, magma mixing, and the generation of epizonal plutons in the Southern Rocky Mountains, Colorado. Contributions to Mineralogy and Petrology, 169(7), 1–23, doi:10.1007/s00410-014-1094-3.

Jiracek, G. R., Gustafson, E. P., & Mitchell, P. S. (1983), Magnetotelluric results opposing magma origin of crustal conductors in the Rio Grande Rift. Tectonophysics, 94, 299–326.

Jones, A. G. (1992), Electrical conductivity of the continental lower crust. In D. M. Fountain, R. J. Arculus, & R. W. Kay (Eds.), Continental Lower Crust (pp. 81–143), Elsevier.

Jones, C. H., Mahan, K. H., Butcher, L. A., Levandowski, W. B., & Farmer, G. L. (2015), Continental uplift through crustal hydration. Geology, 43(4), 355–358, doi:10.1130/G36509.1.

Kariya, K. A., & Shankland, T. J. (1983), Electrical conductivity of dry lower crustal rocks. Geophysics, 48(1), 52–61.

Key, K. (2016), MARE2DEM: a 2-D inversion code for controlled-source electromagnetic and magnetotelluric data. Geophysical Journal International, 207, 571–588, doi:10.1093/gji/ggw290.

Key, K., & Ovall, J. (2011), A parallel goal-oriented adaptive finite element method for 2.5-D electromagnetic modelling. Geophysical Journal International, 186, 137–154, doi:10.1111/j.1365-246X.2011.05025.x.

Landman, R. L., & Flowers, R. M. (2013), (U-Th)/He thermochronologic constraints on the evolution of the northern Rio Grande Rift, Gore Range, Colorado, and implications for rift propagation models. Geosphere, 9(1), doi:10.1130/GES00826.1.

Leat, P. T., Thompson, R. N., Dickin, A. P., Morrison, M. A., & Hendry, G. L. (1989), Quaternary volcanism in northwestern Colorado: Implications for the roles of asthenosphere and lithosphere in the genesis of continental basalts. Journal of Volcanology and Geothermal Research, 37, 291–310.

Lee, D., & Grand, S. P. (1996), Upper mantle shear structure beneath the Colorado Rocky Mountains. Journal of Geophysical Research, 101(B10), 22233–22244.

Levandowski, W. B., Jones, C. H., Shen, W., Ritzwoller, M. H., & Schulte-Pelkum, V. (2014), Origins of topography in the western U.S.: Mapping crustal and upper mantle density variations using a uniform seismic velocity model.

Journal of Geophysical Research: Solid Earth, 119, 2375–2396, doi:10.1002/2013JB010607.

Li, A., Forsyth, D. W., & Fischer, K. M. (2002), Evidence for shallow isostatic compensation of the southern Rocky Mountains from Rayleigh wave tomography. Geology, 30(8), 683–686.

Li, S., Unsworth, M. J., Booker, J. R., Wei, W., Tan, H., & Jones, A. G. (2003), Partial melt or aqueous fluid in the mid-crust of Southern Tibet? Constraints from INDEPTH magnetotelluric data. Geophysical Journal International, 153, 289–304.

Lipman, P. W. (1992), Magmatism in the Cordilleran United States; Progress and problems. In B. C. Burchfiel, P. W. Lipman, & M. L. Zoback (Eds.), The Geology of North America, The Cordilleran Orogen: Conterminous U.S. (pp. 481–514), Boulder, Colorado: The Geological Society of America.

Mallory, W. W. (1958), Pennsylvanian Coarse Arkosic Redbeds and Associated Mountains in Colorado. In Symposium on Pennsylvanian Rocks of Colorado and Adjacent Areas (pp. 17–20), Denver, Colorado: Rocky Mountain Association of Geologists.

Maughan, E. K. (1988), Geology and petroleum potnetial, Colorado Park Basin Province, North-Central Colorado: U.S. Geological Survey Open-File Report 88-450 E.

McCoy, A., Roy, M., Trevino, L., & Keller, G. R. (2005), Gravity Modeling of the Colorado Mineral Belt. In K. E. Karlstrom & G. R. Keller (Eds.), The Rocky

Mountain Region: An Evolving Lithosphere Tectonics, Geochemistry, and Geophysics. Washington, D.C.: American Geophysical Union.

Meqbel, N. M., Egbert, G. D., Wannamaker, P.E., Kelbert, A., & Schultz, A. (2014), Deep electrical resistivity structure of the northwestern U.S. derived from 3-D inversion of USArray magnetotelluric data, Earth and Planetary Science Letters, 402, 290-304.

Mitrovica, J. X., Beaumont, C., & Jarvis, G. T. (1989), Tilting of continental interiors by the dynamical effects of subduction. Tectonics, 8(5), 1079–1094.

Mooney, W. D., & Kaban, M. K. (2010), The North American upper mantle: Density , composition , and evolution. Journal of Geophysical Research, 115(B12424), 1–24, doi:10.1029/2010JB000866.

Nakai, J. S., Sheehan, A. F., & Bilek, S. L. (2017), Seismicity of the rocky mountains and Rio Grande Rift from the EarthScope Transportable Array and CREST temporary seismic networks, 2008-2010. Journal of Geophysical Research: Solid Earth, 122, 2173–2192, doi:10.1002/2016JB013389.

Pakiser, L. C., & Zietz, I. (1965), Transcontinental Crustal and Upper-Mantle Structure. Reivews of Geophysics, 3(4), 505–520.

Phillips, W. S., Mayeda, K. M., & Malagnini, L. (2014), How to Invert Multi-Band, Regional Phase Amplitudes for 2-D Attenuation and Source Parameters: Tests Using the USArray. Pure and Applied Geophysics, 171, 469–484, doi:10.1007/s00024-013-0646-1.

Poe, B. T., Romano, C., Nestola, F., & Smyth, J. R. (2010), Electrical conductivity anisotropy of dry and hydrous olivine at 8 GPa. Physics of the Earth and Planetary Interiors, 181, 103–111, doi:10.1016/j.pepi.2010.05.003.

Pommier, A., & Trong, E. L. (2011), "Sigmelts": A web portal for electrical conductivity calculations in geosciences. Computers and Geosciences, 37, 1450–1459, doi:10.1016/j.cageo.2011.01.002.

Porath, H. (1971), Magnetic Variation Anomalies and Seismic Low-Velocity Zone in the Western United States, Journal of Geophysical Research, 76, 2643-2648.

Porritt, R. W., Allen, R. M., & Pollitz, F. F. (2014), Seismic imaging east of the Rocky Mountains with USArray. Earth and Planetary Science Letters, 402, 16–25, doi:10.1016/j.epsl.2013.10.034.

Porter, K. W., & Weimer, R. J. (1982), Diagenetic Sequence Related to Structural History and Petroleum Accumulation : Spindle Field, Colorado. AAPG Bulletin, 66(12), 2543–2560.

Reitzler, J.S., Gough, D. I., Porath, H., and Anderson III, C. W. (1970), Geomagnetic Deep Sounding and Upper Mantle Structure in the Western United States, Geophys. J. R. astr. Soc., 19, 213-235.

Rowe, M. C., Lassiter, J. C., & Goff, K. (2015), Basalt volatile fluctuations during continental rifting: An example from the Rio Grande Rift, USA. Geochemistry, Geophysics, Geosystems, 16, 1254–1273, doi:10.1002/2014GC005649.

Rumpfhuber, E., & Keller, G. R. (2009), An integrated analysis of controlled and passive source seismic data across an Archean-Proterozoic suture zone in the

Rocky Mountains. Journal of Geophysical Research, 114(B08305), 1–25, doi:10.1029/2008JB005886.

Schmandt, B., & Humphreys, E. (2010), Complex subduction and small-scale convection revealed by body-wave tomography of the western United States upper mantle. Earth and Planetary Science Letters, 297, 435–445, doi:10.1016/j.epsl.2010.06.047.

Schmandt, B., & Lin, F.-C. (2014), P and S wave tomography of the mantle beneath the United States. Geophysical Research Letters, 41, 6342–6349, doi:10.1002/2014GL061231.

Schmandt, B., Lin, F.-C., & Karlstrom, K. E. (2015), Distinct crustal isostasy trends east and west of the Rocky Mountain Front. Geophysical Research Letters, 42, doi:10.1002/2015GL066593.

Schutt, D., Lowry, A. R., & Buehler, J. S. (2012), The temperature of the western U.S. lithosphere. In American Geophysical Union Fall Meeting. San Francisco, California: American Geophysical Union.

Sheehan, A. F., Abers, G. A., Jones, C. H., & Lerner-Lam, A. L. (1995), Crustal thickness variations across the Colorado Rocky Mountains from teleseismic receiver functions. Journal of Geophysical Research, 100(B10), 20391–20404.

Shen, W., Ritzwoller, M. H., & Schulte-Pelkum, V. (2013), A 3-D model of the crust and uppermost mantle beneath the Central and Western US by joint inversion of receiver functions and surface wave dispersion. Journal of Geophysical Research: Solid Earth, 118, 1–15, doi:10.1029/2012JB009602.

Shen, W., & Ritzwoller, M. H. (2016), Crustal and uppermost mantle structure beneath the United States, Journal of Geophysical Research: Solid Earth, 121, 4306-4342, doi:10.1002/2016JB012887.

Shimojuku, A., Yoshino, T., & Yamazaki, D. (2014), Electrical conductivity of brine-bearing quartzite at 1 GPa: implications for fluid content and salinity of the crust. Earth, Planets, and Space, 66(2), 1–9, doi:10.1186/1880-5981-66-2.

Till, C. B., Elkins-Tanton, L. T., & Fischer, K. M. (2010), A mechanism for low-extent melts at the lithosphere-asthenosphere boundary, Geochemistry Geophysics Geosystems, 11, doi:10.1029/2010GC003234.

Tweto, O., & Sims, P. K. (1963), Precambrian Ancestry of the Colorado Mineral Belt. Geological Society of America Bulletin, 74, 991–1014.

Tweto, O. (1979). The Rio Grande Rift system in Colorado. In Rio Grande Rift: Tectonics and magmatism (pp. 33–56). Washington D.C.: American Geophysical Union. http://doi.org/10.1029/SP014p0033

van Wijk, J. W., Baldridge, W. S., van Hunen, J., Goes, S., Aster, R., Coblentz, D. D., Grand, S. P., & Ni, J. (2010), Small-scale convection at the edge of the Colorado Plateau: Implications for topography, magmatism, and evolution of Proterozoic lithosphere. Geology, 38(7), 611–614, doi:10.1130/G31031.1.

Waff, H. S. (1974), Theoretical Considerations of Electrical Conductivity in a Partially Molten Mantle and Implications for Geothermometry. Journal of Geophysical Research, 79(26), 4003–4010.

Walker, J. D., Bowers, T. D., Black, R. A., Glazner, A. F., Farmer, G. L., & Carlson, R. W. (2006), A geochemical database for western North American volcanic and intrusive rocks (NAVDAT), In A. K. Sinha (Ed.), Geoinformatics: Data to Knowledge: Geological Society of America Special Paper 397 (pp. 61–71), doi:10.1130/2006.2397(05).

Wannamaker, P. E., Hasterok, D. P., Johnston, J. M., Stodt, J. A., Hall, D. B., Sodergren, T. L., Pellerin, L., Maris, V., Doerner, W. M., Groenwold, K. A., & Unsworth, M. J. (2008), Lithospheric dismemberment and magmatic processes of the Great Basin-Colorado Plateau transition, Utah, implied from magnetotellurics. Geochemistry, Geophysics, Geosystems, 9(5), doi:10.1029/2007GC001886.

Wannamaker, P. E., Hohmann, G. W., & Ward, S. H. (1984), Magnetotelluric responses of three-dimensional bodies in layered earths. Geophysics, 49(9), 1517–1533.

Wessel, P. and Smith, W. H. F., (1991), Free software helps map and display data. EOS Trans. AGU, 72, 441-446.

Wilson, D., Aster, R. C., Ni, J., Grand, S. P., West, M., Gao, W., Baldridge, W. S., & Semken, S. (2005), Imaging the seismic structure of the crust and upper mantle beneath the Great Plains, Rio Grande Rift, and Colorado Plateau using receiver functions. Journal of Geophysical Research, 110(B05306), doi:10.1029/2004JB003492.

Yang, X. (2011), Origin of High Electrical Conductivity in the Lower Continental Crust: A Review. Surveys in Geophysics, 32, 875–903, doi:10.1007/s10712-011-9145-z.

Yardley, B. W. D., & Valley, J. W. (1997), The petrologic case for a dry lower crust high that rise to a fluid pressure to the rock that is still hot and ductile , the fluid pressure. Journal of Geophysical Research, 102(B6), 12173–12185, doi:10.1029/97JB00508.

Yardley, B. W. D., & Valley, J. W. (2000), Reply. Journal of Geophysical Research, 105(B3), 6065–6068.

Yuan, H., French, S., Cupillard, P., & Romanowicz, B. (2014), Lithospheric expression of geological units in central and eastern North America from full waveform tomography. Earth and Planetary Science Letters, 402, 176–186, doi:10.1016/j.epsl.2013.11.057.

CHAPTER 3

LITHOSPHERIC SIGNATURE OF LATE CENOZOIC EXTENSION IN ELECTRICAL RESISTIVITY STRUCTURE OF THE RIO GRANDE RIFT, NEW MEXICO, USA

3.1 Abstract

We present electrical resistivity models of the crust and upper mantle from two-dimensional (2D) anisotropic inversion of broadband and long period magnetotelluric (MT) data collected in the Rio Grande rift, New Mexico, USA. Previous geophysical studies have identified a low velocity zone several hundred kilometers wide centered beneath the Rio Grande rift, suggesting that the upper mantle beneath the rift in New Mexico is characterized by a very broad zone of lithospheric modification. In contrast, the surface expression of the rift (e.g. high angle normal faults and syn-rift sedimentary units) is confined to a narrow region only a few tens of kilometers wide about the rift axis. Broadband and long period magnetotellurics (100 Hz to 10,000 s) are uniquely suited to probing the depths of the lithosphere that fill the gap between surface geology and mantle velocity, namely the mid- to lower crust and uppermost mantle. We model the electrical resistivity structure of the lithosphere by inverting 73 MT soundings collected along two east-west trending wide-aperture profiles straddling the rift axis at the latitudes of 36.2ºN and 32.0ºN. We present results from both isotropic and anisotropic finite-element 2D inversions of the MT data with a strong preference for

the latter in our interpretation. A key feature of the anisotropic resistivity models is a broad (~200 km wide) zone of enhanced conductivity (<15 Ωm) in the mid- to lower-crust that is imaged beneath both profiles. We interpret this lower crustal conductor as aqueous fluid accumulation that is a direct result of magmatic activity in the rift. Additional conductivity mechanisms are discussed, including partial melt and conductive mineralization, especially in regard to a zone of low resistivity in the mid-crust of the central rift that exhibits pronounced anisotropy.

3.2 Introduction

The Rio Grande rift is a mid- to late-Cenozoic continental rift system in the southwestern United States that separates the Colorado Plateau and Basin and Range to the west from the stable North American interior to the east [e.g., Chapin and Cather, 1994; Keller et al., 1991, Tweto, 1979]. The surface expression of the rift (Figures 3.1 and 3.2) consists of a series of elongate axial basins that form a north-south trending topographic depression through central Colorado and New Mexico before taking a bend to the southeast around the latitude of El Paso, Texas, and broadening into northern Mexico. The rift basins we observe today are, to first order, typically asymmetric half-grabens bounded on one side by a steeply dipping normal fault opposite a hinge zone. Pre-rift sedimentary units that outcrop on the rift flanks at elevations >3 km have been imaged by seismic reflection studies at depths below sea level within the rift basins, suggesting several kilometers of vertical offset on basin bounding normal faults [Russel and Snelson, 1994]. Syn-rift

fill consists of Oligocene to Quaternary fluvial and lacustrine sedimentary units (see Figure 3.1) and volcanic rocks, with the basement (or pre-rift depositional surface) consisting of Mesozoic or Paleozoic sedimentary units and/or Precambrian metamorphic rocks [Baldridge et al., 1983]. The rift is named for the Rio Grande, a through-going river that integrated the rift basins from the San Juan Mountains in Colorado to the Gulf of Mexico over the past 8 m.y. [Repasch et al., 2017].

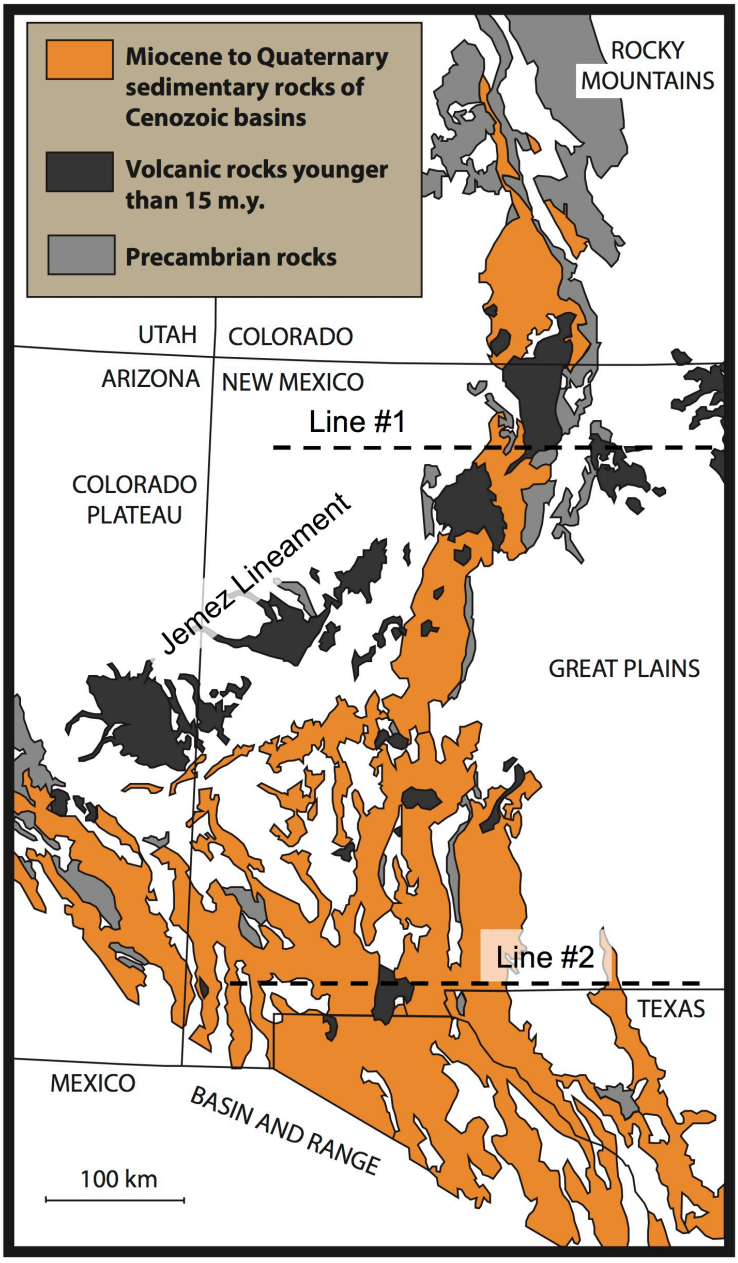

Figure 3.1. Simplified geologic map and tectonic setting of the Rio Grande Rift [modified from Baldridge et al. 1983]. Dashed lines are approximate locations of magnetotelluric profiles.

The earliest evidence of extension along the Rio Grande Rift is Oligocene in age (~30 Ma). A large-scale lithospheric heating event coeval with the onset of rifting may have also weakened the lithosphere and contributed to rift initiation [Eaton, 1987]. The rift progressed in two distinct phases [e.g. Chapin and Cather 1994]. The earlier phase, which lasted from rift initiation to about 20 Ma, produced broad and shallow basins bounded by low-angle normal faults. The second phase of rifting, which began about 10 Ma and continues into the present, produced the relatively narrow (typically less than 50 km wide), asymmetric rift grabens we observe today. Estimates of crustal extension associated with the latter phase of rifting are modest, ranging from 8-12% in the San Luis Basin of south-central Colorado [Kluth and Schaftenaar, 1994] to 28% in the southern Albuquerque basin of central New Mexico [Russell and Snelson, 1994]. This north to south increase in extension, which is apparent in the footprint of mapped syn-rift sedimentary units (Figure 3.1), formed the basis for the hypothesis that the rift opened progressively from south to north. Recent geochronologic studies on rift flank uplifts [Landman and Flowers, 2013; Ricketts et al., 2015] and petrologic studies of Miocene-Quaternary volcanic rocks in northern Colorado [e.g. Cosca et al., 2014] demonstrate that this was not the case and that the rift opened simultaneously along its entire axis in the mid-Cenozoic. Modern geodetic observations reveal that the rift is actively extending at a rate of ~1 nanostrain yr^{-1} [Berglund et al., 2012], with deformation distributed regionally rather than focused on rift-bounding faults.

Volcanic activity associated with rifting is relatively minor compared to other continental rift systems of similar size and age [Keller et al., 1991]. The most prominent volcanic feature in the region is the so-called Jemez lineament (Figure 3.1), a series of relatively young (~15 Ma to 3 ka) volcanic centers and lava flows that roughly follow a northeast trending line from southeast Arizona to northeast New Mexico [Aldrich 1986]. The volcanoes along the lineament are contemporaneous with the latter stage of rifting and may represent reactivation of a pre-existing zone of weakness in the lithosphere that dates to the Proterozoic assembly of the North American continent [Aldrich et al., 1984]. In the central rift near Socorro, New Mexico, seismic reflection and geodetic studies have interpreted a magmatic sill in the mid-crust (~20 km depth), although there are no corresponding recent volcanic rocks at the surface [NAVDAT database, Walker et al., 2006]. Much of what we understand about the chemistry of the lower crust and upper mantle in the rift has come from petrologic work done on eruptive products from Kilbourne hole, a maar in the southern rift created by a phreatomagmatic eruption 24 ka [Gile 1987].

3.2.1 Previous Geophysical Results

The LA RISTRA seismic experiment [e.g. Gok et al., 2003; Gao et al., 2004; Wilson et al., 2005], a high-resolution passive seismic imaging study, provided a detailed examination of upper mantle structure beneath and adjacent to the Rio Grande Rift. The array consisted of dozens of seismic stations deployed along a

profile stretching diagonally across New Mexico from the Four Corners region to west Texas. Gao et al. [2004] used P- and S-wave travel time residuals to image the upper mantle and found a broad low velocity zone several hundred kilometers wide centered on the rift extending to depths >200 km. Imaging of high velocity anomalies at greater depths beneath the rift margins led Gao et al. to interpret the low velocity zone as a high temperature region of the upper mantle emplaced by small scale convection beneath the rift. A study of seismic receiver functions along the LA RISTRA profile [Wilson et al., 2005] revealed no significant perturbation to the 410 and 660 km mantle transitions beneath the region, suggesting that the convection is driven by upper mantle flow rather than a deep-sourced mantle plume. Examination of shear-wave splitting directions [Gok et al., 2003] showed a consistent N40°E fast-direction along the majority of the LA RISTRA profile. This result led the authors to conclude that the predominant driver of mantle anisotropy beneath the rift is North American plate motion rather than active convection. Anomalous north-south oriented fast-directions were detected beneath westernmost Texas, suggesting that east-west convection may be more prominent in the southern rift [Gok et al., 2003].

The EarthScope USArray seismic project has made it possible to develop continental scale models of seismic velocity and velocity perturbations in the mantle for most of the United States [e.g., Schmandt et al., 2015; Shen et al., 2013, Obrebski et al., 2011; Schmandt and Humphreys, 2010]. All of these models show a

region of relatively low velocity extending deep into the mantle (>100 km depth) beneath the rift.

More recent seismic studies with sensitivity to crustal structure [e.g. Fu and Li, 2015; Shen et al., 2013; Gilbert 2012] reveal a thinned crust beneath much of the Rio Grande Rift in New Mexico. In the central rift, the crust ranges from 45 km thick beneath the Great Plains, to 40 km thick beneath the Colorado Plateau, to 35 km thick beneath the rift axis. Farther south the crust is thinner still, as thin as 30 km near the U.S.-Mexico border. A thinned crust beneath the rift axis is supported by Bouguer gravity, which when filtered to intermediate wavelengths shows a high beneath the rift that is interpreted as an upwelling of denser mantle material [Roy et al., 2005].

3.2.2 Previous Electromagnetic Studies

The earliest conclusive investigations into the large-scale electrical resistivity structure of the Rio Grande Rift were conducted by Hermance and Pedersen [1980]. Using four long period (>1,000 s) magnetotelluric soundings collected in two locations Hermance and Pedersen identified a thin zone of high electrical conductivity (conductivity-thickness product of 1600-2200 Siemens) at mid-crustal levels in both the north-central rift near Santa Fe, New Mexico and in the southern rift near El Paso, Texas. They associated the conductor with the then-recently identified Socorro magma body [Rinehart et al., 1979] and concluded that a thin (~1 km thick) sill of basaltic magma could explain both the seismic results in Socorro

and the MT results to the north and south. They proposed that the interpreted basaltic sill at mid-crustal levels was a ubiquitous feature of the Rio Grande Rift given that they observed similar conductive features several hundred kilometers apart along the rift axis.

Subsequent magnetotelluric investigations near the Socorro magma body by Jiracek et al. [1983] yielded the surprisingly result of a resistive mid-crust in the location of the known magmatic sill. This led to the interpretation that mid-crustal conductors in the rift might be attributed to saline fluids trapped at the brittle ductile transition. The rational at Socorro was that recent magma injection into the upper crust had breached whatever impermeable layer had caused the accumulation of saline fluid in the mid-crust, resulting in buoyant fluid escaping to shallower depths [Jiracek et al., 1983]. Networks of free aqueous fluid, often interpreted to be interconnected along grain boundaries rather than fracture networks, have been proposed to explain mid-crustal conductors in other active tectonic environments (e.g., the Basin and Range [Wannamaker et al., 2008] and Tibet [Li et al., 2003]).

Numerous other electrical resistivity studies conducted in the Rio Grande Rift have focused on smaller and/or shallower geophysical targets and do not comment on deep and/or tectonic-scale features. The resistivity structure of the Jemez Mountains volcanic complex, the largest volcanic center along the Jemez lineament and source of two massive caldera forming eruptions at 1.65 Ma and 1.25 Ma, has been investigated for geothermal potential [e.g., Hermance 1979] and

tectonic interpretation [Jiracek et al., 1996; Nettleton 1997; this dissertation, Chapter 4]. Those studies reveal an exceptionally conductive body beneath the Valles caldera, the top of which lies at 5-15 km beneath the surface. However, limited station distribution has prevented further characterization of the geometry of that conductor as well as the interpretation of it in a regional tectonic context. The United States Geological Survey has conducted numerous magnetotelluric studies of rift basins in southern Colorado and northern New Mexico [e.g. Rodriguez and Sawyer, 2013], however, those studies have generally focused on interpreting stratigraphic relationships and shallow geologic structure rather than large-scale tectonic features.

The Summer of Applied Geophysical Experience (SAGE) [Baldridge et al., 2012], an undergraduate- and graduate-level geophysical field camp that operates out of Santa Fe, New Mexico, has also collected dozens of magnetotelluric soundings in the central Rio Grande Rift. These MT data have been studied along with gravity and seismic data (also collected by SAGE) to image and interpret basin-scale structure of the Española and San Luis basins of the Rio Grande Rift [Biehler et al., 1991; Baldridge et al., 1994]. While these data are of sufficiently high quality and long period (>1000 s) to image the mid-crustal conductor first identified by Hermance and Pederson [1980] near Santa Fe, New Mexico, the limited station distribution (all stations are within ~50 km of Santa Fe) prevents further characterization of this conductor beyond point observations of its depth.

3.3 Methods and Data

In this paper, we present modeling results from the first magnetotelluric investigation of the Rio Grande Rift that was expressly designed to image deep, regional scale electrical resistivity structure of the rift and the surrounding environment. This was achieved by a combination of (1) long period magnetotelluric instrumentation to sense structure at upper-mantle depths, (2) wide-aperture profiles with dense station spacing to capture crustal structure and (3) purposeful collection of data off-axis from the rift (e.g. in the Colorado Plateau and Great Plains) so as to discriminate rift-related structure from the tectonic collage on which it is superimposed.

3.3.1 Magnetotellurics

Magnetotelluric data is collected by measuring spatial and temporal variations in the naturally occurring electric (E) and magnetic (H) fields at the surface of the earth. Small-scale perturbations to the background geomagnetic field, which are produced by natural phenomena occurring in the magnetosphere, induce low voltage telluric currents in the conductive subsurface of the Earth. The local and regional resistivity structure at the point of observation acts as a filter, altering the induced electric field. Horizontal magnetic fields are related to the induced horizontal electric fields in the frequency domain by a stationary, or time-invariant, transfer function, known as the magnetotelluric impedance tensor (Z), which serves as a mathematical representation of Earth structure in terms of resistivity. The

four components of the complex, frequency-dependent impedance tensor can be represented as scaled amplitude (apparent resistivity, ρ_a, units of Ωm) and phase.

These transfer functions vary both spatially according to the electrical resistivity structure of the subsurface and with frequency as a function of changes in subsurface resistivity with depth. A magnetotelluric sounding consists of estimates of impedance as a function of period, obtained via spectral analysis of surface electric- and magnetic-field time series.

The magnetotelluric method is in particular sensitive to electrical resistivity, or its reciprocal conductivity, which is dependent upon mineralogy, fluid content, partial melting, chemical alteration of the subsurface, and to a lesser extent, bulk temperature and composition of the subsurface.

3.3.2 Deep Rift Electrical Resistivity Data

Seventy-three magnetotelluric soundings were collected in New Mexico as part of the Deep Rift Electrical Resistivity (DRIFTER) experiment conducted by the University of Colorado Boulder and the United States Geological Survey in 2012 and 2013. Data were collected along two 400-450 km profiles located at 36.2ºN and 32ºN latitude (Figure 3.2). Time series data at each MT site were recorded for five channels: two orthogonal components of the horizontal electric field and three orthogonal components of the magnetic field. Broadband magnetotelluric data (100 Hz - 1000 s) were collected using Electromagnetic Instruments low-frequency MT24 data loggers and three orthogonal Schlumberger magnetic induction coils. Long

period MT data (10 - 11,000 s) were collected using NIMS data loggers and three-component fluxgate magnetometers. Electric field measurements were collected using two orthogonal dipoles each consisting of two non-polarizing electrodes connected by approximately 100 m of insulated copper wire. Each station was outfitted with a broadband instrumentation for 1-3 nights and/or long period instrumentation for up to six weeks (see Figure 3.1). Nominal station spacing was 5-15 km, with a select few data gaps of up to 30 km due to permitting and land access complications. Data were collected at several (2-8) stations simultaneously to permit multi-station remote-reference processing [Egbert, 1997; Gamble et al., 1979].

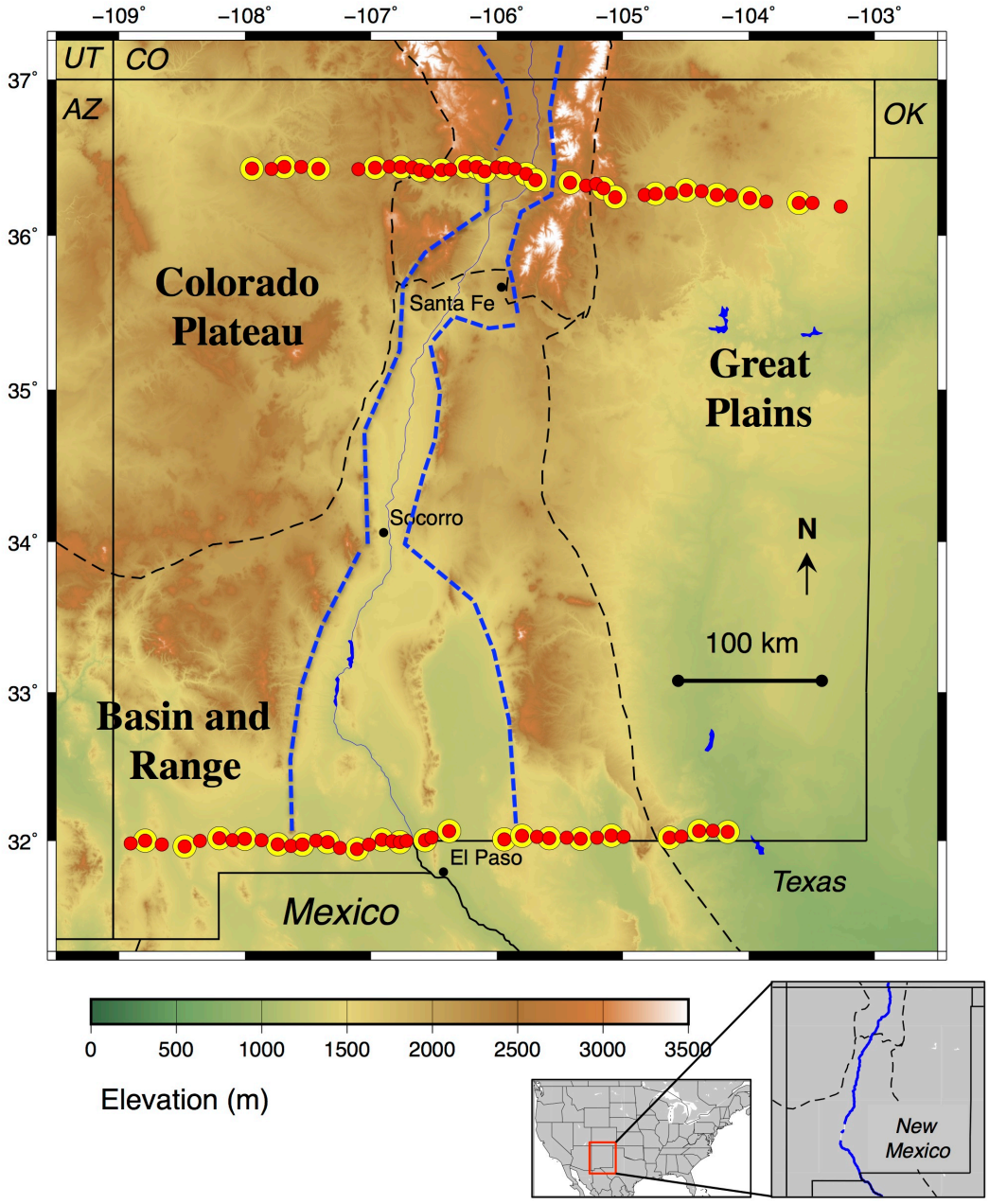

Figure 3.2. Map of magnetotelluric station locations of the DRIFTER experiment. Yellow dots represent long period MT recordings (3-6 weeks duration) and red dots are broadband MT recordings (18-48 hour duration). Black dashed lines show physiographic boundaries [Fenneman 1946]. Blue dashed lines delineate major axial basins of the Rio Grande Rift. AZ = Arizona; CO = Colorado; UT = Utah; OK = Oklahoma

Time-series processing and transfer-function estimation were performed using the same approach as Chapter 2 [Egbert et al., 1997; Gamble et al., 1979].

3.3.3 Dimensionality

An important consideration in the modeling of magnetotelluric data is the local and regional dimensionality of the electrical resistivity structure being imaged. One dimensional earth structure consists of vertically varying resistivity (layer cake). Two-dimensional (2D) resistivity structure allows for lateral variation in one direction but uniform resistivity structure in the corresponding perpendicular direction (i.e. cross sectional resistivity structure beneath a profile is approximately representative of structure beneath parallel profiles to either side). Three-dimensional resistivity structure includes complex scenarios in which resistivity varies along all three axes of a model.

The magnetotelluric method is sensitive to Earth structure in three-dimensions at a variety of scales. Three-dimensional Earth structure of sufficiently small scale relative to the station spacing is considered a source of distortion [e.g. Groom and Bailey, 1989] and must be taken into consideration prior to inversion. Sufficiently large three-dimensional structure is of geologic interest and demands 3D modeling. In this study we perform 2D modeling of data collected along east-west oriented profiles. Justification of this approach requires two assumptions. The first assumption is that the data are predominantly sensitive to a regional two-dimensional resistivity structure. That is to say that any three-dimensional features

beneath or adjacent to our profile are sufficiently small in scale to either be considered sources of distortion that may be accounted for, or these anomalies are sufficiently distant from our profile so as to not influence our magnetotelluric observations. The second assumption is that the predominant trend of the 2D regional resistivity structure, or geoelectric strike, is oriented perpendicular to our profile trace. We can confirm that these two assumptions are valid for our data set by examining the behavior of two magnetotelluric transfer functions: the magnetotelluric phase tensor and the magnetic transfer function, or tipper.

The MT phase tensor [Caldwell et al., 2004] is a mathematical transformation of the impedance tensor that is represented in map view as an ellipse. The major and minor axes of the phase tensor ellipse are proportional to the rotationally-invariant maximum and minimum principal values of the represented phase tensor, with non-circular ellipses indicating higher order electrical resistivity structure (i.e. lateral variations in resistivity). In the two-dimensional (2D) case, the major axis of the ellipse will align either perpendicular or parallel to the predominant geo-electric strike for data collected on the conductive or resistive side, respectively, of a geo-electrical contact. The scalar value β, another rotationally-invariant phase tensor parameter, is an indicator of 3D geo-electric structure. Typically, $| \beta | > 3^{o}$ is taken as an indication of 3D structure [Booker, 2014].

The magnetic-field transfer function (Tz), or tipper, is a complex unitless vector quantity that relates the horizontal magnetic field to the vertical magnetic field. Tipper is often represented in map view as an induction vector, an arrow that

either points towards (Parkinson convention) or away (Weise convention) from a conductive anomaly. In the case of 2D earth structure, induction vectors are oriented 90º from geoelectric strike. Tipper magnitude, represented as the length of an induction vector, is proportional to local resistivity with shorter induction vectors indicating lower resistivity values.

Figure 3.3 is a map view plot of phase tensor ellipses, shaded by β value, and induction vectors plotted in the Parkinson convention for both profiles at a period of 1000 s. In the absence of *a priori* information on geoelectric strike it is helpful to plot these two dimensionality indicators together. Phase tensor ellipses have an inherent 90º ambiguity in strike direction that may be resolved by simultaneous examination of the tipper, as that in the case of 2D structure tippers are oriented perpendicular to geoelectric strike. Plotting of phase tensor ellipses shaded by β value provides an indication of whether the data are 2D or 3D.

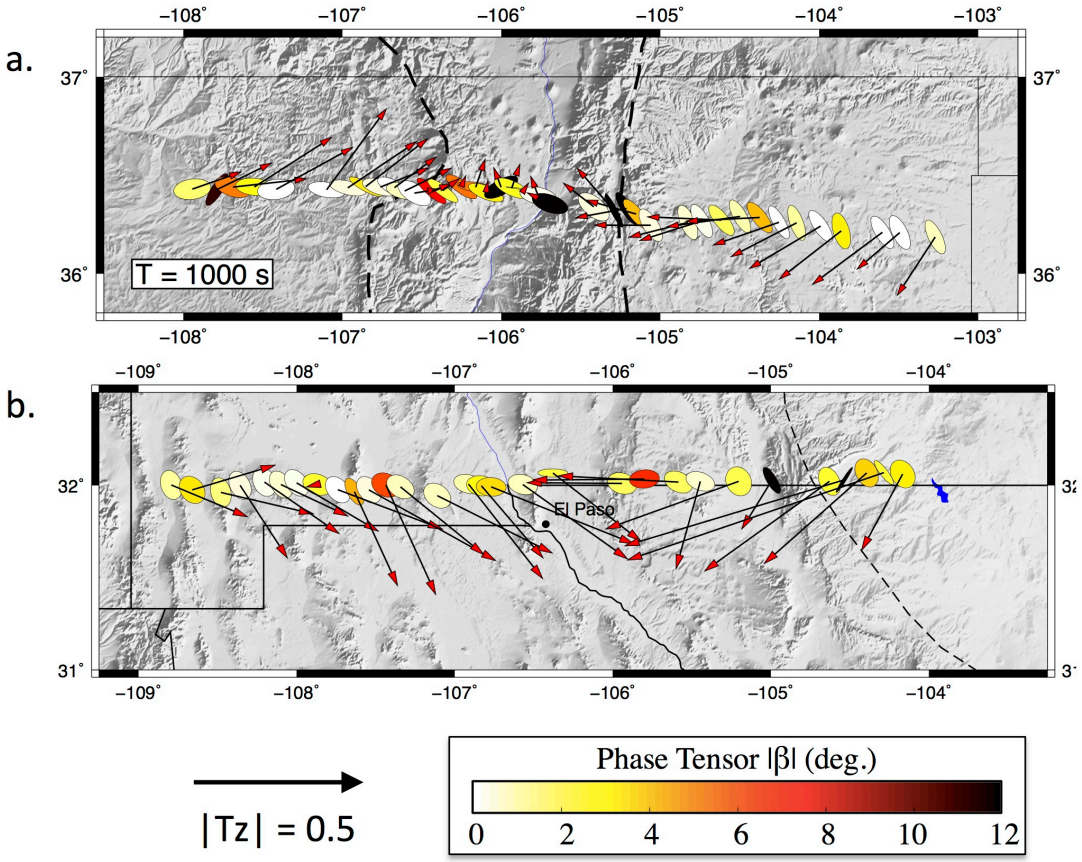

Figure 3.3. Dimensionality of (a) Line #1 and (b) Line #2. Phase tensor ellipses with fill color corresponding to beta value. Arrows are real component of magnetic transfer function Tz at period of 1000 s in the Parkinson convention (pointing towards conductive anomalies).

In modeling these profiles in two-dimensions we assume that the regional geoelectric strike is predominantly perpendicular to the profile trace (i.e. north-south). This assumption was inherent to the survey design and based on the orientation of both surface geologic features (e.g. Quaternary faults and the rift axis) and geophysical gradients at depth (e.g. gravity, heat flow, and seismic

velocity contours). We note that, in general, phase tensor ellipses along both profiles have one axis (either major or minor) oriented sub-parallel to the assumed north-south geo-electric strike and that induction vectors are predominantly pointed along profile (east-west), consistent with a north-south geoelectric strike direction. We also observe that β values are generally below the accepted 3D threshold; the highest values (black ellipses) are isolated to single sites and reflect noisy data at the displayed period rather than exceptionally 3D structure. Detailed examination of the induction vectors reveals that the vectors tend to point towards the center of the profile and also decrease in magnitude upon approaching the center stations. This pattern is indicative of a deep conductive anomaly centered along the axis of the Rio Grande rift.

3.3.4 2-D Inversion

We invert for two-dimensional isotropic and anisotropic electrical resistivity structure along our profile using the finite-element inversion algorithm MARE2DEM [Key 2016]. The MARE2DEM algorithm utilizes an Occam's inversion approach [Constable et al., 1987], which seeks to iteratively determine the smoothest possible electrical resistivity structure that minimizes the functional

$$U = \| \boldsymbol{\partial} \mathbf{m} \|^2 + \mu^{-1} \left[\| \mathbf{W}\left(\mathbf{d} - F(\mathbf{m})\right) \|^2 - \chi^2 \right] \quad (1)$$

where **d** is the magnetotelluric data, F(**m**) is the forward MT response, **W** is a diagonal matrix of inverse data standard errors, μ is a regularization factor, χ^2 is a user-defined misfit tolerance, and **δm** is a model roughness term. The inversion progresses by first automatically sweeping through values of μ to find the best fitting model and iterating until the χ^2 target misfit is achieved. The second phase of the inversion involves searching for the smoothest model that also achieves the desired misfit. Model updates are performed at each iteration via linearizing the functional about a starting model. The inclusion of the χ^2 tolerance in the functional allows the inversion to avoid extreme local minima based on select noisy or non-physical data.

Anisotropy for the purposes of this study refers to strictly horizontal anisotropy, wherein the electrical resistivity of each grid cell is allowed to vary in two directions: parallel (ρ_{yy}) and perpendicular (ρ_{xx}) to the profile trace. Resistivity structure in the z-direction is fixed to resemble that in the y-direction. Vertical electric fields induced by naturally occurring magnetic fields are sufficiently low in magnitude that the magnetotelluric method is not sensitive to vertical anisotropy. It is expected that anisotropic structure oriented at an oblique angle to the profile trace will partition into ρ_{xx} and ρ_{yy} components. Anisotropy is incorporated into the inversion through the model roughness term, which contains a measure of the difference between the ρ_{xx} and ρ_{yy} resistivity models, regularized by an anisotropy penalty factor, α. The value of α varies from 0 (completely anisotropic) to 1 (isotropic) and is defined by the user prior to inversion. For the anisotropic inverse

models shown in this study we set $\alpha = 0.1$ to favor isotropic structure except where strongly required by the data.

3.3.5 Data Preparation

Inputs into the inversion include apparent resistivity and phase of the principal impedances (Z_{XY} and Z_{YX}) and the complex 2D component of the tipper (T_Y). The apparent resistivity of the transverse electric (TE) mode, $\rho_{a,xy}$, was omitted from the inversion input due to its sensitivity to off-profile (i.e. 3D) electrical resistivity structure [Wannamaker et al., 1984], which we do not take into account within a 2D inversion. The data were decimated to five periods per decade, yielding a total of 25 inverted periods distributed logarithmically over five decades (0.1 - 10,923 s). A subset of the decimated data (~15% and ~18% for the central and southern profiles, respectively) was manually culled via visual inspection of transfer function curves to eliminate obvious outliers. For the central profile, 3715 data points distributed across all 39 stations were inverted for 2D isotropic and anisotropic resistivity structure. For the southern profile, 3151 data points distributed across all 34 stations were used. Prior to inversion, data errors for apparent resistivity and phase were increased to a minimum threshold, or error floor, of 10% $|Z_{ij}|$, corresponding to an error in phase of 2.8º, to reduce the likelihood of over-fitting data points with exceptionally small statistically-determined errors. An error floor of 0.03 was applied to all tipper components. Inverted tipper data were also limited to a period range of 1 to 10,923 s to eliminate

the need for small grid cells in the near-surface. Data inputs for the isotropic and anisotropic inversions were identical.

3.3.6 Mesh Preparation

Resistivity models for each inversion were parameterized as unstructured meshes using the graphical user interface Mamba2D (http://mare2dem.ucsd.edu/). Mamba2D is a MATLAB based program that uses Delaunay triangulation to automatically populate regions within the mesh with triangular grid cells of similar size, where size is defined by the nominal side length of each triangular grid cell. An "area of interest" extending from the surface to 150 km depth (approximately one-third of the survey aperture) and 25 km laterally beyond the first and last stations along the profile was divided into three layers populated by triangles of similar size. Outside the region of interest, triangles increase exponentially in size towards the edges of the model domain that extends 1000 km in all directions. The atmosphere is parameterized as a 1000 km thick layer with a fixed resistivity value of $1x10^9$ Ωm. Topography is not incorporated into the model. The resistivity of the isotropic half-space starting models, 80 Ωm and 30 Ωm for the central and southern lines, respectively, were selected by determining which among a series of isotropic half-space models with varying resistivity values exhibited the smallest initial misfit to the data. Model grid parameterization and the starting model for the isotropic and anisotropic inversions were identical for each particular line.

3.4 Results

Figure 3.4 shows the 2D isotropic electrical resistivity models obtained by inverting the magnetotelluric data along our two profiles. The model for the central rift (Figure 3.4a) achieved the target RMS of 1.2 given the applied errors. This represents a reduction in data residual of 86% relative to the 80 Ωm starting model (initial RMS value of 8.31). The model for the southern rift (Figure 3.4b) also achieved the target RMS of 1.2. This represents a reduction in data residual of 86% relative to the 30 Ωm starting model (initial RMS value of 8.55).

Figures 3.5 and 3.6 show our preferred 2D anisotropic resistivity models for the central and southern rift, respectively. For these models, the top plot (Figures 3.5a and 3.6a) shows ρ_{xx}, which reflects the electrical resistance to north-south current flow, while the bottom plot (Figures 3.5b and 3.6b) shows ρ_{yy}, which reflects the electrical resistance to east-west current flow. The model for the central rift (Figure 3.5) required 16 iterations: six to achieve the target RMS of 1.2 given the applied errors and 10 for model smoothing. The model for the southern rift (Figure 3.6) required 10 iterations: five to achieve the target RMS of 1.2 and five for model smoothing. Reduction of data residuals for both models was 86% relative to the respective starting models.

The alternating pattern of vertically aligned conductive and resistive anomalies visible in both models in the mid-crust to upper mantle (25-100 km depth) provides additional justification for anisotropic modeling. This pattern is reminiscent of the modeling results of Heise and Pous [2001] on the isotropic

inversion of anistropic data. They observed that 2D isotropic inversions of azimuthally anisotropic magnetotelluric data produce characteristic artifacts in modeled resistivity structure, including alternating regions of high and low resistivity such as those in Figure 3.4. Section A.1 of the Appendix details a modeling study confirming this same behavior in MARE2DEM.

Figures 3.7 and 3.8 show pseudo-section plots of magnetotelluric transfer functions for the central and southern rift, respectively. These plots show the magnetotelluric data that was input into both inversions, as well as the model response to the isotropic and preferred anisotropic models. We can see from these plots that neither mode of inversion produces a qualitatively better reproduction of the data. The use of a target RMS that we force each model to achieve also makes it difficult to quantify the benefits of anisotropic inversion. Model roughness is defined as the difference in resistivity values of each finite element relative to the adjacent elements, summed and averaged over the entire model space. In order to achieve a similar fit to the data, the isotropic models must be exceptionally more complex than the anisotropic models with a similar data residual (e.g. model roughness of 56 for the anisotropic model compared to 86 for the isotropic case). In an effort to avoid overstating our resolution, we prefer the smoothest model that fits the data equally well, in this case the anisotropic models.

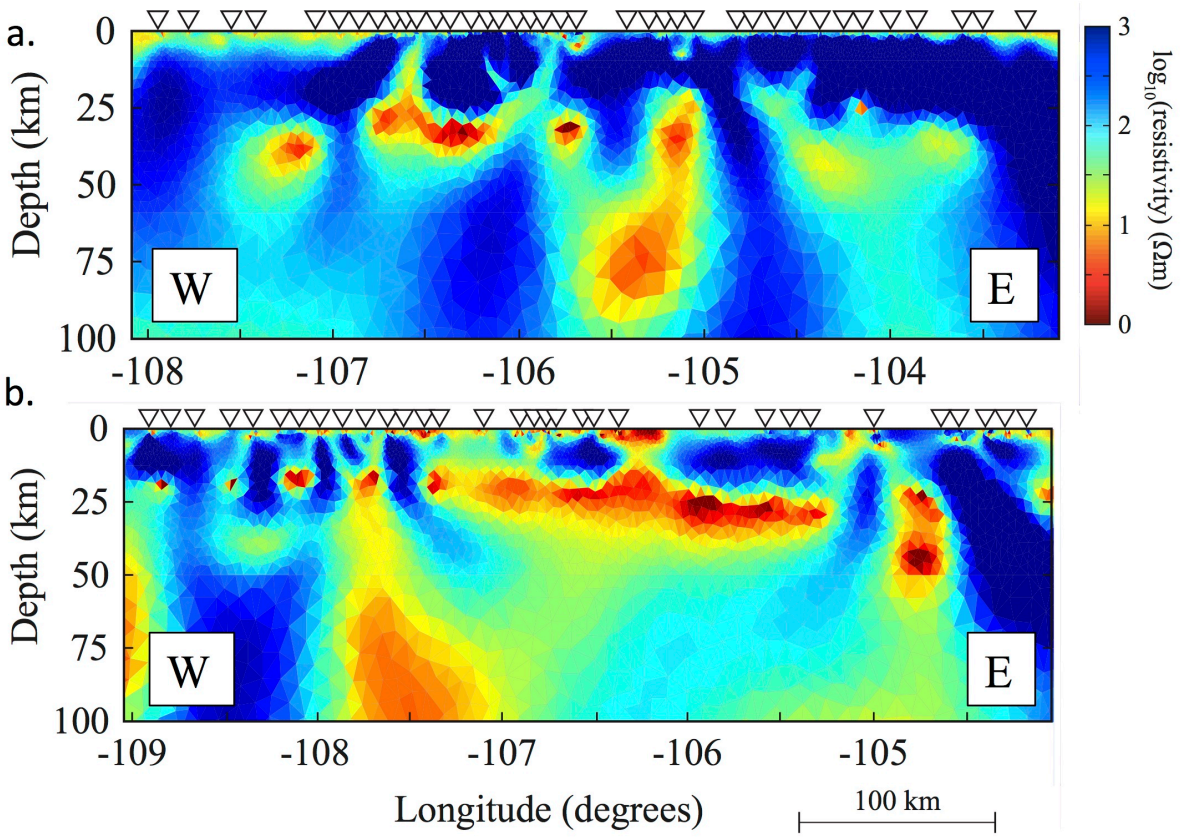

Figure 3.4. Isotropic resistivity models for (a) the central rift (Line #1) and (b) the southern rift (Line #2). Both models achieved a chi-squared misfit of 1.3 and 2-3 iterations of model smoothing. Note the alternating resistor-conductor-resistor pattern and vertical smearing in the lower crust along both profiles. This pattern is reminiscent of that generated by modeling anisotropic resistivity structure with a 2D isotropic inversion routine [Heise and Pous, 2001].

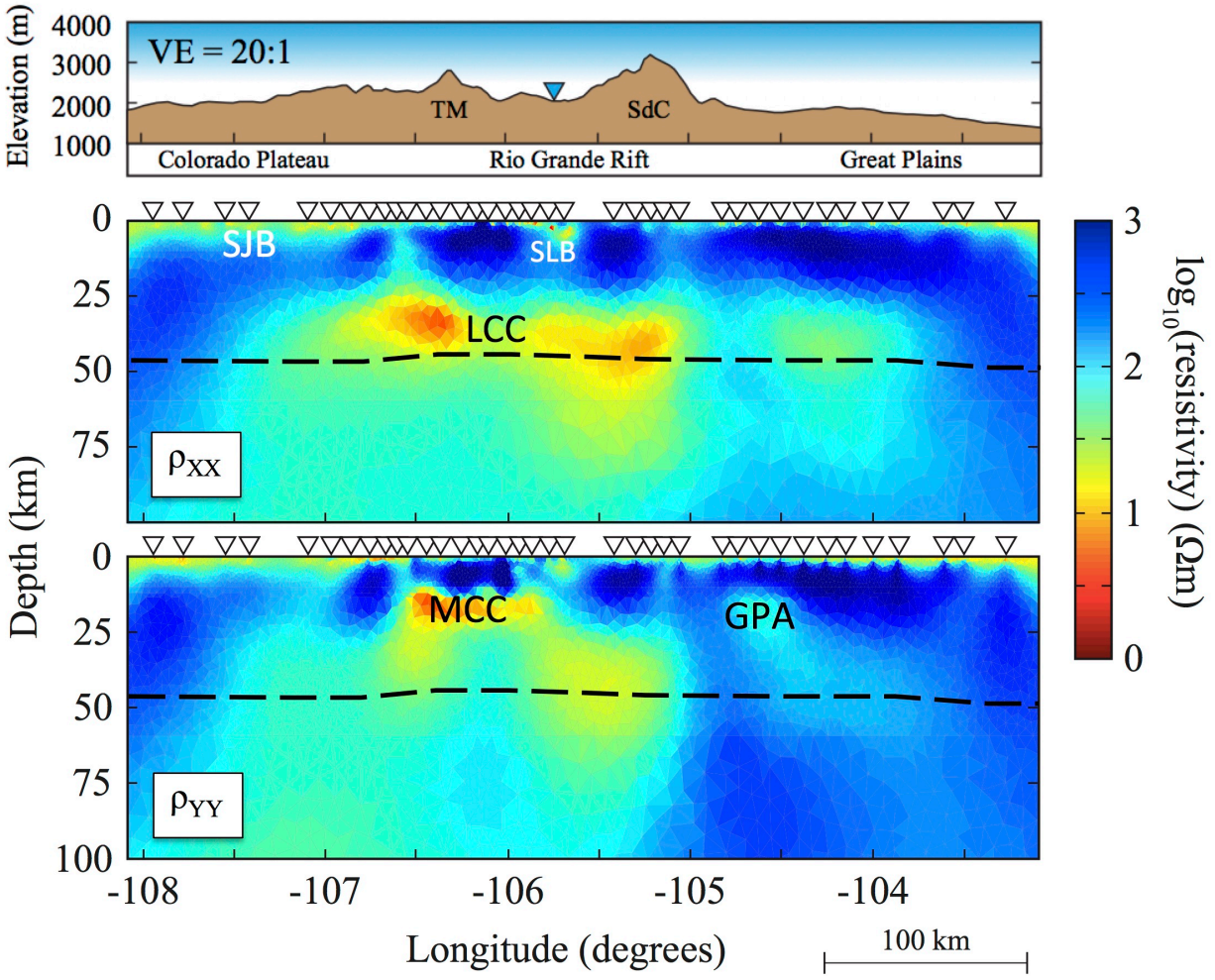

Figure 3.5. Line #1 (central rift) anisotropic electrical resistivity model. Includes topography and approximate physiographic province boundaries along profile. Inverted white triangles indicate MT station locations. Inverted blue triangle indicates location of Rio Grande. Black dashed line is Moho estimate from Shen et al. [2013]. LCC = lower crustal conductor; MCC = mid-crustal conductor; SJB = San Juan Basin; SLB = San Luis Basin; TM = Tusas Mountains; SdC = Sangre de Cristo Mountains, GPA = Great Plains Anomaly

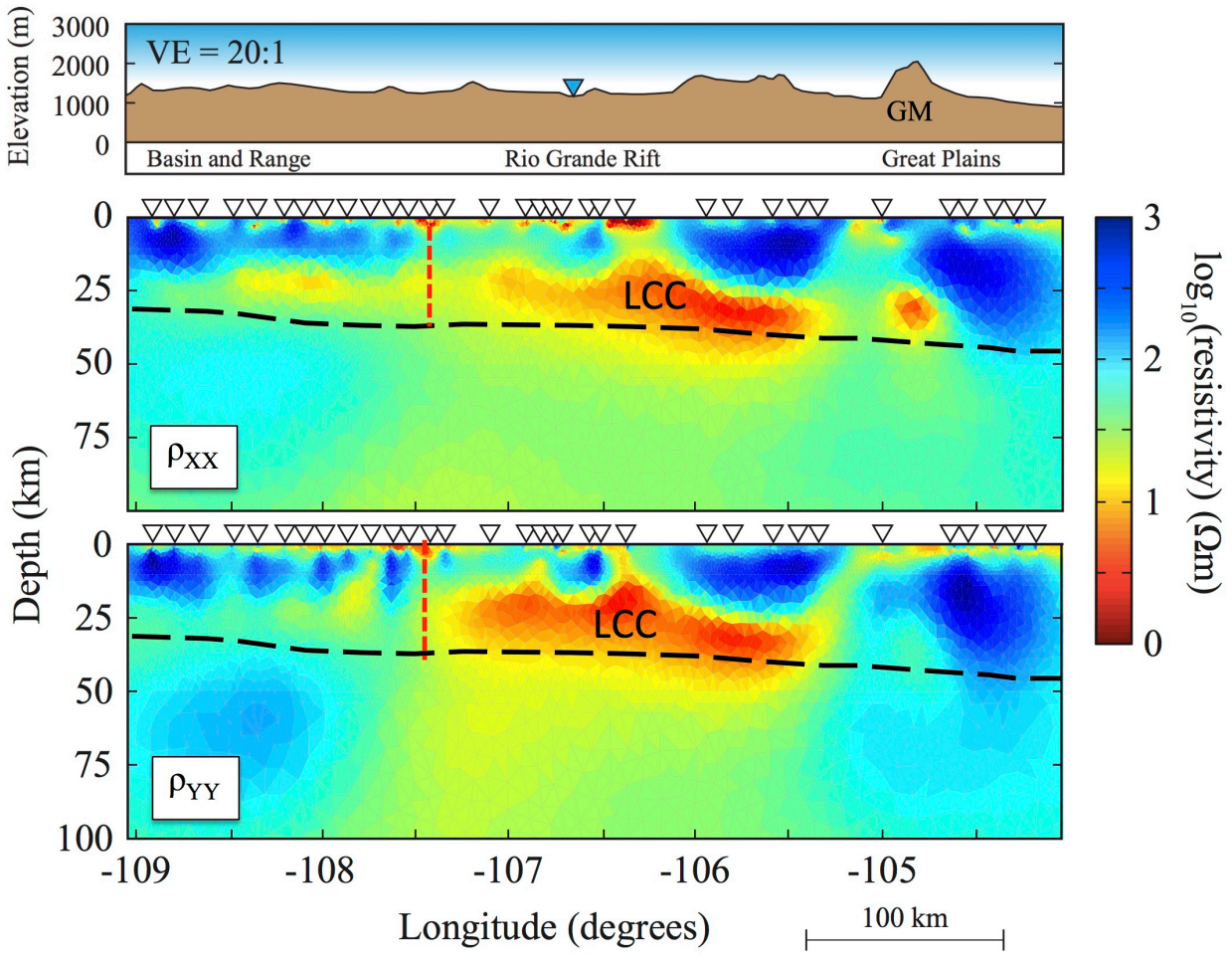

Figure 3.6. Line #2 (southern rift) anisotropic electrical resistivity model. Includes topography and approximate physiographic province boundaries along profile. Inverted white triangles indicate MT station locations. Inverted blue triangle indicates location of Rio Grande. Black dashed line is Moho estimate from Shen et al. [2013]. Red dashed line indicates crustal boundary between Basin and Range and Rio Grande Rift at ~107.5ºW as inferred from electrical resistivity structure, this study. LCC = lower crustal conductor; GM = Guadalupe Mountains

3.4.1 Central Rift

In general, the 2D anisotropic resistivity model of the central rift is characterized by a high resistivity upper crust to depths of 15-25 km, a low resistivity mid- to lower crust beneath the rift axis that extends laterally beneath both the Colorado Plateau and Great Plains, and a steep lateral increase in upper mantle resistivity from west to east across the Rocky Mountain Front.

In the uppermost crust we note two significant zones of low resistivity near the surface, one extending from the western edge of the model to 106º 45' W (SJB in Figure 3.5) and another located within the rift axis centered on 105º 45' W (SLB in Figure 3.5). These features correspond to known sedimentary basins, the San Juan Basin of the Colorado Plateau and the southern San Luis Basin of the Rio Grande Rift.

The mid- to lower crust of the central rift exhibits the most pronounced anisotropic structure of either profile. The lower crust (depths >25 km) is characterized by a broad zone (~200 km wide) of low resistivity in both the profile parallel and profile perpendicular resistivity models (the so-called lower crustal conductor, LCC in Figures 3.5 and 3.6). We note, however, that electrical conductivity in the LCC is enhanced in the north-south direction (parallel to geo-electric strike) relative to the east-west direction across the entire model. We note that the real direction of enhanced conductivity may actually be within a few tens of degrees of the north-south direction due to the manner in which MARE2DEM partitions anisotropy between the two orthogonal directions. Furthermore, the ρ_{yy}

model (resistivity perpendicular to profile strike) additionally shows (1) a strong mid-crustal conductor at a depth of ~12 km in a region that is highly resistive in the ρ_{xx} model (MCC in Figure 3.5b) and (2) a more modest conductivity anomaly at similar mid-crustal depths beneath the western Great Plains (GPA in Figure 3.5b). The change in the direction of enhanced conductivity between the middle and lower crust suggests distinct conductivity enhancing mechanisms that vary within the crustal column.

Detailed resistivity structure of the upper mantle (depths >45 km [Shen et al., 2013]) beneath our profile of the central rift is difficult to resolve owing to the masking effect of high conductivity throughout the crust. We observe that the mantle is relatively conductive directly beneath the lower crustal conductor (10-100 Ωm) and resistive beneath the Great Plains and Colorado Plateau. The lateral transition from conductive to resistive upper mantle appears as a sharp vertical boundary in both cases, although the relationship to the lower crustal conductor differs. To the west, beneath the Colorado Plateau transition zone, the western extent of the LCC corresponds directly with the lateral contrast in upper mantle resistivity structure. To the east, relatively low resistivity (<50 Ωm) in the lower crust extends into the Great Plains (to longitude ~104ºW) while the mantle is resistive east of ~105ºW. This suggests that the zone of high conductivity in the mantle is narrower than the zone of enhanced conductivity in the crust by at least ~100 km. It is possible that the width discrepancy is even greater, but the enhanced

conductance of the San Juan Basin prevents imaging of resistive upper mantle beneath the western extend of the lower crustal conductor.

3.4.2 Southern Rift

In general, the 2D anisotropic resistivity structure of Line #2 can be divided into three broadly similar vertical sections along the profile. The first, from the western edge of the model to 107º30'W, is characterized by a resistive upper crust, moderately conductive lower crust and generally resistive upper mantle. The second, from 107º30'W to 105ºW, exhibits a highly variable upper crust and a lower crust exhibiting extremely low resistivity lower crust (i.e. lower crustal conductor, LCC in Figure 3.6). The mantle beneath this middle section is imaged as conductive, although the high conductance of the lower crust likely obscures our ability to resolve upper-mantle structure. The third section, from 105ºW to the eastern edge of the profile, shows relatively resistive crust and upper mantle, with the marginal exception of near-surface low resistivity.

Anisotropy in this model, in comparison to the central rift profile, is minor. Careful examination of Figure 3.6 reveals a slight enhancement of conductivity in the north-south direction (parallel to the rift axis) within the lower crustal conductor. The near-surface conductor east of the rift axis (106º30'W) exhibits the strongest degree of anisotropy of any feature in the southern rift model. This conductor is the Hueco Basin, a several kilometers deep sedimentary basin elongated parallel to the rift axis. Sedimentary units within the Hueco Basin are

presumed to be isotropically conductive. The imaged anisotropic response of this basin highlights both a limitation and advantage of 2D anisotropic inversion. While the 3D structure of the basin cannot be recovered within a 2D model, the inclusion of anisotropy permits the inversion to fit the measured data, something an isotropic 2D inversion cannot accomplish.

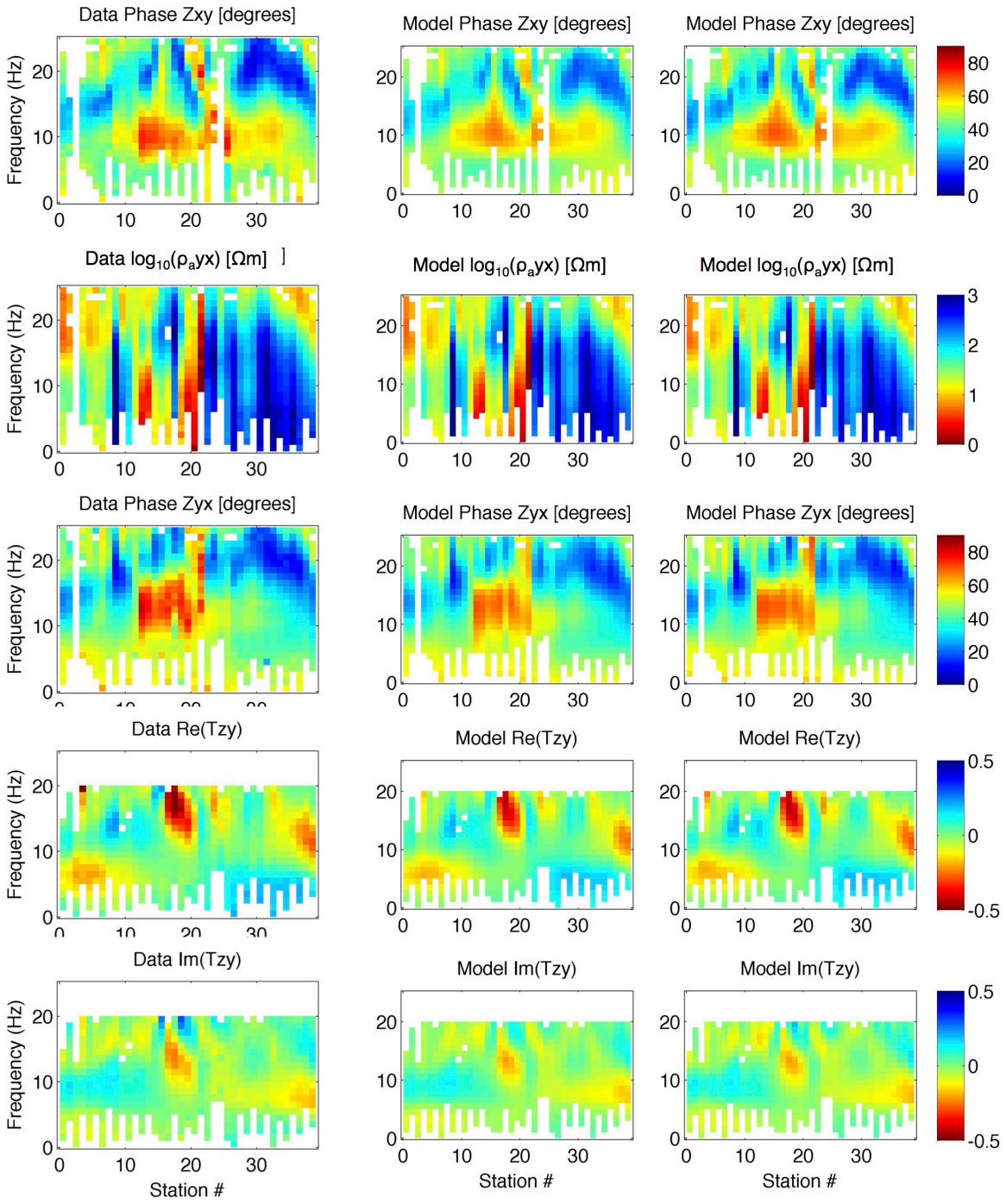

Figure 3.7. Pseudo sections plots of data and forward model response for Line #1. Magnetotelluric transfer functions (TE phase, TM apparent resistivity and phase, tipper) plotted at all stations as a function of period (high frequency at the top of each plot). Columns are data (left), anisotropic model response (center) and isotropic model response (right).

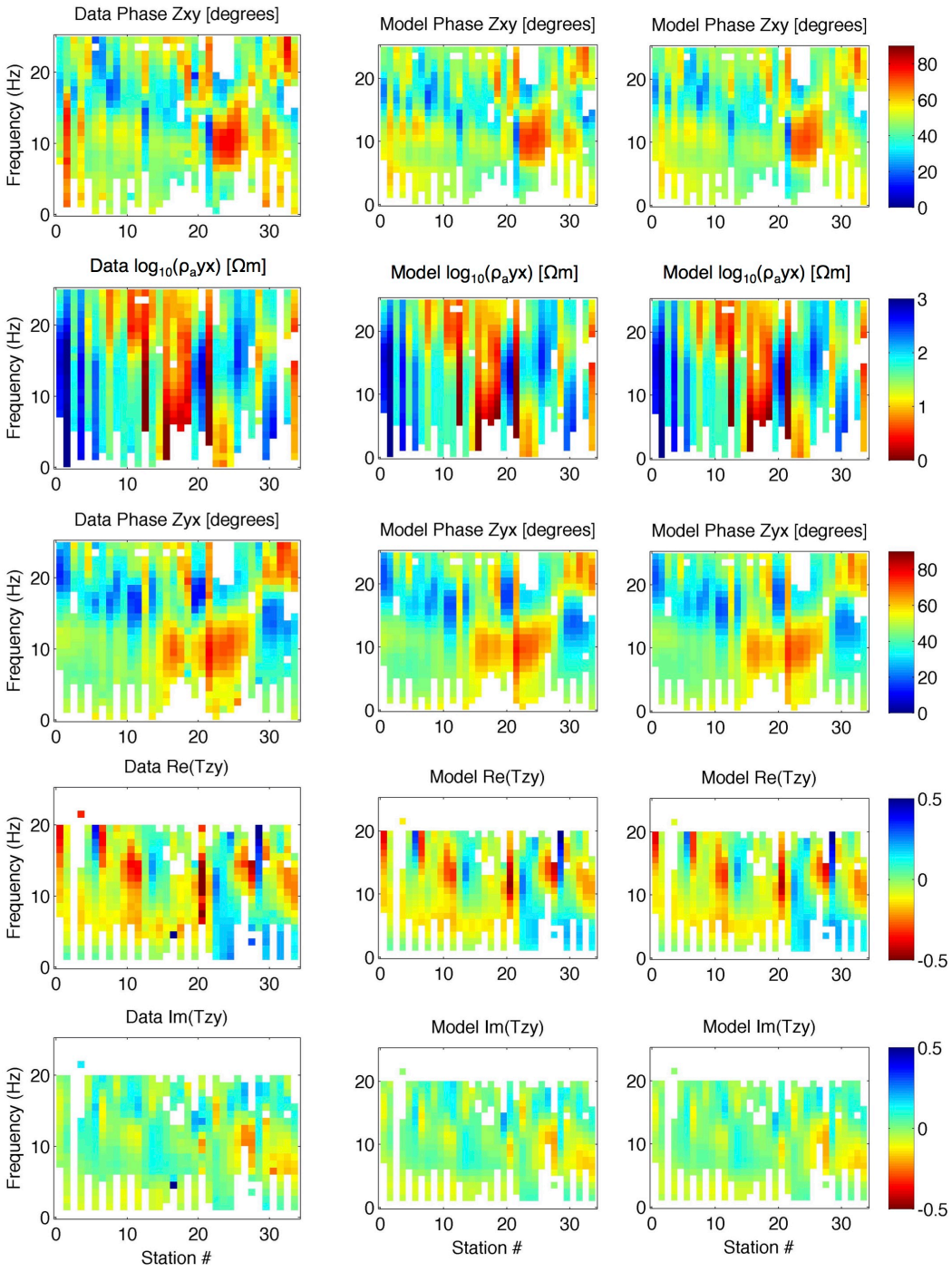

Figure 3.8. Pseudo sections plots of data and forward model response for Line #2. Magnetotelluric transfer functions (TE phase, TM apparent resistivity and phase, tipper) plotted at all stations as a function of period (high frequency at the top of each plot). Columns are data (left), anisotropic model response (center) and isotropic model response (right).

3.5 Discussion

3.5.1 Central Rift

The lower crustal conductor that we image beneath the rift is broad (~200 km wide), highly conductive (<20 Ωm), and exhibits enhanced conductivity in a direction parallel or sub-parallel to the axis of the Rio Grande Rift. With a top at 20-25 km depth across the majority of our profile, we are confident in suggesting that this is the same crustal conductor originally observed by Hermance and Pederson [1980].

Geochemical and electromagnetic geophysical studies of the rift suggest that this conductor can be explained as free saline fluid, first proposed by Jiracek et al. [1983]. A large volume of interconnected, ponded fluid residing in the crust requires (1) a source of crustal fluids and (2) a means by which to retain buoyant and reactive free fluids in equilibrium at depth. Crustal fluids in an active tectonic environment are not unusual. Young volcanic eruptions in and around the rift and the identification of present day crustal magma storage near Socorro and in the Jemez Mountain volcanic complex provide evidence of recent injection of magmatic fluids into the crust. As injected melt cools, it exsolves fluids into the surrounding country rock. Furthermore, the interaction of melt with hydrated and/or metamorphic minerals in the crust and upper mantle may also release fluids in high temperature reactions.

The second factor, an impermeable barrier, may be accomplished in a variety of ways. Metamorphic reactions at the 300-400ºC isotherm may precipitate silica and other minerals out of crustal fluids, reducing permeability and inhibiting fluid migration upward. Structural sources of impermeability include ductile shear zones in the mid-crust. Seismic reflection studies performed by COCORP in the Albuquerque basin in the central Rio Grande Rift found detachment faults beneath the basin, suggesting that high-angle, basin bounding normal faults shallow into listric faults at depths of ~15 km [de Voogd et al., 1988]. Averill and Miller [2013] interpreted similar listric-type faults to exist in the southern rift west of the Rio Grande based on the tomography results of an active-source seismic experiment.

One feature of our results that was not considered in previous interpretations of the mid-crustal conductor is the anisotropic behavior of the conductivity anomaly. Enhanced conductivity oriented parallel to the rift axis, perpendicular to the extension direction, implies a rift-parallel structural grain or fabric that preferentially passes electric current. A reasonable structure that could accomplish this would be rift parallel fracture networks filled with conductive material.

There is a possibility that partial melt is contributing to the high conductivity observed in the lower crust. There is, for example, evidence for recent magma injection into the crust at Socorro [Pearse and Fialko, 2010]. Additionally, the majority of eruptive products from recent volcanism along the Jemez lineament exhibit geochemical characteristics suggestive of significant crustal contamination that in turn implies residence time in the crust [e.g. Nielsen and Dungan, 1985].

How do we differentiate partial melt from saline fluids in a tectonic environment that may produce both types of fluid? Seismic tomography and heat flow suggest that the crust is elevated in temperature beneath the rift. In an otherwise tectonically stable region this would favor the melt interpretation, with the implication that elevated heat flow and slow velocity are a result of melt injection. However, in the Rio Grande Rift, the close proximity of a hot upper mantle to the base of an already thin crust could produce these same observations without the need for melt. Modeling heat flow data in the rift with the assumption of a conductive geotherm produces temperatures above the solidus at depths above the Moho [Decker et al., 1988], suggesting that either the entire lower crust is melted, or more likely, there has been advective heat transfer into the crust from the mantle. The caveat to this interpretation is that the crust is conductive in the present day, and the effects of advective heat transfer may be observed in heat flow today long after partial melt has frozen and become resistive. Seismic attenuation in the crust beneath the rift is high [Philips et al., 2014], which would support the presence of melt if we assume intrinsic attenuation rather than scattering attenuation. However, a vast network of rift-aligned, fluid filled cracks would likely also enhance attenuation due to both intrinsic physical properties and wave scattering. In summary, it is difficult to differentiate between partial melt and crustal fluids in a tectonic environment in which both are reasonable [e.g. Li et al., 2003]. Indeed, thse two conductive species often exist simultaneously, especially in active tectonic environments [e.g. Wannamaker et al., 2008]. In our view the rift-

parallel enhance conductivity observed in the anisotropic model suggests the presence of partial melt, as a rift-parallel fracture network filled with purely aqueous fluid would be difficult to maintain in the high-pressure ductile regime of the lower crust. However, the melt-rock interactions in the lower crust likely also exsolve fluids that occupy grain boundary spaces in the deep crust. Indeed, grain boundary aqueous fluid would explain the rift-perpendicular component of enhanced conductivity in the lower crust, as we would expect a fluid saturated layer to exhibit isotropic conductivity.

Interestingly, high conductivity in the lower crust extends beneath the westernmost Great Plains. Based on the high resistivity values imaged in the upper mantle east of 105°15'W, and the spatial correlation with a similarly sharp increase in seismic velocity observed in teleseismic tomography studies [e.g. Shen et al., 2013], we conclude that the sub-continental lithosphere beneath the western Great Plains is likely cold and relatively water-free. This is in contrast to the low resistivity observed farther north beneath the western-most Great Plains in Colorado [Chapter 2]. That the lower crust above a resistive upper mantle is conductive suggests some mechanism for supplying partial melt (or more likely fluids) through stable lithosphere. We do not advocate for the possibility of lateral fluid flow from the rift axis through the lower crust towards the Plains, as those fluid pathways would likely generate enhanced conductivity oriented in an east-west direction, rather than the north-south preferred direction observed for the lower crustal anomaly in Figure 3.5. Vertical transport of fluids and/or melt through

tectonically stable lithosphere is not completely unreasonable, as the Rayton-Clayton volcanic field of northeastern New Mexico has produced many cinder cones and lava flows in Holocene times despite being underlain by lithosphere that appears cold and dry.

Figure 3.9 is a plot of integrated model conductance (conductivity-thickness product) that highlights the anisotropy and lateral variations in resistivity structure at different depth intervals of the lithosphere. The mid-crustal conductor that is preferentially aligned perpendicular to the rift axis (see blue line Figure 3.9 - Upper Crust) does not have an immediately obvious interpretation. Other than the Rio Grande Rift, the major crustal structure closest to the MCC anomaly is the Laramide-age Naciemento fault, which trends north-south. The only known fabric in the region that trends predominantly east-west is the Yavapai-Mazatzal transition zone, a Proterozoic-age continental suture zone that resulted from the collision of two major tectonic terranes during the assembly of North America [Whitmeyer and Karlstrom, 2007]. While estimates of the exact location of the suture differ, the east-northeast trend of the boundary is widely agreed upon [Magnani et al., 2004] and also runs parallel to the Embudo fault zone, a more local Quaternary feature associated with the northwestern boundary of the Espanola Basin of the Rio Grande Rift. We note that while the Yavapai-Mazatzal suture zone is proposed to extend across several hundred kilometers, our MCC anomaly is limited in lateral extent to ~80 km. This reason for this disparity could be (1) our profile crosses the suture zone at a discrete location at an oblique angle, thus only

capturing a small section of it and/or (2) the eastern and western extent of the suture zone fabric has been destroyed over >1 Gyr of active tectonic history and we only capture a remnant of what remains. Hydrothermal circulation of fluids, infiltration of partial melt, and structural deformation of the crust, all of which have occurred in Cenozoic time in northern New Mexico, could all contribute to destroying interconnected mineral fabrics within the mid-crust. Alternatively, as stated previously, this featre could also be an artifact of imaging more local 3D structure (the Embudo fault zone) using a 2D anisotropic inversion.

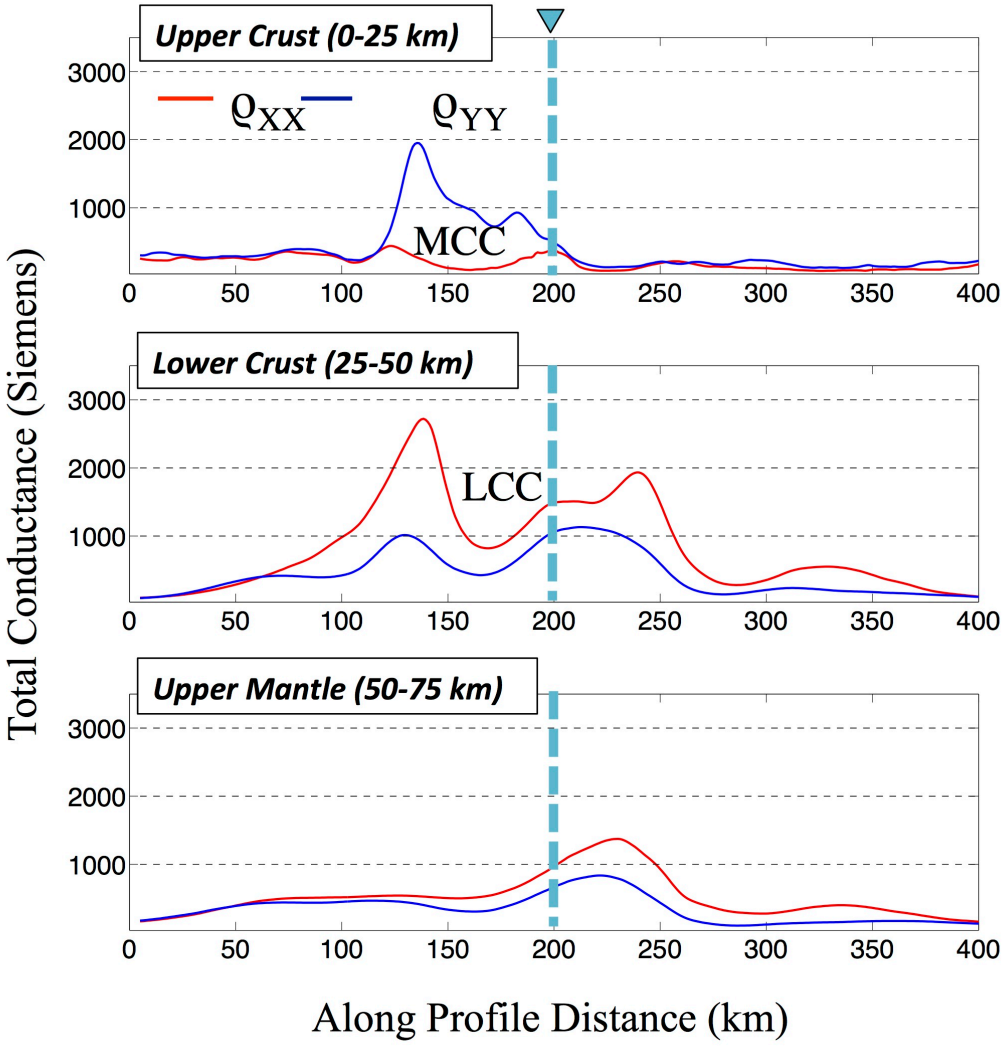

Figure 3.9. Vertically integrated conductance (conductivity thickness product) of central rift resistivity models for upper crust, lower crust, and upper mantle (layers defined by depth ranges shown). Blue dashed line indicates location of Rio Grande. models. MCC = mid-crustal conductor; LCC = lower crustal conductor.

3.5.2 Southern Rift

The most prominent feature of the 2D anisotropic inversion result for the southern rift is the pronounced lower crustal conductor in the middle section of the profile (107°30'W to 105°W) The well resolved top of the conductor varies in depth

from ~10 to 20 km and as a general trend dips to the east, parallel to the dip of the Moho observed by Shen et al. [2013].

The conductor appears to shallow beneath, and in the case of ρ_{yy} model connect with, the near-surface low resistivity anomaly associated with the Hueco Basin at ~106º30'W. We assume that this apparent connection is an artifact of the inversion, specifically a parameterization that prefers smoothly varying resistivity structure. The extremely low resistivity of the Hueco basin atop a moderately resistive upper crust is likely difficult for the inversion to accommodate without permitting a tear in the model smoothness at the level of the basement-sediment contact. Thus, the inversion will bring the lower crustal conductor up in the section so as to minimize vertical gradients in resistivity structure. The lack of stations on the Fort Bliss military base due east of the Hueco basin makes this connection at best poorly constrained if it is real.

Much of the analysis described above for the lower crustal conductor beneath the central rift also applies to the lower crustal anomaly imaged beneath the southern rift. It is again difficult to discriminate fluid from partial melt in an active tectonic environment with a recent history of volcanism, and more than likely both are present. We focus instead on the geometry, placement, and lateral variability of this lower crustal conductor.

The eastern boundary of the Rio Grande Rift in southern New Mexico may be defined in terms of structure, geology, and/or geophysical properties. Structurally and geologically, the eastern margin of the Tularosa basin (~106ºW) is the

easternmost exposure of syn-rift sediments and is bounded by high-angle normal faults that have been active in the Quaternary. If we take the lower crustal conductor to represent rift-related lithospheric modification, the eastern boundary of the rift extents about 100 km farther east than the structural or geologic boundary, beneath the Great Plains. The surface expression of the Rio Grande Rift is wider at this latitude than it is anywhere further north, implying that lithospheric modification due to rifting would also be wider than that observed in the central or northern rift [Chapter 2]. However, it is surprising that unlike the surface expression, the lateral extent of the geophysical signature of rifting appears to be offset to the east (the main river valley is located at 106º40'W in the profile in Figure 3.6). Furthermore, we note that the lateral extent of enhanced lower crustal conductivity is similar in scale to that imaged beneath the central rift, despite a pronounced discrepancy in the surface expression of the central and southern rift.

The lower crust beneath Line #2 exhibits low resistivity values across almost the entire profile; however, the magnitude of the conductivity anomaly does decrease towards the western edge of the profile. Coincident with this change in the character of the lower crustal conductor is an increase in upper mantle resistivity. We interpret this lateral change in lithospheric resistivity structure as the geophysical boundary between the Basin and Range to the west and the Rio Grande Rift to the east. While physiographically similar, it appears that these two provinces are distinct on the basis of their geophysical signatures. We note that while this observation is well supported in the crust, lateral variations in the upper

mantle resistivity structure may be artificially enhanced due to screening effects of the LCC.

3.5.3 Synthesis

Despite significant variability in inherited lithospheric structure, crustal thickness, degree of extension, and surface geology along the axis of the Rio Grande rift, the resistivity structure of the lower crust appears to be remarkably uniform (Figure 3.10). The low resistivity zones that we image in this study are also observed in regional (Chapter 2) and local (Chapter 4) studies of Rio Grande rift conductivity. This suggests some similar mechanism of lithospheric modification has been active along the entire axis of the rift from northern Mexico to central Colorado.

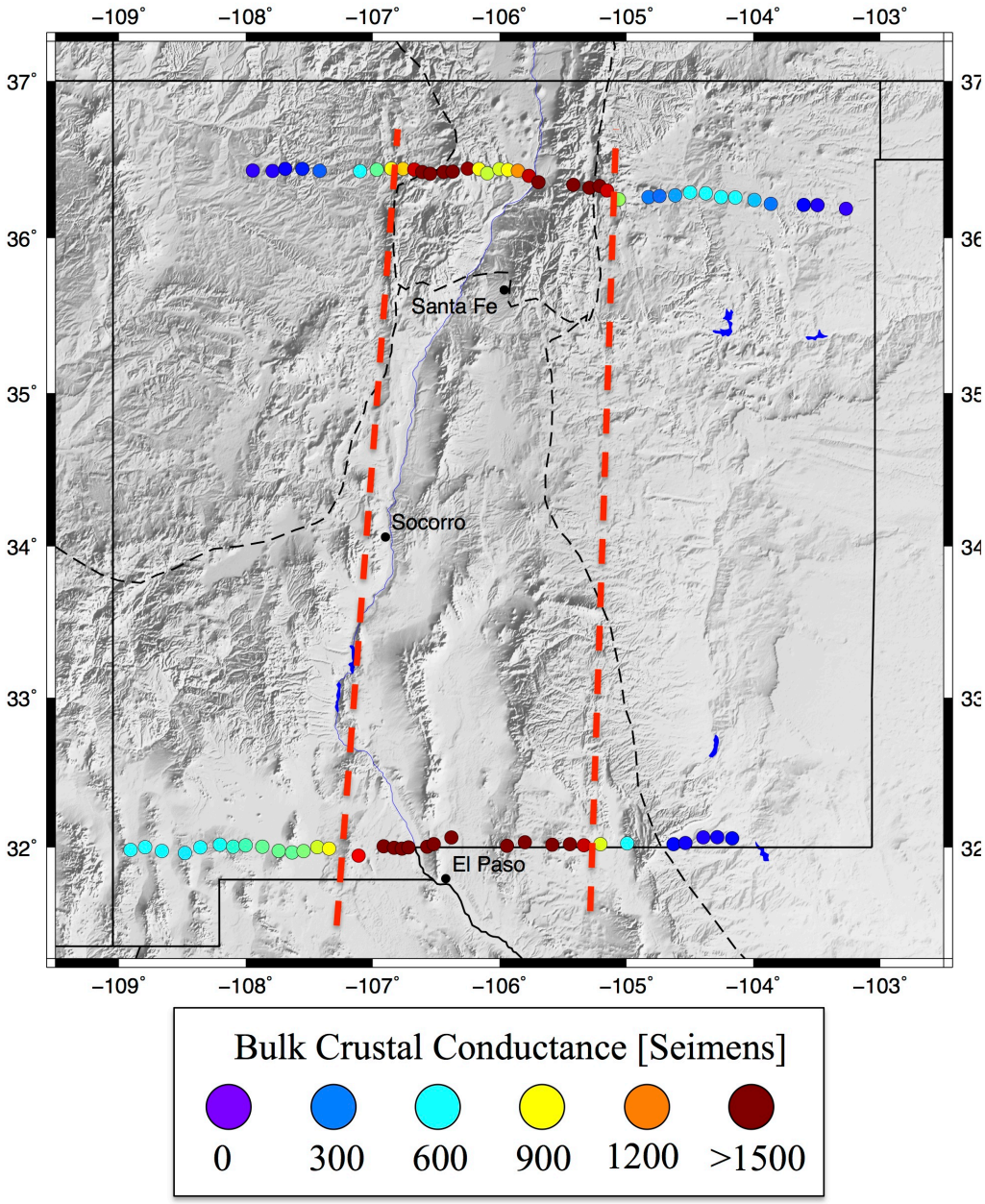

Figure 3.10. Bulk crustal conductance in map view. Conductance of the entire crustal column not including basins (5-50 km for Line #1, 5-40 km for Line #2). Conductance is vertically integrated conductivity thickness product for the 2D ρ_{xx} resistivity models in Figures 3.5 and 3.6. Black dashed lines are physiographic provinces; red dashed lines denote conductance above ~1000 S. Note the uniformity in width of the crustal conductance anomaly (~200 km).

3.6 Conclusions

Our results confirm the existence of a previously identified mid-crustal conductor beneath the central and southern regions of the Rio Grande Rift. By inverting broadband and long period magnetotelluric data for 2D anisotropic resistivity structure along two wide-aperture, high-resolution profiles we show that this feature is not laterally confined to the surface expression of the rift and is in reality much wider. High conductivity in the lower crust in this tectonic environment serves as a marker of late-Cenozoic lithospheric modification. The observed high conductivity is attributed primarily to saline fluids that occupy interconnected grain boundary networks within a high-temperature lower crust, although the presence of partial melt is difficult to rule out. The source of wide-scale modification is likely a long wavelength or broadly distributed source of heat and/or volatiles in the mantle. Geodynamic modeling [van Wijk et a., 2010] and seismic tomography [e.g. Gao et al., 2004] suggest that small-scale edge convection at a step in lithospheric thickness could supply heat and volatiles to the lower crust. Anisotropic modeling reveals a partitioning of low resistivity between the mid and lower crust, suggesting an alternative mechanism for enhancing conductivity at different depths. The low resistivity in the mid-crust, which is enhanced perpendicular to the rift axis, may represent a relic mineralogic fabric inherited from a Proterozoic continental suture zone or simply an artifact of local 3D resistivity structure.

3.7 Acknowledgments

The authors thank John Ferguson, George Jiracek, Scott Baldridge, and Jenny Nakai for valuable discussions. We thank Kerry Key and the Seafloor Electromagnetic Methods Consortium for the use of MARE2DEM and advice on its use. Our magnetotelluric data were collected over two summer field campaigns through a joint effort by the United States Geological Survey and the University of Colorado Boulder. Georgianna Zelenak, Daniel Zietlow, Andrew Adams, Jennifer Harding, and Robert Kowalski provided significant contributions to the field effort. Instrumentation was provided by the United States Geological Survey in Denver, CO and by Martyn Unsworth at the University of Alberta. This work was supported by the University of Colorado Boulder Geological Sciences Department W.O. Thompson Award and Spetzler Award, the Society of Exploration Geophysicists, the Geological Society of America, and National Science Foundation grants EAR-1249669 and EAR-1053596. Additional support was provided by EarthScope (EAR-0323309). This work would not have been possible without land access granted by the National Forest Service, the State of New Mexico, the Bureau of Land Management, and several private landowners. Various maps and graphics were created using Generic Mapping Tools [Wessel and Smith, 1991].

3.8 References

Aldrich, M.J., Ander, M.E., & Laughlin, A.W. (1984) Geological and geophysical signature of the Jemez Lineament: A reactivated Precambrian structure,

International Basement Tectonics, 4, 77-85. Basement Tectonics Committee Inc., Denver, CO, 1984.

Aldrich, M. J. (1986). Tectonics of the Jemez Lineament in the Jemez Mountains and Rio Grande Rift. Journal of Geophysical Research, 91(B2), 1753–1762.

Averill, M. G., & Miller, K. C. (2013). Upper crustal structure of the southern Rio Grande rift: A composite record of rift and pre-rift tectonics. Geological Society of America Special Papers, 494(17), 463–474. http://doi.org/10.1130/2013.2494(17)

Baldridge, W. S., Olsen, K. H., & Callender, J. F. (1983). Rio Grande Rift: Problems and Perspectives.

Baldridge, W. S., Ferguson, J. F., & Wang, B. H. (1994). The western margin of the Rio Grande Rift in northern New Mexico: An aborted boundary? Geological Society of America Bulletin, 106, 1538–1551.

Baldridge, W. S., Braile, L. W., Biehler, S., Jiracek, G. R., Ferguson, J. F., Hasterok, D., Pellerin, L., Bedrosian, P. A., McPhee, D., & Snelson, C. M. (2012). SAGE at 30. The Leading Edge, 31(6), 702-708.

Berglund, H. T., Sheehan, A. F., Murray, M. H., Roy, M., Lowry, A. R., Nerem, R. S., & Blume, F. (2012). Distributed deformation across the Rio Grande Rift, Great Plains, and Colorado Plateau. Geology, 40(1), 23–26. http://doi.org/10.1130/G32418.1

Biehler, S., Ferquson, J., Baldridge, W. S., Jiracek, G. R., Aldern, J. L., Martinez, M., Fernandez, R., Romo, J., Gilpin, B., Braile, L.W., Hersey, D. R., Luyendyk,

B. P., & Aiken, C. L. (1991). A geophysical model of the Española Basin, Rio Grande rift, New Mexico. Geophysics, 56(3), 340–353.

Booker, J. R. (2014). The Magnetotelluric Phase Tensor : A Critical Review. Surveys in Geophysics, 35, 7–40. http://doi.org/10.1007/s10712-013-9234-2

Caldwell, T. G., Bibby, H. M., & Brown, C. (2004). The magnetotelluric phase tensor. Geophysical Journal International, 158, 457–469. http://doi.org/10.1111/j.1365-246X.2004.02281.x

Chapin, C. E., & Cather, S. M. (1994). Tectonic setting of the axial basins of the northern and central Rio Grande rift. In G. R. Keller & S. M. Cather (Eds.), Basins of the Rio Grande Rift: Structure, Stratigraphy, and Tectonic Setting: Geological Society of America Special Paper (Vol. 291, pp. 5–26). Boulder, Colorado. http://doi.org/10.1130/SPE291-p5

Constable, S. C., Parker, R. L., & Constable, C. G. (1987). Occam's inversion: A practical algorithm for generating smooth models from electromagnetic sounding data. Geophysics, 52(3), 289–300.

Constable, S., Shankland, T. J., & Duba, A. (1992). The Electrical Conductivity of an Isotropic Olivine Mantle. Journal of Geophysical Research, 97(B3), 3397–3404. http://doi.org/10.1029/91JB02453

Cosca, M. A., Thompson, R. A., Lee, J. P., Turner, K. J., Neymark, L. A., & Premo, W. R. (2014). Ar / 39 Ar geochronology , isotope geochemistry (Sr , Nd , Pb), and petrology of alkaline lavas near Yampa , Colorado : Migration of alkaline

volcanism and evolution of the northern Rio Grande rift, (2), 1–27. http://doi.org/10.1130/GES00921.1

Dai, L., & Karato, S. (2009). Electrical conductivity of orthopyroxene: Implications for the water content of the asthenosphere. Proc. Jpn. Acad. Ser., 85, 466–475. http://doi.org/10.2183/pjab.85.466

de Voogd, B., Serpa, L., & Brown, L. (1988). Crustal extension and magmatic processes: COCORP profiles from Death Valley and the Rio Grande rift. Geological Society of America Bulletin, 100, 1550–1567.

Eaton, G. P. (1987), Topography and origin of the southern Rocky Mountains and Alvarado Ridge. In M. P. Coward, J. F. Dewey, & P. L. Hancock (Eds.), Continental Extensional Tectonics, Geological Society Special Publication (Vol. 28, pp. 355–369), Geological Society.

Egbert, G. D. (1997). Robust multiple-station magnetotelluric data processing. Geophysical Journal International, 130, 475–496.

Fenneman, N. M. (1946). Physical divisions of the United States.

Fu, Y. V., & Li, A. (2015). Journal of Geophysical Research : Solid Earth. Journal of Geophysical Research: Solid Earth, 120, 1–15. http://doi.org/10.1002/2014JB011602.

Gamble, T. D., Goubau, W. M., & Clarke, J. (1979). Magnetotellurics with a remote magnetic reference. Geophysics, 44(1), 53–68.

Gao, W., Grand, S. P., Baldridge, W. S., Wilson, D., West, M., Ni, J. F., & Aster, R. (2004). Upper mantle convection beneath the central Rio Grande rift imaged by

P and S wave tomography. Journal of Geophysical Research, 109(B03305), 1–16. http://doi.org/10.1029/2003JB002743

Gilbert, H. (2012). Crustal structure and signatures of recent tectonism as influenced by ancient terranes in the western United States. Geopshere, 8(1), 141–157. http://doi.org/10.1130/GES00720.1

Gile, L. (1987). A pedogenic chronology for Kilbourne Hole, southern New Mexico-II. Time of explosions and soil events before explosions. Soil Society of America Journal, 51, 746-760.

Gok, R., Ni, J. F., West, M., Sandvol, E., Wilson, D., Aster, R., Baldridge, W. S., Grand, S., Gao, W., Tillmann, F., & Semken, S. (2003). Shear wave splitting and mantle flow beneath LA RISTRA. Geophysical Research Letters, 30, 1614.

Groom R.W., & Bailey, R.C. (1989), Decomposition of the magnetotelluric tensors in the presence of local three-dimensional galvanic distortion, Journal of Geophysical Research, 94, 1913-1925.

Heise, W., & Pous, J. (2001). Effects of anisotropy on the two-dimensional inversion procedure. Geophysical Journal International, 147, 610–621.

Hermance, J. F. (1979). Toward Assessing the Geothermal Potential of the Jemez Mountains Volcanic Complex: A Telluric-Magnetotelluric Survey.

Hermance, J. F., & Neumann, G. A. (1991). The Rio Grande Rift: new electromagnetic constraints on the Socorro magma body. Physics of the Earth and Planetary Interiors, 66, 101–117.

Hermance, J. F., & Pedersen, J. (1980). Deep Structure of the Rio Grande Rift: A Magnetotelluric Interpretation. Journal of Geophysical Research, 85(B7), 3899–3912. http://doi.org/10.1029/JB085iB07

Humphreys, E. D., & Dueker, K. G. (1994). Western U.S. upper mantle structure. Journal of Geophysical Research, 99(B5), 9615–9634.

Jiracek, G. R., Gustafson, E. P., & Mitchell, P. S. (1983). Magnetotelluric results opposing magma origin of crustal conductors in the Rio Grande Rift. Tectonophysics, 94, 299–326.

Jones, A. G., & Craven, J. A. (1990). The North American Central Plains conductivity anomaly and its correlation with gravity, magnetic, seismic and heat flow data in Saskatchewan, Canada. Physics of the Earth and Planetary Interiors, 60, 169–194.

Keller, G. R., Khan, M. A., Morgan, P., Wendlandt, R. F., Baldridge, W. S., Olsen, K. H., Prodehl, C., & Braile, L. W. (1991). A comparative study of the Rio Grande and Kenya rifts. Tectonophysics, 197, 355–371.

Key, K. (2016). MARE2DEM: a 2-D inversion code for controlled-source electromagnetic and magnetotelluric data. Geophysical Journal International, 207, 571–588. http://doi.org/10.1093/gji/ggw290

Kluth, C. F., & Schaftenaar, C. H. (1994). Depth and geometry of the northern Rio Grande rift in the San Luis Basin, south-central Colorado. In G. R. Keller & S. M. Cather (Eds.), Basins of the Rio Grande Rift: Structure, Stratigraphy, and

Tectonic Setting: Geological Society of America Special Paper 291 (pp. 27–37). Boulder, Colorado: Geological Society of America.

Landman, R. L., & Flowers, R. M. (2013). (U-Th)/He thermochronologic constraints on the evolution of the northern Rio Grande Rift, Gore Range, Colorado, and implications for rift propagation models. Geosphere, 9(1). http://doi.org/10.1130/GES00826.1

Li, S., Unsworth, M. J., Booker, J. R., Wei, W., Tan, H., & Jones, A. G. (2003). Partial melt or aqueous fluid in the mid-crust of Southern Tibet? Constraints from INDEPTH magnetotelluric data. Geophysical Journal International, 153, 289–304.

Magnani, M. B., Miller, K. C., Levander, A., & Karlstrom, K. (2004). The Yavapai-Mazatzal boundary: A long-lived tectonic element in the lithosphere of southwestern North America. Geological Society of America Bulletin, 116(7), 1137–1142. http://doi.org/10.1130/B25414.1

Nettleton, C. (1997). Magnetotelluric modeling of the Valles caldera, New Mexico. Masters thesis. Department of Geological Sciences, San Diego State University.

Nielsen, R. L., & Dungan, M. A. (1985). The petrology and geochemistry of the Ocate volcanic field, north-central New Mexico. Geological Society of America Bulletin, 96, 296–312.

Obrebski, M., Allen, R. M., Pollitz, F., & Hung, S.-H. (2011). Lithosphere-asthenosphere interaction beneath the western United States from the joint inversion of body-wave traveltimes and surface-wave phase velocities.

Geophysical Journal International, 185, 1003–1021. http://doi.org/10.1111/j.1365-246X.2011.04990.x

Pearse, J., & Fialko, Y. (2010). Mechanics of active magmatic intraplating in the Rio Grande Rift near Socorro, New Mexico. Journal of Geophysical Research, 115(B07413), 1–16. http://doi.org/10.1029/2009JB006592

Phillips, W. S., Mayeda, K. M., & Malagnini, L. (2014). How to Invert Multi-Band, Regional Phase Amplitudes for 2-D Attenuation and Source Parameters: Tests Using the USArray. Pure and Applied Geophysics, 171, 469–484. http://doi.org/10.1007/s00024-013-0646-1

Poe, B. T., Romano, C., Nestola, F., & Smyth, J. R. (2010). Electrical conductivity anisotropy of dry and hydrous olivine at 8 GPa. Physics of the Earth and Planetary Interiors, 181, 103–111. http://doi.org/10.1016/j.pepi.2010.05.003

Repasch, M., Karlstrom, K., Heizler, M., & Pecha, M. (2017). Borth and evolution of the Rio Grande fluvial system in the past 8 Ma: Progressive downward integration and the influence of tectonics, volcanism, and climate. Earth-Science Reviews, 168, 113-164.

Ricketts, J. W., Kelley, S. A., Karlstrom, K. E., Schmandt, B., Donahue, M. S., & van Wijk, J. (2015). Synchronous opening of the Rio Grande rift along its entire length at 25–10 Ma supported by apatite (U-Th)/He and fission-track thermochronology, and evaluation of possible driving mechanisms. Geological Society of America Bulletin. http://doi.org/10.1130/B31223.1

Rodriguez, B. D., & Sawyer, D. A. (2013). Geophysical constraints on Rio Grande rift structure and stratigraphy from magnetotelluric models and borehole resistivity logs, northern New Mexico. In M. R. Hudson & V. J. S. Grauch (Eds.), New Perspectives on Rio Grande Rift Basins: From Tectonics to Groundwater: Geological Society of America Special Paper 494 (pp. 323–344). Geological Society of America. http://doi.org/10.1130/2013.2494(13).

Roy, M., MacCarthy, J. K., & Selverstone, J. (2005). Upper mantle structure beneath the eastern Colorado Plateau and Rio Grande rift revealed by Bouguer gravity, seismic velocities, and xenolith data. Geochemistry, Geophysics, Geosystems, 6(10), 1–19. http://doi.org/10.1029/2005GC001008

Schmandt, B., & Humphreys, E. (2010). Complex subduction and small-scale convection revealed by body-wave tomography of the western United States upper mantle. Earth and Planetary Science Letters, 297, 435–445. http://doi.org/10.1016/j.epsl.2010.06.047

Schmandt, B., Lin, F.-C., & Karlstrom, K. E. (2015). Distinct crustal isostasy trends east and west of the Rocky Mountain Front. Geophysical Research Letters, 42. http://doi.org/10.1002/2015GL066593

Shen, W., Ritzwoller, M. H., & Schulte-Pelkum, V. (2013). A 3-D model of the crust and uppermost mantle beneath the Central and Western US by joint inversion of receiver functions and surface wave dispersion. Journal of Geophysical Research: Solid Earth, 118, 1–15. http://doi.org/10.1029/2012JB009602

Tweto, O. (1979). The Rio Grande Rift system in Colorado. In Rio Grande Rift: Tectonics and magmatism (pp. 33–56). Washington D.C.: American Geophysical Union. http://doi.org/10.1029/SP014p0033

Walker, J. D., Bowers, T. D., Black, R. A., Glazner, A. F., Farmer, G. L., & Carlson, R. W. (2006), A geochemical database for western North American volcanic and intrusive rocks (NAVDAT), In A. K. Sinha (Ed.), Geoinformatics: Data to Knowledge: Geological Society of America Special Paper 397 (pp. 61–71), doi:10.1130/2006.2397(05).

Wannamaker, P. E., Hohmann, G. W., & Ward, S. H. (1984). Magnetotelluric responses of three-dimensional bodies in layered earths. Geophysics, 49(9), 1517–1533.

Wannamaker, P. E., Hasterok, D. P., Johnston, J. M., Stodt, J. A., Hall, D. B., Sodergren, T. L., Pellerin, L., Maris, V., Doerner, W. M., Groenwold, K. A., & Unsworth, M. J. (2008), Lithospheric dismemberment and magmatic processes of the Great Basin-Colorado Plateau transition, Utah, implied from magnetotellurics. Geochemistry, Geophysics, Geosystems, 9(5), doi:10.1029/2007GC001886.

Wessel, P. and Smith, W. H. F., (1991), Free software helps map and display data. EOS Trans. AGU, 72, 441-446.

Whitmeyer, S., and Karlstrom, K. E. (2007). Tectonic model for the Proterozoic growth of North America. Geosphere, 3(4), 220–259. http://doi.org/10.1130/GES00055.1

Wilson, D., Aster, R. C., Ni, J., Grand, S. P., West, M., Gao, W., Baldridge, W. S., & Semken, S. (2005), Imaging the seismic structure of the crust and upper mantle beneath the Great Plains, Rio Grande Rift, and Colorado Plateau using receiver functions. Journal of Geophysical Research, 110(B05306), doi:10.1029/2004JB003492

.

CHAPTER FOUR

2D AND 3D RESISTIVITY STRUCTURE OF THE JEMEZ MOUNTAINS VOLCANIC FIELD AND VALLES CALDERA

4.1 Abstract

The Valles caldera, in north-central New Mexico, USA, is a 20-km wide topographic depression in the Jemez Mountains volcanic field (JMVF) that formed during two massive ignimbrite eruptions at 1.65 and 1.26 Ma. Post-collapse volcanic activity in the caldera includes the rise of a 1 km high resurgent dome, periodic eruptions of the Valles rhyolite along ring fractures, and the presence of a geothermal reservoir beneath the western caldera with temperatures in excess of 300°C at a mere 2 km depth. We present electrical resistivity models of the upper crust from two-dimensional and three-dimensional inversion of broadband (100 Hz to 2000 s) magnetotelluric (MT) data collected in and around the Valles caldera. The Summer of Applied Geophysical Experience (SAGE) has been acquiring geophysical data in the northern Rio Grande rift for more than three decades (1983-2017). Included in that vast dataset are over 60 broadband magnetotelluric soundings that have recently been cataloged, geo-located, and digitized for use in modern geophysical processing and modeling. The resistivity models presented here were produced by inverting a subset of SAGE MT data along with 30 broadband MT soundings acquired by the Unocal Corporation in 1983. Two-dimensional inversion of regional MT data images a thick package (>2 km) of rift and caldera fill

sediments, a pervasive mid-crustal conductor starting at depths of 10-20 km, and an anomalous low resistivity zone directly beneath the Valles caldera at a depth of ~7km. Detailed three-dimensional inversion of the MT data collected within the caldera images conductive caldera fill near the surface, the very top of the mid-crustal conductor at a depth of ~10 km, and an exceptionally low resistivity anomaly at 1.5 km depth associated with the high-temperature geothermal reservoir of the western caldera.

4.2 Introduction

The Jemez Mountain volcanic field (JMVF) [e.g. Smith and Bailey, 1966; Smith et al., 1970] is a long-lived late Cenozoic volcanic center in northern New Mexico, USA, that lies at the intersection of the Rio Grande Rift, a north-south trending mid- to late Cenozoic continental rift system [e.g. Chapin and Cather, 1994], and the so-called Jemez lineament [Aldrich 1986], a series of recently active (16 Ma - 3000 y.b.p.) volcanic centers oriented along a northeast trending line across New Mexico (see Figure 4.1). The most significant volcanic activity associated with the volcanic field are two massive caldera-forming eruptions at 1.65 Ma and 1.25 Ma [e.g. Zimmerer et al., 2013]. These two eruptions occurred in approximately the same location and together produced the Valles caldera [Smith et al, 1961], a crater-like depression over 20 km in diameter that forms the most striking feature of the Jemez Mountains volcanic field.

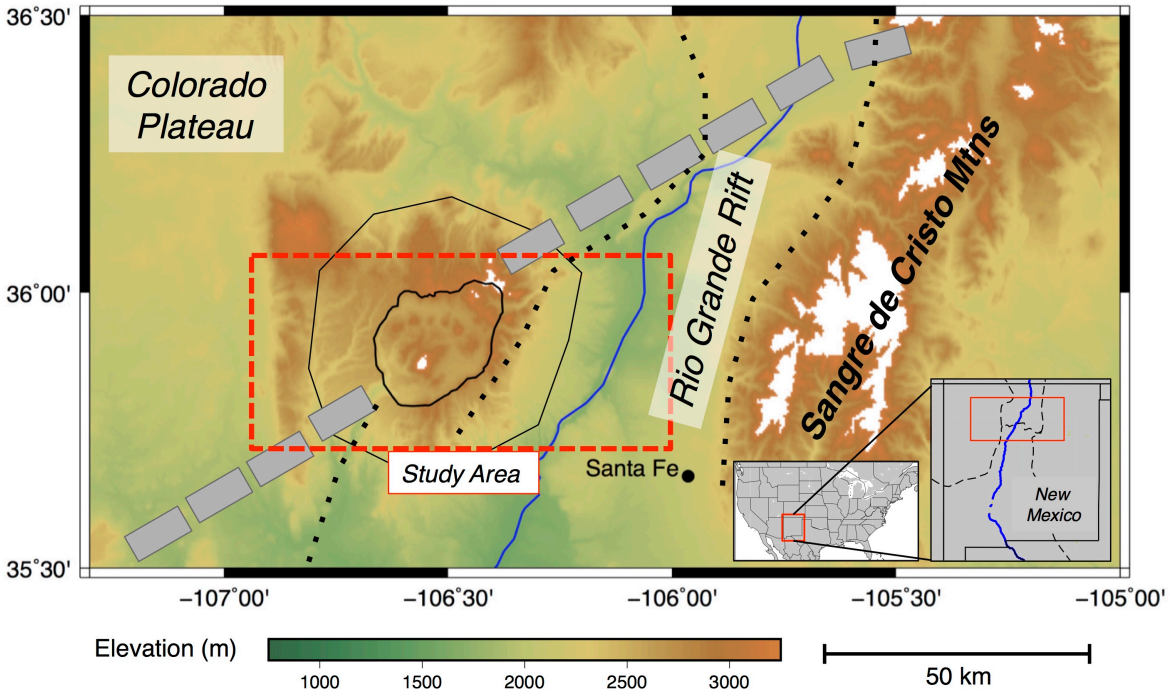

Figure 4.1. Tectonic context of the Jemez Mountains Volcanic Field. Bold dashed grey line is inferred Jemez Lineament [Aldrich 1986], Concentric solid black lines are the topographic rim of the Valles caldera nested inside the approximate extent of the Jemez Mountains Volcanic Field. Red dashed line indicates location of Figure 4.2. Black dotted lines are the boundaries of the Rio Grande Rift. Black dotted line within the area of Figure 4.2 is approximate trace of the Pajarito Fault. Black dashed line within New Mexico inset map represents physiographic province boundaries [Fenneman 1946].

The post-collapse history of the caldera has been varied and active [Self et al., 1986]. Within 100 kyr of the second caldera-forming eruption a resurgent dome rose to a height almost 1000 m above the caldera floor. The next 500 kyr were punctuated by a series of rhyolitic eruptions along ring fractures surrounding the resurgent dome. The Battleship Rock ignimbrite and the Banco Bonito lava, the two youngest eruptions within the caldera, erupted at ~74 and ~68 ka, respectively,

following a hiatus in volcanic activity lasting 0.45 m.y. [Zimmerer et al., 2013]. The apparent reactivation of the caldera, in conjunction with geophysical imaging of a potentially molten magma chamber [e.g. Ankeny et al., 1986; Roberts et al., 1991], led Wolff and Gardener [1995] to suggest the caldera may be entering a new phase of silicic magma production spurred by injection of basaltic magma into the continental crust.

4.2.1 The Bandelier Magma Chamber

The Caldera and Rift Deep Experiment (CARDEX) [Olsen et al., 1986; Ankeny et al., 1986] was the first seismic investigation to identify a low velocity anomaly beneath the Valles caldera. Using six explosions and shallow local earthquakes observed at 78 recording stations, Ankeny et al. [1986] performed a simultaneous inversion for three-dimensional (3D) P-wave velocity structure and hypocenter locations beneath the Valles caldera. They found a low velocity zone beneath the caldera of magnitude -0.4 km/s (absolute velocity of 5.6 km/s, relative to 6.0 km/s for the surrounding crust). The depth to the anomaly was estimated to be between 5-10 km below sea level, although this was poorly constrained given the sparse vertical parameterization of the model grid (nodes at -1.7, 0.0, 10.0. and 20.0 km). Ankeny et al. concluded that they could explain the anomaly with high-temperature alone, assuming the rocks beneath the caldera at 6-8 km depth were at least 500-600ºC.

The deployment of seismic recording instruments inside the ring fracture for the first time allowed Roberts et al. [1991] to use teleseismic travel time delays to further constrain the size, shape, location and velocity of the low velocity zone. The best fit to the delay times was provided by a forward model consisting of (1) a low velocity layer of caldera fill constrained by geology and (2) a lens shaped low velocity zone (LVZ) directly beneath the caldera. The LVZ was 17 km wide at maximum lateral extent, up to 8 km thick, centered at 10 km depth, and had a velocity anomaly of negative 30-40% relative to the surrounding upper crust. Based on the amplitude of the velocity anomaly, as well as the depth and lateral position of the LVZ, Roberts et al. concluded that they had imaged a region of partial melt, either the residual magma chamber from the caldera-forming event at 1.25 Ma or a more recent magmatic injection responsible for post-caldera volcanism.

The Jemez Tomography Experiment (JTEX) [Lutter et al., 1995; Steck et al., 1998; Aprea et al., 2002] provided the first high-resolution images of 2D and 3D velocity structure beneath the caldera. Lutter et al., [1995], using a similar array geometry to Roberts et al. [1991] but with denser station coverage, produced a 2D cross section of velocity structure beneath the caldera to depths of 50 km. The resulting image of upper crustal velocity structure revealed a low velocity zone consistent in depth and amplitude with the LVZ of Roberts et al., [1991] although much narrower in width (6 km vs. 17 km). The results of subsequent 3D inversion of the same data set [Steck et al., 1998] were consistent with previous interpretations: a low velocity zone imaged beneath the Valles caldera at upper crustal depths with

a velocity perturbation of -35% relative to the surrounding nodes (see Figure 4.2). Steck et al., [1998] were able to quantify the melt fraction required to produce the LVZ and interpreted the anomaly as a zone of partial melt with a minimum melt fraction of 10%.

None of the seismic investigations outlined above [esp. Roberts et al., 1991; Lutter et al., 1995; and Steck et al., 1998] could rule out the Bandelier magma chamber (i.e. the residual melt remaining from the latest caldera forming eruption), but all shared a preferred interpretation, based on recent volcanic and hydrothermal activity, that the LVZ is a result of post-caldera magmatic activity and relatively recent injection of melt into the continental crust.

4.2.2 Previous MT Investigations of the Valles Caldera

The most thorough investigation into the deep electrical resistivity structure of the Valles caldera and Jemez Mountains volcanic field was done by C. Nettleton [1997] for a master's thesis completed at San Diego State University. Building upon the preliminary findings of Jiracek et al. [1996], Nettleton performed a two-dimensional modeling study on a set of broadband (300 Hz to 600 s) magnetotelluric data collected in and around the Valles caldera by industry contractors and the Summer of Applied Geophysical Experience (SAGE), an educational summer field camp operating out of Santa Fe, New Mexico [Baldridge et al., 2012]. Much of those same data are used in this study. Nettleton inverted for two-dimensional resistivity structure along two east-west oriented profiles crossing the caldera. Beneath both

profiles he imaged an electrically conductive near-surface feature, interpreted as caldera fill and/or pre-caldera sedimentary units, and a low resistivity anomaly that appeared beneath all stations but shallowed beneath the Valles caldera to a minimum depth of 7 km. The top of this conductor was imaged as deepening to the west to depths of >25 km beneath the Nacimiento Uplift. The behavior of the conductor east of the caldera was undetermined owing to a lack of data coverage in this region.

In interpreting this low resistivity feature, Nettleton noted that (1) it was much broader than the previously identified low velocity zones, (2) it was deeper than the LVZ identified as partial melt by Lutter at el. [1995] and Steck et al. [1998], and (3) the contour of the top of the conductor paralleled isotherm contours modeled by Sass and Morgan [1986] for the shallow subsurface (upper few kilometers) of the caldera. These observations led Nettleton to interpret the mid-crustal conductor as an accumulation of saline brine, sourced from meteoric water, crystallizing magma, or metamorphic reactions, which had been trapped beneath an impermeable barrier preventing upward migration of those fluids. A lack of permeability within the upper crust was attributed to the brittle ductile transition. Furthermore, the topography along the top of the conductor was interpreted to represent the 450ºC isotherm associated with the brittle ductile transition.

Our study benefits from additional data and geophysical modeling tools that Nettleton [1997] and Jiracek et al., [1996] did not have at their disposal. Two-dimensional inversion of magnetotelluric data has become much less

computationally expensive in the 20 years since those previous studies were conducted, allowing for rapid model assessment and sensitivity testing. In a similar vein, three-dimensional inversion has only recently been made accessible to academic researchers working without high performance computing power. We also benefit from the additional years of MT data collection at SAGE, which has allowed us to increase the aperture of our study to the east, into the Rio Grande Rift, and expand the scope of our tectonic interpretation.

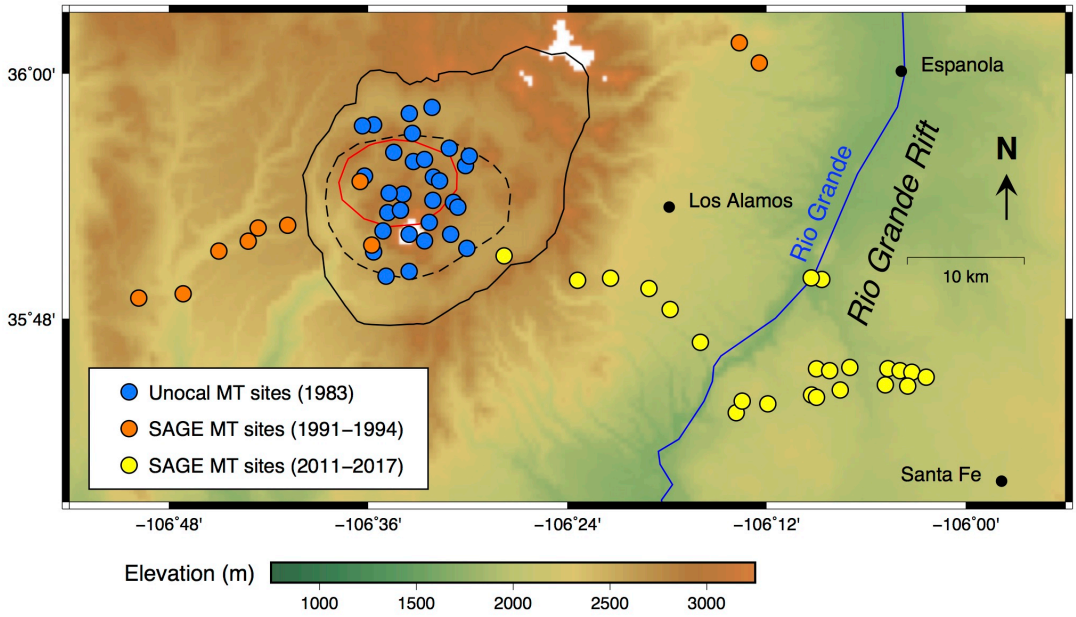

Figure 4.2. Station locations of SAGE and Unocal magnetotelluric data. Station color indicates acquisition year. Concentric circles are topographic rim of the Valles and Toledo calderas (solid black line), ring fracture (dashed black line), and <-10% Vp anomaly at 7.5 km from teleseismic P-wave tomography of Steck et al., [1998] (red line).

4.3 Magnetotelluric Data

Magnetotelluric data used in this study comes from both the geothermal industry and the Summer of Applied Geophysical Experience. In 1983, the Unocal Company collected broadband magnetotelluric data (300 Hz to 600 s) at 30 station locations within the Valles caldera (blue dots, Figure 4.2). These data, which are of variable but generally good quality (Appendix section A.3), were intended for use in an assessment of the geothermal potential of the caldera. From 1991-1994 the SAGE program supplemented these data with 10 broadband MT stations (200 Hz to 1600 s) in the Jemez Mountains (orange dots, Figure 4.2), including reoccupation of two locations within the caldera that had previously been surveyed in the Unocal study. Beginning in 2011, and continuing in 2012, 2013, and 2016, the SAGE program collected broadband MT data (100 Hz to 1000 s) on the Cerros del Rio volcanic field (yellow dots, Figure 4.2), the latter consisting principally of a basalt flow originating from the Jemez Mountains that pre dates caldera formation and is located approximately 30 km southeast of the modern Valle Grande. Finally, in 2017, SAGE collected five additional stations in Bandelier National Monument along Highway 4 and one inside the caldera, closing the data gap between the Valles caldera and the Cerros del Rio volcanic field. The resulting distribution of ~60 broadband MT stations provides relatively dense MT data coverage along a profile straddling the western margin of the Rio Grande Rift as well as an array inside the caldera with a geometry well-suited for three-dimensional modeling.

Appendix section A.3 shows plots of magnetotelluric transfer functions (off-diagonal components of apparent resistivity and phase, and tipper data where available) for all stations used in this study. The details of the data processing steps involved in producing the transfer functions for the pre-2011 data are unknown. As such, minimum data errors for these stations were by default set equal to an applied error of 20% of the log value of impedance magnitude (i.e. apparent resistivity), corresponding to a phase error of 5.6º. The modern SAGE data (2011-2017) were collected as remote referenced station pairs [Gamble et al., 1979] and processed using the multi-station processing approach of Egbert [1997], which provides robust estimates of data errors.

4.3.1 Dimensionality

Figure 4.3 shows magnetotelluric phase tensor ellipses for the data used in 2D and 3D modeling. The magnetotelluric phase tensor [Caldwell et al., 2004] provides a data based and relatively distortion free means of assessing the dimensionality of regional geoelectric structure. Phase tensors are represented in Figure 4.3 as ellipses shaded by Φ_2, the geometric mean of the minimum and maximum principal values of the phase tensor. The rotationally invariant value Φ_2 (typically ranging from 0-90º) provides a first-order approximation of the vertical resistivity gradient for a given site at a particular period. High [low] Φ_2 values corresponding to decreasing [increasing] resistivity with depth. Higher order resistivity structures (i.e. 2D and 3D features) are represented by non-circular

ellipses. Three-dimensional structure is indicated by rotation of phase tensor ellipses with period at a single site and/or a variation in ellipse orientation at a single period among several sites located close together.

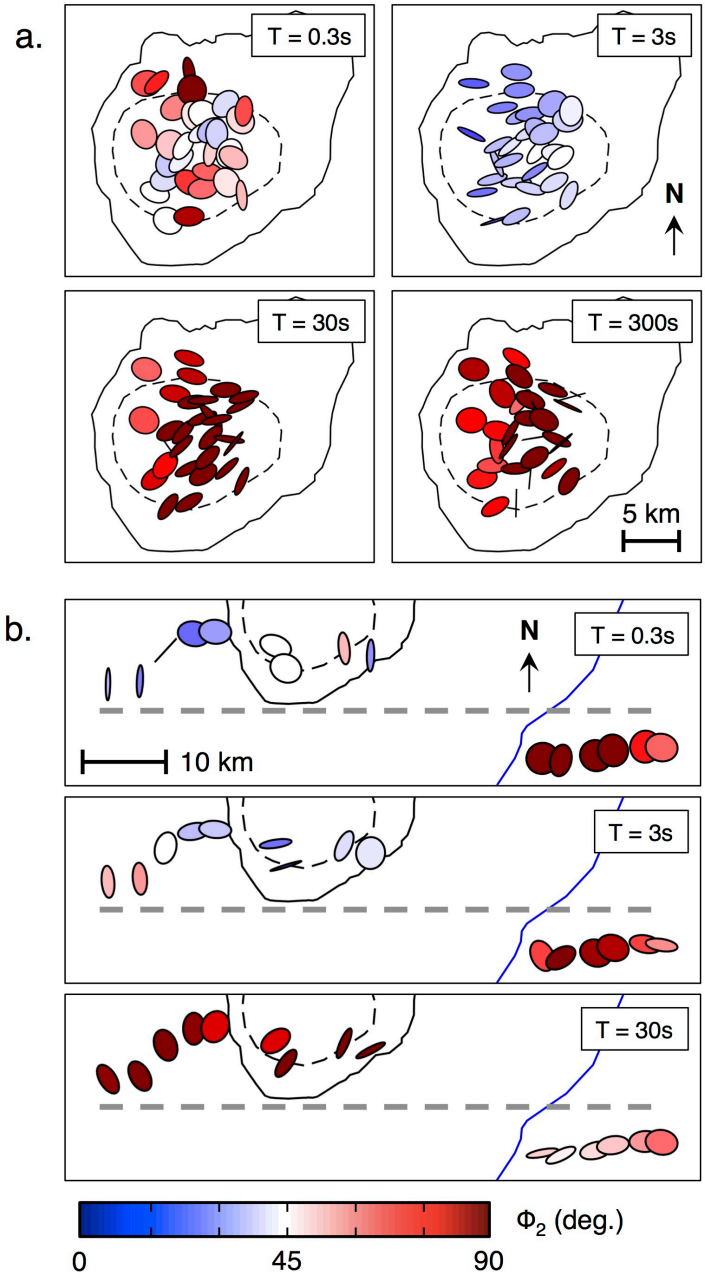

Figure 4.3. [previous page] Phase tensor ellipses for data used in (a) 3D and (b) 2D magnetotelluric inversions. Ellipses are shaded by Φ_2, a first-order estimate of the vertical resistivity gradient at a particular site and period [blue = increasing resistivity with depth; red = decreasing resistivity]. Caldera rim and ring fracture denoted as in Figure 4.2, gray line in (b) shows 2D profile trace, blue line in (b) is Rio Grande, T = period of MT data.

Figure 4.3a shows phase tensor ellipses for the data used in the 3D inversion at four pseudo-slices (period = 0.3, 3, 30, and 300 s). The most coherent orientation grouping of phase tensor ellipses is observed for the eastern caldera stations at T = 30s (approximate orientation of the major axes is N60°E). However, this orientation is not consistent across the array and does not persist at higher or lower frequencies. In general, the caldera stations exhibit high variability in phase tensor ellipse orientations both spatially and as a function of period, indicating that 3D modeling would be the appropriate tool for imaging resistivity structure here.

Figure 4.3b shows phase tensor ellipses for the data used in the 2D inversion at three pseudo-slices (period = 0.3, 3, 30s). The major axes of the phase tensor ellipses at these stations are generally oriented either parallel or perpendicular to the 2D profile trace (gray dashed line), providing a good indication that the data at these stations are at least nominally 2D. An apparent 90° difference in ellipse orientation between adjacent stations at a similar period (see westernmost stations at 3s period) is not an indication of 3D structure but more likely represents stations positioned on either side of a geoelectric contact.

We observe a similar variability in Φ_2 values as a function of period in both Figures 4.2a and 4.2b. At the highest frequencies (T = 0.3s), Φ_2 values encompass a

large range of values, reflecting heterogeneous resistivity structure in the near-surface. At intermediate frequencies (T = 3s), Φ_2 is consistently low beneath the caldera, indicating the influence of more resistive structure at depth. By 30 s period, all stations show high values of Φ_2. This is evidence for a ubiquitous low resistivity structure present across the array.

4.3.2 Data Selection

Ultimately, 15 stations were selected for 2D inversion: five SAGE stations west of the caldera, six SAGE stations east of the caldera, and four stations within the caldera (one from SAGE 2017, one from SAGE 1991, and two from the Unocal data set). An east-west profile through the available data was chosen based on the observation that a subset of the data displayed characteristics of north-south geoelectric strike (Figure 4.3b). This subset of data was then examined for overall data quality and proximity to the proposed profile trace and a final selection was made. Detailed masking of outliers (<20% of the full data set) via visual inspection of transfer function curves was performed for the selected data prior to inversion. Our preferred 2D resistivity model is the result of inverting TM mode apparent resistivity and phase, TE mode phase and the complex in-line component of the tipper (Re(Tzy) and Im(Tzy)) at 21 periods distributed logarithmically between 200 Hz and 1365 s. Transverse electric (TE) mode apparent resistivity was initially excluded from the inversion due to an assumed sensitivity to off-profile (i.e. 3D) structure [Wannamaker et al., 1984] and a desire to avoid contamination from such

features. However, subsequent tests of the inversion including TE apparent resistivity produced broadly similar resistivity structure, indicating that there was no substantial benefit to including it.

For the 3D inversion, we limited our selection to stations located inside the caldera in order to focus on the detailed structure of the caldera itself. Thirty stations were selected for input into the 3D inversion, including 28 of the Unocal stations and two SAGE stations from 1991. Inversion inputs from each site consisted of full impedance tensors at 20 periods distributed logarithmically between 100 Hz and 600 s. A few individual data points were manually culled prior to inversion based on visual inspection of impedance elements. Tipper data were not included in the inversion that produced our preferred 3D model. Early attempts at inverting for tipper did not converge. This was likely a result of the generally low magnitude tipper data for most stations inside the caldera.

4.4 2D and 3D Magnetotelluric Inversion

For the two-dimensional inversion of the regional electrical resistivity structure of the Jemez Mountains volcanic field, we used MARE2DEM [Key et al., 2016], which utilizes an Occam's inversion approach [Constable et al., 1987] to iteratively solve for the smoothest resistivity structure that adheres to a user defined target data residual. MARE2DEM is a 2D finite element regularized inversion developed for marine magnetotelluric and controlled source electromagnetic inversion problems but with functionality for terrestrial

magnetotelluric data as well. Prior to 2D inversion, minimum error thresholds, or error floors, of 20% the log amplitude of the apparent resistivity, corresponding to 5.6º phase error, were applied to the data. Error floors of 0.03 were applied to all tipper components.

For the three-dimensional inversion of the local resistivity structure of the Valles caldera we utilized ModEM [Egbert and Kelbert, 2012], a 3D finite-element regularized magnetotelluric inversion. Prior to input into the inversion, error floors of 10 and 20% |Zij| were applied to off-diagonal and diagonal components of the impedance tensor, respectively.

4.5 Results

4.5.1 2D Resistivity Structure of the Jemez Mountains

Figure 4.4 shows the regional two-dimensional resistivity structure along the rift boundary profile. This model required ten iterations to achieve the target RMS of 1.75 given the applied errors, representing a reduction in data residual of 63% relative to the 30 Ωm half-space starting model. The inversion continued to run for an additional ten iterations in order to achieve the smoothest possible model while maintaining the target RMS.

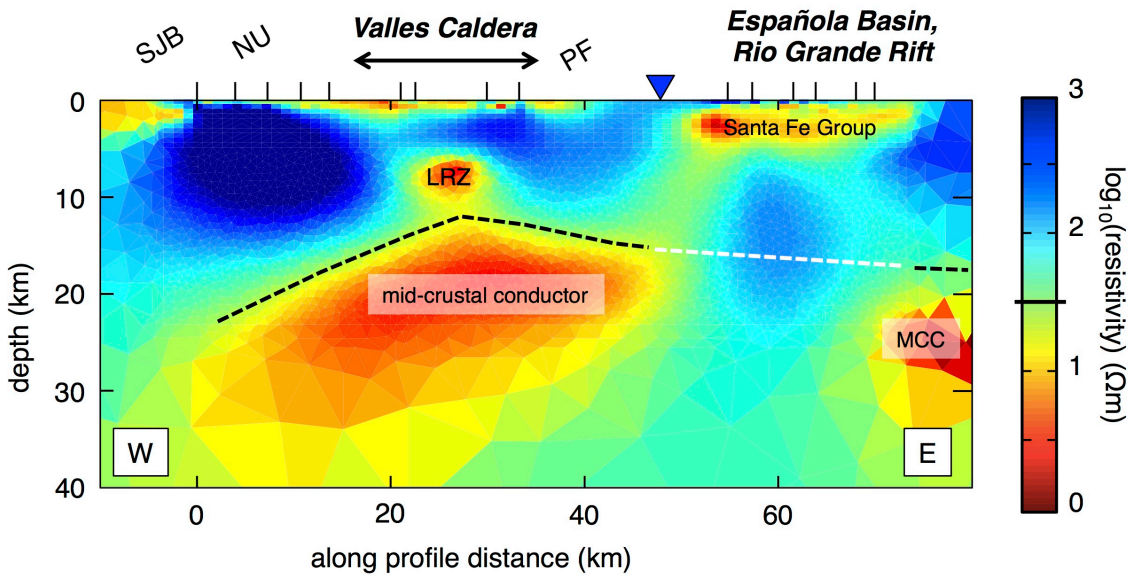

Figure 4.4. Two-dimensional electrical resistivity model of the western margin of the Rio Grande Rift. Labels above the model correspond to geographic features, including the San Juan Basin (SJB), Nacimiento Uplift (NU), and surface trace of the Pajarito Fault (PF) - considered the western margin of modern Rio Grande Rift. The dashed line corresponds to the top of the mid-crustal conductor (MCC). The white portion of the dashed line represents inferred lateral continuity of the MCC beneath conductive rift sediments. LRZ = low resistivity zone (see text). Tick marks indicate MT station locations at the surface. Blue triangle represents location of the Rio Grande. Resistivity of half-space starting model is indicated by black line on color bar.

We highlight four significant low resistivity features imaged in Figure 4.4. Beneath the eastern third of the model (50-70 km along profile) is a region of high conductivity extending from near the surface to ~5 km depth (labeled Santa Fe Group in Figure 4.4). Directly beneath the Valles caldera is a circular shaped zone of low resistivity (3-10 Ωm) that is approximately 5 km wide and 5 km thick, beginning at a depth of ~7 km (LRZ in Figure 4.4). The two remaining low resistivity zones are in the mid- to lower-crust (Moho depth of 35-40 km [Aprea et

al., 2002]). These two zones are of exceptionally low resistivity (1-10 Ωm) and range in minimum depth from ~12 km directly beneath the caldera to more than 20 km beneath the Española Basin and Nacimiento Uplift. Because the magnetotelluric method is primarily sensitive to the conductance (conductivity thickness product) of low resistivity anomalies (Section A.1) we cannot resolve with certainty the absolute thickness of these deeper anomalies. Although in Figure 4.4 they appear to be 10-15 km thick, there is an equal likelihood, absent additional geophysical or geological constraints, that they are in fact much thinner and consequently of much lower resistivity.

It is significant that these mid-crustal conductors extend outside the lateral boundaries of the caldera and reside at similar depths to a pervasive mid-crustal conductor that has been previously identified in the Rio Grande rift [e.g. Hermance and Pedersen, 1980; Biehler et al., 1991; this dissertation, Chapter 3] and other active extensional environments [e.g. Wannamaker et al., 2008]. We note that the near-surface conductor on the eastern side of the profile is located directly above a resistive gap in the mid-crust between these two anomalies (50-70 km along profile). If these mid-crustal conductors are laterally continuous beneath the near-surface conductor, there is a possibility that the shallower body is masking that continuity. Based on similarities in depth, resistivity, and tectonic environment to previously identified mid-crustal conductors, we infer that the two deeper conductors in Figure 4.4 are likely part of a laterally continuous feature in the mid-crust that shallows beneath the Valles caldera (dashed line, Figure 4.4).

4.5.2 3D Resistivity Structure of the Valles Caldera

Figure 4.5 shows depth slices through a 3D electrical resistivity model of the upper crust beneath the Valles caldera. This model achieved an RMS of 2.3 given the applied errors, representing a reduction in data residuals of 83% relative to a 100 Ωm half-space starting model (initial RMS 13.7). Only three stations were inverted in both the 3D and 2D models, all of which were located along the southern margin of the caldera. Additionally, this inversion used all four components of the impedance tensor and did not incorporate tipper, while the 2D modeling used the in-line component of the tipper (Tzy) and only a partial set of off-diagonal impedance elements.

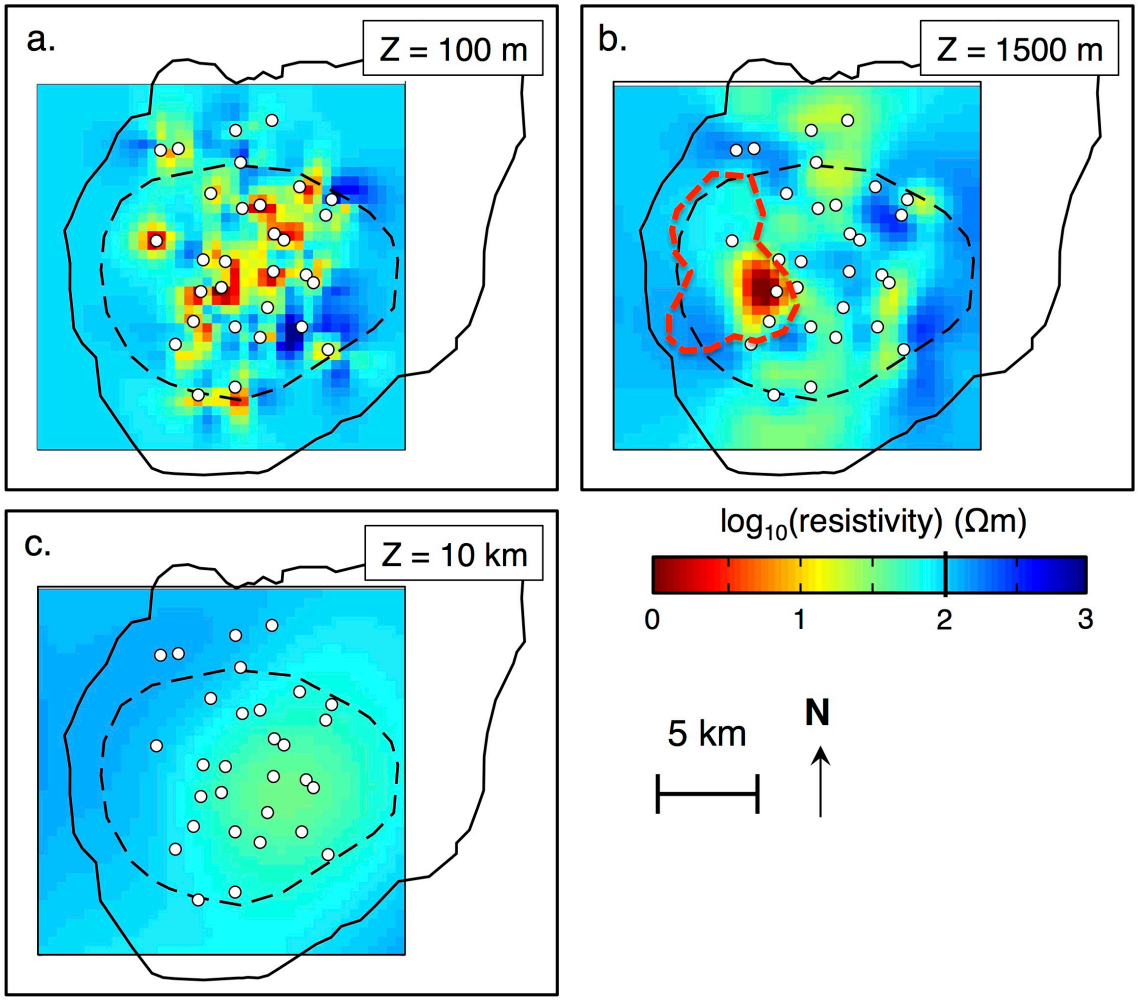

Figure 4.5. Depth slices through the preferred 3D resistivity model at (a) 100 m (b) 1.5 km and (c) 10 km, projected onto an outline of the caldera rim (solid black contour), the ring fracture (dashed black contour), and station distribution (white dots). Red dashed contour in (b) is 350 mW/m^2 surface heat flow contour from Sass and Morgan [1988] indicating geothermal system of the western caldera.

Each depth slice in Figure 4.5 shows a significant low resistivity feature of the 3D model. Figure 4.5a (100 m depth) shows generally high conductivity values directly beneath the majority of station locations. The high frequency data that

informs the resistivity of the model slice at 100 m is largely insensitive to lateral structure between stations (station spacing > 500 m). Rather than interpolate these high conductivity values between stations, the ModEM inversion algorithm is designed to maintain background (i.e. starting model) resistivity values for regions of the model for which it lacks resolution. This feature of the inversion prevents overstating model resolution and results in the stippled pattern observed in Figure 4.5a.

Figure 4.5b (1500 km depth) shows a circular zone of low resistivity beneath the southwest quadrant of the Valles caldera that is approximately 4 km in diameter. While there are no MT stations directly within the footprint of this anomaly, seven stations bound it to the north, east, and south, including two high quality SAGE stations collected in 1991.

Figure 4.5c (10 km depth) shows a zone of enhanced conductivity centered under the caldera beneath most stations. This zone is similar in size to the caldera itself (15 km diameter) and is much broader than the low resistivity zone (LRZ) imaged in Figure 4.4. Further examination of intermediate depth slices of the 3D model between 1.5 and 10 km does not reveal a low resistivity anomaly of similar dimension or resistivity to the LRZ. In terms of relating the 2D and 3D models, the generally high conductivity of the 10 km depth slice likely represents the top of the mid-crustal conductor imaged in Figure 4.4. Possible explanations for the lack of an LRZ anomaly in the 3D model are discussed below.

4.6 Discussion

4.6.1 The Western Margin of the Rio Grande Rift

The 2D electrical resistivity model in Figure 4.4 shows both expected and surprising geoelectric features that are distributed throughout the upper crust. A series of thin near-surface conductors in the regional model and include a westward dipping conductor on the western edge of the profile, a broad shallow conductor centered on the Valles caldera, and the 3-5 km thick, <10 Ωm conductor beneath the six easternmost stations of the profile. The western near-surface conductor is the eastern edge of the San Juan Basin, a broad, largely undeformed sedimentary basin that covers the Colorado Plateau over much of northeastern New Mexico and southwestern Colorado. This basin is comprised of Mesozoic sedimentary units that are expected to be conductive due to the presence of sheet silicates (e.g. clay minerals) and porous sedimentary units. The eastern boundary of the San Juan Basin is juxtaposed against the Nacimiento uplift in a dramatic example of contrasting landscapes. The Nacimiento uplift is a Laramide-age uplift of Precambrian crystalline rocks that has been reactivated in the late Cenozoic as a normal fault accommodating extension. The massive resistive body that we image above the mid-crustal conductor at 0-20 km along profile is likely the core of this uplift. Resistive Precambrian and Paleozoic rocks outcrop on top of the Nacimiento uplift.

The Pajarito fault (PF in Figure 4.4, ~40 km along profile), which trends north-northeast and is marked by a down to the east, several hundred meter tall

faultline scarp just a few kilometers outside the Valles caldera, is considered the modern-day western boundary of the Rio Grande Rift in the Jemez Mountains [Garner and Goff, 1984]. To the east of the Pajarito fault is the Española Basin, one of several asymmetric half-graben structures that comprise the axial basins of the Rio Grande Rift in New Mexico. The Española Basin is filled with a package of syn-rift sedimentary units known as the Santa Fe Group that thickens to the west (Biehler et al., 1991), with depth to basement reaching values of several kilometers in the vicinity of the Rio Grande. The low resistivity of the Santa Fe Group is well documented [e.g. Hermance and Pederson, 1980; Biehler et al., 1991; Rodriguez and Sawyer, 2013; this dissertation, Chapter 3]. Indeed, we image a low resistivity zone beneath all six stations located east of the Pajarito fault.

The Santa Fe Group extends beneath the volcanic rocks of the Jemez Mountains volcanic field and has been found in drill core within the Valles caldera [Self et al., 1986]. We expect that the high conductivity of the broad shallow conductor located from 15-40 km along our profile is partially due to the presence of syn-rift sedimentary units beneath the caldera. The caldera fill itself should also be conductive, especially if it harbors hydrothermal alteration products or high-temperature fluids [Sass and Morgan, 1986].

The identification of a mid-crustal conductor beneath the western Española Basin and Jemez Mountain volcanic field was expected. As outlined in the previous section, a feature of similar depth range and resistivity has been imaged at nearly every location within the Rio Grande Rift where geoelectric structure has been

investigated (with the odd exception of the Socorro magma body, the site of a known magmatic sill [Jiracek et al., 1983]). Indeed, the depth to the top of the mid-crustal conductor was arguably the most significant finding of the only previous modeling of these data [Nettleton 1997; Jiracek et al., 1996]. A novel result of our new modeling, however, is the ability to place the mid-crustal conductor beneath the Valles caldera within the larger geologic context of the Rio Grande Rift. Although the two mid-crustal anomalies in Figure 4.4 do not connect, and in fact appear to be separated by a high resistivity feature, we infer that they do form a laterally continuous feature that is obscured by the conductive sediments of the Española Basin. The eastern extent of the larger MCC anomaly (extending to 50 km along profile) is beneath a 20 km gap in data coverage (modern SAGE data does exist in this gap but it was not of sufficiently high quality and/or did not exhibit the proper geoelectric strike to warrant inclusion in the 2D inversion). Knowing that the Santa Fe group is laterally continuous, although offset vertically by faulting, from the Española Basin to the caldera, we expect that denser station coverage through this gap would further obscure the mid-crustal conductor. It is only by coincidence of poor station distribution that we image this feature as well as we do. As imaged, we are able to resolve relatively detailed topography of the top of the conductor that has important implications for its interpretation.

4.6.2. Comparing Regional and Local Resistivity Structure

To the limited degree that they image overlapping structure the 2D and 3D modeling studies are generally consistent. The top several hundred meters of the caldera interior is conductive, likely due to the presence of weathered and porous caldera fill as well as conductive pre- and syn-rift sedimentary units. The top of the mid-crustal conductor directly beneath the caldera appears to be imaged at a similar depth in both models (10-12 km). However, the 2D model contains a striking feature that the 3D model does not: the low resistivity zone (LRZ) at 6-8 km depth directly beneath the caldera.

In preparing to model the Valles caldera magnetotelluric data, Jiracek et al. [1996] performed a modeling study to test the sensitivity of their data to a partial melt zone of 10% melt fraction, similar to that proposed by Lutter et al. [1995] to explain an observed low velocity zone beneath the caldera. Using a 2D forward modeling approach, Jiracek et al. generated a synthetic "magma chamber" anomaly of 5 Ωm with the same shape, depth and location as the 2D low velocity zone imaged by Roberts et al. [1991]. They then computed the forward response, in terms of apparent resistivity and phase of both TE and TM modes, to models in which the "magma chamber" was isolated and models in which it represented simply a local upwarping of a ubiquitous mid-crustal zone of high conductivity. They concluded that they could not reliably image such an anomaly and indeed neither Jiracek et al. [1996] or Nettleton [1997] imaged a zone of low resistivity in the vicinity of the anomalous velocity identified by Lutter et al. [1995] and Steck et al. [1998]. This

lack of a “magma chamber” anomaly, and the preceding modeling study that seemingly proved an inability to image the expected partial melt fraction at the appropriate depths, contributed to the previous interpretation of the imaged low resistivity as saline fluid. Interestingly though, the low resistivity zone (LRZ) in Figure 4.4 is of very similar size, depth, and along profile position to the LVZ imaged by the previous seismic experiments.

The key difference between the various magnetotelluric inversions is the inclusion of tipper data. The inversions performed in the 3D modeling study presented here and in the previous work done by Jiracek et al. [1996] and Nettleton [1997] did not include modeling of tipper data in any form. The 2D inversion performed in this study did attempt to solve for the in-line component of the tipper. To test the hypothesis that the LRZ is a consequence of inverting for tipper, we performed a 2D inversion identical to the inversion that produced our preferred model, with the exception that we did not include tipper data. The model resulting from that inversion does not image a low resistivity anomaly in the region of the LRZ and looks strikingly similar to the 2D inversion results from Nettleton [1997]. We also performed model sensitivity tests in which we replaced the LRZ in Figure 4.4 with the background upper crustal resistivity value (~250 Ωm) and used that altered model as a starting model for subsequent inversions. The low resistivity zone was quickly reintroduced to the model upon subsequent iterations, suggesting that it is feature required by the data.

Model sensitivity testing reveals that the low resistivity zone in Figure 4.4 is the result of fitting tipper data from a single station located inside the caldera. That particular station is of the modern SAGE data collected in 2017, with high quality tipper data to a period of >300 s. The possibility that standard magnetotelluric inversion excluding tipper data may be completely blind to major geologic features is worth investigating. Given the low amplitude tipper data observed for the Valles stations, and the difficulties in getting tipper inclusive inversions to converge when modeling the Valles data in 3D, we speculate that the caldera-adjacent tipper data may permit imaging of the LRZ if it is a true anomaly rather than an artifact of a single station. A straightforward method for testing this would be to invert the caldera stations in 3D with additional constraints provided by tipper data from the adjacent SAGE MT stations located just outside the caldera rim. The stations immediately adjacent to the caldera (e.g. within 5 km of the topographic rim) do not meet the geoelectric strike or dimensionality criteria for inclusion into the 2D inversion performed in this study.

4.6.3. Geologic Interpretation

It is difficult to justify interpretations other than partial melt for the low resistivity zone in Figure 4.4. Nettleton [1997] interprets the top of the mid-crustal conductor beneath the LRZ as coincident with the brittle ductile transition and the 450ºC isotherm. Extending that logic to the LRZ implies a temperature of 450ºC at relatively shallow depths (5-7 km), requiring an exceptionally steep geothermal

gradient on the order of 70-80ºC/km. Assuming the 450ºC isotherm has been warped upward to encompass the LRZ, whatever event caused the up warping of the isotherm, likely advection of heat via magmatic intrusion or fluid fracturing of the colder rock above, would also compromise the impermeable cap required to maintain a conductive saline fluid reservoir. Furthermore, it stands to reason that if a broad region of high conductivity caused by a similar conduction mechanism may be imaged at 10-20 km depth without the need for tipper data, a shallower anomaly within a few vertical kilometers of a dense array of stations would also be detectable using the same inversion scheme. The reliance on tipper data in imaging the LRZ, or conversely the insensitivity of apparent resistivity and phase data to the anomaly, suggests that the LRZ is a relatively subtle anomaly caused by a different conduction mechanism than that of the mid-crustal conductor. The extremely low velocity of the coincident LVZ (-10% to -35% relative to the adjacent crust) has led seismic interpreters to conclude that the physical properties of the region are altered by more than anomalously high-temperature. The identification of a zone of partial melt in the shallow crust is consistent with the assessment that the Valles caldera may be entering a new phase of silicic magma production [Wolff and Gerdener, 1995], as silicic magma tends to pond within the upper crust at depths consistent with the location of the seismic LVZ and electromagnetic LRZ.

When identified elsewhere in the vicinity of the Valles caldera and Jemez Mountains volcanic field, the mid-crustal conductor, such as that imaged in Figures 4.4 and 4.5c, has been interpreted as neutrally buoyant basaltic melt [Hermance

and Pedersen, 1980], but more often it is assumed to be saline fluids that have been impeded from ascending through the crust by one of a variety of mechanisms. The interpretation of the LRZ as a zone of partial melt that has ascended through the top of the previously imaged mid-crustal conductor makes it difficult to reconcile the interpretation of the mid-crustal conductor as an accumulation of ponded fluid. The action of melt ascending through the top of the MCC is precisely the mechanism that Jiracek et al. [1983] proposed to explain the lack of a mid-crustal conductor at the site of the Socorro magma body. They argued that magma transiting the impermeable cap would allow accumulated brines to escape to the upper crust, leaving a resistive middle crust. However, given the inferred genetic connection between the Valles caldera MCC and the broader MCC of the Rio Grande Rift as implied by our regional resistivity model, we must consider the possibility of similar conductivity mechanisms. One possible way to reconcile the seemingly contrasting interpretations of the LRZ and the MCC is to suggest the development or restoration of an impermeable fluid cap in the wake of magmatic ascent. Crystallization of magmatic fluids in the upper crust can release saline fluids into the surrounding rock. Similarly, deep circulation of meteoric water can produce high-temperature hydrothermal fluids at depth. As these fluids cool, silica and other precipitate minerals may precipitate from solution and accumulate along grain boundaries and in fracture networks, effectively reducing permeability. These precipitation reactions are partially temperature dependent and occur at similar

temperatures inferred by Nettleton [1997] for the top of the mid-crustal conductor (300-400ºC) [Hyndman and Shearer, 1989].

4.7 Conclusions

We present regional 2D and local 3D electrical resistivity models of the Valles caldera and Jemez Mountains volcanic field derived from inversion of magnetotelluric data collected over the past 35 years by both industry contractors and the Summer of Applied Geophysical Experience. In our preferred 2D regional model, we image the transition from the Colorado Plateau to the Española Basin of the Rio Grande Rift across the Jemez Mountains. We reliably resolve Mesozoic sedimentary cover of the San Juan Basin, Cenozoic rift fill of the Rio Grande Rift within the rift basin and beneath the volcanic rocks, and porous and weathered caldera fill. In the mid-crust we image the top of a previously identified low resistivity anomaly beneath the Valles caldera that we infer to be genetically related to the ubiquitous and well studied mid-crustal conductor of the Rio Grande Rift. We interpret this conductor as others have before as an accumulation of saline fluids. By incorporating magnetic transfer functions into our 2D inversion, we successfully image an isolated zone of low resistivity at a depth of 7-12 km directly beneath the Valles caldera. Previously only identified in seismic tomography studies, we interpret this low resistivity zone as a region of partial melt related to resurgent magmatic activity in the Valles caldera over the past 100 kyr.

Our preferred 3D model of the Valles caldera, which relies exclusively on MT data collected in 1991 and earlier, reveals detailed lateral variations in the resistivity structure of the Valles caldera, most notably a zone of high conductivity at 1.5 km depth that corresponds to a known hydrothermal system within the western caldera.

4.8 Acknowledgements

The authors acknowledge the efforts of the faculty and students of the Summer of Applied Geophysical Experience (SAGE) for a continued commitment to the collection of high quality geophysical data in an educational environment. In particular we thank SAGE faculty G. R. Jiracek and L. Pellerin for their efforts in archiving SAGE MT data over the years. Modern SAGE data (2011-2013) were downloaded from the IRIS SPUD database for electromagnetic transfer functions (http://ds.iris.edu/spud/emtf). The most recent SAGE data (2016-2017) were collected by P. Bedrosian, L. Pellerin, J. Peacock, M. Folsom, and D. Feucht, along with numerous SAGE students and teaching assistants. Unocal MT data were previously published in Nettleton [1997] and provided in digital form by C. Nettleton's thesis advisor, G. R. Jiracek. The authors thank Kerry Key and the Seafloor Electromagnetic Methods Consortium for the use of MARE2DEM. This work was supported by the National Science Foundation grants EAR-1249669 and EAR-1053596. Additional support was provided by EarthScope (EAR-0323309).

Various maps and graphics were created using Generic Mapping Tools [Wessel and Smith, 1991].

4.9 References

Aldrich, M. J. (1986). Tectonics of the Jemez Lineament in the Jemez Mountains and Rio Grande Rift. Journal of Geophysical Research, 91(B2), 1753–1762.

Ankeny, L. A., Braile, L. W., & Olsen, K. H. (1986). Upper Crustal Structure Beneath the Jemez Mountains Volcanic Field, New Mexico , Determined by Three-Dimensional Simultaneous Inversion of Seismic Refraction and Earthquake Data. Journal of Geophysical Research, 91(B6), 6188–6198. http://doi.org/10.1029/JB091iB06p06188

Aprea, C. M., Hildebrand, S., Fehler, M., Steck, L., Baldridge, W. S., Roberts, P., Thurber, C. H., & Lutter, W. J. (2002). Three-dimensional Kirchhoff migration: Imaging of the Jemez volcanic field using teleseismic data. Journal of Geophysical Research, 107(B10), 2247. http://doi.org/10.1029/2000JB000097

Baldridge, W. S., Braile, L. W., Biehler, S., Jiracek, G. R., Ferguson, J. F., Hasterok, D., Pellerin, L., Bedrosian, P. A., McPhee, D., & Snelson, C. M. (2012). SAGE at 30. The Leading Edge, 31(6), 702-708.

Biehler, S., Ferquson, J., Baldridge, W. S., Jiracek, G. R., Aldern, J. L., Martinez, M., Fernandez, R., Romo, J., Gilpin, B., Braile, L.W., Hersey, D. R., Luyendyk, B. P., & Aiken, C. L. (1991). A geophysical model of the Española Basin, Rio Grande rift, New Mexico. Geophysics, 56(3), 340–353.

Caldwell, T. G., Bibby, H. M., & Brown, C. (2004). The magnetotelluric phase tensor. Geophysical Journal International, 158, 457–469. http://doi.org/10.1111/j.1365-246X.2004.02281.x

Chapin, C. E., & Cather, S. M. (1994). Tectonic setting of the axial basins of the northern and central Rio Grande rift. In G. R. Keller & S. M. Cather (Eds.), Basins of the Rio Grande Rift: Structure, Stratigraphy, and Tectonic Setting: Geological Society of America Special Paper (Vol. 291, pp. 5–26). Boulder, Colorado. http://doi.org/10.1130/SPE291-p5

Constable, S. C., Parker, R. L., & Constable, C. G. (1987). Occam's inversion: A practical algorithm for generating smooth models from electromagnetic sounding data. Geophysics, 52(3), 289–300.

Egbert, G. D. (1997). Robust multiple-station magnetotelluric data processing. Geophysical Journal International, 130, 475–496.

Egbert, G. D., & Kelbert, A. (2012). Computational recipes for electromagnetic inverse problems. Geophysical Journal International, 189, 251–267. http://doi.org/10.1111/j.1365-246X.2011.05347.x

Fenneman, N. M. (1946). Physical divisions of the United States.

Gamble, T. D., Goubau, W. M., & Clarke, J. (1979). Magnetotellurics with a remote magnetic reference. Geophysics, 44(1), 53–68.

Gardner, J. N., & Goff, F. E. (1984). Potassium-argon dates from the Jemez volcanic field: implications for tectonic activity in the north-central Rio Grande rift. New

Mexico Geological Society Guidebook, 35th Field Conference, Rio Grande Rift: Northern New Mexico, 75–81.

Hermance, J. F., & Pedersen, J. (1980). Deep Structure of the Rio Grande Rift: A Magnetotelluric Interpretation. Journal of Geophysical Research, 85(B7), 3899–3912. http://doi.org/10.1029/JB085iB07

Hyndman, R. D., & Shearer, P. M. (1989), Water in the lower continental crust: modelling magnetotelluric and seismic reflection results. Geophysical Journal International, (98), 343–365.

Jiracek, G. R., Kinn, C. L., Scott, C. L., Kuykendall, M. G., Baldridge, W. S., Biehler, S., Braile, L. W., Ferguson, J. F., & Gilpin, B. (1996). Tracing crustal isotherms under the western margin of the Jemez Mountains using SAGE and industry magnetotelluric data. New Mexico Geological Society Guidebook. 47th Conference, Jemez Mountains Region.

Jiracek, G. R., Gustafson, E. P., & Mitchell, P. S. (1983). Magnetotelluric results opposing magma origin of crustal conductors in the Rio Grande Rift. Tectonophysics, 94, 299–326.

Key, K. (2016). MARE2DEM: a 2-D inversion code for controlled-source electromagnetic and magnetotelluric data. Geophysical Journal International, 207, 571–588. http://doi.org/10.1093/gji/ggw290

Lutter, W. J., Roberts, P. M., Thurber, C. H., Steck, L., Fehler, M. C., Stafford, D. G., Baldridge, W. S., & Zeichert, T. A. (1995). Teleseismic P-wave image of the crust and upper mantle structure beneath the Valles caldera, New Mexico:

Initial results from the 1993 JTEX passive array. Geophysical Research Letters, 22(4), 505–508.

Nettleton, C. (1997). Magnetotelluric modeling of the Valles caldera, New Mexico. Masters thesis. Department of Geological Sciences, San Diego State University.

Olsen, K. H., Braile, L. W., Stewart, J. N., Daudt, C. R., Keller, G. R., Ankeny, L. A., & Wolff, J. J. (1986). Jemez Mountains volcanic field, New Mexico: Time term interpretation of the CARDEX seismic experiment and comparison with Bouguer gravity. Journal of Geophysical Research, 91(B6), 6175–6187. http://doi.org/10.1029/JB091iB06p06175

Roberts, P. M., Aki, K., & Fehler, M. C. (1991). A Low-Velocity Zone in the Basement Beneath the Valles Caldera, New Mexico. Journal of Geophysical Research, 96(B13), 21583–21596. http://doi.org/10.1029/91JB02048

Rodriguez, B. D., & Sawyer, D. A. (2013). Geophysical constraints on Rio Grande rift structure and stratigraphy from magnetotelluric models and borehole resistivity logs, northern New Mexico. In M. R. Hudson & V. J. S. Grauch (Eds.), New Perspectives on Rio Grande Rift Basins: From Tectonics to Groundwater: Geological Society of America Special Paper 494 (pp. 323–344). Geological Society of America. http://doi.org/10.1130/2013.2494(13).

Sass, J. H., & Morgan, P. (1988). Conductive heat flux in VC-1 and the thermal regime of Valles Caldera, Jemez Mountains, New Mexico. Journal of Geophysical Research, 93(B6), 6027–6039. http://doi.org/10.1029/JB093iB06p06027

Self, S., Goff, F. E., Gardner, J. N., Wright, J. V., & Kite, W. M. (1986). Explosive Rhyolitic Volcanism in the Jemez Mountains: Vent Locations, Caldera Development and Relation to Regional Structure. Journal of Geophysical Research, 91(B2), 1779–1798. http://doi.org/10.1029/JB091iB02p01779

Smith, R. L., Bailey, R. A., & Ross, C. S. (1970) Geologic map of the Jemez Mountains, New Mexico. Scale 1:125,000. U. S. Geological Survey.

Smith, R. L., & Bailey, R. A. (1966). The Bandelier Tuff: A study in the ash-flow eruption cycles from zoned magma chambers. Bulletin of Volcanology, 29, 83-104.

Smith, R. L., Bailey, R. A., & Ross, C. S. (1961) Structural evolution of the Valles caldera, New Mexico, and its bearing on the emplacement of ring dikes. Short Papers in the Geologic and Hydrologic Sciences. U. S. Geological Survey Professional Paper 424-D. D145-D149.

Steck, L. K., Thurber, C. H., Fehler, M. C., Lutter, W. J., Roberts, P. M., Baldridge, W. S., Stafford, D. G., & Sessions, R. (1998). Crust and upper mantle P wave velocity structure beneath Valles caldera, New Mexico: Results from the Jemez teleseismic tomography experiment. Journal of Geophysical Research, 103(B10), 24301–24320.

Wannamaker, P. E., Hohmann, G. W., & Ward, S. H. (1984). Magnetotelluric responses of three-dimensional bodies in layered earths. Geophysics, 49(9), 1517–1533.

Wannamaker, P. E., Hasterok, D. P., Johnston, J. M., Stodt, J. A., Hall, D. B., Sodergren, T. L., Pellerin, L., Maris, V., Doerner, W. M., Groenwold, K. A., & Unsworth, M. J. (2008), Lithospheric dismemberment and magmatic processes of the Great Basin-Colorado Plateau transition, Utah, implied from magnetotellurics. Geochemistry, Geophysics, Geosystems, 9(5), doi:10.1029/2007GC001886.

Wessel, P. and Smith, W. H. F., (1991), Free software helps map and display data. EOS Trans. AGU, 72, 441-446.

Wolff, J. A., & Gardner, J. N. (1995). Is the Valles caldera entering a new cycle of activity? Geology, 23(5), 411–414.

Zimmerer, M. J., Lafferty, J., & Coble, M. A. (2016). The eruptive and magmatic history of the youngest pulse of volcanism at the Valles caldera: Implications for successfully dating late Quaternary eruptions. Journal of Volcanology and Geothermal Research, 310, 50–57. http://doi.org/10.1016/j.jvolgeores.2015.11.021

CUMULATIVE BIBLIOGRAPHY

Abraham, J. D., Cannia, J. C., Bedrosian, P. A., Johnson, M. R., Ball, L. B., & Sibray, S. S. (2012), Airborne electromagnetic mapping of the base of aquifer in areas of western Nebraska: U.S. Geological Survey Scientific Investigations Report 2011-5219.

Ackermann, H. D. (1974), Shallow seismic compressional and shear wave refraction and electrical resistivity investigations at Rocky Flats, Jefferson County, Colorado. Journal of Research of the U.S. Geological Survey, 2(4), 421–430.

Aldrich, M. J. (1986). Tectonics of the Jemez Lineament in the Jemez Mountains and Rio Grande Rift. Journal of Geophysical Research, 91(B2), 1753–1762.

Aldrich, M.J., Ander, M.E., & Laughlin, A.W. (1984) Geological and geophysical signature of the Jemez Lineament: A reactivated Precambrian structure, International Basement Tectonics, 4, 77-85. Basement Tectonics Committee Inc., Denver, CO, 1984.

Ankeny, L. A., Braile, L. W., & Olsen, K. H. (1986). Upper Crustal Structure Beneath the Jemez Mountains Volcanic Field, New Mexico , Determined by Three-Dimensional Simultaneous Inversion of Seismic Refraction and Earthquake Data. Journal of Geophysical Research, 91(B6), 6188–6198. http://doi.org/10.1029/JB091iB06p06188

Annen, C., Blundy, J. D., & Sparks, R. S. J. (2005), The Genesis of Intermediate and Silicic Magmas in Deep Crustal Hot Zones. Journal of Petrology, 47(3), 505–539, doi:10.1093/petrology/egi084

Aprea, C. M., Hildebrand, S., Fehler, M., Steck, L., Baldridge, W. S., Roberts, P., Thurber, C. H., & Lutter, W. J. (2002). Three-dimensional Kirchhoff migration: Imaging of the Jemez volcanic field using teleseismic data. Journal of Geophysical Research, 107(B10), 2247. http://doi.org/10.1029/2000JB000097

Averill, M. G., & Miller, K. C. (2013). Upper crustal structure of the southern Rio Grande rift: A composite record of rift and pre-rift tectonics. Geological Society of America Special Papers, 494(17), 463–474. http://doi.org/10.1130/2013.2494(17)

Baldridge, W. S., Braile, L. W., Biehler, S., Jiracek, G. R., Ferguson, J. F., Hasterok, D., Pellerin, L., Bedrosian, P. A., McPhee, D., & Snelson, C. M. (2012). SAGE at 30. The Leading Edge, 31(6), 702-708.

Baldridge, W. S., Ferguson, J. F., & Wang, B. H. (1994). The western margin of the Rio Grande Rift in northern New Mexico: An aborted boundary? Geological Society of America Bulletin, 106, 1538–1551.

Baldridge, W. S., Olsen, K. H., & Callender, J. F. (1983). Rio Grande Rift: Problems and Perspectives.

Bedrosian, P. A. (2016), Making it and breaking it in the Midwest: Continental assembly and rifting from modeling of EarthScope magnetotelluric data. Precambrian Research, 278, 337–361, doi:10.1016/j.precamres.2016.03.009

Bedrosian, P. A., & Box, S. E. (2016), Highly conductive horizons in the Mesoproterozoic Belt-Purcell Basin: Sulfidic early basin strata as key markers of Cordilleran shortening and Eocene extension. In J. S. MacLean & J. W. Sears (Eds.), Belt Basin: Window to Mesoproterozoic Earth: Geological Society of America Special Paper 522 (pp. 305–339), doi:10.1130/2016.2522(12).

Berglund, H. T., Sheehan, A. F., Murray, M. H., Roy, M., Lowry, A. R., Nerem, R. S., & Blume, F. (2012), Distributed deformation across the Rio Grande Rift, Great Plains, and Colorado Plateau. Geology, 40(1), 23–26, doi:10.1130/G32418.1

Biehler, S., Ferquson, J., Baldridge, W. S., Jiracek, G. R., Aldern, J. L., Martinez, M., Fernandez, R., Romo, J., Gilpin, B., Braile, L.W., Hersey, D. R., Luyendyk, B. P., & Aiken, C. L. (1991). A geophysical model of the Española Basin, Rio Grande rift, New Mexico. Geophysics, 56(3), 340–353.

Boerner, D. E., Kurtz, R. D., & Craven, J. A. (1996), Electrical conductivity and Paleo-Proterozoic foredeeps. Journal of Geophysical Research, 101(B6), 13775–13791, doi:10.1029/96JB00171.

Booker, J. R. (2014). The Magnetotelluric Phase Tensor : A Critical Review. Surveys in Geophysics, 35, 7–40. http://doi.org/10.1007/s10712-013-9234-2

Boyd, O. S., & Sheehan, A. F. (2005), Attenuation Tomography Beneath the Rocky Mountain Front: Implications for the Physical State of the Upper Mantle. In The Rocky Mountain Region: An Evolving Lithosphere (pp. 361–377), Washington D.C.: American Geophysical Union.

Caldwell, T. G., Bibby, H. M., & Brown, C. (2004). The magnetotelluric phase tensor. Geophysical Journal International, 158, 457–469. http://doi.org/10.1111/j.1365-246X.2004.02281.x

Caldwell, W. B., Klemperer, S. L., Rai, S. S., & Lawrence, J. F. (2009), Tectonophysics Partial melt in the upper-middle crust of the northwest Himalaya revealed by Rayleigh wave dispersion. Tectonophysics, 477, 58–65, doi:10.1016/j.tecto.2009.01.013.

Chapin, C. E., & Cather, S. M. (1994). Tectonic setting of the axial basins of the northern and central Rio Grande rift. In G. R. Keller & S. M. Cather (Eds.), Basins of the Rio Grande Rift: Structure, Stratigraphy, and Tectonic Setting: Geological Society of America Special Paper (Vol. 291, pp. 5–26). Boulder, Colorado. http://doi.org/10.1130/SPE291-p5

Constable, S. C., Parker, R. L., & Constable, C. G. (1987). Occam's inversion: A practical algorithm for generating smooth models from electromagnetic sounding data. Geophysics, 52(3), 289–300.

Constable, S., Shankland, T. J., & Duba, A. (1992). The Electrical Conductivity of an Isotropic Olivine Mantle. Journal of Geophysical Research, 97(B3), 3397–3404. http://doi.org/10.1029/91JB02453

Cosca, M. A., Thompson, R. A., Lee, J. P., Turner, K. J., Neymark, L. A., & Premo, W. R. (2014). Ar / 39 Ar geochronology , isotope geochemistry (Sr , Nd , Pb), and petrology of alkaline lavas near Yampa , Colorado : Migration of alkaline

volcanism and evolution of the northern Rio Grande rift, (2), 1–27. http://doi.org/10.1130/GES00921.1

Currie, C. A., & Beaumont, C. (2011), Are diamond-bearing Cretaceous kimberlites related to low-angle subduction beneath western North America?, Earth and Planetary Science Letters, 303, 59-70

Dai, L., & Karato, S. (2009). Electrical conductivity of orthopyroxene: Implications for the water content of the asthenosphere. Proc. Jpn. Acad. Ser., 85, 466–475. http://doi.org/10.2183/pjab.85.466

de Voogd, B., Serpa, L., & Brown, L. (1988). Crustal extension and magmatic processes: COCORP profiles from Death Valley and the Rio Grande rift. Geological Society of America Bulletin, 100, 1550–1567.

DeCelles, P. G. (2004), Late Jurassic to Eocene evolution of the Cordilleran thrust belt and foreland basin system, western U.S.A. American Journal of Science, 304, 105–168.

Decker, E. R., Heasler, H. P., Buelow, K. L., Baker, K. H., & Hallin, J. S. (1988), Significance of past and recent heat-flow and radioactivity studies in the Southern Rocky Mountains region. Geological Society of America Bulletin, 100, 1851–1885.

Desissa, M., Johnson, N. E., Whaler, K. A., Hautot, S., Fisseha, S., & Dawes, G. J. K. (2013), A mantle magma reservoir beneath an incipient mid-ocean ridge in Afar, Ethiopia. Nature Geoscience, 6, 861–865, doi:10.1038/ngeo1925.

Dickinson, W. R., Klute, M. A., Hayes, M. J., Janecke, S. U., Lundin, E. R., McKittrick, M. A., & Olivares, M. D. (1988), Paleogeographic and paleotectonic setting of Laramide sedimentary basins in the central Rocky Mountain region. Geological Society of America Bulletin, 100, 1023–1039.

Eaton, G. P. (1980), Geophysical and geological characteristics of the crust of the Basin and Range province. In Studies in Geophysics-Continental Tectonics (pp. 96–113), Washington D.C.: National Academy of Science.

Eaton, G. P. (1987), Topography and origin of the southern Rocky Mountains and Alvarado Ridge. In M. P. Coward, J. F. Dewey, & P. L. Hancock (Eds.), Continental Extensional Tectonics, Geological Society Special Publication (Vol. 28, pp. 355–369), Geological Society.

Eaton, G. P. (2008), Epeirogeny in the Southern Rocky Mountains region: Evidence and origin. Geosphere, 4(5), 764–784, doi:10.1130/GES00149.1.

Egbert, G. D. (1997), Robust multiple-station magnetotelluric data processing. Geophysical Journal International, 130, 475–496.

Egbert, G. D., & Kelbert, A. (2012). Computational recipes for electromagnetic inverse problems. Geophysical Journal International, 189, 251–267. http://doi.org/10.1111/j.1365-246X.2011.05347.x

Epis, R. C., & Chapin, C. E. (1975), Geomorphic and Tectonic Implications of the Post-Laramide, Late Eocene Erosion Surface in the Southern Rocky Mountains. Geological Society of America Memoir, 144, 45–74.

Fenneman, N. M. (1946), Physical divisions of the United States.

Fu, Y. V., & Li, A. (2015). Journal of Geophysical Research : Solid Earth. Journal of Geophysical Research: Solid Earth, 120, 1–15. http://doi.org/10.1002/2014JB011602.

Gamble, T. D., Goubau, W. M., & Clarke, J. (1979). Magnetotellurics with a remote magnetic reference. Geophysics, 44(1), 53–68.

Gao, W., Grand, S. P., Baldridge, W. S., Wilson, D., West, M., Ni, J. F., & Aster, R. (2004). Upper mantle convection beneath the central Rio Grande rift imaged by P and S wave tomography. Journal of Geophysical Research, 109(B03305), 1–16. http://doi.org/10.1029/2003JB002743

Gardes, E., Gaillard, F., & Tarits, P. (2014), Toward a unified hydrous olivine electrical conductivity law. Geochemistry, Geophysics, Geosystems, 15, 4984–5000, doi:10.1002/2014GC005496.

Gardner, J. N., & Goff, F. E. (1984). Potassium-argon dates from the Jemez volcanic field: implications for tectonic activity in the north-central Rio Grande rift. New Mexico Geological Society Guidebook, 35th Field Conference, Rio Grande Rift: Northern New Mexico, 75–81.

Gilbert, H. (2012). Crustal structure and signatures of recent tectonism as influenced by ancient terranes in the western United States. Geopshere, 8(1), 141–157. http://doi.org/10.1130/GES00720.1

Gile, L. (1987). A pedogenic chronology for Kilbourne Hole, southern New Mexico-II. Time of explosions and soil events before explosions. Soil Society of America Journal, 51, 746-760.

Gok, R., Ni, J. F., West, M., Sandvol, E., Wilson, D., Aster, R., Baldridge, W. S., Grand, S., Gao, W., Tillmann, F., & Semken, S. (2003). Shear wave splitting and mantle flow beneath LA RISTRA. Geophysical Research Letters, 30, 1614.

Groom R.W., & Bailey, R.C. (1989), Decomposition of the magnetotelluric tensors in the presence of local three-dimensional galvanic distortion, Journal of Geophysical Research, 94, 1913-1925.

Hansen, S. M., Dueker, K. G., Stachnik, J. C., Aster, R. C., & Karlstrom, K. E. (2013), A rootless rockies - Support and lithospheric structure of the Colorado Rocky Mountains inferred from CREST and TA seismic data. Geochemistry, Geophysics, Geosystems, 14(8), 2670–2695, doi:10.1002/ggge.20143.

Hansen, S. M., Dueker, K., & Schmandt, B. (2015), Thermal classification of lithospheric discontinuities beneath USArray. Earth and Planetary Science Letters, 431, 36–47, doi:10.1016/j.epsl.2015.09.009.

Hasterok, D., & Chapman, D. S. (2011), Heat production and geotherms for the continental lithosphere. Earth and Planetary Science Letters, 307, 59–70, doi:10.1016/j.epsl.2011.04.034.

Heise, W., & Pous, J. (2001), Effects of anisotropy on the two-dimensional inversion procedure. Geophysical Journal International, 147, 610–621.Heise, W., & Pous, J. (2001). Effects of anisotropy on the two-dimensional inversion procedure. Geophysical Journal International, 147, 610–621.

Hermance, J. F. (1979). Toward Assessing the Geothermal Potential of the Jemez Mountains Volcanic Complex: A Telluric-Magnetotelluric Survey.

Hermance, J. F., & Neumann, G. A. (1991). The Rio Grande Rift: new electromagnetic constraints on the Socorro magma body. Physics of the Earth and Planetary Interiors, 66, 101–117.

Hermance, J. F., & Pedersen, J. (1980). Deep Structure of the Rio Grande Rift: A Magnetotelluric Interpretation. Journal of Geophysical Research, 85(B7), 3899–3912. http://doi.org/10.1029/JB085iB07

Hirschmann, M. M. (2000), Mantle solidus: experimental constraints and the effects of peridotite composition. Geochem. Geophys, Geosyst. 1 (10).

Humphreys, E. D., & Dueker, K. G. (1994). Western U.S. upper mantle structure. Journal of Geophysical Research, 99(B5), 9615–9634.

Humphreys, E., Hessler, E., Dueker, K., Farmer, G. L., Erslev, E., & Atwater, T. (2003), How Laramide-Age Hydration of North American Lithosphere by the Farallon Slab Controlled Subsequent Activity in the Western United States. International Geology Review, 45(7), 575–595, doi:10.2747/0020-6814.45.7.575.

Hyndman, R. D., & Shearer, P. M. (1989), Water in the lower continental crust: modelling magnetotelluric and seismic reflection results. Geophysical Journal International, (98), 343–365.

Izett, G. A., Cobban, W. A., & Gill, J. R. (1971), The Pierre Shale Near Kremmling, Colorado, And Its Correlation to The East and the West: Geological Survey Professional Paper 684-A.

Jackson, J. A., Austrheim, H., McKenzie, D., & Priestley, K. (2004), Metastability, mechanical strength, and the support of mountain belts. Geology, 32, 625-628, doi:10.1130/G20397.1.

Jacob, K. H., Farmer, G. L., Buchwaldt, R., & Bowring, S. A. (2015), Deep crustal anatexis, magma mixing, and the generation of epizonal plutons in the Southern Rocky Mountains, Colorado. Contributions to Mineralogy and Petrology, 169(7), 1–23, doi:10.1007/s00410-014-1094-3.

Jiracek, G. R., Gustafson, E. P., & Mitchell, P. S. (1983). Magnetotelluric results opposing magma origin of crustal conductors in the Rio Grande Rift. Tectonophysics, 94, 299–326.

Jiracek, G. R., Kinn, C. L., Scott, C. L., Kuykendall, M. G., Baldridge, W. S., Biehler, S., Braile, L. W., Ferguson, J. F., & Gilpin, B. (1996). Tracing crustal isotherms under the western margin of the Jemez Mountains using SAGE and industry magnetotelluric data. New Mexico Geological Society Guidebook. 47th Conference, Jemez Mountains Region.

Jones, A. G. (1992), Electrical conductivity of the continental lower crust. In D. M. Fountain, R. J. Arculus, & R. W. Kay (Eds.), Continental Lower Crust (pp. 81–143), Elsevier.

Jones, A. G., & Craven, J. A. (1990). The North American Central Plains conductivity anomaly and its correlation with gravity, magnetic, seismic and heat flow data in Saskatchewan, Canada. Physics of the Earth and Planetary Interiors, 60, 169–194.

Jones, C. H., Mahan, K. H., Butcher, L. A., Levandowski, W. B., & Farmer, G. L. (2015), Continental uplift through crustal hydration. Geology, 43(4), 355–358, doi:10.1130/G36509.1.

Kariya, K. A., & Shankland, T. J. (1983), Electrical conductivity of dry lower crustal rocks. Geophysics, 48(1), 52–61.

Keller, G. R., Khan, M. A., Morgan, P., Wendlandt, R. F., Baldridge, W. S., Olsen, K. H., Prodehl, C., & Braile, L. W. (1991). A comparative study of the Rio Grande and Kenya rifts. Tectonophysics, 197, 355–371.

Key, K. (2016). MARE2DEM: a 2-D inversion code for controlled-source electromagnetic and magnetotelluric data. Geophysical Journal International, 207, 571–588. http://doi.org/10.1093/gji/ggw290

Key, K., & Ovall, J. (2011). A parallel goal-oriented adaptive finite element method for 2.5-D electromagnetic modelling. Geophysical Journal International, 186, 137–154. http://doi.org/10.1111/j.1365-246X.2011.05025.x

Kluth, C. F., & Schaftenaar, C. H. (1994). Depth and geometry of the northern Rio Grande rift in the San Luis Basin, south-central Colorado. In G. R. Keller & S. M. Cather (Eds.), Basins of the Rio Grande Rift: Structure, Stratigraphy, and Tectonic Setting: Geological Society of America Special Paper 291 (pp. 27–37). Boulder, Colorado: Geological Society of America.

Landman, R. L., & Flowers, R. M. (2013). (U-Th)/He thermochronologic constraints on the evolution of the northern Rio Grande Rift, Gore Range, Colorado, and

implications for rift propagation models. Geosphere, 9(1). http://doi.org/10.1130/GES00826.1

Leat, P. T., Thompson, R. N., Dickin, A. P., Morrison, M. A., & Hendry, G. L. (1989), Quaternary volcanism in northwestern Colorado: Implications for the roles of asthenosphere and lithosphere in the genesis of continental basalts. Journal of Volcanology and Geothermal Research, 37, 291–310.

Lee, D., & Grand, S. P. (1996), Upper mantle shear structure beneath the Colorado Rocky Mountains. Journal of Geophysical Research, 101(B10), 22233–22244.

Levandowski, W. B., Jones, C. H., Shen, W., Ritzwoller, M. H., & Schulte-Pelkum, V. (2014), Origins of topography in the western U.S.: Mapping crustal and upper mantle density variations using a uniform seismic velocity model. Journal of Geophysical Research: Solid Earth, 119, 2375–2396, doi:10.1002/2013JB010607.

Li, A., Forsyth, D. W., & Fischer, K. M. (2002), Evidence for shallow isostatic compensation of the southern Rocky Mountains from Rayleigh wave tomography. Geology, 30(8), 683–686.

Li, S., Unsworth, M. J., Booker, J. R., Wei, W., Tan, H., & Jones, A. G. (2003), Partial melt or aqueous fluid in the mid-crust of Southern Tibet? Constraints from INDEPTH magnetotelluric data. Geophysical Journal International, 153, 289–304.

Lipman, P. W. (1992), Magmatism in the Cordilleran United States; Progress and problems. In B. C. Burchfiel, P. W. Lipman, & M. L. Zoback (Eds.), The Geology

of North America, The Cordilleran Orogen: Conterminous U.S. (pp. 481–514), Boulder, Colorado: The Geological Society of America.

Lutter, W. J., Roberts, P. M., Thurber, C. H., Steck, L., Fehler, M. C., Stafford, D. G., Baldridge, W. S., & Zeichert, T. A. (1995). Teleseismic P-wave image of the crust and upper mantle structure beneath the Valles caldera, New Mexico: Initial results from the 1993 JTEX passive array. Geophysical Research Letters, 22(4), 505–508.

Magnani, M. B., Miller, K. C., Levander, A., & Karlstrom, K. (2004). The Yavapai-Mazatzal boundary: A long-lived tectonic element in the lithosphere of southwestern North America. Geological Society of America Bulletin, 116(7), 1137–1142. http://doi.org/10.1130/B25414.1

Mallory, W. W. (1958), Pennsylvanian Coarse Arkosic Redbeds and Associated Mountains in Colorado. In Symposium on Pennsylvanian Rocks of Colorado and Adjacent Areas (pp. 17–20), Denver, Colorado: Rocky Mountain Association of Geologists.

Maughan, E. K. (1988), Geology and petroleum potnetial, Colorado Park Basin Province, North-Central Colorado: U.S. Geological Survey Open-File Report 88-450 E.

McCoy, A., Roy, M., Trevino, L., & Keller, G. R. (2005), Gravity Modeling of the Colorado Mineral Belt. In K. E. Karlstrom & G. R. Keller (Eds.), The Rocky Mountain Region: An Evolving Lithosphere Tectonics, Geochemistry, and Geophysics. Washington, D.C.: American Geophysical Union.

Meqbel, N. M., Egbert, G. D., Wannamaker, P.E., Kelbert, A., & Schultz, A. (2014), Deep electrical resistivity structure of the northwestern U.S. derived from 3-D inversion of USArray magnetotelluric data, Earth and Planetary Science Letters, 402, 290-304.

Mitrovica, J. X., Beaumont, C., & Jarvis, G. T. (1989), Tilting of continental interiors by the dynamical effects of subduction. Tectonics, 8(5), 1079–1094.

Mooney, W. D., & Kaban, M. K. (2010), The North American upper mantle: Density , composition , and evolution. Journal of Geophysical Research, 115(B12424), 1–24, doi:10.1029/2010JB000866.

Nakai, J. S., Sheehan, A. F., & Bilek, S. L. (2017), Seismicity of the rocky mountains and Rio Grande Rift from the EarthScope Transportable Array and CREST temporary seismic networks, 2008-2010. Journal of Geophysical Research: Solid Earth, 122, 2173–2192, doi:10.1002/2016JB013389.

Nettleton, C. (1997). Magnetotelluric modeling of the Valles caldera, New Mexico. Masters thesis. Department of Geological Sciences, San Diego State University.

Nielsen, R. L., & Dungan, M. A. (1985). The petrology and geochemistry of the Ocate volcanic field, north-central New Mexico. Geological Society of America Bulletin, 96, 296–312.

Obrebski, M., Allen, R. M., Pollitz, F., & Hung, S.-H. (2011). Lithosphere-asthenosphere interaction beneath the western United States from the joint inversion of body-wave traveltimes and surface-wave phase velocities.

Geophysical Journal International, 185, 1003–1021. http://doi.org/10.1111/j.1365-246X.2011.04990.x

Olsen, K. H., Braile, L. W., Stewart, J. N., Daudt, C. R., Keller, G. R., Ankeny, L. A., & Wolff, J. J. (1986). Jemez Mountains volcanic field, New Mexico: Time term interpretation of the CARDEX seismic experiment and comparison with Bouguer gravity. Journal of Geophysical Research, 91(B6), 6175–6187. http://doi.org/10.1029/JB091iB06p06175

Pakiser, L. C., & Zietz, I. (1965), Transcontinental Crustal and Upper-Mantle Structure. Reivews of Geophysics, 3(4), 505–520.

Pearse, J., & Fialko, Y. (2010). Mechanics of active magmatic intraplating in the Rio Grande Rift near Socorro, New Mexico. Journal of Geophysical Research, 115(B07413), 1–16. http://doi.org/10.1029/2009JB006592

Phillips, W. S., Mayeda, K. M., & Malagnini, L. (2014). How to Invert Multi-Band, Regional Phase Amplitudes for 2-D Attenuation and Source Parameters: Tests Using the USArray. Pure and Applied Geophysics, 171, 469–484. http://doi.org/10.1007/s00024-013-0646-1

Poe, B. T., Romano, C., Nestola, F., & Smyth, J. R. (2010). Electrical conductivity anisotropy of dry and hydrous olivine at 8 GPa. Physics of the Earth and Planetary Interiors, 181, 103–111. http://doi.org/10.1016/j.pepi.2010.05.003

Pommier, A., & Trong, E. L. (2011), "Sigmelts": A web portal for electrical conductivity calculations in geosciences. Computers and Geosciences, 37, 1450–1459, doi:10.1016/j.cageo.2011.01.002.

Porath, H. (1971), Magnetic Variation Anomalies and Seismic Low-Velocity Zone in the Western United States, Journal of Geophysical Research, 76, 2643-2648.

Porritt, R. W., Allen, R. M., & Pollitz, F. F. (2014), Seismic imaging east of the Rocky Mountains with USArray. Earth and Planetary Science Letters, 402, 16–25, doi:10.1016/j.epsl.2013.10.034.

Porter, K. W., & Weimer, R. J. (1982), Diagenetic Sequence Related to Structural History and Petroleum Accumulation : Spindle Field, Colorado. AAPG Bulletin, 66(12), 2543–2560.

Reitzler, J.S., Gough, D. I., Porath, H., and Anderson III, C. W. (1970), Geomagnetic Deep Sounding and Upper Mantle Structure in the Western United States, Geophys. J. R. astr. Soc., 19, 213-235.

Repasch, M., Karlstrom, K., Heizler, M., & Pecha, M. (2017). Borth and evolution of the Rio Grande fluvial system in the past 8 Ma: Progressive downward integration and the influence of tectonics, volcanism, and climate. Earth-Science Reviews, 168, 113-164.

Ricketts, J. W., Kelley, S. A., Karlstrom, K. E., Schmandt, B., Donahue, M. S., & van Wijk, J. (2015). Synchronous opening of the Rio Grande rift along its entire length at 25–10 Ma supported by apatite (U-Th)/He and fission-track thermochronology, and evaluation of possible driving mechanisms. Geological Society of America Bulletin. http://doi.org/10.1130/B31223.1

Roberts, P. M., Aki, K., & Fehler, M. C. (1991). A Low-Velocity Zone in the Basement Beneath the Valles Caldera, New Mexico. Journal of Geophysical Research, 96(B13), 21583–21596. http://doi.org/10.1029/91JB02048

Rodriguez, B. D., & Sawyer, D. A. (2013). Geophysical constraints on Rio Grande rift structure and stratigraphy from magnetotelluric models and borehole resistivity logs, northern New Mexico. In M. R. Hudson & V. J. S. Grauch (Eds.), New Perspectives on Rio Grande Rift Basins: From Tectonics to Groundwater: Geological Society of America Special Paper 494 (pp. 323–344). Geological Society of America. http://doi.org/10.1130/2013.2494(13).

Rowe, M. C., Lassiter, J. C., & Goff, K. (2015), Basalt volatile fluctuations during continental rifting: An example from the Rio Grande Rift, USA. Geochemistry, Geophysics, Geosystems, 16, 1254–1273, doi:10.1002/2014GC005649.

Rumpfhuber, E., & Keller, G. R. (2009), An integrated analysis of controlled and passive source seismic data across an Archean-Proterozoic suture zone in the Rocky Mountains. Journal of Geophysical Research, 114(B08305), 1–25, doi:10.1029/2008JB005886.

Sass, J. H., & Morgan, P. (1988). Conductive heat flux in VC-1 and the thermal regime of Valles Caldera, Jemez Mountains, New Mexico. Journal of Geophysical Research, 93(B6), 6027–6039. http://doi.org/10.1029/JB093iB06p06027

Schmandt, B., & Humphreys, E. (2010), Complex subduction and small-scale convection revealed by body-wave tomography of the western United States

upper mantle. Earth and Planetary Science Letters, 297, 435–445, doi:10.1016/j.epsl.2010.06.047.

Schmandt, B., & Lin, F.-C. (2014), P and S wave tomography of the mantle beneath the United States. Geophysical Research Letters, 41, 6342–6349, doi:10.1002/2014GL061231.

Schmandt, B., Lin, F.-C., & Karlstrom, K. E. (2015), Distinct crustal isostasy trends east and west of the Rocky Mountain Front. Geophysical Research Letters, 42, doi:10.1002/2015GL066593.

Schutt, D., Lowry, A. R., & Buehler, J. S. (2012), The temperature of the western U.S. lithosphere. In American Geophysical Union Fall Meeting. San Francisco, California: American Geophysical Union.

Self, S., Goff, F. E., Gardner, J. N., Wright, J. V., & Kite, W. M. (1986). Explosive Rhyolitic Volcanism in the Jemez Mountains: Vent Locations, Caldera Development and Relation to Regional Structure. Journal of Geophysical Research, 91(B2), 1779–1798. http://doi.org/10.1029/JB091iB02p01779

Sheehan, A. F., Abers, G. A., Jones, C. H., & Lerner-Lam, A. L. (1995), Crustal thickness variations across the Colorado Rocky Mountains from teleseismic receiver functions. Journal of Geophysical Research, 100(B10), 20391–20404.

Shen, W., & Ritzwoller, M. H. (2016), Crustal and uppermost mantle structure beneath the United States, Journal of Geophysical Research: Solid Earth, 121, 4306-4342, doi:10.1002/2016JB012887.

Shen, W., Ritzwoller, M. H., & Schulte-Pelkum, V. (2013). A 3-D model of the crust and uppermost mantle beneath the Central and Western US by joint inversion of receiver functions and surface wave dispersion. Journal of Geophysical Research: Solid Earth, 118, 1–15. http://doi.org/10.1029/2012JB009602

Shimojuku, A., Yoshino, T., & Yamazaki, D. (2014), Electrical conductivity of brine-bearing quartzite at 1 GPa: implications for fluid content and salinity of the crust. Earth, Planets, and Space, 66(2), 1–9, doi:10.1186/1880-5981-66-2.

Smith, R. L., & Bailey, R. A. (1966). The Bandelier Tuff: A study in the ash-flow eruption cycles from zoned magma chambers. Bulletin of Volcanology, 29, 83-104.

Smith, R. L., Bailey, R. A., & Ross, C. S. (1961) Structural evolution of the Valles caldera, New Mexico, and its bearing on the emplacement of ring dikes. Short Papers in the Geologic and Hydrologic Sciences. U. S. Geological Survey Professional Paper 424-D. D145-D149.

Smith, R. L., Bailey, R. A., & Ross, C. S. (1970) Geologic map of the Jemez Mountains, New Mexico. Scale 1:125,000. U. S. Geological Survey.

Steck, L. K., Thurber, C. H., Fehler, M. C., Lutter, W. J., Roberts, P. M., Baldridge, W. S., Stafford, D. G., & Sessions, R. (1998). Crust and upper mantle P wave velocity structure beneath Valles caldera, New Mexico: Results from the Jemez teleseismic tomography experiment. Journal of Geophysical Research, 103(B10), 24301–24320.

Till, C. B., Elkins-Tanton, L. T., & Fischer, K. M. (2010), A mechanism for low-extent melts at the lithosphere-asthenosphere boundary, Geochemistry Geophysics Geosystems, 11, doi:10.1029/2010GC003234.

Tweto, O. (1979). The Rio Grande Rift system in Colorado. In Rio Grande Rift: Tectonics and magmatism (pp. 33–56). Washington D.C.: American Geophysical Union. http://doi.org/10.1029/SP014p0033

Tweto, O., & Sims, P. K. (1963), Precambrian Ancestry of the Colorado Mineral Belt. Geological Society of America Bulletin, 74, 991–1014.

van Wijk, J. W., Baldridge, W. S., van Hunen, J., Goes, S., Aster, R., Coblentz, D. D., Grand, S. P., & Ni, J. (2010), Small-scale convection at the edge of the Colorado Plateau: Implications for topography, magmatism, and evolution of Proterozoic lithosphere. Geology, 38(7), 611–614, doi:10.1130/G31031.1.

Waff, H. S. (1974), Theoretical Considerations of Electrical Conductivity in a Partially Molten Mantle and Implications for Geothermometry. Journal of Geophysical Research, 79(26), 4003–4010.

Walker, J. D., Bowers, T. D., Black, R. A., Glazner, A. F., Farmer, G. L., & Carlson, R. W. (2006), A geochemical database for western North American volcanic and intrusive rocks (NAVDAT), In A. K. Sinha (Ed.), Geoinformatics: Data to Knowledge: Geological Society of America Special Paper 397 (pp. 61–71), doi:10.1130/2006.2397(05).

Wannamaker, P. E., Hasterok, D. P., Johnston, J. M., Stodt, J. A., Hall, D. B., Sodergren, T. L., Pellerin, L., Maris, V., Doerner, W. M., Groenwold, K. A., &

Unsworth, M. J. (2008), Lithospheric dismemberment and magmatic processes of the Great Basin-Colorado Plateau transition, Utah, implied from magnetotellurics. Geochemistry, Geophysics, Geosystems, 9(5), doi:10.1029/2007GC001886.

Wannamaker, P. E., Hohmann, G. W., & Ward, S. H. (1984). Magnetotelluric responses of three-dimensional bodies in layered earths. Geophysics, 49(9), 1517–1533.

Wessel, P. and Smith, W. H. F., (1991), Free software helps map and display data. EOS Trans. AGU, 72, 441-446.

Whitmeyer, S., and Karlstrom, K. E. (2007). Tectonic model for the Proterozoic growth of North America. Geosphere, 3(4), 220–259. http://doi.org/10.1130/GES00055.1

Wilson, D., Aster, R. C., Ni, J., Grand, S. P., West, M., Gao, W., Baldridge, W. S., & Semken, S. (2005), Imaging the seismic structure of the crust and upper mantle beneath the Great Plains, Rio Grande Rift, and Colorado Plateau using receiver functions. Journal of Geophysical Research, 110(B05306), doi:10.1029/2004JB003492.

Wolff, J. A., & Gardner, J. N. (1995). Is the Valles caldera entering a new cycle of activity? Geology, 23(5), 411–414.

Yang, X. (2011), Origin of High Electrical Conductivity in the Lower Continental Crust: A Review. Surveys in Geophysics, 32, 875–903, doi:10.1007/s10712-011-9145-z.

Yardley, B. W. D., & Valley, J. W. (1997), The petrologic case for a dry lower crust high that rise to a fluid pressure to the rock that is still hot and ductile , the fluid pressure. Journal of Geophysical Research, 102(B6), 12173–12185, doi:10.1029/97JB00508.

Yardley, B. W. D., & Valley, J. W. (2000), Reply. Journal of Geophysical Research, 105(B3), 6065–6068.

Yuan, H., French, S., Cupillard, P., & Romanowicz, B. (2014), Lithospheric expression of geological units in central and eastern North America from full waveform tomography. Earth and Planetary Science Letters, 402, 176–186, doi:10.1016/j.epsl.2013.11.057.

Zimmerer, M. J., Lafferty, J., & Coble, M. A. (2016). The eruptive and magmatic history of the youngest pulse of volcanism at the Valles caldera: Implications for successfully dating late Quaternary eruptions. Journal of Volcanology and Geothermal Research, 310, 50–57. http://doi.org/10.1016/j.jvolgeores.2015.11.021

APPENDIX

A.1. Sensitivity of Magnetotelluric Data to a Lower Crustal Conductor

Forward modeling tests were performed to investigate three aspects of the lower crustal conductor (LCC) imaged in Chapter 2 (Figure 2.4): (1) the sensitivity of the data to total conductance of the LCC, rather than absolute conductivity or thickness, (2) the lateral continuity of the conductor across the station gap from approximately 106.25ºW to 107.5ºW and (3) the necessity of anisotropic modeling. A series of simple forward models were created with features approximating the main resistivity structure of the preferred ρ_{xx} model in Figure 2.4a. These features included a conductive Denver Basin, a resistive crust, a lower crustal conductor, and a resistive mantle keel beneath the plains. The thickness, electrical resistivity, lateral connectivity, and anisotropy of the LCC were varied for each forward model while the remaining features were held fixed. Sensitivity testing was carried out as follows: (1) synthetic MT responses were generated for each forward model at along-profile distances and periods corresponding to those available in the real data set, (2) random noise and error bars were added to the synthetic responses, and (3) the synthetic data were inverted for isotropic resistivity structure using the same mesh, starting model, and inversion parameters as described in Section 2.3. For simplicity, anisotropy was not included in the first two synthetic tests (i.e. the anisotropy penalty factor was fixed at 1.0). The third synthetic test also included modeling the synthetic data using the anisotropic inversion parameters described in Section 2.3.

Figure A.1 shows the results of the test performed to assess the need for anisotropic modeling. Figure A.1a shows the anisotropic forward model used for this synthetic test. Note that only the lower crustal conductor is anisotropic and that the degree of anisotropy is relatively modest (0.5 decades in $\log_{10}$(resistivity)). Figure A.1b shows that MARE2DEM successfully reproduces the anisotropic resistivity structure of the lower crust from an initially isotropic half-space starting model. Figure A.1c shows that isotropic modeling of anisotropic data introduces artifacts into the resistivity structure, specifically in the anisotropic regions of the model. These artifacts include alternating vertical stripes of resistive and conductive bodies. The similarities between Figure A.1c and the isotropic inversion results in Figure 2.3 and 3.4 motivated the use of anisotropic inversion in the studies outlined in Chapters 2 and 3.

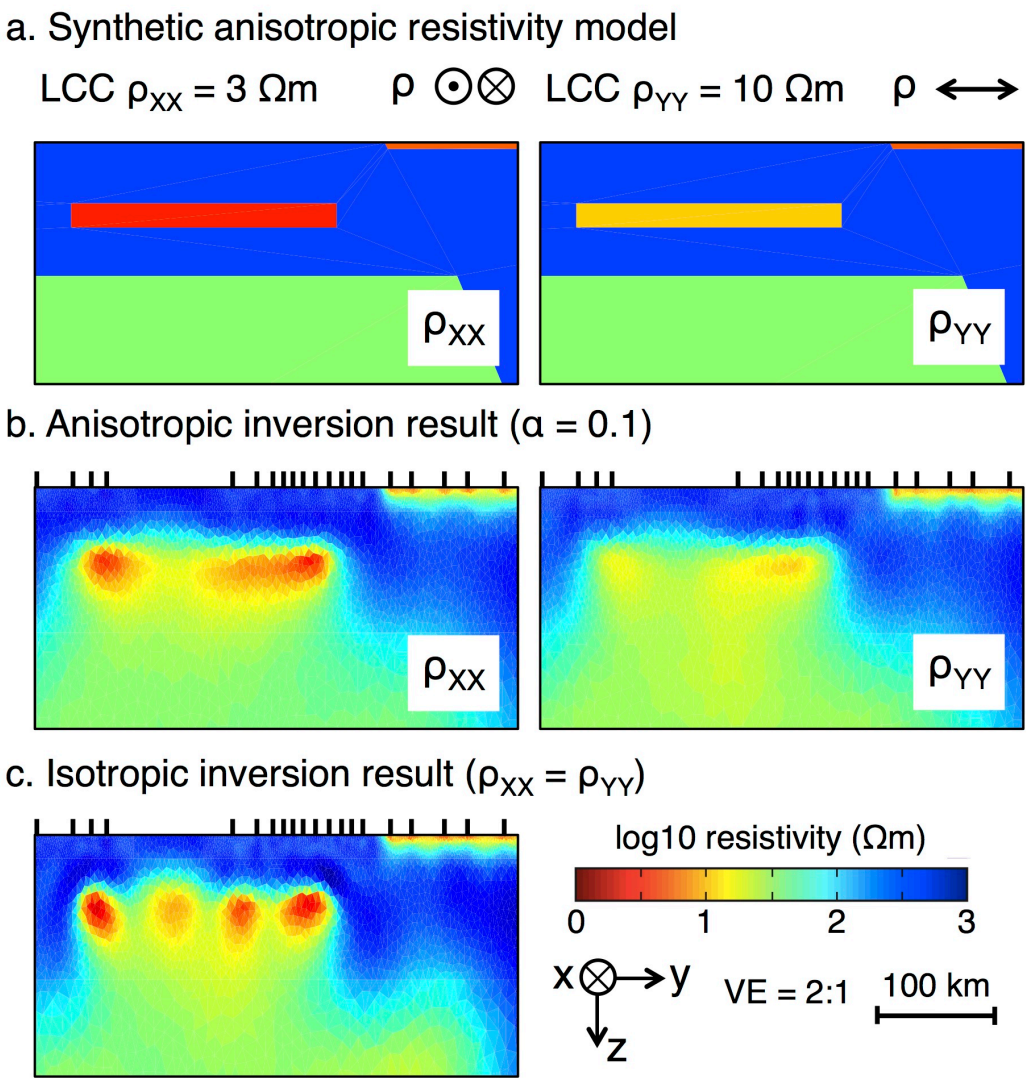

Figure A.1. Results of the test for MARE2DEM response to anisotropic resistivity structure. An anisotropic forward model [a] representing a simplified version of the preferred ρ_{xx} model in Fig. 2.4, in this case with a 10 km thick lower crustal conductor with resistivity 3 Ωm in the x-direction [N-S] and 10 Ωm in the y-direction [E-W]. Results of inverting synthetic anisotropic data using anisotropic [b] and isotropic [c] inversion parameters. Note similarity between result of isotropic inversion of anisotropic data in [c] to isotropic inversion results in Fig. 3. Approximate model view is surface to 100 km depth and 0 to 400 km along profile. Tick marks on [b] and [c] indicate location of synthetic MT data.

The results of the test on sensitivity to conductance are shown in Figure A.2. Each of the five forward models used for this test was parameterized with a laterally continuous conductor, the top of which was fixed at a depth of 25 km. The thickness of the conductor was varied from 300 m to 30 km while the resistivity was varied from 0.15 Ωm to 15 Ωm to maintain a total conductance of ~2000 S (the contribution of any remaining resistive lower crust to the total conductance was minimal, reaching a maximum of 100 S for the model with the thinnest conductor). Four out of the five models produced from inverting the various synthetic MT data sets are nearly identical (Figure A.2b-e) despite vast differences in the geometry and electrical properties of the input LCC. The most distinct result (Figure A.2e) was obtained for the only synthetic model with the LCC in contact with the conductive upper mantle. Figure A.2g shows the integrated lower crustal conductance for each of the five forward models alongside that of the preferred ρ_{xx} model from the anisotropic inversion of the measured data. From this we conclude that our data are primarily sensitive to the total conductance of the LCC rather than its absolute resistivity or thickness.

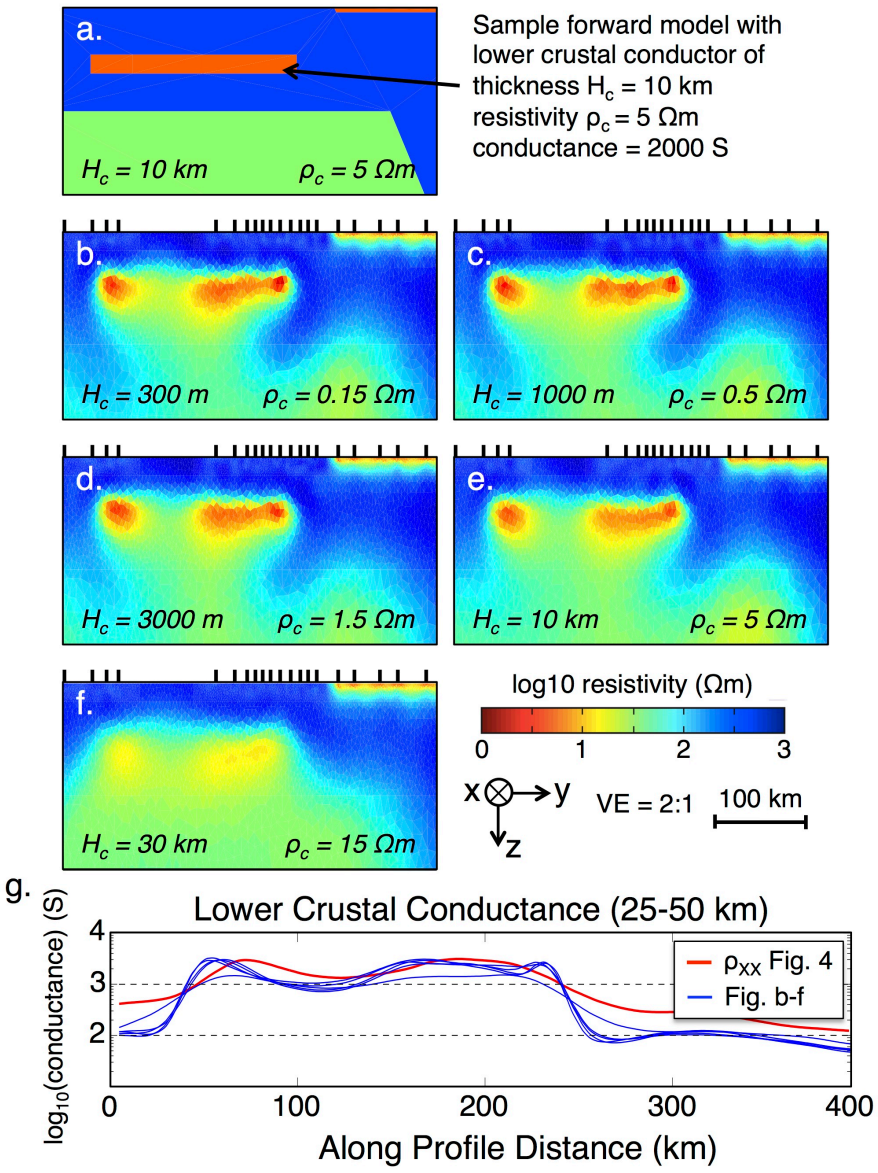

Figure A.2. Results of the test for sensitivity to lower crustal conductor [LCC] thickness and resistivity. A sample isotropic forward model [a] representing a simplified version of the preferred ρ_{xx} model in Fig. 2.4, in this case with a 10 km thick lower crustal conductor with resistivity 5 Ωm. Each of [b]-[f] represents the result of inverting synthetic forward models with different LCC thicknesses [Hc] and resistivity values [ρc] as labeled on each model. Approximate model view is surface to 100 km depth and 0 to 400 km along profile. Tick marks on [b]-[f] indicate location of synthetic MT data. Vertically integrated lower crustal conductance is shown in [g] for the ρ_{xx} model in Fig. 2.4 [25-50 km depth] and each of the synthetic inversion results in Figure A.2[b]-[f] [25-55 km depth].

The results of the test on lateral continuity of the conductor are shown in Figure A.3. Each of the five forward models used for this test was parameterized with a 10 km thick lower crustal conductor with resistivity of 5 Ωm. A lateral resistive "tear" was inserted into each conductor, with the width of the tear varying for each forward model from 15-75 km and the resistivity value matching that of the background lower crust (300 Ωm). The tear was centered at the midpoint between the two stations bounding the ~100 km gap in station coverage (Figure 2.1). The resistive tear was successfully imaged in each synthetic test (Figure A.3b-f). The inversion result from Figure A.2e is reproduced in Figure A.3g to show the case of a laterally continuous conductor of the same thickness and resistivity. Figure A.3h shows the total lower crustal conductance for the models in Figure A.3b-g and the ρ_{xx} model in Figure 2.4. From this we conclude that the apparent gap in the lower crustal conductor within the anisotropic inverse model is a reflection of the station coverage and is to be expected even for a laterally continuous conductor. That the model with a laterally continuous conductor does the best job of reproducing the lower crustal conductance curve of the ρ_{xx} model suggests that the lower crustal conductor is laterally continuous.

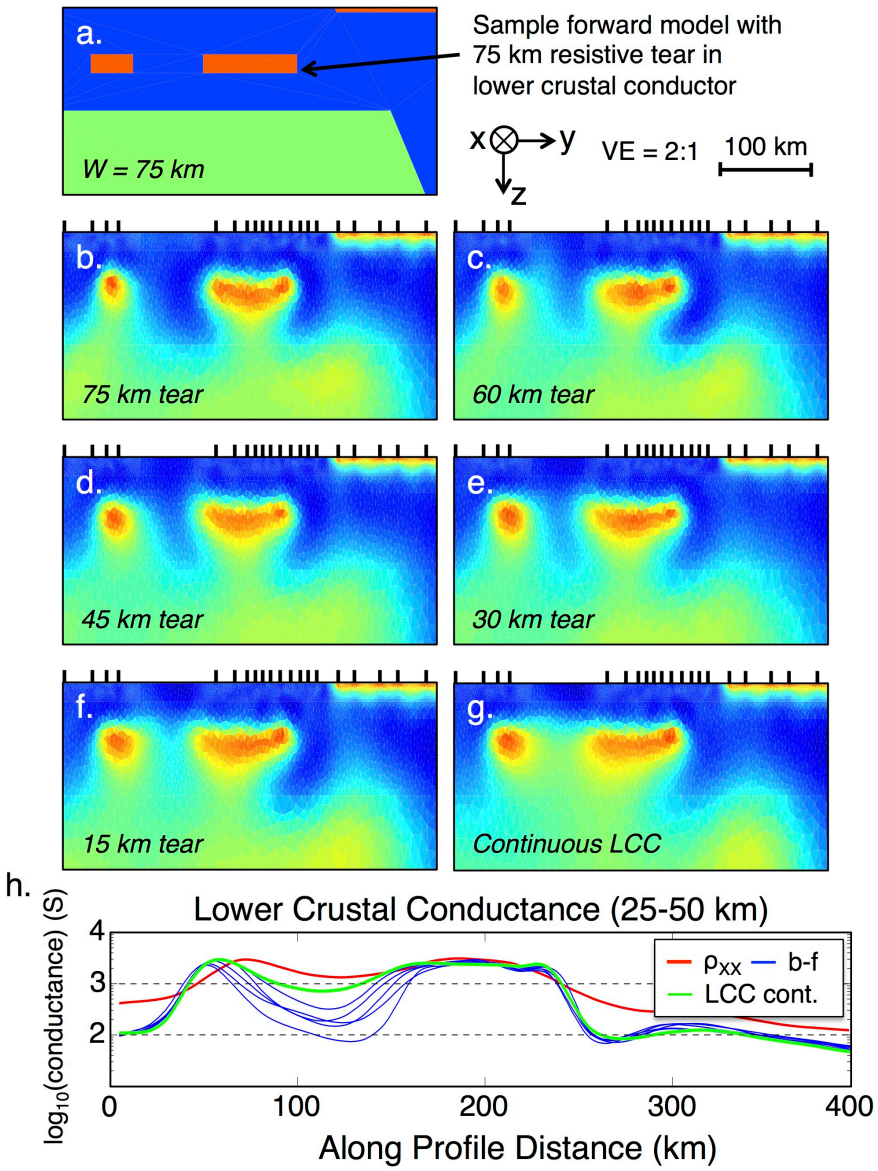

Figure A.3. Test for sensitivity to lateral continuity of the lower crustal conductor. Each of [b]-[f] represents the result of inverting synthetic forward models with different resistive tear widths. Conductor thickness and resistivity are fixed for these models. The synthetic results from Figure A.2[d] are provided in [g] for comparison to the case of a laterally continuous conductor of similar thickness and resistivity. Approximate model view is surface to 100 km depth and 0 to 400 km along profile. Tick marks on [b]-[g] indicate location of synthetic MT data. Vertically integrated lower crustal conductance is shown in [h] for the ρ_{xx} model from Fig. 2.4 [25-50 km depth] and each of the synthetic inversion results in Figure A.3[b]-[g] [25-55 km depth]. Resistivity color scale is identical to that shown in Figure A.2.

A.2 Magnetotelluric Data and Station Information

The following section is provided to allow the community access to view and evaluate the magnetotelluric (MT) data used in the preceding chapters. The following tables provide a subset of station metadata for all stations used in the modeling presented in Chapters 2-4. There are five tables, one for each of five data subgroups: three for data collected in Colorado and New Mexico for the Deep Rift Electrical Resistivity (DRIFTER) experiment, one for Summer of Applied Geophysical Experience (SAGE) MT data collected in the northern Rio Grande Rift from 1991 to 2017, and one for the industry MT data collected by the Unocal Company in the Valles caldera in 1983. Following the tables are plots of magnetotelluric transfer functions for each station listed in the metadata tables

Station metadata provided in the following tables include station location (latitude, longitude, and elevation), acquisition year, the maximum period of available transfer function estimates (Max T), and qualitative static shift corrections for those stations for which such a correction was deemed necessary prior to inversion. Elevation data were provided by the National Map Elevation Point Query Service (https://nationalmap.gov/epqs/) using the known horizontal coordinates of each MT station. The need for static shift correction at a given MT site was based on the observation of the following: (1) TE and TM mode apparent resistivity curves that appear parallel but vertically offset from one another at high frequency and (2) impedance phase values that appear to be overlapping at those same frequencies. Qualitative static shift corrections were selected such that the

apparent resistivity of both modes would converge at high frequency to the apparent resistivity value of neighboring stations.

Transfer function plots show apparent resistivity, phase, and tipper as a function of period for all stations. Apparent resistivity and phase are only shown for off-diagonal components (Zxy and Zyx) of the impedance tensor. Data in these plots have been rotated to a true north (i.e. geographic north) coordinate frame. Static shift corrections have not been applied.

The majority of the data presented here has either already been made publically available or will be available shortly. The U.S. Geological Survey is in the process of preparing a public data release of the DRIFTER MT data set through the web based data portal ScienceBase. The data release will include standard format magnetotelluric data files, called EDI files, which are readable by most inversion and data analysis software used in MT modeling. Station metadata, instrument response files, and ASCII formatted files of all electric and magnetic field time series recorded at those stations will also be provided. Magnetotelluric data from SAGE 2011-2013 and 2016 were provided by the Incorporated Research Institutions for Seismology (IRIS) electromagnetic transfer function database. Early SAGE data (1991-94), the most recent SAGE data (2017), and the Unocal MT data have not been released, although the information provided in the following section would be sufficient for skilled MT practitioners to perform rudimentary modeling and assessment of these data.

Table A.1. DRIFTER Metadata - Colorado MT Stations

Site Name	Latitude	Longitude	Elev. (m)	Year	Max T (s)	Static
rgr003	39.28200	-108.15820	1803.07	2012	10923	
rgr104	39.41235	-107.79856	2368.63	2012	10923	
rgr105	39.31224	-107.62350	2365.86	2012	10923	
rgr006	39.36374	-107.47213	2579.23	2012	10923	
rgr113	39.25160	-106.27370	3180.97	2014	10923	
rgr114	39.18730	-106.02380	3049.02	2014	6989	
rgr015	39.20560	-105.87670	2895.50	2014	10923	
rgr115	39.18350	-105.78030	2918.80	2014	6989	
rgr016	39.19844	-105.68767	2819.48	2012	10923	TE down
rgr116	39.18039	-105.59614	2919.58	2012	6989	
rgr017	39.15921	-105.47481	2647.94	2012	10923	
rgr018	39.20695	-105.34172	2394.37	2012	10923	
rgr118	39.15979	-105.22184	2525.28	2012	6989	
rgr019	39.16214	-105.12747	2321.63	2012	10923	
rgr119	39.18219	-105.00945	2677.71	2012	6989	
rgr120	39.15455	-104.74866	2184.85	2012	6989	
rgr021	39.16733	-104.55661	2169.60	2012	10923	
rgr022	39.15989	-104.22961	1954.96	2012	10923	
rgr122	39.13464	-104.01128	1843.79	2012	6989	
rgr023	39.08411	-103.66054	1663.14	2012	10923	
rgr024	39.12249	-103.39029	1543.55	2012	10923	
rgr025	39.12983	-103.04601	1533.06	2014	10923	
rgr026	39.13070	-102.71770	1408.84	2014	10923	

Table A.2. DRIFTER Metadata - Northern Rift MT Stations

Site Name	Latitude	Longitude	Elev. (m)	Year	Max T (s)	Static
rgr202	36.43098	-107.94409	1990.61	2013	10923	
rgr302	36.42914	-107.78815	2011.72	2013	6989	
rgr203	36.44162	-107.68787	2001.18	2013	10923	
rgr303	36.44278	-107.55363	2112.31	2013	6989	
rgr204	36.43007	-107.41610	2033.24	2013	10923	
rgr305	36.42771	-107.09913	2222.18	2013	6989	
rgr206	36.43747	-106.96597	2296.16	2012	10923	
rgr306	36.44382	-106.85316	2258.53	2012	6989	
rgr207	36.44172	-106.76070	2438.22	2012	10923	
rgr307	36.43880	-106.67202	2389.34	2013	6989	TM up
rgr208	36.42175	-106.60809	2308.10	2012	10923	
rgr308	36.41087	-106.54648	2346.10	2012	6989	
rgr209	36.42208	-106.43878	2333.82	2012	10923	TE down
rgr309	36.42416	-106.36909	2475.70	2013	6989	TM up
rgr210	36.44326	-106.25105	2640.43	2013	10923	
rgr310	36.44069	-106.16138	2484.76	2012	10923	
rgr211	36.41367	-106.09653	2188.99	2012	10923	
rgr311	36.44091	-106.00140	2215.77	2013	6989	
rgr212	36.43616	-105.93457	2155.55	2012	10923	
rgr312	36.43046	-105.85497	2229.63	2013	6989	TM up
rgr213	36.39753	-105.76787	2103.98	2013	10923	
rgr313	36.35759	-105.69360	2047.56	2013	10923	
rgr315	36.34124	-105.41830	3093.02	2012	10923	
rgr216	36.32167	-105.29111	2645.44	2013	6989	
rgr316	36.33285	-105.21180	2982.42	2013	6989	
rgr217	36.30445	-105.15226	2842.15	2013	10923	
rgr317	36.24735	-105.06020	2350.36	2013	10923	
rgr318	36.26165	-104.82703	1920.85	2013	6989	
rgr219	36.26908	-104.73964	1900.50	2013	10923	
rgr319	36.27341	-104.61523	1837.10	2013	6989	
rgr220	36.29221	-104.49808	1747.06	2013	10923	
rgr320	36.28709	-104.37458	1811.74	2013	6989	
rgr221	36.26262	-104.25327	1834.01	2013	10923	
rgr321	36.25954	-104.14237	1879.62	2013	6989	
rgr222	36.24277	-103.99133	1827.91	2013	10923	TM down
rgr322	36.21843	-103.86189	1699.11	2013	6989	
rgr223	36.21140	-103.60280	1674.75	2013	10923	
rgr323	36.21016	-103.49334	1625.44	2013	6989	
rgr224	36.18739	-103.27059	1486.74	2013	6989	

Table A.3. DRIFTER Metadata - Southern Rift MT Stations

Site Name	Latitude	Longitude	Elev. (m)	Year	Max T (s)	Static
rgr501	31.98295	-108.90786	1316.55	2013	6989	TM up
rgr402	32.00200	-108.79300	1371.67	2013	10923	
rgr502	31.97579	-108.66056	1356.85	2013	6989	
rgr403	31.96221	-108.47906	1410.63	2013	10923	
rgr503	32.00000	-108.35770	1372.61	2013	6989	
rgr404	32.01799	-108.20358	1490.62	2013	10923	
rgr504	32.00428	-108.09954	1437.67	2013	6989	
rgr405	32.01358	-108.00038	1373.42	2013	10923	
rgr505	32.00483	-107.86887	1287.98	2013	6989	
rgr406	31.97672	-107.73907	1269.99	2013	10923	
rgr506	31.96635	-107.63463	1257.12	2013	6989	
rgr407	31.97570	-107.54323	1229.94	2013	10923	
rgr507	32.00180	-107.43520	1222.97	2013	6989	
rgr408	31.99200	-107.34324	1270.59	2013	10923	
rgr409	31.94465	-107.11018	1367.53	2013	10923	
rgr410	32.00750	-106.91301	1279.70	2013	10923	
rgr510	31.99777	-106.83110	1275.20	2013	6989	
rgr411	31.99188	-106.76952	1254.08	2013	10923	
rgr511	32.00031	-106.71788	1253.74	2013	6989	
rgr412	32.00470	-106.56926	1214.98	2013	10923	
rgr512	32.02245	-106.51824	1329.87	2013	6989	
rgr413	32.06681	-106.37894	1240.61	2013	10923	
rgr515	32.01036	-105.94121	1638.35	2013	10923	TE up
rgr416	32.03426	-105.79975	1585.28	2013	10923	TE up
rgr417	32.01805	-105.58430	1584.81	2013	10923	
rgr517	32.02166	-105.44575	1360.61	2013	6989	
rgr418	32.01458	-105.33549	1232.50	2013	10923	
rgr518	32.02168	-105.20377	1153.19	2013	6989	
rgr519	32.02724	-104.99375	1121.08	2013	6989	
rgr421	32.02181	-104.62928	1342.74	2013	10923	
rgr521	32.02968	-104.53536	1190.98	2013	6989	TM up
rgr422	32.06725	-104.39376	1131.12	2013	10923	
rgr522	32.06912	-104.28469	1036.92	2013	6989	
rgr423	32.06107	-104.16635	983.90	2013	10923	

Table A.4. SAGE MT Stations Metadata

Site Name	Latitude	Longitude	Elev. (m)	Year	Max T (s)	Static
sage91--11	35.86010	-106.59630	2480.25	1991	1667	
sage91--12	35.91200	-106.60810	2598.69	1991	1667	
sage91--13	35.87630	-106.68070	2626.68	1991	1667	
sage91--14	35.87400	-106.71040	2583.87	1991	1667	TM down
sage92--15	35.86319	-106.72030	2396.98	1992	1365	
sage92--16	35.85518	-106.74984	2319.33	1992	1820	
sage92-CP1	36.00870	-106.20730	2064.22	1992	1820	TE up
sage92-CP2	36.02510	-106.22740	2171.45	1992	1820	
sage94--17	35.82019	-106.78567	2222.33	1994	1820	
sage94--18	35.81672	-106.83029	2439.41	1994	1820	
sage2011-01	35.75892	-106.14990	2079.05	2011	6989	
sage2011-02	35.75999	-106.11640	1969.47	2011	6989	
sage2011-03	35.75910	-106.07820	1959.00	2011	6989	
sage2011-04	35.75732	-106.06590	1981.03	2011	6989	
sage2012-01	35.72301	-106.23039	1980.36	2012	6989	TM up
sage2012-02	35.73020	-106.19870	2050.04	2012	6989	
sage2012-03	35.73756	-106.15480	2025.32	2012	6989	TM up
sage2012-04	35.75741	-106.13660	2045.72	2012	6989	TE up
sage2013-01	35.75610	-106.05420	2018.93	2013	6989	TM up
sage2013-02	35.83199	-106.14450	1738.78	2013	1049	
sage2013-03	35.83321	-106.15510	1696.57	2013	6989	
sage2013-04	35.75208	-106.03970	2038.87	2013	6989	
sage2016-01	35.73250	-106.22439	2051.27	2016	1365	
sage2016-02	35.73562	-106.14984	2019.44	2016	1365	TE down
sage2016-03	35.74153	-106.12601	1979.42	2016	1365	
sage2016-04	35.74578	-106.08073	1921.68	2016	1365	
sage2016-05	35.74480	-106.05822	1962.05	2016	1365	TE up
bnd002	35.78061	-106.26619	1987.73	2017	1365	
bnd004	35.80939	-106.29889	2141.70	2017	341	
bnd005	35.82450	-106.31739	2210.77	2017	1024	
bnd006	35.83250	-106.35639	2313.95	2017	1365	
bnd007	35.83181	-106.38811	2561.97	2017	1365	
bnd009	35.84939	-106.46389	2647.29	2017	341	

Table A.5. Unocal MT Stations Metadata

Site Name	Latitude	Longitude	Elev. (m)	Year	Max T (s)	Static
jmz001	35.92830	-106.55444	2782.45	1983	605	
jmz002	35.92996	-106.54332	2685.36	1983	605	
jmz003	35.91552	-106.53444	2804.40	1983	605	
jmz004	35.91245	-106.52833	2714.90	1983	605	TE down
jmz005	35.92496	-106.50224	2673.12	1983	605	
jmz006	35.93274	-106.49850	2672.65	1983	605	TE down
jmz008	35.97246	-106.53582	2593.26	1983	605	TM down
jmz009	35.90163	-106.56499	2936.25	1983	524	
jmz010	35.96746	-106.55860	2579.50	1983	524	
jmz111	35.88858	-106.56749	2906.79	1983	605	
jmz012	35.86885	-106.55888	3394.58	1983	605	TE up
jmz013	35.95746	-106.60554	2614.09	1983	524	
jmz014	35.95830	-106.59443	2621.87	1983	79	
jmz015	35.90247	-106.57888	2943.37	1983	524	
jmz016	35.91636	-106.60360	2593.39	1983	524	TM up
jmz017	35.95135	-106.55555	2643.84	1983	524	TM down
jmz018	35.93913	-106.51859	2622.24	1983	605	
jmz019	35.87163	-106.58499	2709.21	1983	524	
jmz020	35.85746	-106.50083	2600.67	1983	605	TE up
jmz021	35.86885	-106.51720	2670.12	1983	605	TE down
jmz022	35.87858	-106.53860	3070.94	1983	605	
jmz023	35.93579	-106.57415	2681.39	1983	524	
jmz024	35.88663	-106.58027	2695.41	1983	524	
jmz025	35.85441	-106.59443	2469.86	1983	605	
jmz026	35.89497	-106.51444	2955.95	1983	605	
jmz027	35.89107	-106.50999	2833.81	1983	605	
jmz028	35.86358	-106.54332	3124.48	1983	605	
jmz029	35.83469	-106.58194	2618.47	1983	605	
jmz030	35.83858	-106.55888	2642.33	1983	605	TM up
jmz031	35.89663	-106.53498	2842.96	1983	605	

A.2.1. DRIFTER MT stations in Colorado

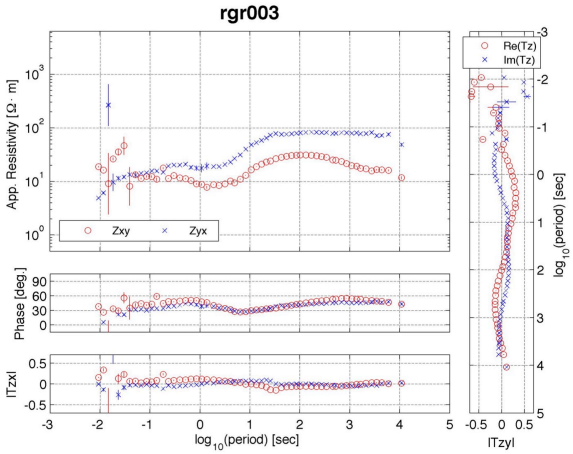

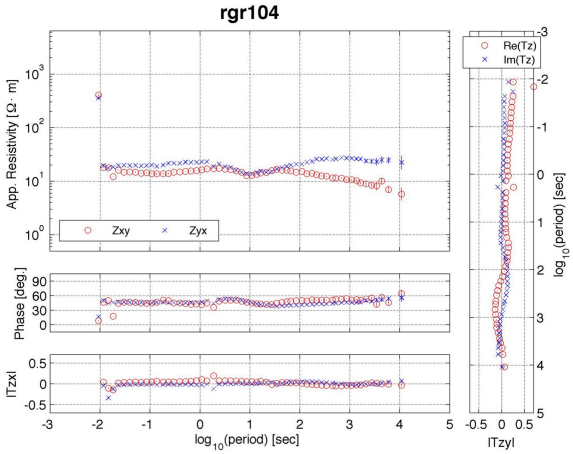

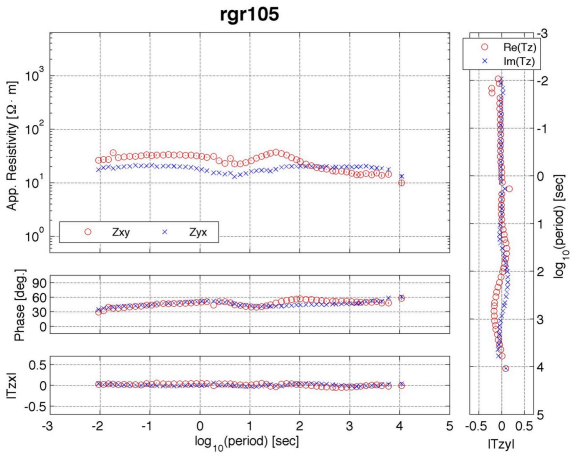

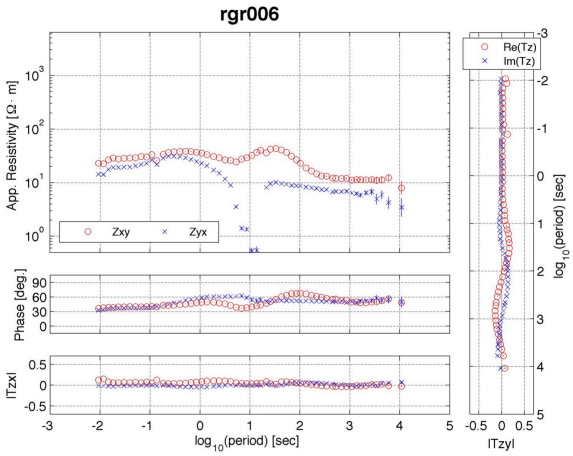

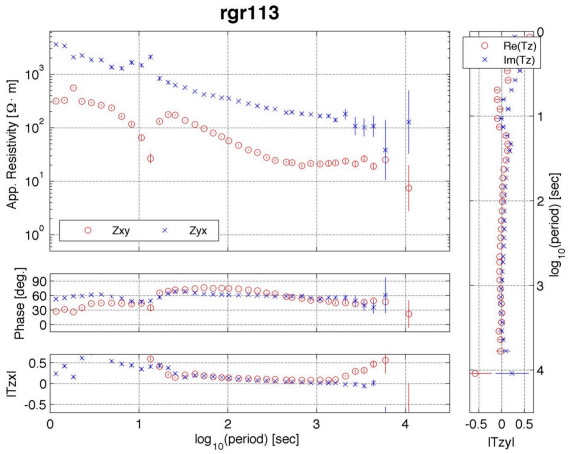
rgr113
App. Resistivity [Ω · m]
Zxy
Zyx
Phase [deg.]
|Tzx|
log10(period) [sec]
Re(Tz)
Im(Tz)
|Tzy|
log10(period) [sec]

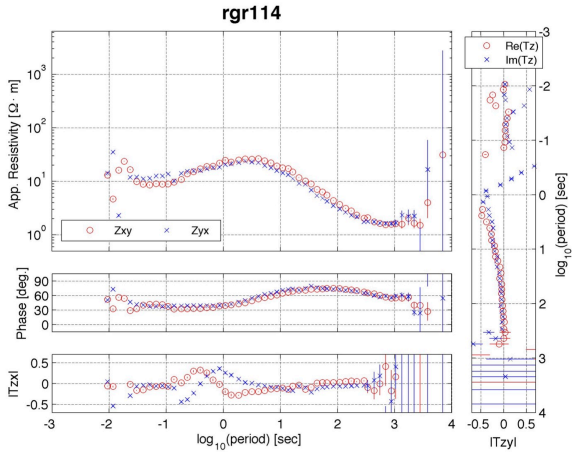
rgr114
App. Resistivity [Ω · m]
Zxy
Zyx
Phase [deg.]
|Tzx|
log10(period) [sec]
Re(Tz)
Im(Tz)
|Tzy|
log10(period) [sec]

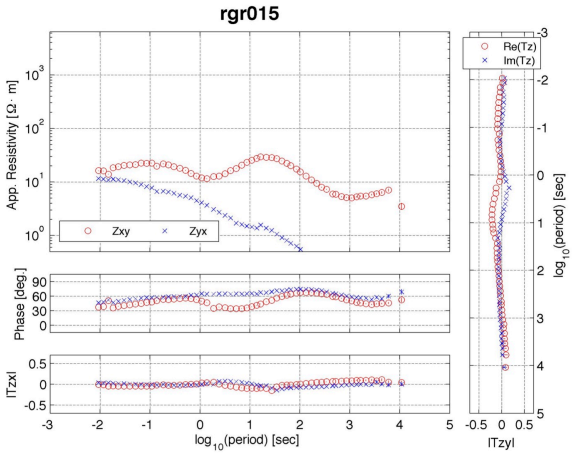
rgr015
App. Resistivity [Ω · m]
Zxy
Zyx
Phase [deg.]
|Tzx|
log10(period) [sec]
Re(Tz)
Im(Tz)
|Tzy|
log10(period) [sec]

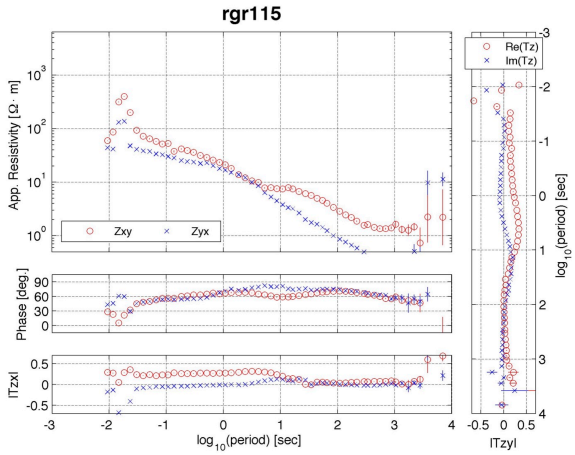
rgr115
App. Resistivity [Ω · m]
Zxy
Zyx
Phase [deg.]
|Tzx|
log10(period) [sec]
Re(Tz)
Im(Tz)
|Tzy|
log10(period) [sec]

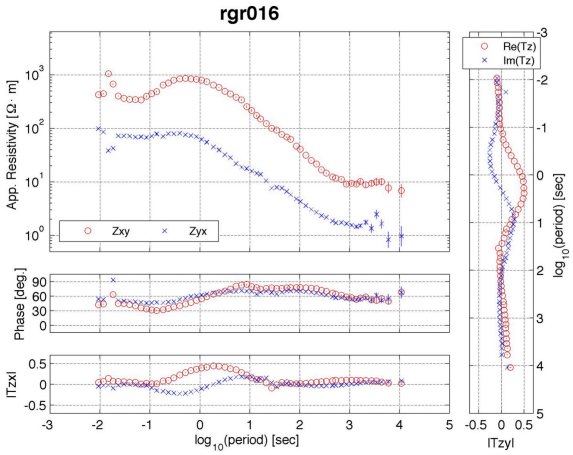
rgr016
App. Resistivity [Ω · m]
Zxy
Zyx
Phase [deg]
|Tzx|
log10(period) [sec]
Re(Tz)
Im(Tz)
log10(period) [sec]
|Tzy|

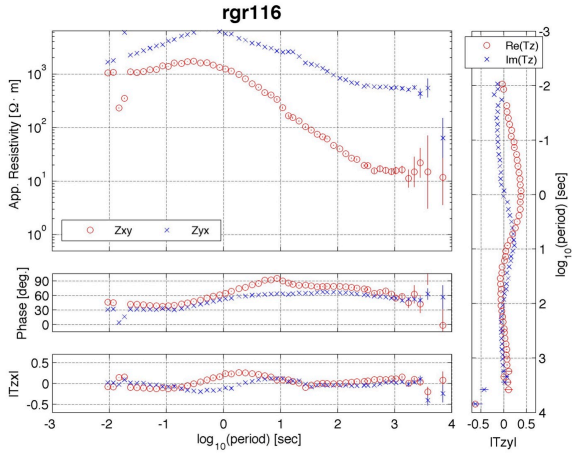
rgr116
App. Resistivity [Ω · m]
Zxy
Zyx
Phase [deg]
|Tzx|
log10(period) [sec]
Re(Tz)
Im(Tz)
log10(period) [sec]
|Tzy|

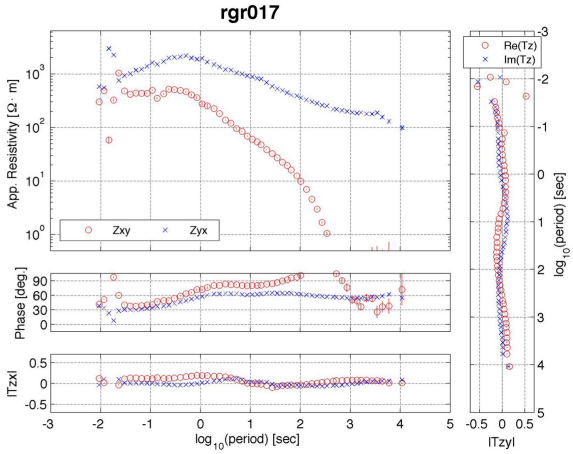
rgr017
App. Resistivity [Ω · m]
Zxy
Zyx
Phase [deg]
|Tzx|
log10(period) [sec]
Re(Tz)
Im(Tz)
log10(period) [sec]
|Tzy|

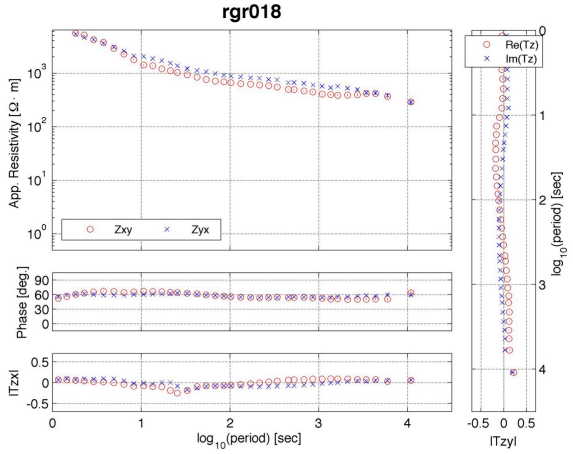
rgr018
App. Resistivity [Ω · m]
Zxy
Zyx
Phase [deg]
|Tzx|
log10(period) [sec]
Re(Tz)
Im(Tz)
log10(period) [sec]
|Tzy|

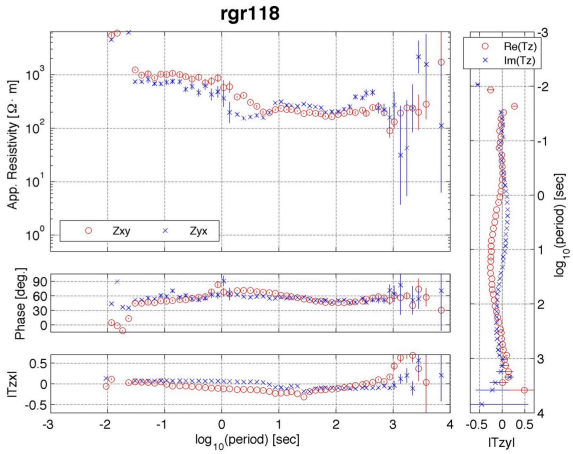
rgr118
App. Resistivity [Ω · m]
Zxy
Zyx
Phase [deg.]
|Tzx|
log10(period) [sec]
Re(Tz)
Im(Tz)
|Tzy|
log10(period) [sec]

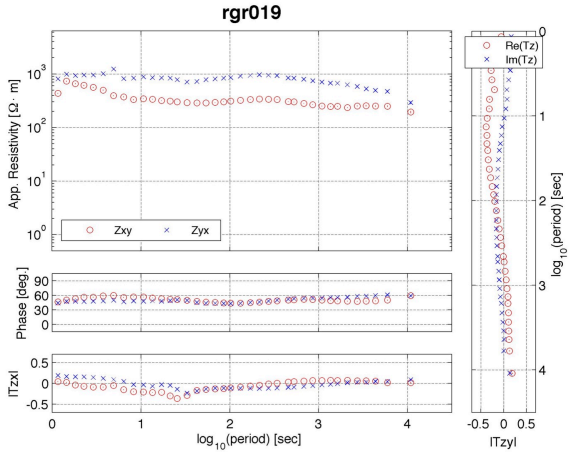
rgr019
App. Resistivity [Ω · m]
Zxy
Zyx
Phase [deg.]
|Tzx|
log10(period) [sec]
Re(Tz)
Im(Tz)
|Tzy|
log10(period) [sec]

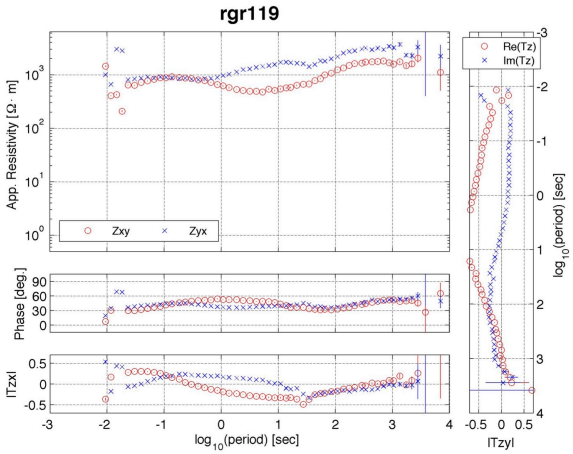
rgr119
App. Resistivity [Ω · m]
Zxy
Zyx
Phase [deg.]
|Tzx|
log10(period) [sec]
Re(Tz)
Im(Tz)
|Tzy|
log10(period) [sec]

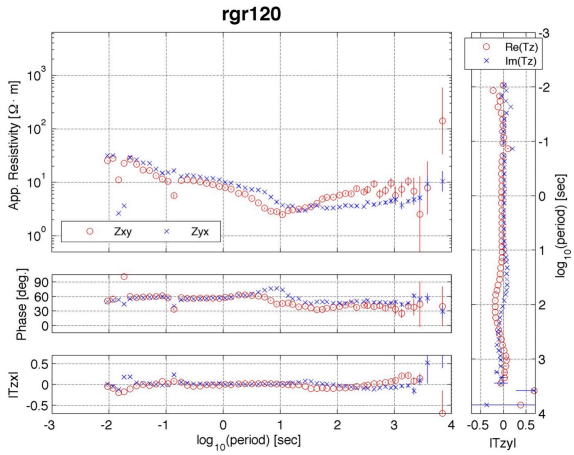
rgr120
App. Resistivity [Ω · m]
Zxy
Zyx
Phase [deg.]
|Tzx|
log10(period) [sec]
Re(Tz)
Im(Tz)
|Tzy|
log10(period) [sec]

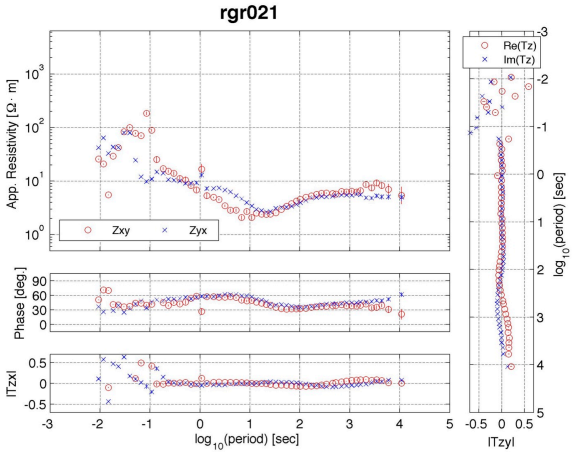
rgr021
App. Resistivity [Ω · m]
Zxy
Zyx
Phase [deg.]
ITzxI
log10(period) [sec]
Re(Tz)
Im(Tz)
ITzyI
log10(period) [sec]

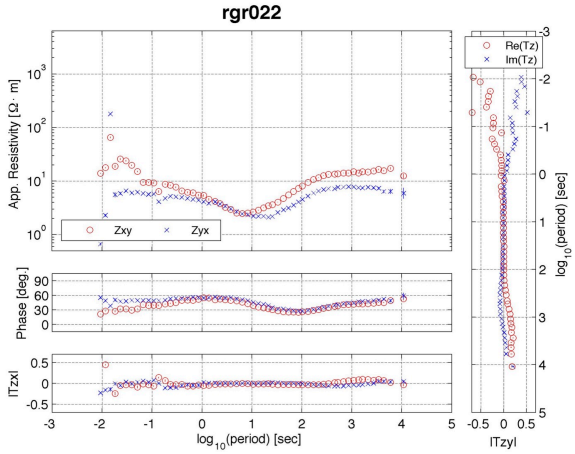
rgr022
App. Resistivity [Ω · m]
Zxy
Zyx
Phase [deg.]
ITzxI
log10(period) [sec]
Re(Tz)
Im(Tz)
ITzyI
log10(period) [sec]

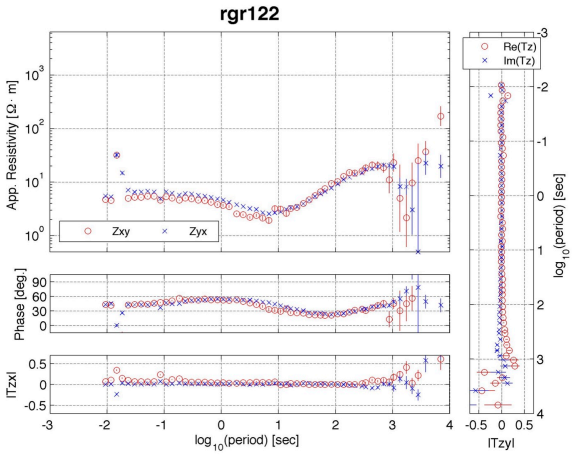
rgr122
App. Resistivity [Ω · m]
Zxy
Zyx
Phase [deg.]
ITzxI
log10(period) [sec]
Re(Tz)
Im(Tz)
ITzyI
log10(period) [sec]

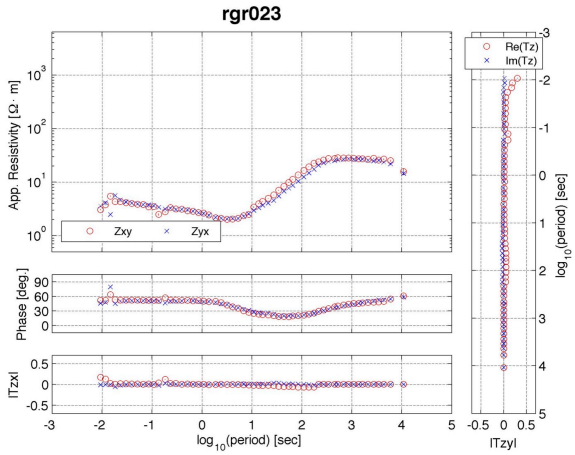
rgr023
App. Resistivity [Ω · m]
Zxy
Zyx
Phase [deg.]
ITzxI
log10(period) [sec]
Re(Tz)
Im(Tz)
ITzyI
log10(period) [sec]

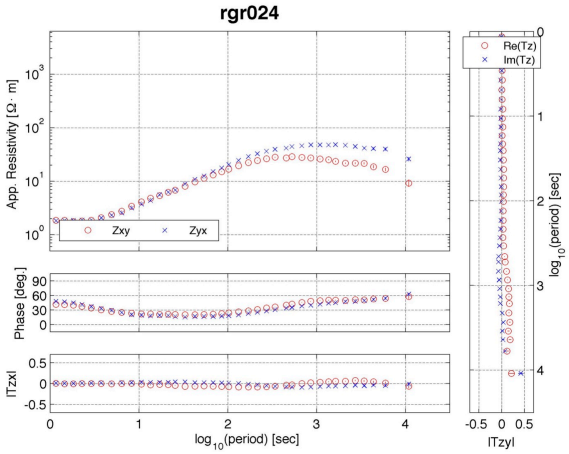
rgr024
App. Resistivity [Ω · m]
Zxy
Zyx
Phase [deg.]
|Tzx|
log10(period) [sec]
Re(Tz)
Im(Tz)
|Tzy|
log10(period) [sec]

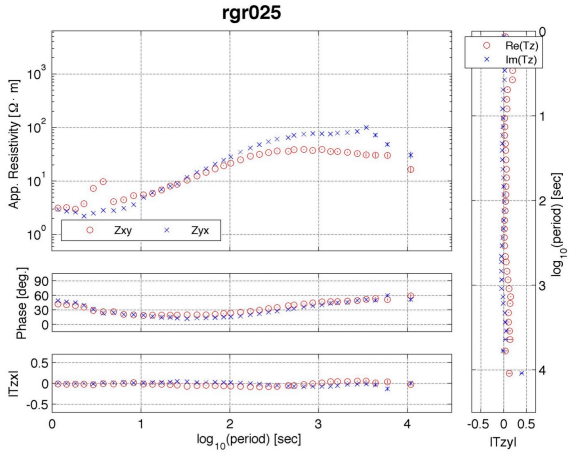
rgr025
App. Resistivity [Ω · m]
Zxy
Zyx
Phase [deg.]
|Tzx|
log10(period) [sec]
Re(Tz)
Im(Tz)
|Tzy|
log10(period) [sec]

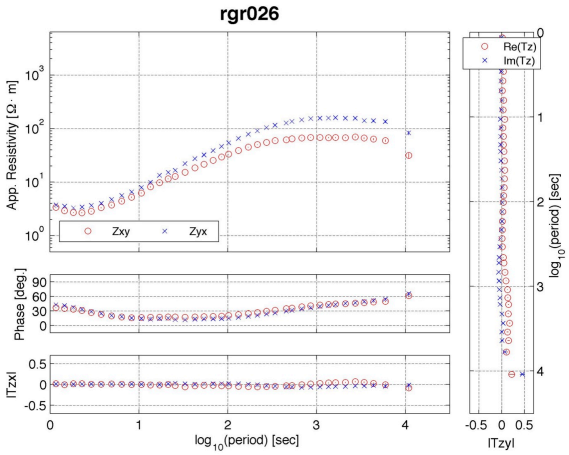
rgr026
App. Resistivity [Ω · m]
Zxy
Zyx
Phase [deg.]
|Tzx|
log10(period) [sec]
Re(Tz)
Im(Tz)
|Tzy|
log10(period) [sec]

A.2.2. DRIFTER MT stations in northern New Mexico

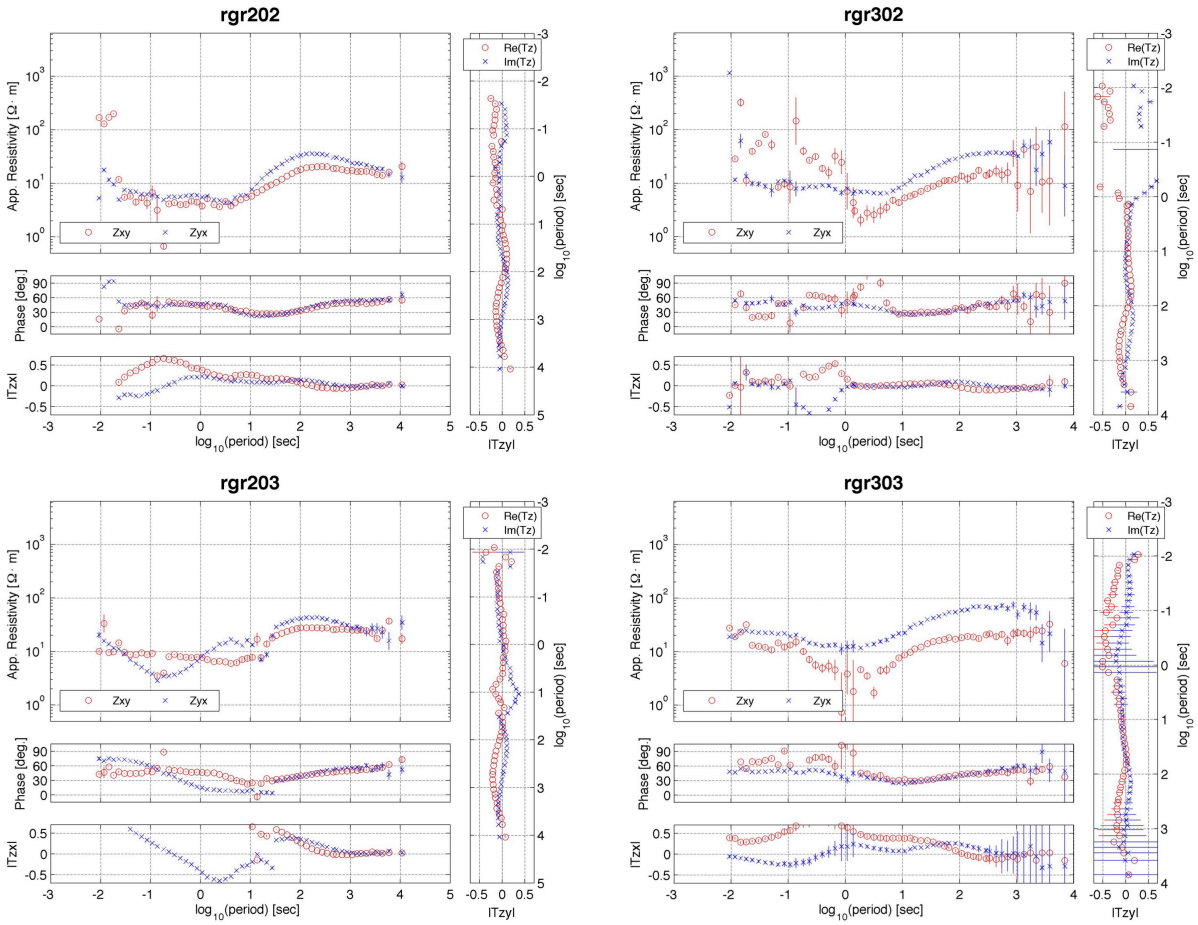

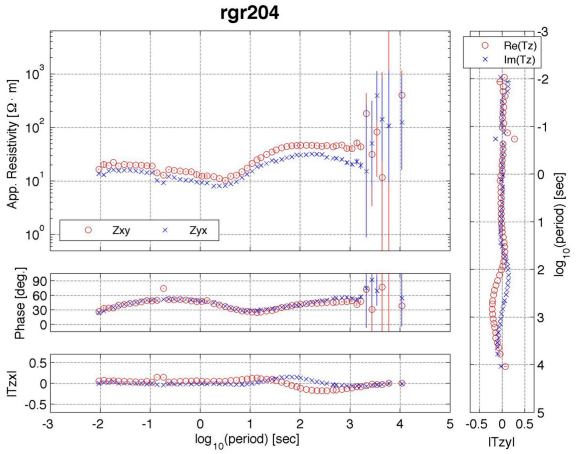
rgr204
App. Resistivity [Ω · m]
Zxy
Zyx
Phase [deg.]
|Tzx|
log10(period) [sec]
Re(Tz)
Im(Tz)
|Tzy|
log10(period) [sec]

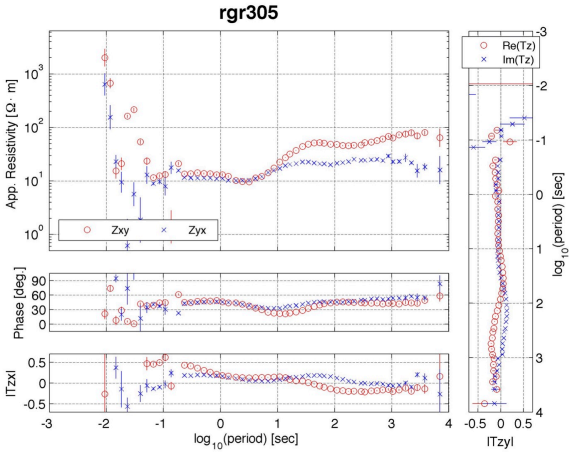
rgr305
App. Resistivity [Ω · m]
Zxy
Zyx
Phase [deg.]
|Tzx|
log10(period) [sec]
Re(Tz)
Im(Tz)
|Tzy|
log10(period) [sec]

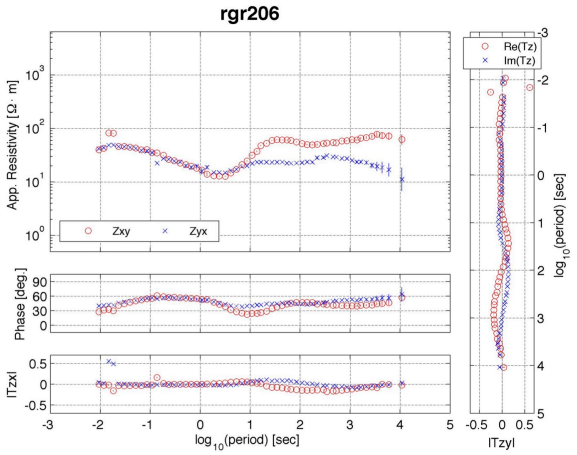
rgr206
App. Resistivity [Ω · m]
Zxy
Zyx
Phase [deg.]
|Tzx|
log10(period) [sec]
Re(Tz)
Im(Tz)
|Tzy|
log10(period) [sec]

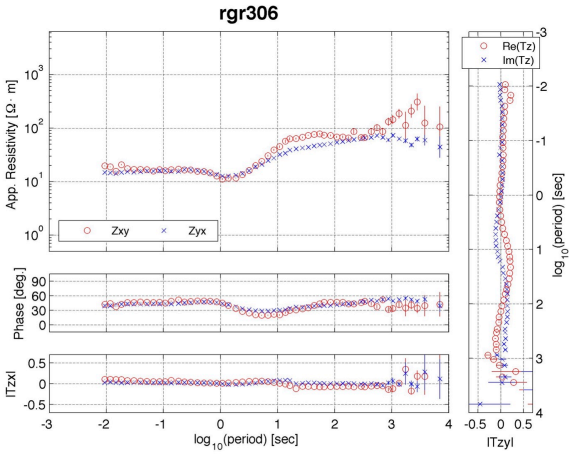
rgr306
App. Resistivity [Ω · m]
Zxy
Zyx
Phase [deg.]
|Tzx|
log10(period) [sec]
Re(Tz)
Im(Tz)
|Tzy|
log10(period) [sec]

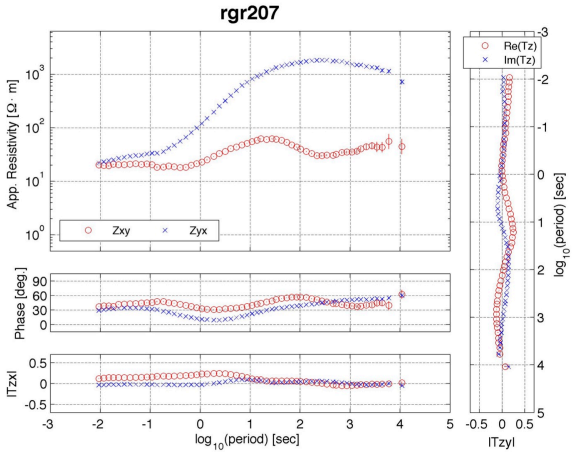
rgr207
App. Resistivity [Ω · m]
Zxy
Zyx
Phase [deg.]
|Tzx|
log10(period) [sec]
Re(Tz)
Im(Tz)
|Tzy|
log10(period) [sec]

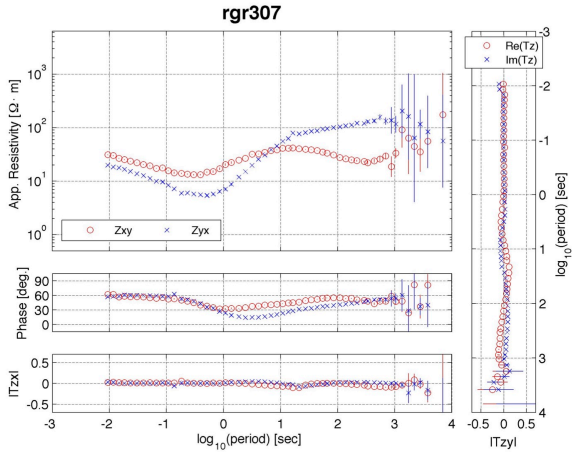
rgr307
App. Resistivity [Ω · m]
Zxy
Zyx
Phase [deg.]
|Tzx|
log10(period) [sec]
Re(Tz)
Im(Tz)
|Tzy|
log10(period) [sec]

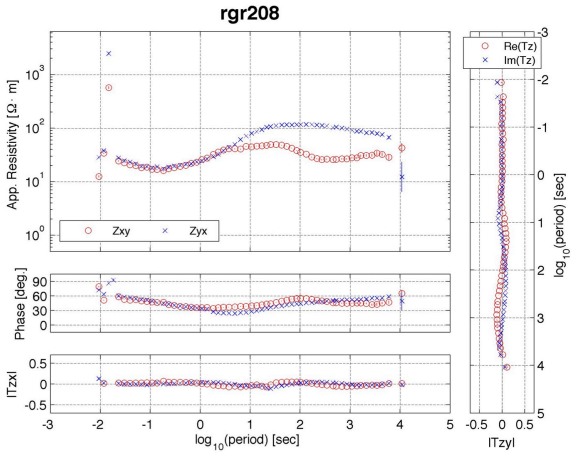
rgr208
App. Resistivity [Ω · m]
Zxy
Zyx
Phase [deg.]
|Tzx|
log10(period) [sec]
Re(Tz)
Im(Tz)
|Tzy|
log10(period) [sec]

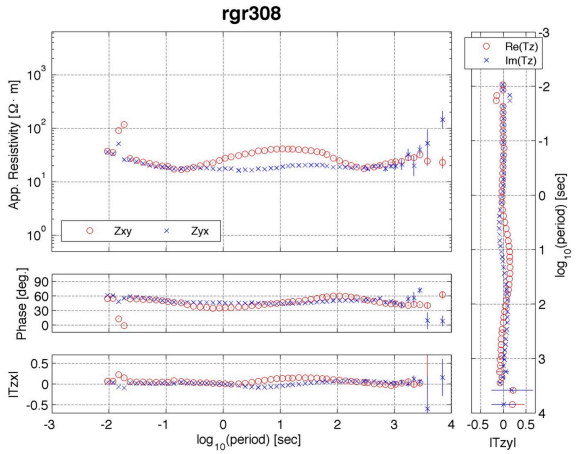
rgr308
App. Resistivity [Ω · m]
Zxy
Zyx
Phase [deg.]
|Tzx|
log10(period) [sec]
Re(Tz)
Im(Tz)
|Tzy|
log10(period) [sec]

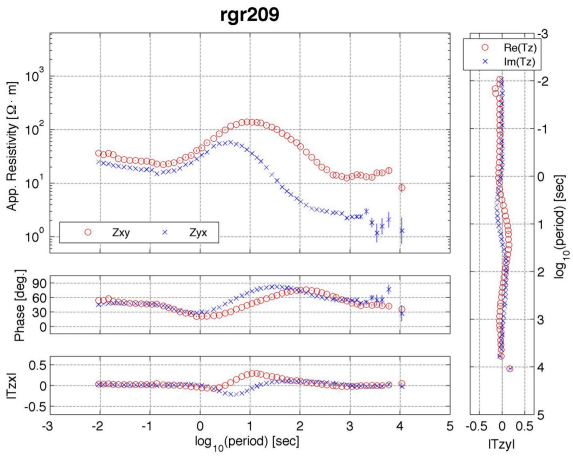
rgr209
App. Resistivity [Ω · m]
Zxy
Zyx
Phase [deg.]
|Tzx|
log10(period) [sec]
Re(Tz)
Im(Tz)
|Tzy|
log10(period) [sec]

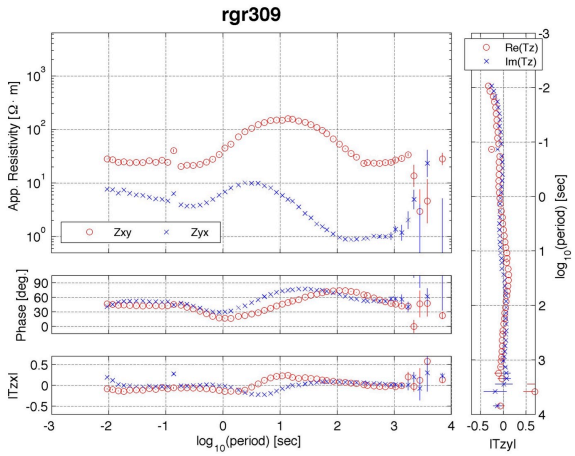
rgr309
App. Resistivity [Ω · m]
Zxy
Zyx
Phase [deg.]
|Tzx|
log10(period) [sec]
Re(Tz)
Im(Tz)
|Tzy|
log10(period) [sec]

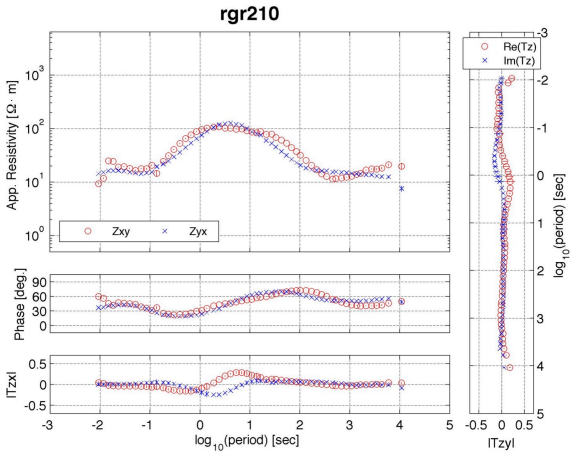
rgr210
App. Resistivity [Ω · m]
Zxy
Zyx
Phase [deg.]
|Tzx|
log10(period) [sec]
Re(Tz)
Im(Tz)
|Tzy|
log10(period) [sec]

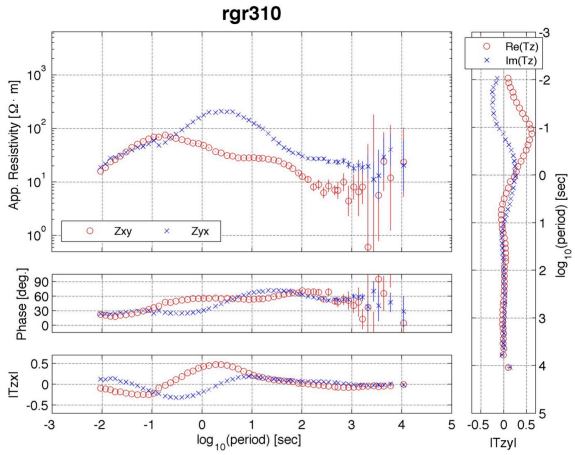
rgr310
App. Resistivity [Ω · m]
Zxy
Zyx
Phase [deg.]
|Tzx|
log10(period) [sec]
Re(Tz)
Im(Tz)
|Tzy|
log10(period) [sec]

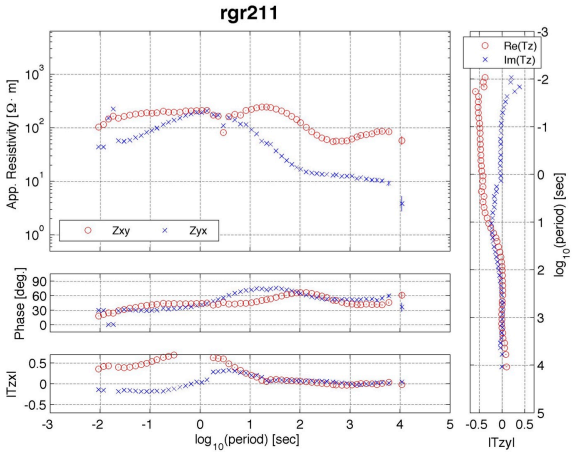
rgr211
App. Resistivity [Ω· m]
Zxy
Zyx
Phase [deg.]
ITzxI
log10(period) [sec]
Re(Tz)
Im(Tz)
ITzyI
log10(period) [sec]

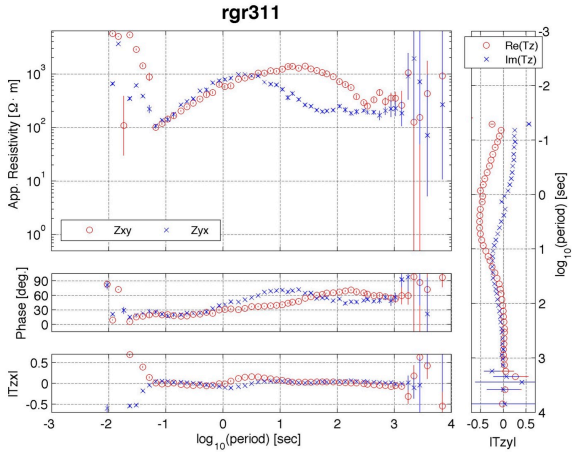
rgr311
App. Resistivity [Ω· m]
Zxy
Zyx
Phase [deg.]
ITzxI
log10(period) [sec]
Re(Tz)
Im(Tz)
ITzyI
log10(period) [sec]

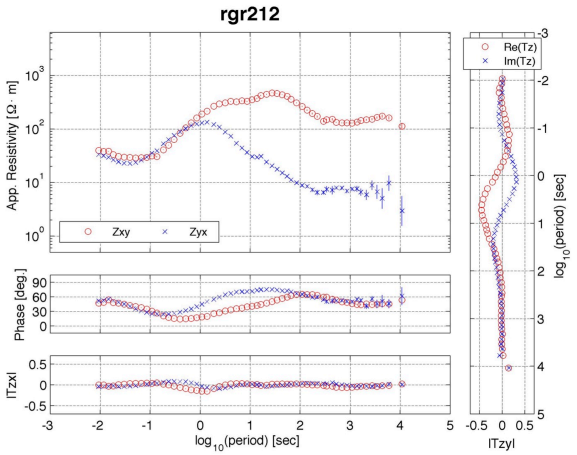
rgr212
App. Resistivity [Ω· m]
Zxy
Zyx
Phase [deg.]
ITzxI
log10(period) [sec]
Re(Tz)
Im(Tz)
ITzyI
log10(period) [sec]

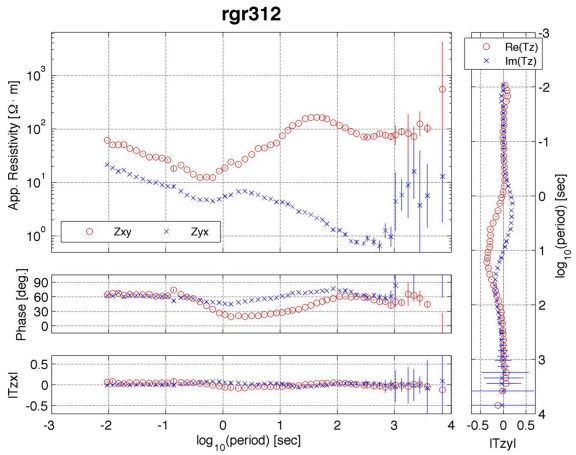
rgr312
App. Resistivity [Ω· m]
Zxy
Zyx
Phase [deg.]
ITzxI
log10(period) [sec]
Re(Tz)
Im(Tz)
ITzyI
log10(period) [sec]

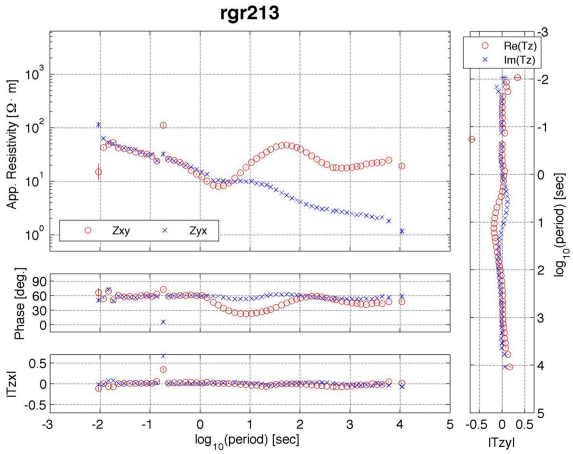
rgr213
App. Resistivity [Ω · m]
Zxy
Zyx
Phase [deg.]
|Tzx|
log10(period) [sec]
Re(Tz)
Im(Tz)
|Tzy|
log10(period) [sec]

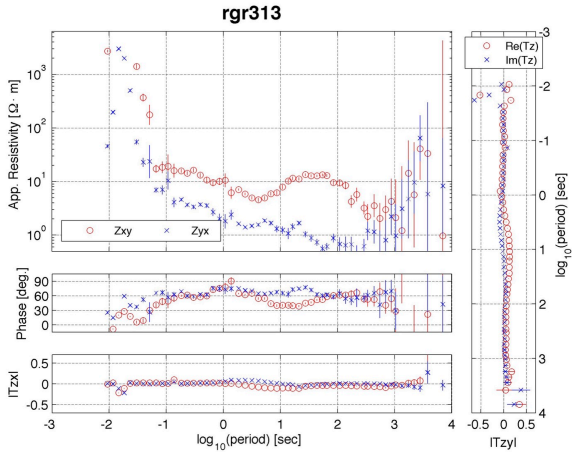
rgr313
App. Resistivity [Ω · m]
Zxy
Zyx
Phase [deg.]
|Tzx|
log10(period) [sec]
Re(Tz)
Im(Tz)
|Tzy|
log10(period) [sec]

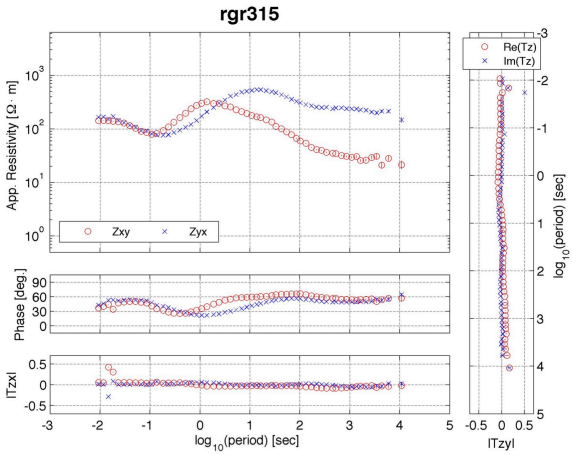
rgr315
App. Resistivity [Ω · m]
Zxy
Zyx
Phase [deg.]
|Tzx|
log10(period) [sec]
Re(Tz)
Im(Tz)
|Tzy|
log10(period) [sec]

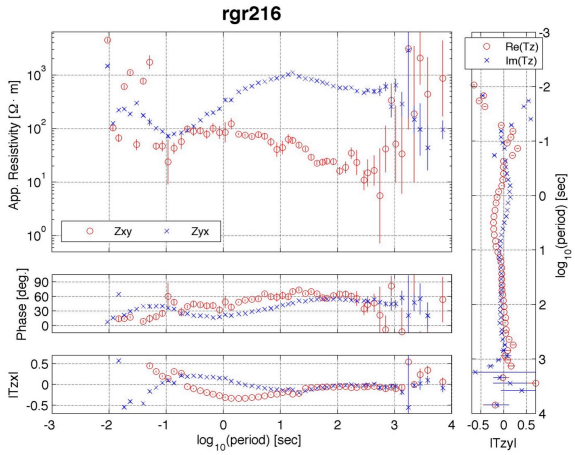
rgr216
App. Resistivity [Ω · m]
Zxy
Zyx
Phase [deg.]
|Tzx|
log10(period) [sec]
Re(Tz)
Im(Tz)
|Tzy|
log10(period) [sec]

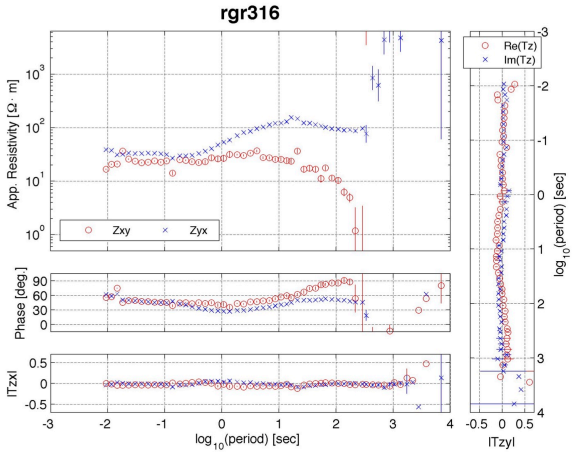
rgr316
App. Resistivity [Ω · m]
Zxy
Zyx
Phase [deg.]
|Tzx|
log10(period) [sec]
Re(Tz)
Im(Tz)
|Tzy|
log10(period) [sec]

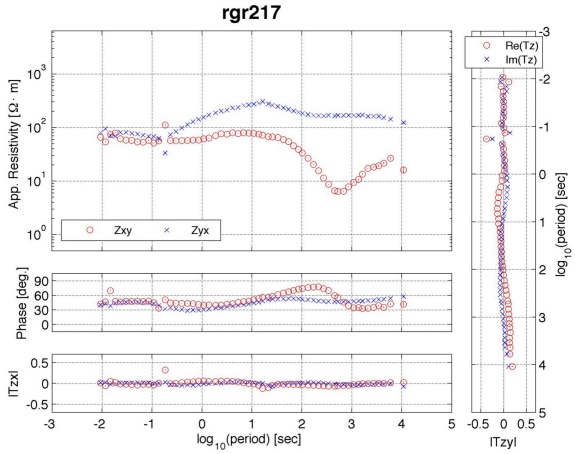
rgr217
App. Resistivity [Ω · m]
Zxy
Zyx
Phase [deg.]
|Tzx|
log10(period) [sec]
Re(Tz)
Im(Tz)
|Tzy|
log10(period) [sec]

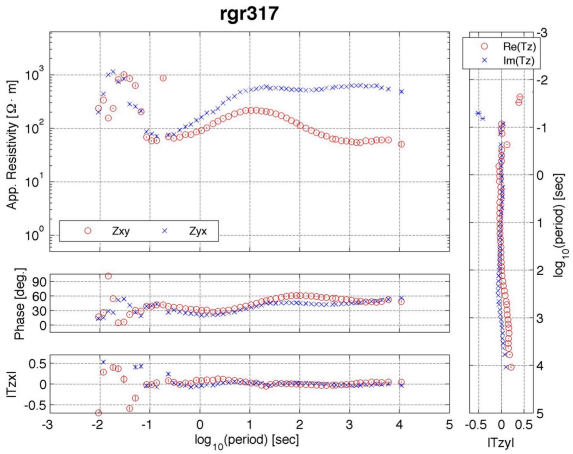
rgr317
App. Resistivity [Ω · m]
Zxy
Zyx
Phase [deg.]
|Tzx|
log10(period) [sec]
Re(Tz)
Im(Tz)
|Tzy|
log10(period) [sec]

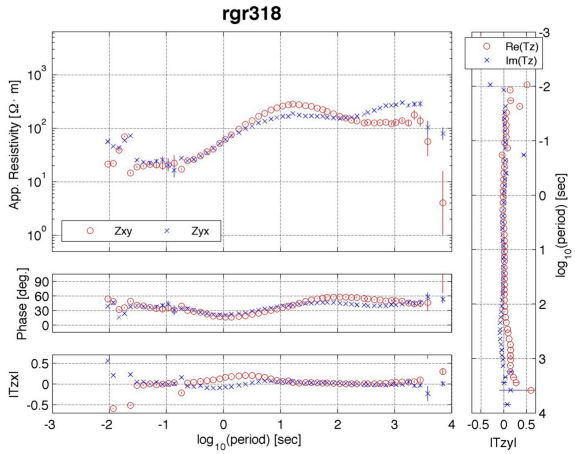
rgr318
App. Resistivity [Ω · m]
Zxy
Zyx
Phase [deg.]
|Tzx|
log10(period) [sec]
Re(Tz)
Im(Tz)
|Tzy|
log10(period) [sec]

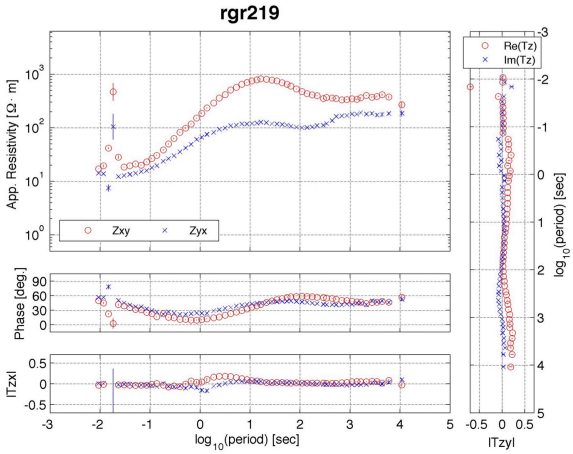
rgr219
App. Resistivity [Ω · m]
Zxy
Zyx
Phase [deg.]
|Tzx|
log10(period) [sec]
Re(Tz)
Im(Tz)
|Tzy|
log10(period) [sec]

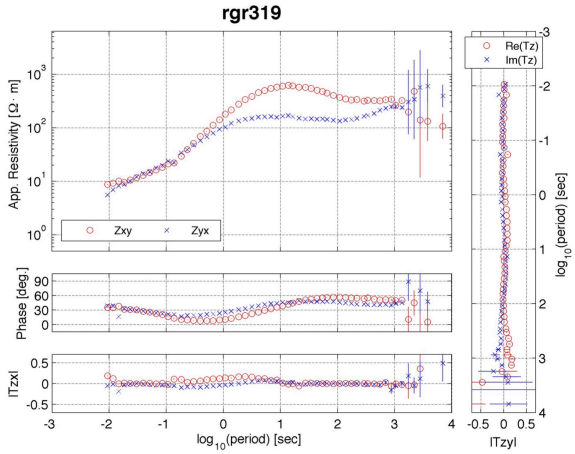
rgr319
App. Resistivity [Ω · m]
Zxy
Zyx
Phase [deg.]
|Tzx|
log10(period) [sec]
Re(Tz)
Im(Tz)
|Tzy|
log10(period) [sec]

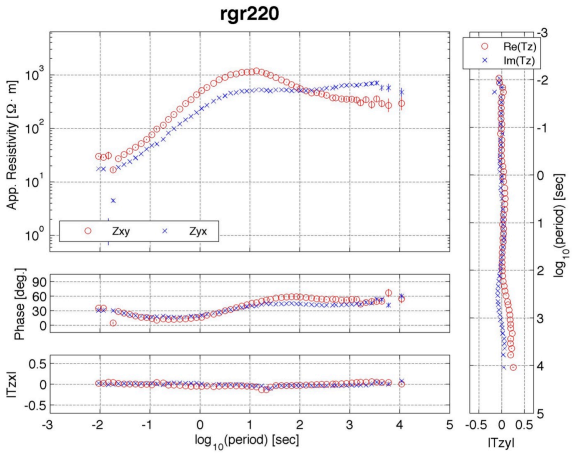
rgr220
App. Resistivity [Ω · m]
Zxy
Zyx
Phase [deg.]
|Tzx|
log10(period) [sec]
Re(Tz)
Im(Tz)
|Tzy|
log10(period) [sec]

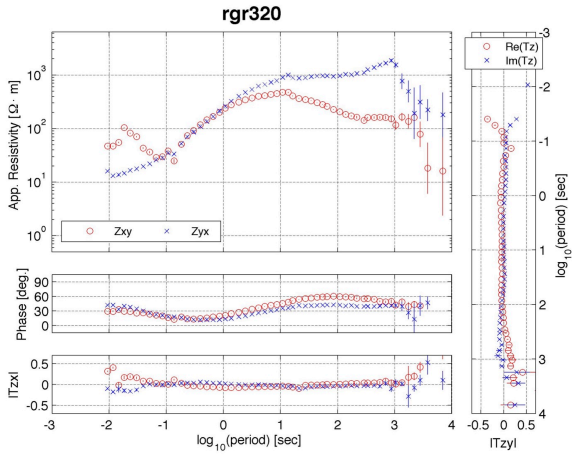
rgr320
App. Resistivity [Ω · m]
Zxy
Zyx
Phase [deg.]
|Tzx|
log10(period) [sec]
Re(Tz)
Im(Tz)
|Tzy|
log10(period) [sec]

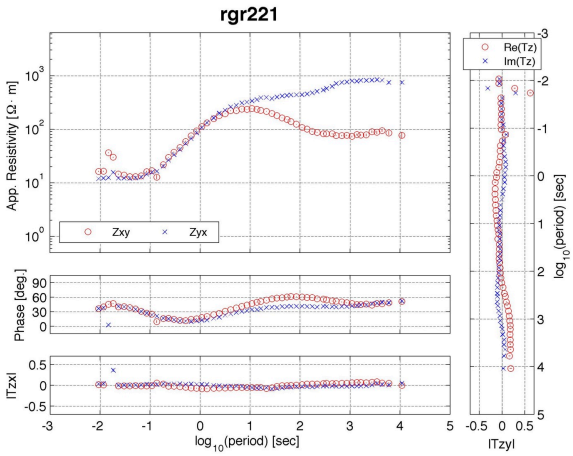
rgr221
App. Resistivity [Ω· m]
Zxy
Zyx
Phase [deg.]
|Tzx|
log10(period) [sec]
Re(Tz)
Im(Tz)
|Tzy|
log10(period) [sec]

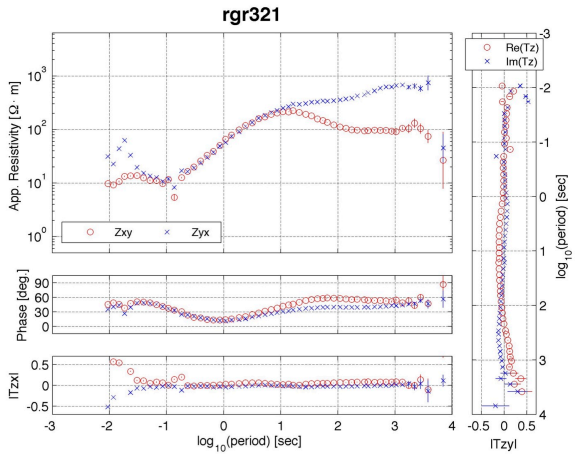
rgr321
App. Resistivity [Ω· m]
Zxy
Zyx
Phase [deg.]
|Tzx|
log10(period) [sec]
Re(Tz)
Im(Tz)
|Tzy|
log10(period) [sec]

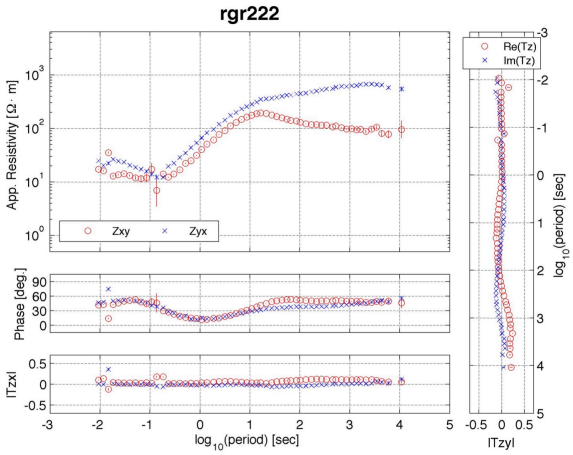
rgr222
App. Resistivity [Ω· m]
Zxy
Zyx
Phase [deg.]
|Tzx|
log10(period) [sec]
Re(Tz)
Im(Tz)
|Tzy|
log10(period) [sec]

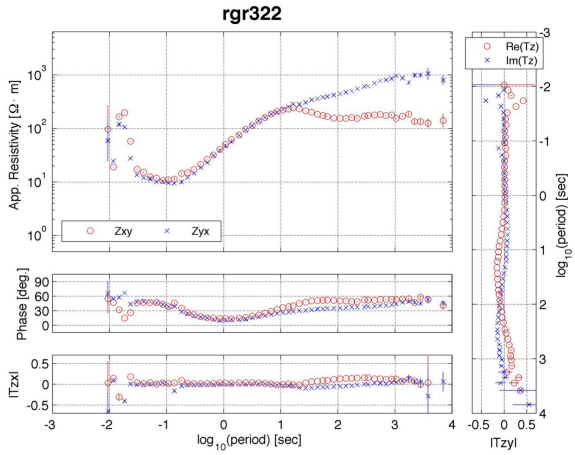
rgr322
App. Resistivity [Ω· m]
Zxy
Zyx
Phase [deg.]
|Tzx|
log10(period) [sec]
Re(Tz)
Im(Tz)
|Tzy|
log10(period) [sec]

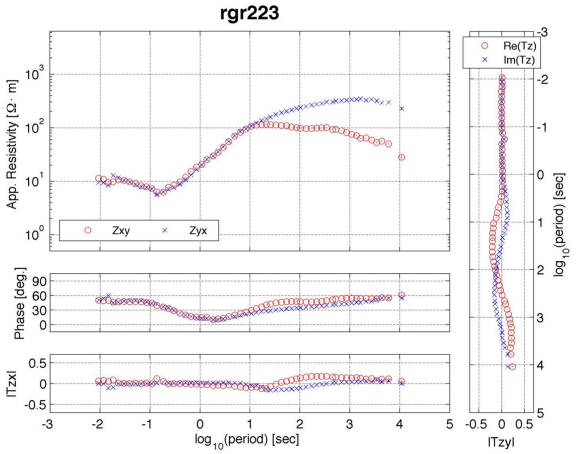
rgr223
App. Resistivity [Ω · m]
Zxy
Zyx
Phase [deg.]
|Tzx|
log10(period) [sec]
Re(Tz)
Im(Tz)
|Tzy|
log10(period) [sec]

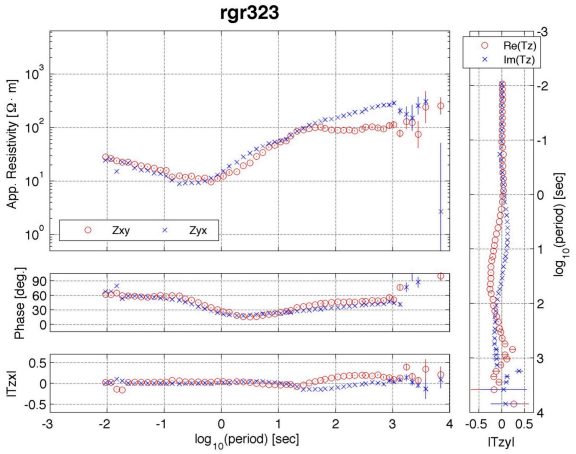
rgr323
App. Resistivity [Ω · m]
Zxy
Zyx
Phase [deg.]
|Tzx|
log10(period) [sec]
Re(Tz)
Im(Tz)
|Tzy|
log10(period) [sec]

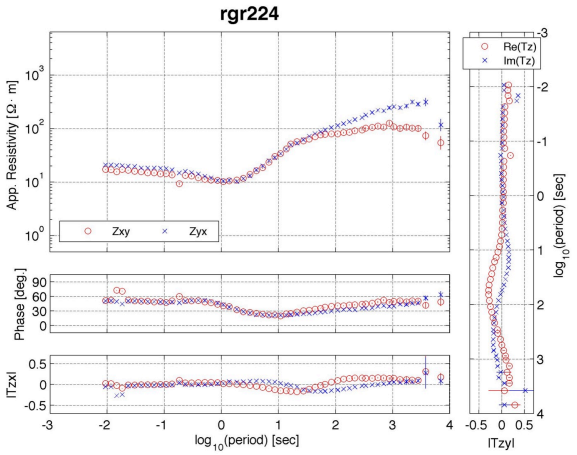
rgr224
App. Resistivity [Ω · m]
Zxy
Zyx
Phase [deg.]
|Tzx|
log10(period) [sec]
Re(Tz)
Im(Tz)
|Tzy|
log10(period) [sec]

A.2.3. DRIFTER MT stations in southern New Mexico

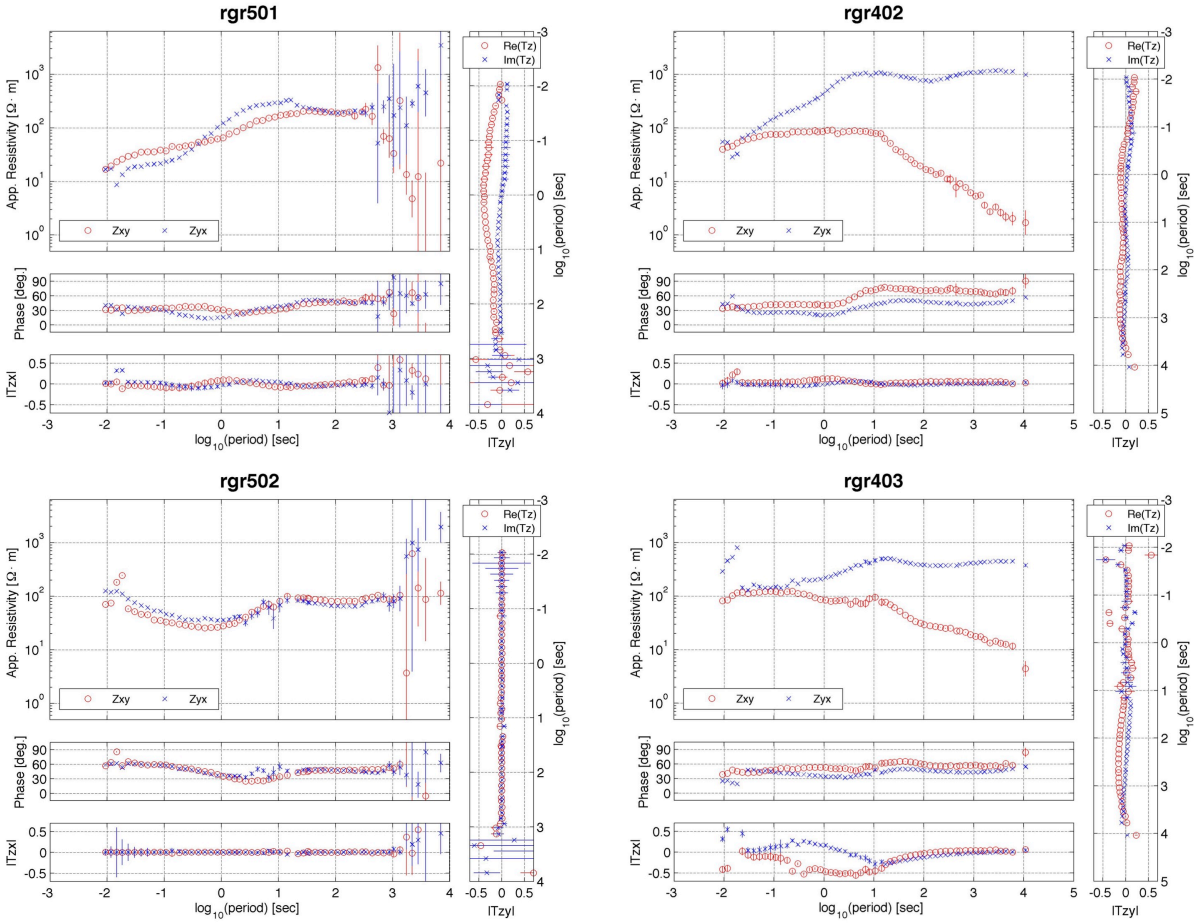

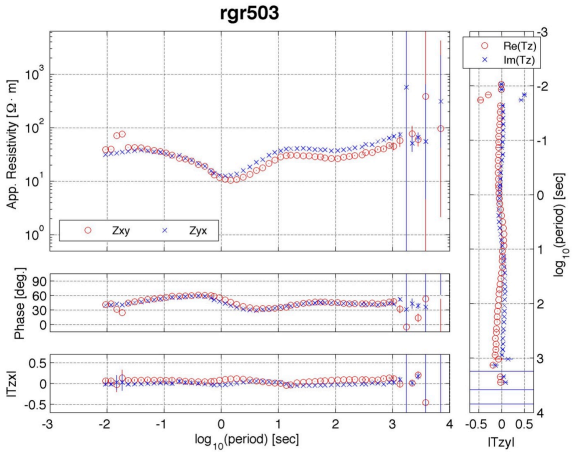
rgr503
App. Resistivity [Ω · m]
Zxy
Zyx
Phase [deg.]
|Tzx|
log10(period) [sec]
Re(Tz)
Im(Tz)
|Tzy|
log10(period) [sec]

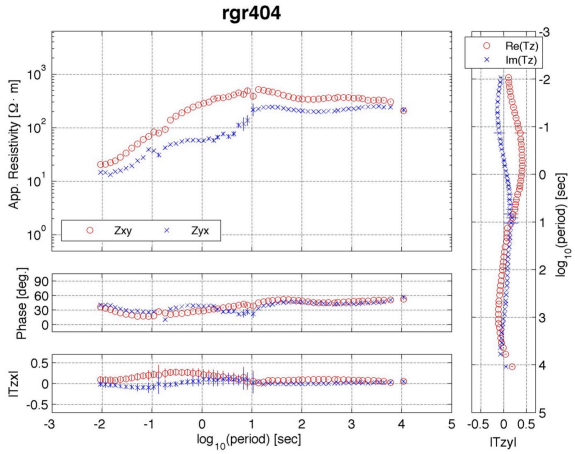
rgr404
App. Resistivity [Ω · m]
Zxy
Zyx
Phase [deg.]
|Tzx|
log10(period) [sec]
Re(Tz)
Im(Tz)
|Tzy|
log10(period) [sec]

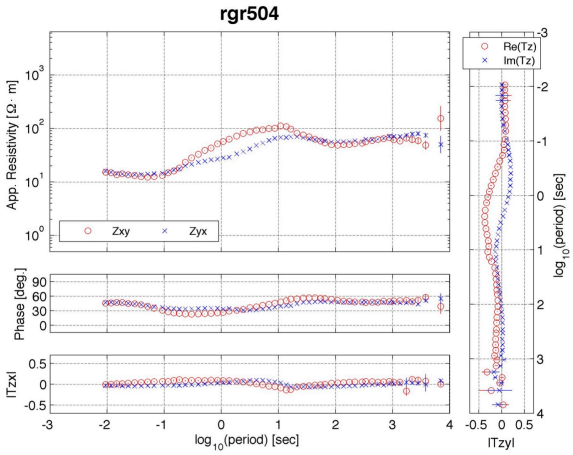
rgr504
App. Resistivity [Ω · m]
Zxy
Zyx
Phase [deg.]
|Tzx|
log10(period) [sec]
Re(Tz)
Im(Tz)
|Tzy|
log10(period) [sec]

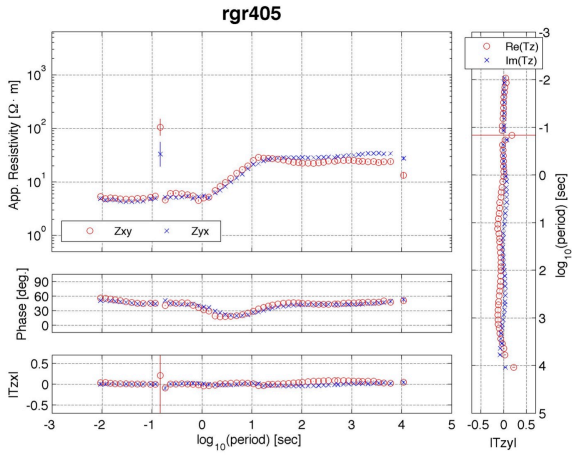
rgr405
App. Resistivity [Ω · m]
Zxy
Zyx
Phase [deg.]
|Tzx|
log10(period) [sec]
Re(Tz)
Im(Tz)
|Tzy|
log10(period) [sec]

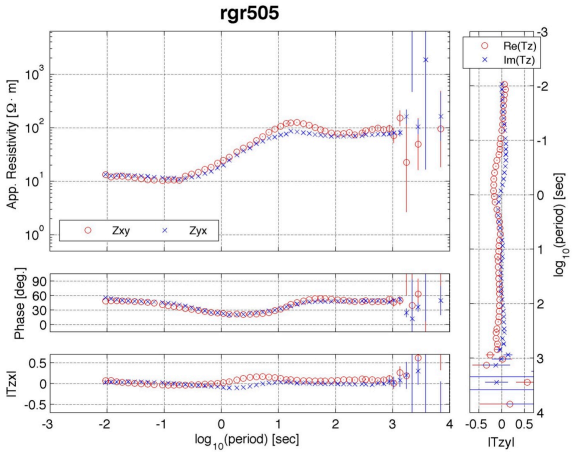
rgr505
App. Resistivity [Ω · m]
Zxy
Zyx
Phase [deg.]
|Tzx|
log10(period) [sec]
Re(Tz)
Im(Tz)
|Tzy|
log10(period) [sec]

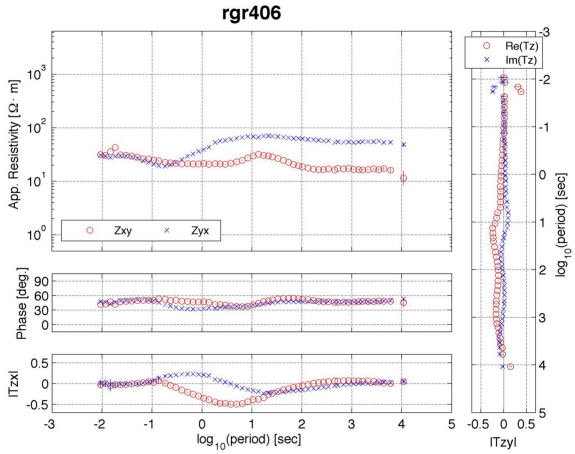
rgr406
App. Resistivity [Ω · m]
Zxy
Zyx
Phase [deg.]
|Tzx|
log10(period) [sec]
Re(Tz)
Im(Tz)
|Tzy|
log10(period) [sec]

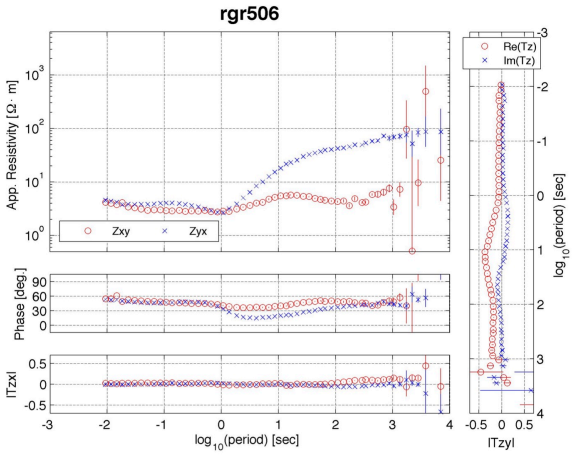
rgr506
App. Resistivity [Ω · m]
Zxy
Zyx
Phase [deg.]
|Tzx|
log10(period) [sec]
Re(Tz)
Im(Tz)
|Tzy|
log10(period) [sec]

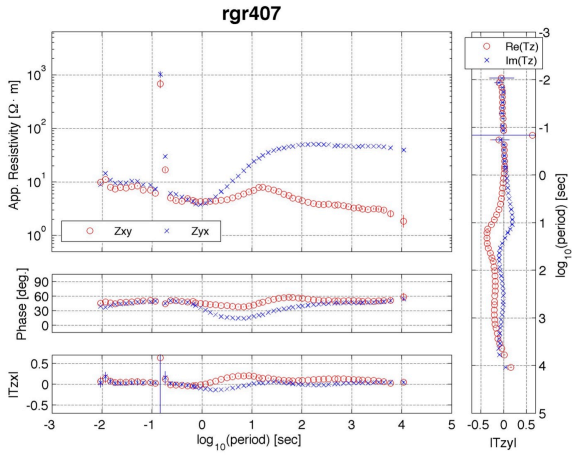
rgr407
App. Resistivity [Ω · m]
Zxy
Zyx
Phase [deg.]
|Tzx|
log10(period) [sec]
Re(Tz)
Im(Tz)
|Tzy|
log10(period) [sec]

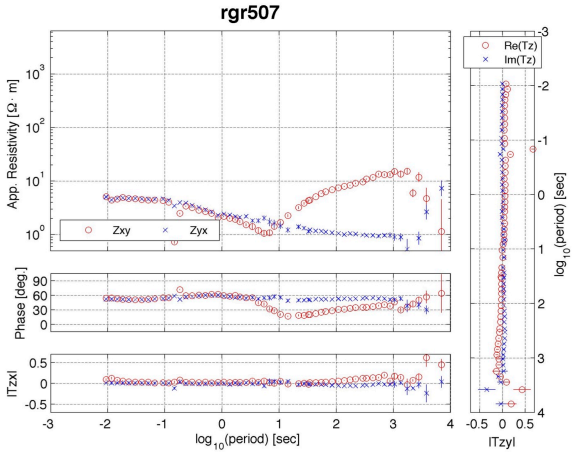
rgr507
App. Resistivity [Ω · m]
Zxy
Zyx
Phase [deg.]
|Tzx|
log10(period) [sec]
Re(Tz)
Im(Tz)
|Tzy|
log10(period) [sec]

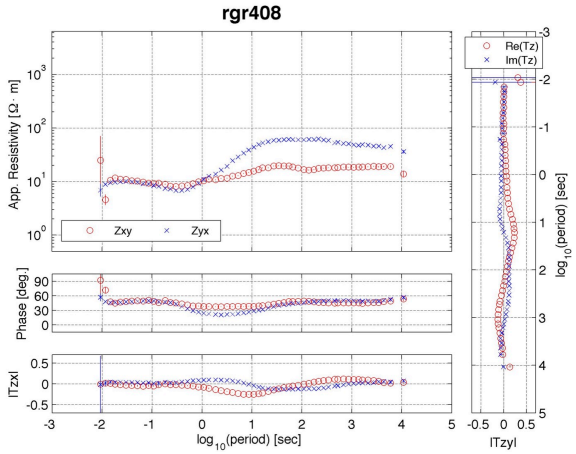
rgr408
App. Resistivity [Ω · m]
Zxy
Zyx
Phase [deg.]
|Tzx|
log10(period) [sec]
Re(Tz)
Im(Tz)
|Tzy|
log10(period) [sec]

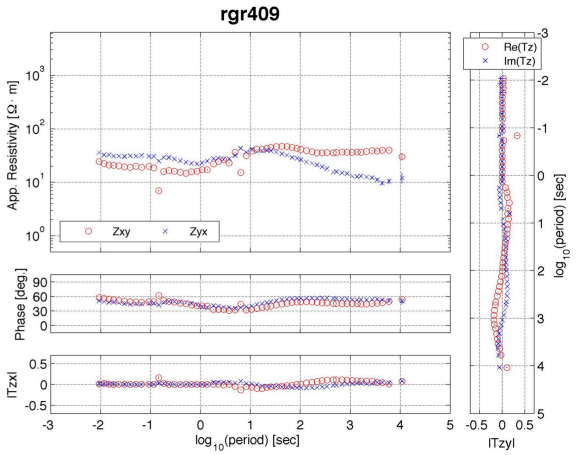
rgr409
App. Resistivity [Ω · m]
Zxy
Zyx
Phase [deg.]
|Tzx|
log10(period) [sec]
Re(Tz)
Im(Tz)
|Tzy|
log10(period) [sec]

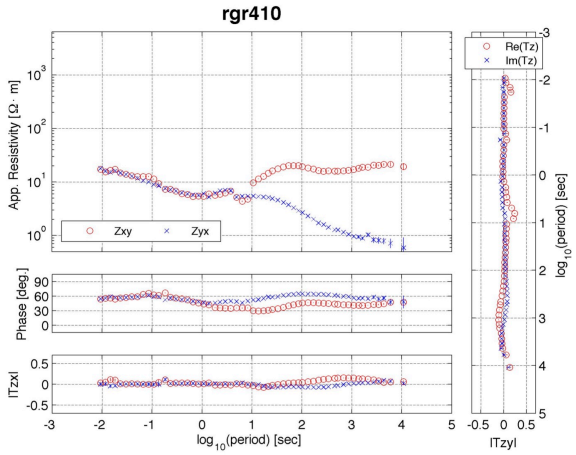
rgr410
App. Resistivity [Ω · m]
Zxy
Zyx
Phase [deg.]
|Tzx|
log10(period) [sec]
Re(Tz)
Im(Tz)
|Tzy|
log10(period) [sec]

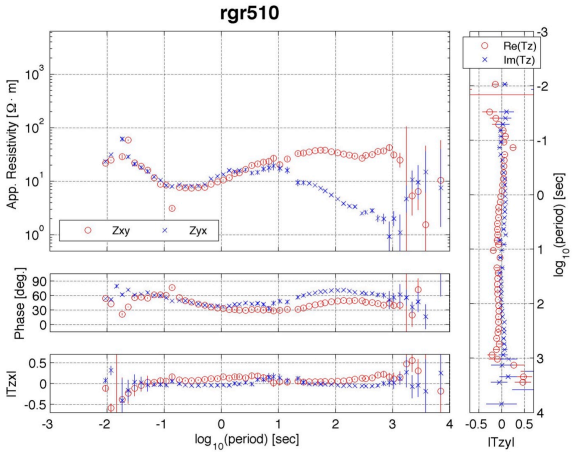
rgr510
App. Resistivity [Ω · m]
Zxy
Zyx
Phase [deg.]
ITzxI
log10(period) [sec]
Re(Tz)
Im(Tz)
log10(period) [sec]
ITzyI

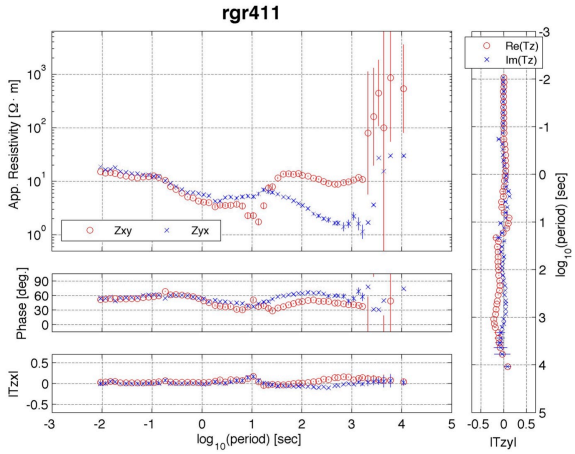
rgr411
App. Resistivity [Ω · m]
Zxy
Zyx
Phase [deg.]
ITzxI
log10(period) [sec]
Re(Tz)
Im(Tz)
log10(period) [sec]
ITzyI

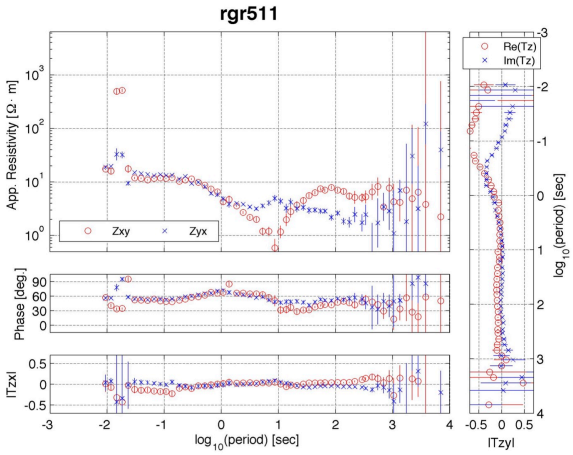
rgr511
App. Resistivity [Ω · m]
Zxy
Zyx
Phase [deg.]
ITzxI
log10(period) [sec]
Re(Tz)
Im(Tz)
log10(period) [sec]
ITzyI

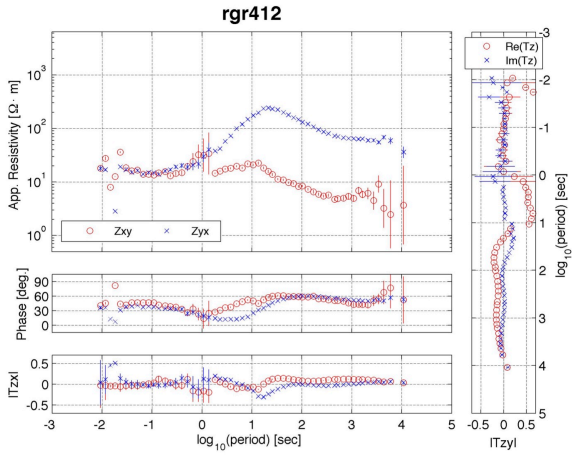
rgr412
App. Resistivity [Ω · m]
Zxy
Zyx
Phase [deg.]
ITzxI
log10(period) [sec]
Re(Tz)
Im(Tz)
log10(period) [sec]
ITzyI

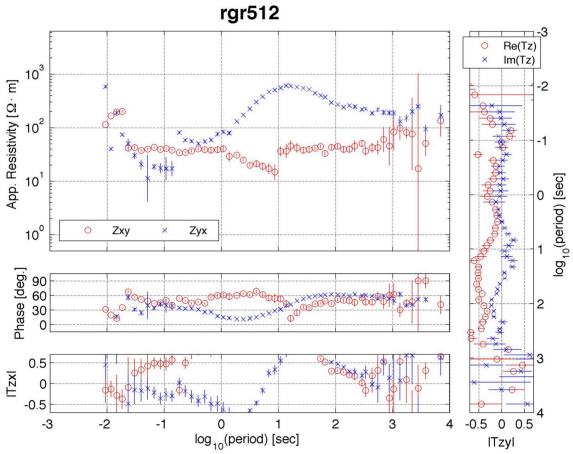
rgr512
App. Resistivity [Ω · m]
Zxy
Zyx
Phase [deg.]
|Tzx|
log10(period) [sec]
Re(Tz)
Im(Tz)
|Tzy|
log10(period) [sec]

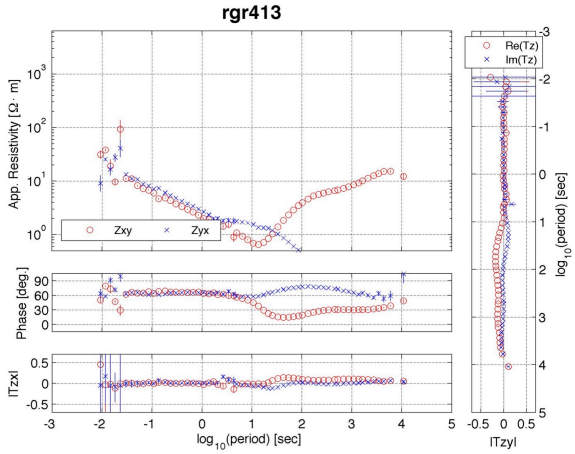
rgr413
App. Resistivity [Ω · m]
Zxy
Zyx
Phase [deg.]
|Tzx|
log10(period) [sec]
Re(Tz)
Im(Tz)
|Tzy|
log10(period) [sec]

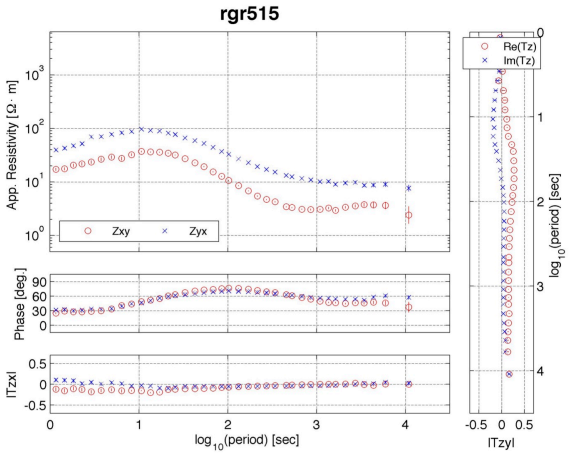
rgr515
App. Resistivity [Ω · m]
Zxy
Zyx
Phase [deg.]
|Tzx|
log10(period) [sec]
Re(Tz)
Im(Tz)
|Tzy|
log10(period) [sec]

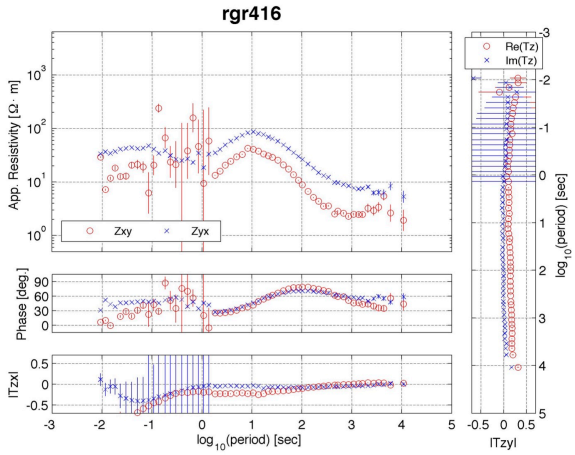
rgr416
App. Resistivity [Ω · m]
Zxy
Zyx
Phase [deg.]
|Tzx|
log10(period) [sec]
Re(Tz)
Im(Tz)
|Tzy|
log10(period) [sec]

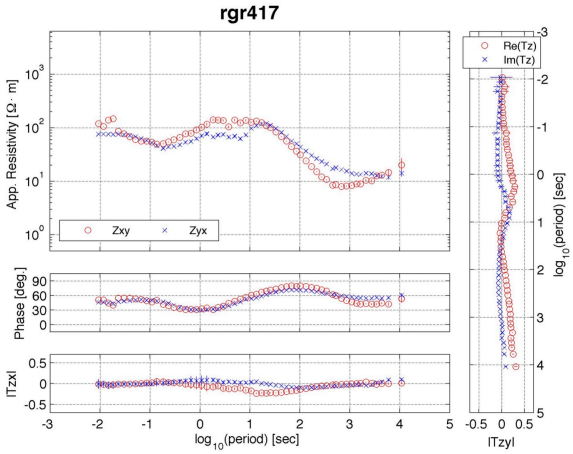
rgr417
App. Resistivity [Ω · m]
Zxy
Zyx
Phase [deg.]
|Tzx|
log10(period) [sec]
Re(Tz)
Im(Tz)
|Tzy|
log10(period) [sec]

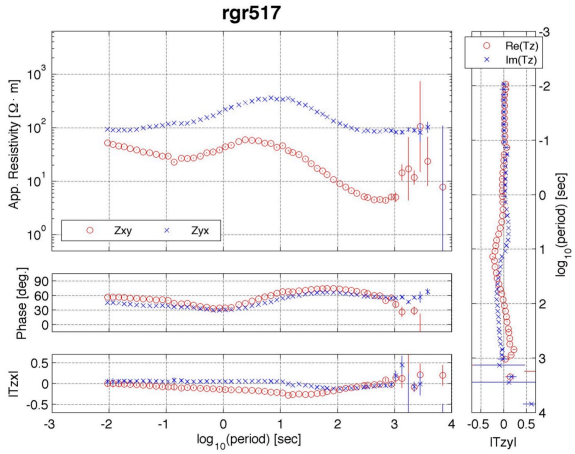
rgr517
App. Resistivity [Ω · m]
Zxy
Zyx
Phase [deg.]
|Tzx|
log10(period) [sec]
Re(Tz)
Im(Tz)
|Tzy|
log10(period) [sec]

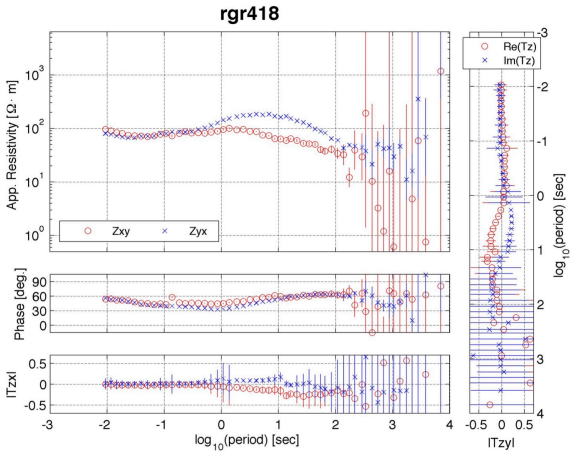
rgr418
App. Resistivity [Ω · m]
Zxy
Zyx
Phase [deg.]
|Tzx|
log10(period) [sec]
Re(Tz)
Im(Tz)
|Tzy|
log10(period) [sec]

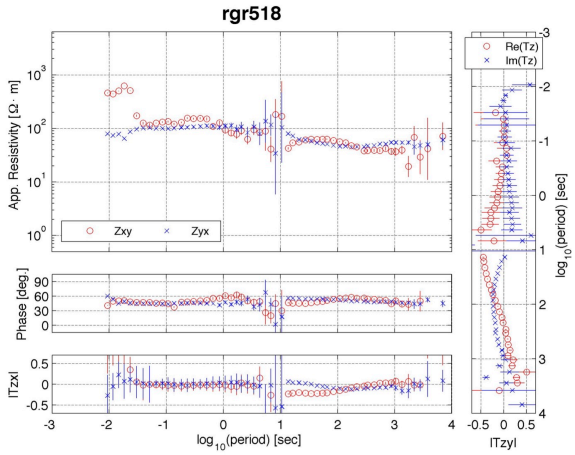
rgr518
App. Resistivity [Ω · m]
Zxy
Zyx
Phase [deg.]
|Tzx|
log10(period) [sec]
Re(Tz)
Im(Tz)
|Tzy|
log10(period) [sec]

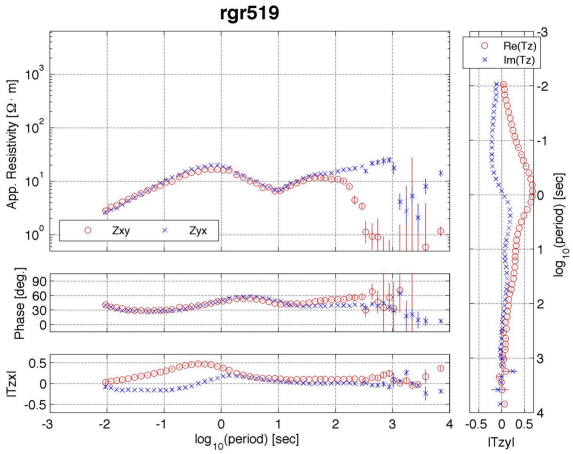
rgr519
App. Resistivity [Ω · m]
Zxy
Zyx
Phase [deg.]
|Tzx|
log10(period) [sec]
Re(Tz)
Im(Tz)
|Tzy|
log10(period) [sec]

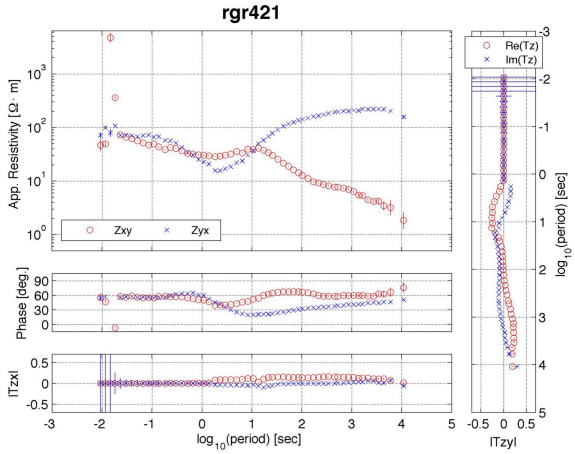
rgr421
App. Resistivity [Ω · m]
Zxy
Zyx
Phase [deg.]
|Tzx|
log10(period) [sec]
Re(Tz)
Im(Tz)
|Tzy|
log10(period) [sec]

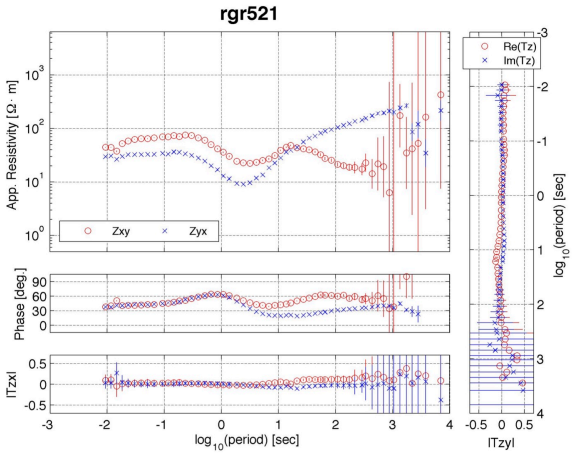
rgr521
App. Resistivity [Ω · m]
Zxy
Zyx
Phase [deg.]
|Tzx|
log10(period) [sec]
Re(Tz)
Im(Tz)
|Tzy|
log10(period) [sec]

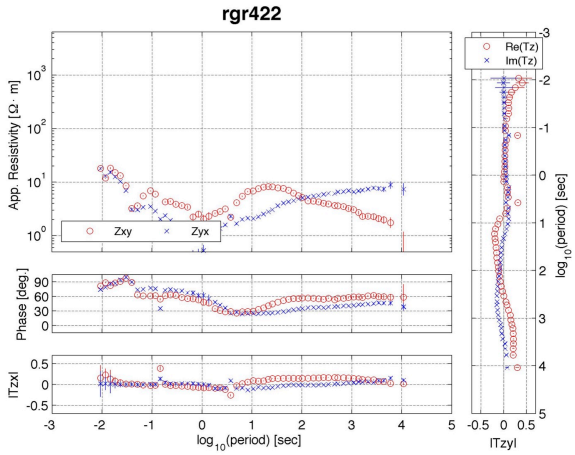
rgr422
App. Resistivity [Ω · m]
Zxy
Zyx
Phase [deg.]
|Tzx|
log10(period) [sec]
Re(Tz)
Im(Tz)
|Tzy|
log10(period) [sec]

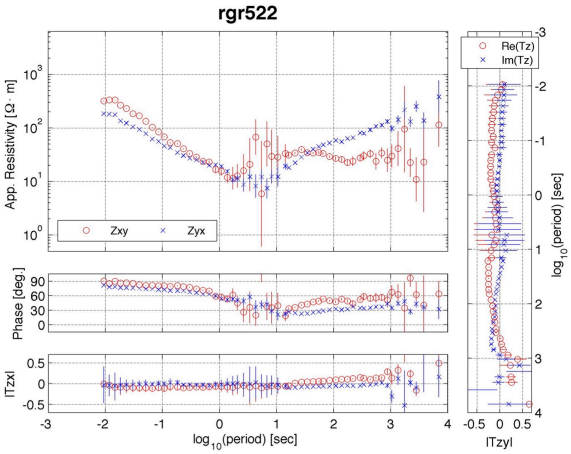
rgr522
App. Resistivity [Ω · m]
Zxy
Zyx
Phase [deg.]
|Tzx|
log10(period) [sec]
Re(Tz)
Im(Tz)
|Tzy|
log10(period) [sec]

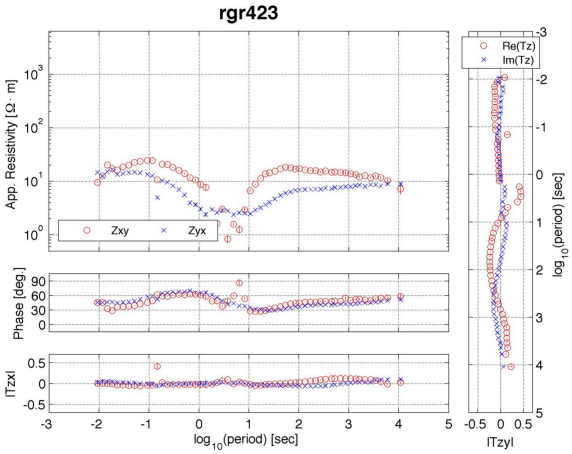
rgr423
App. Resistivity [Ω · m]
Zxy
Zyx
Phase [deg.]
|Tzx|
log10(period) [sec]
Re(Tz)
Im(Tz)
|Tzy|
log10(period) [sec]

A.2.4. SAGE MT stations (1991-2017)

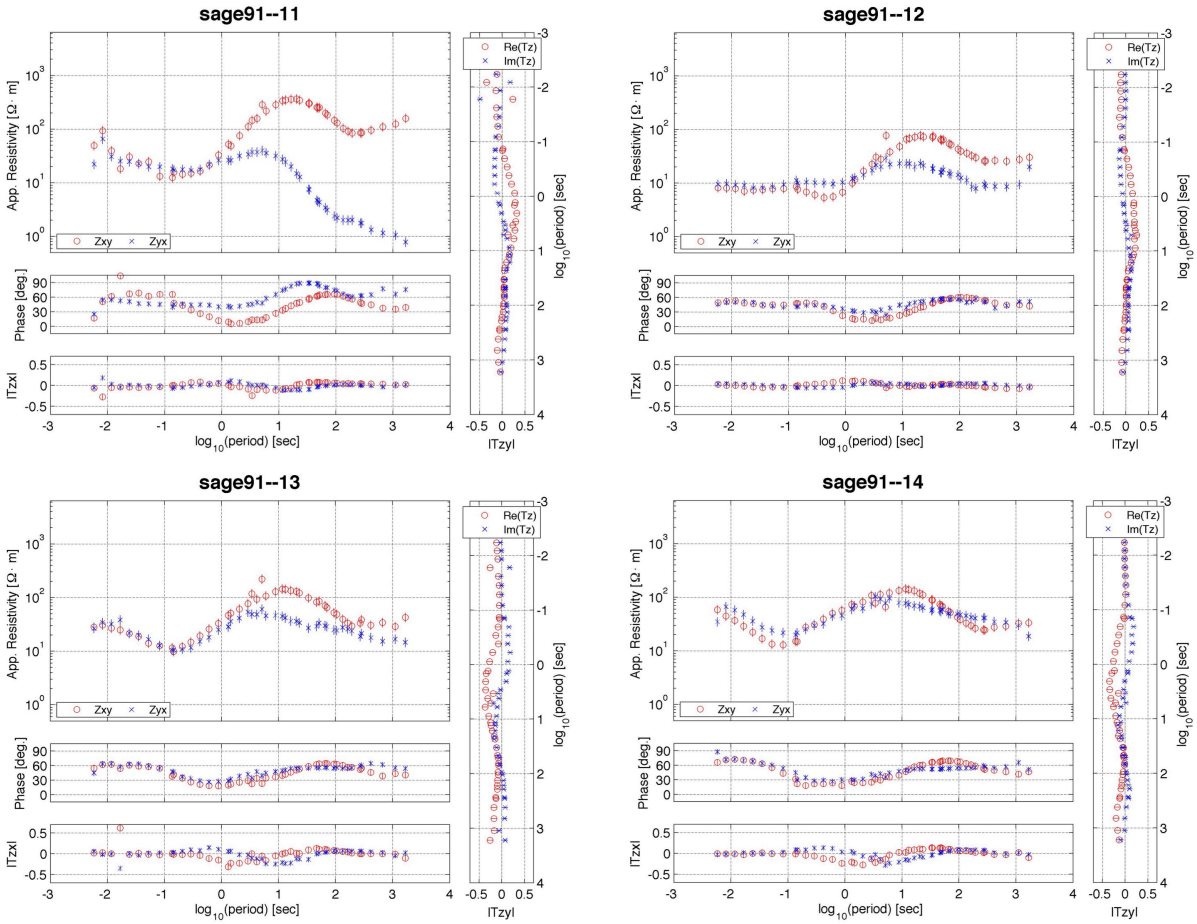

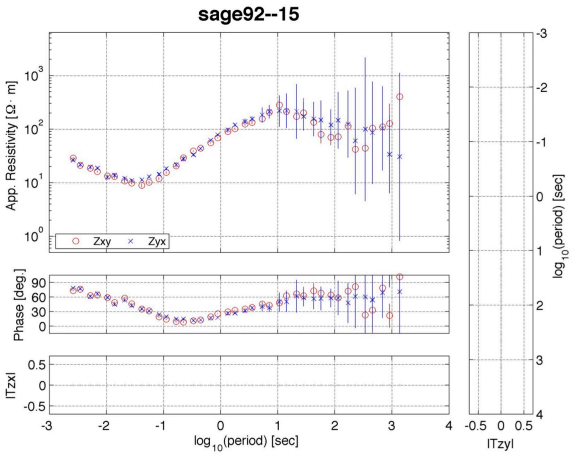
sage92--15
App. Resistivity [Ω· m]
Zxy
Zyx
Phase [deg.]
|Tzx|
log10(period) [sec]
|Tzy|
log10(period) [sec]

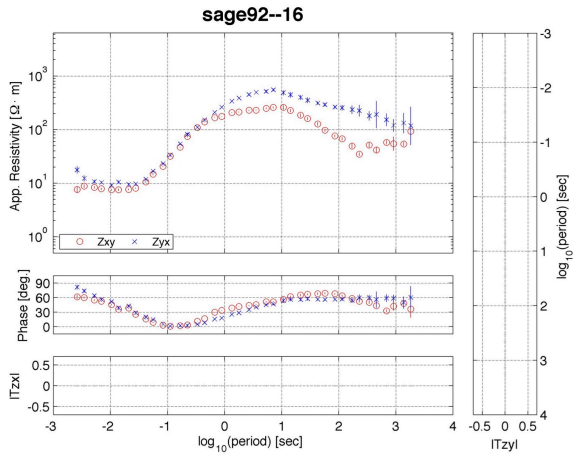
sage92--16
App. Resistivity [Ω· m]
Zxy
Zyx
Phase [deg.]
|Tzx|
log10(period) [sec]
|Tzy|
log10(period) [sec]

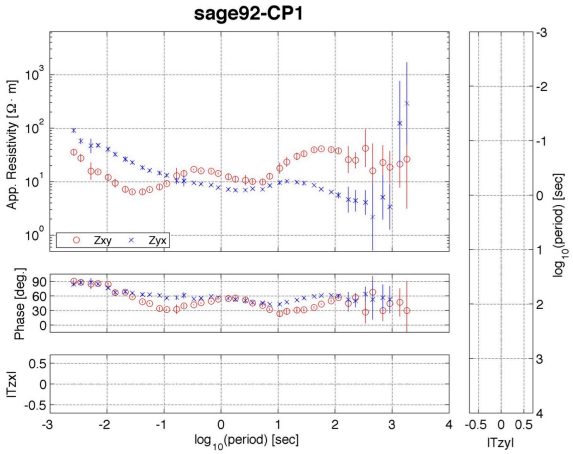
sage92-CP1
App. Resistivity [Ω· m]
Zxy
Zyx
Phase [deg.]
|Tzx|
log10(period) [sec]
|Tzy|
log10(period) [sec]

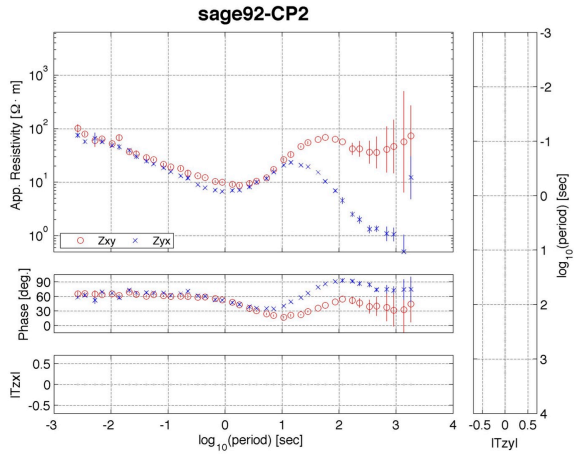
sage92-CP2
App. Resistivity [Ω· m]
Zxy
Zyx
Phase [deg.]
|Tzx|
log10(period) [sec]
|Tzy|
log10(period) [sec]

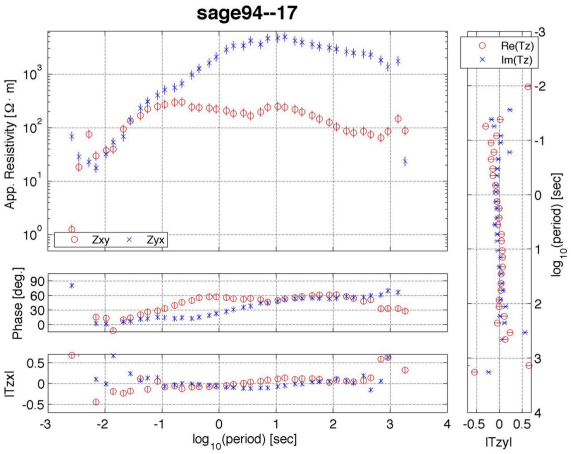
sage94--17
App. Resistivity [Ω · m]
Zxy
Zyx
Phase [deg]
|Tzx|
log10(period) [sec]
Re(Tz)
Im(Tz)
|Tzy|
log10(period) [sec]

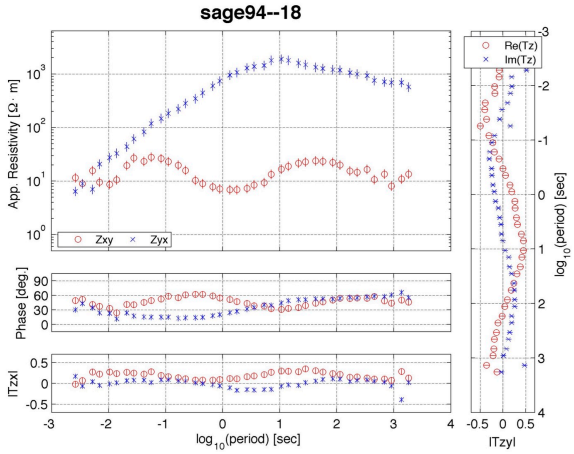
sage94--18
App. Resistivity [Ω · m]
Zxy
Zyx
Phase [deg]
|Tzx|
log10(period) [sec]
Re(Tz)
Im(Tz)
|Tzy|
log10(period) [sec]

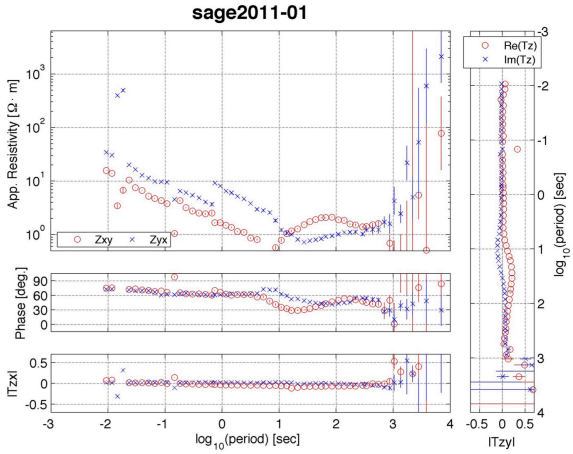
sage2011-01
App. Resistivity [Ω · m]
Zxy
Zyx
Phase [deg.]
|Tzx|
log10(period) [sec]
Re(Tz)
Im(Tz)
|Tzy|
log10(period) [sec]

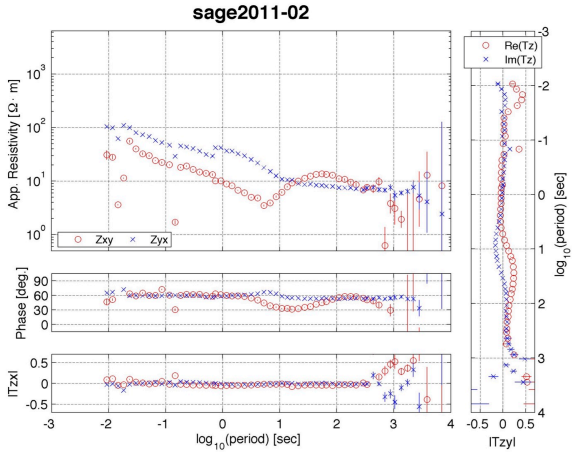
sage2011-02
App. Resistivity [Ω · m]
Zxy
Zyx
Phase [deg.]
|Tzx|
log10(period) [sec]
Re(Tz)
Im(Tz)
|Tzy|
log10(period) [sec]

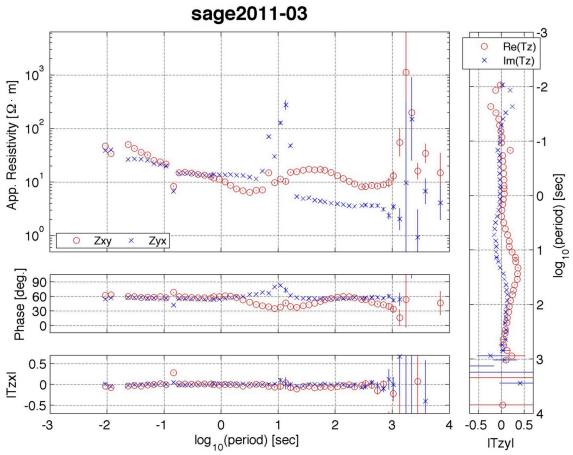
sage2011-03
App. Resistivity [Ω · m]
Zxy
Zyx
Phase [deg.]
|Tzx|
log10(period) [sec]
Re(Tz)
Im(Tz)
|Tzy|
log10(period) [sec]

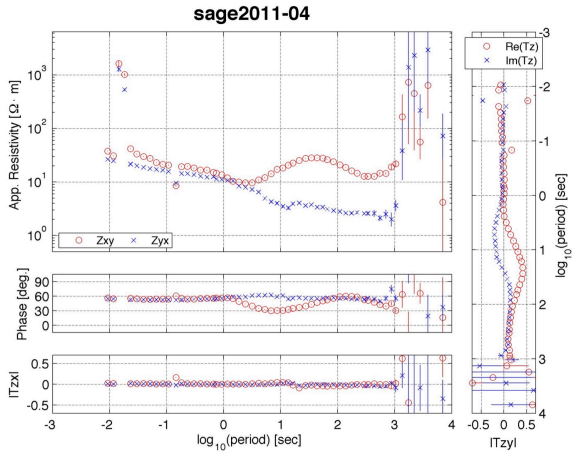
sage2011-04
App. Resistivity [Ω · m]
Zxy
Zyx
Phase [deg.]
|Tzx|
log10(period) [sec]
Re(Tz)
Im(Tz)
|Tzy|
log10(period) [sec]

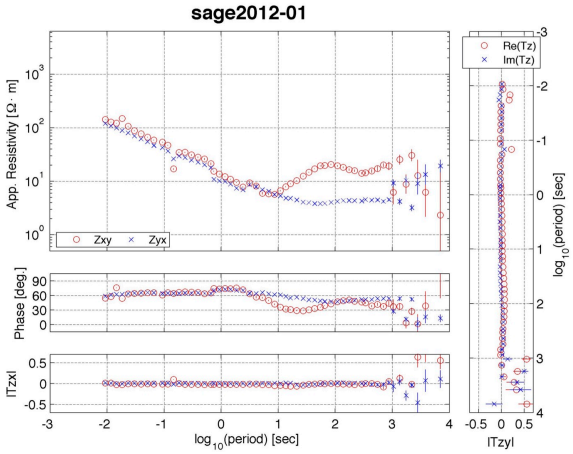
sage2012-01
App. Resistivity [Ω· m]
Zxy
Zyx
Phase [deg.]
ITzxI
log10(period) [sec]
Re(Tz)
Im(Tz)
ITzyI
log10(period) [sec]

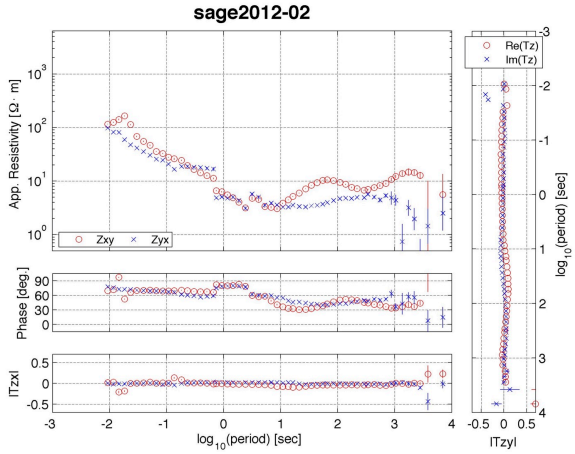
sage2012-02
App. Resistivity [Ω· m]
Zxy
Zyx
Phase [deg.]
ITzxI
log10(period) [sec]
Re(Tz)
Im(Tz)
ITzyI
log10(period) [sec]

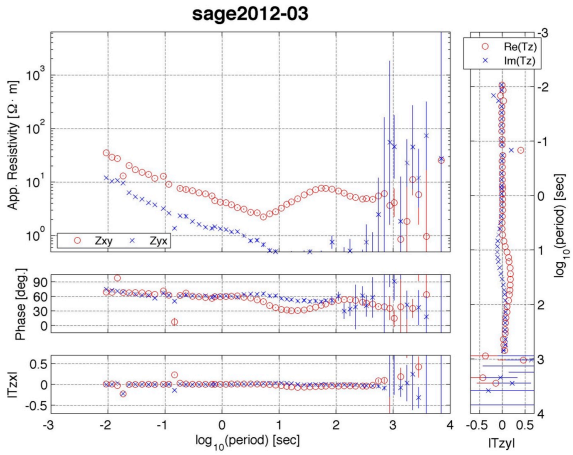
sage2012-03
App. Resistivity [Ω· m]
Zxy
Zyx
Phase [deg.]
ITzxI
log10(period) [sec]
Re(Tz)
Im(Tz)
ITzyI
log10(period) [sec]

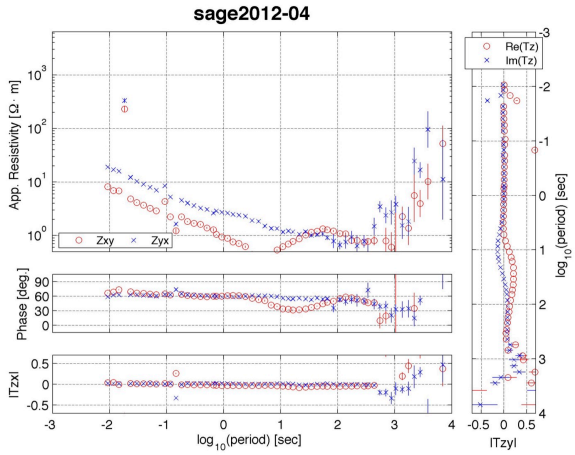
sage2012-04
App. Resistivity [Ω· m]
Zxy
Zyx
Phase [deg.]
ITzxI
log10(period) [sec]
Re(Tz)
Im(Tz)
ITzyI
log10(period) [sec]

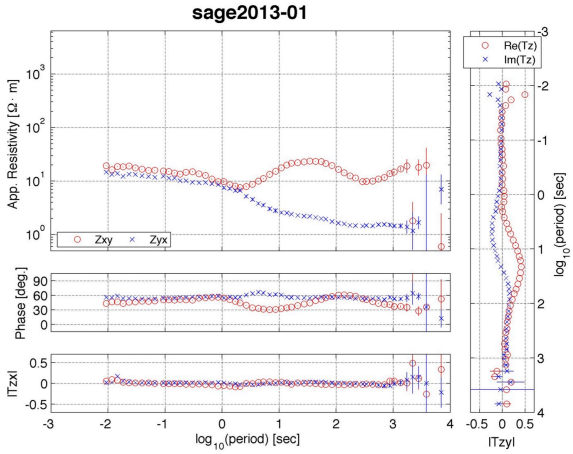
sage2013-01
App. Resistivity [Ω· m]
Zxy
Zyx
Phase [deg.]
|Tzx|
log10(period) [sec]
Re(Tz)
Im(Tz)
|Tzy|
log10(period) [sec]

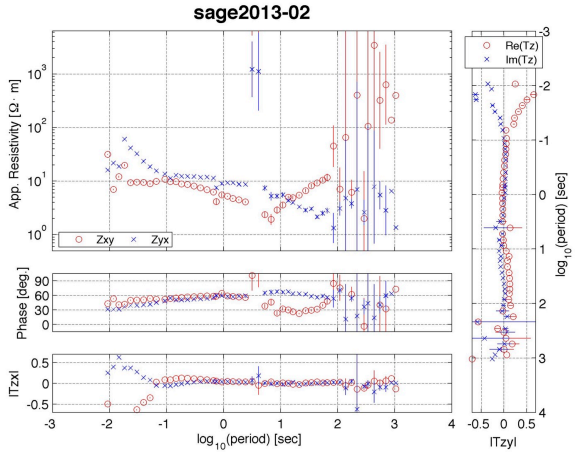
sage2013-02
App. Resistivity [Ω· m]
Zxy
Zyx
Phase [deg.]
|Tzx|
log10(period) [sec]
Re(Tz)
Im(Tz)
|Tzy|
log10(period) [sec]

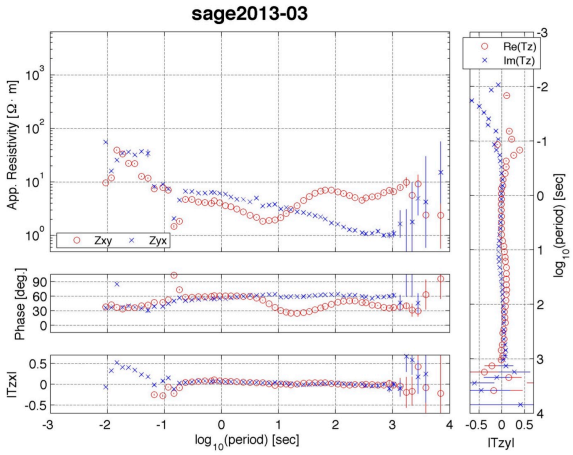
sage2013-03
App. Resistivity [Ω· m]
Zxy
Zyx
Phase [deg.]
|Tzx|
log10(period) [sec]
Re(Tz)
Im(Tz)
|Tzy|
log10(period) [sec]

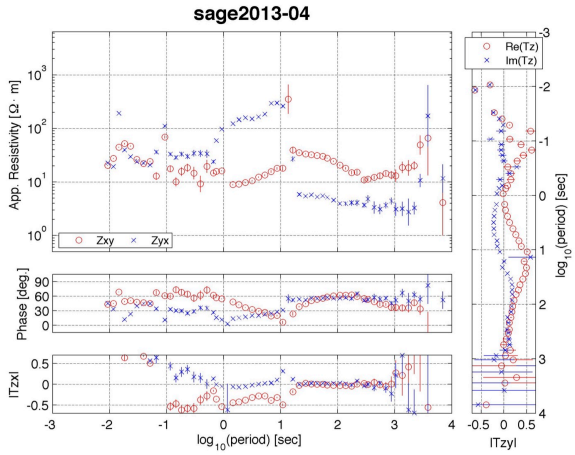
sage2013-04
App. Resistivity [Ω· m]
Zxy
Zyx
Phase [deg.]
|Tzx|
log10(period) [sec]
Re(Tz)
Im(Tz)
|Tzy|
log10(period) [sec]

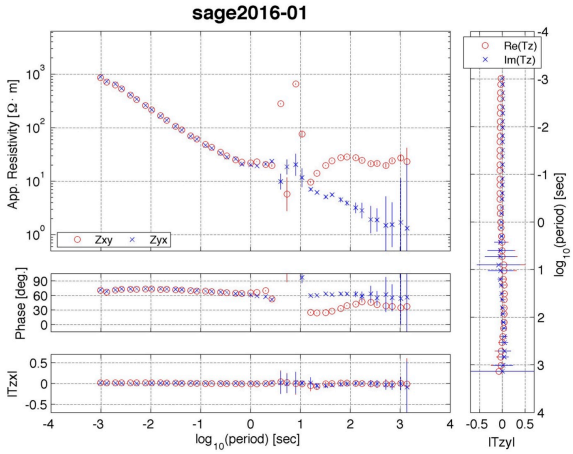
sage2016-01
App. Resistivity [Ω· m]
Zxy
Zyx
Phase [deg.]
|Tzx|
log10(period) [sec]
Re(Tz)
Im(Tz)
|Tzy|
log10(period) [sec]

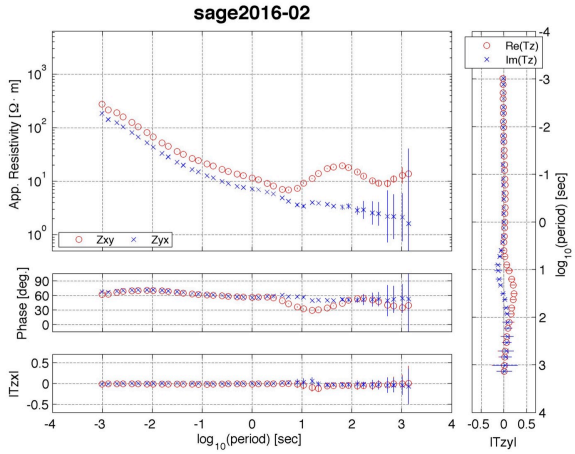
sage2016-02
App. Resistivity [Ω· m]
Zxy
Zyx
Phase [deg.]
|Tzx|
log10(period) [sec]
Re(Tz)
Im(Tz)
|Tzy|
log10(period) [sec]

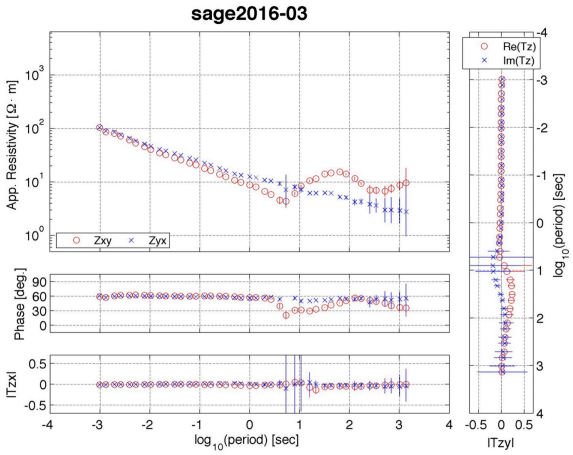
sage2016-03
App. Resistivity [Ω· m]
Zxy
Zyx
Phase [deg.]
|Tzx|
log10(period) [sec]
Re(Tz)
Im(Tz)
|Tzy|
log10(period) [sec]

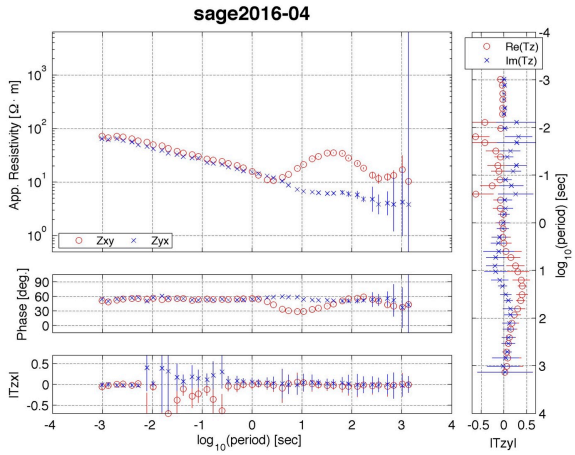
sage2016-04
App. Resistivity [Ω· m]
Zxy
Zyx
Phase [deg.]
|Tzx|
log10(period) [sec]
Re(Tz)
Im(Tz)
|Tzy|
log10(period) [sec]

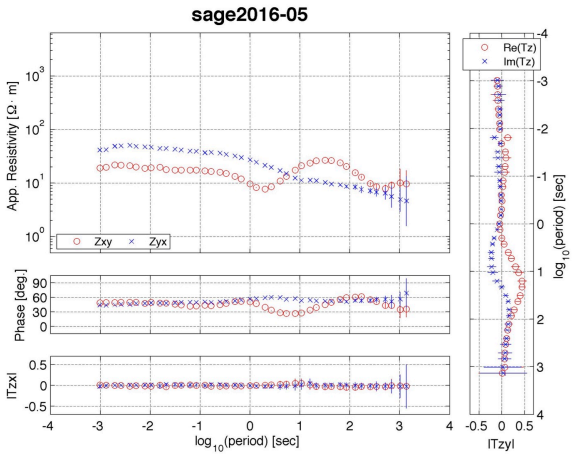
sage2016-05
App. Resistivity [Ω· m]
Zxy
Zyx
Phase [deg.]
|Tzx|
log10(period) [sec]
Re(Tz)
Im(Tz)
|Tzy|
log10(period) [sec]

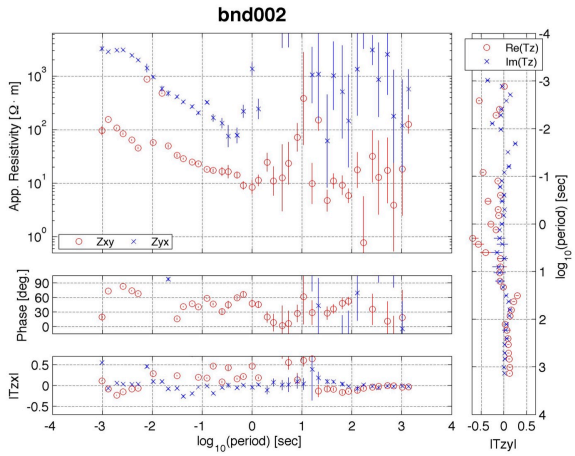
bnd002
App. Resistivity [Ω· m]
Zxy
Zyx
Phase [deg.]
|Tzx|
log10(period) [sec]
Re(Tz)
Im(Tz)
|Tzy|
log10(period) [sec]

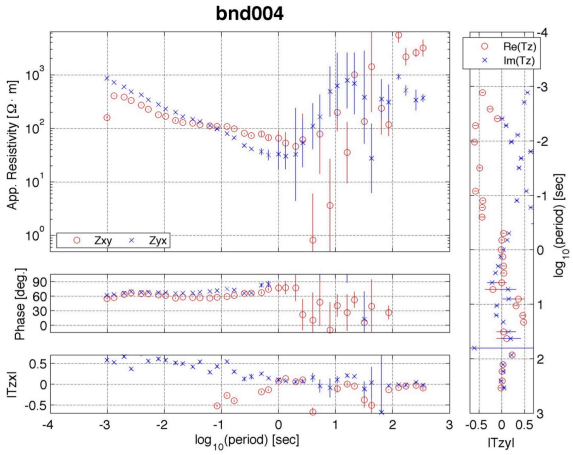
bnd004
App. Resistivity [Ω· m]
Zxy
Zyx
Phase [deg.]
|Tzx|
log10(period) [sec]
Re(Tz)
Im(Tz)
|Tzy|
log10(period) [sec]

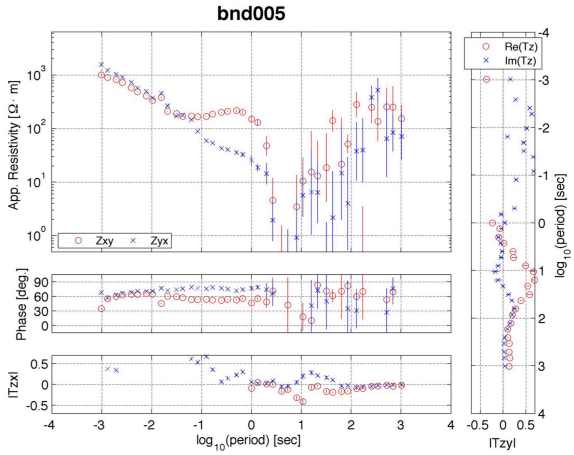
bnd005
App. Resistivity [Ω· m]
Zxy
Zyx
Phase [deg.]
|Tzx|
log10(period) [sec]
Re(Tz)
Im(Tz)
|Tzy|
log10(period) [sec]

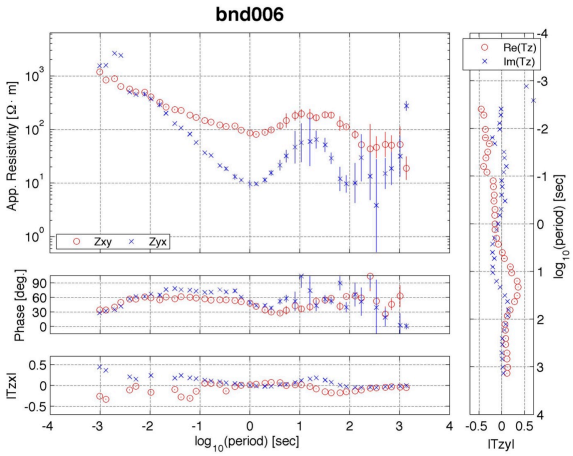
bnd006
App. Resistivity [Ω · m]
Zxy
Zyx
Phase [deg.]
|Tzx|
log10(period) [sec]
Re(Tz)
Im(Tz)
|Tzy|
log10(period) [sec]

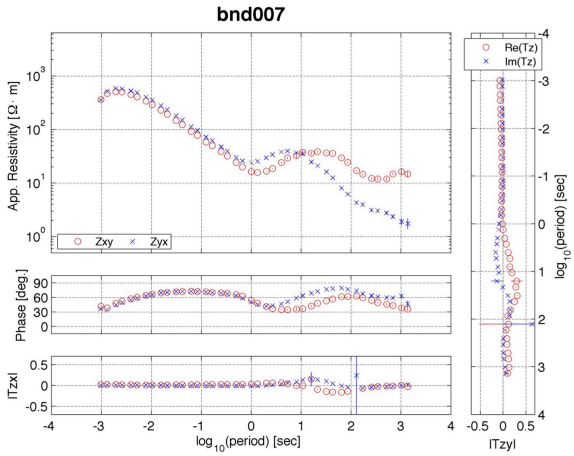
bnd007
App. Resistivity [Ω · m]
Zxy
Zyx
Phase [deg.]
|Tzx|
log10(period) [sec]
Re(Tz)
Im(Tz)
|Tzy|
log10(period) [sec]

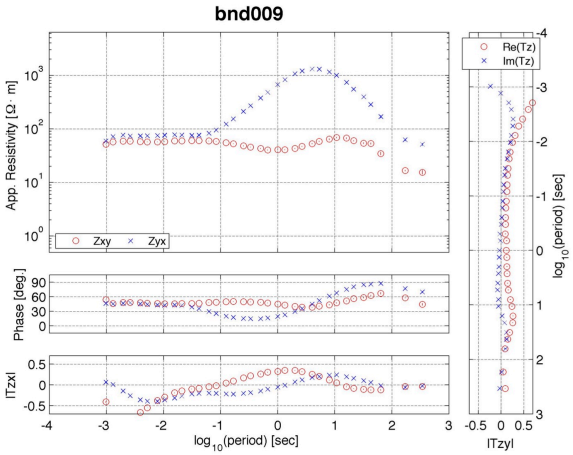
bnd009
App. Resistivity [Ω · m]
Zxy
Zyx
Phase [deg.]
|Tzx|
log10(period) [sec]
Re(Tz)
Im(Tz)
|Tzy|
log10(period) [sec]

A.2.5. MT stations from Unocal Company (1983) - Valles Caldera

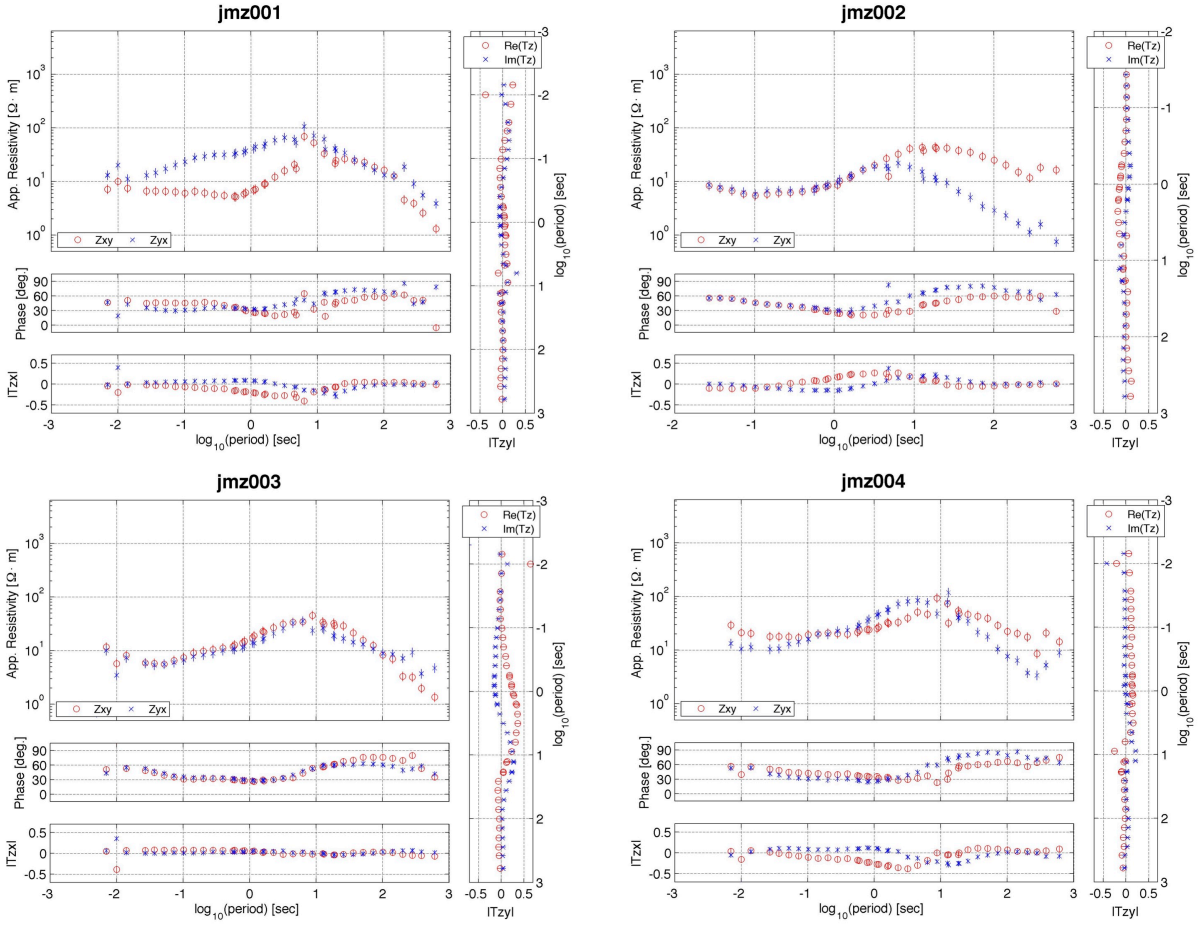

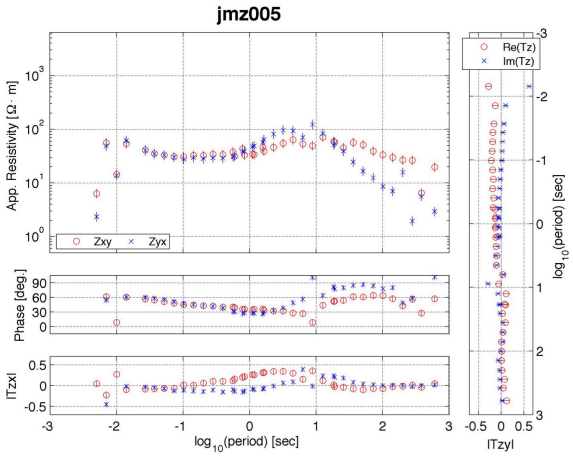
jmz005
App. Resistivity [Ω· m]
Zxy
Zyx
Phase [deg.]
ITzxI
log10(period) [sec]
Re(Tz)
Im(Tz)
ITzyI
log10(period) [sec]

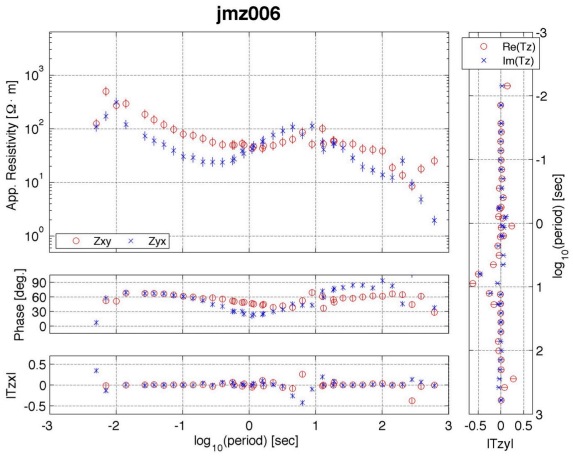
jmz006
App. Resistivity [Ω· m]
Zxy
Zyx
Phase [deg.]
ITzxI
log10(period) [sec]
Re(Tz)
Im(Tz)
ITzyI
log10(period) [sec]

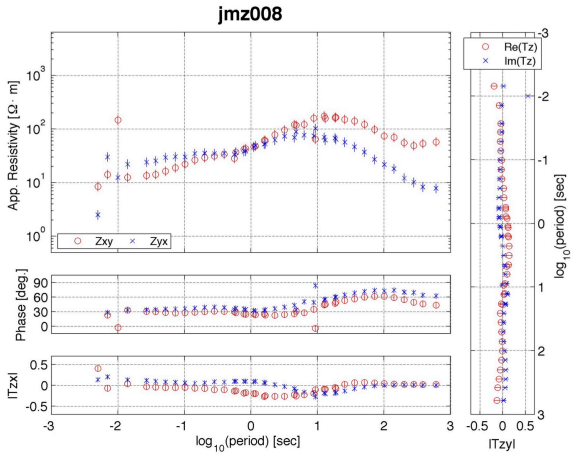
jmz008
App. Resistivity [Ω· m]
Zxy
Zyx
Phase [deg.]
ITzxI
log10(period) [sec]
Re(Tz)
Im(Tz)
ITzyI
log10(period) [sec]

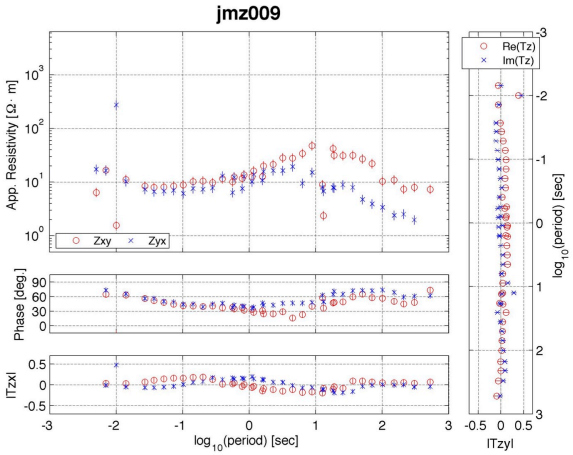
jmz009
App. Resistivity [Ω· m]
Zxy
Zyx
Phase [deg.]
ITzxI
log10(period) [sec]
Re(Tz)
Im(Tz)
ITzyI
log10(period) [sec]

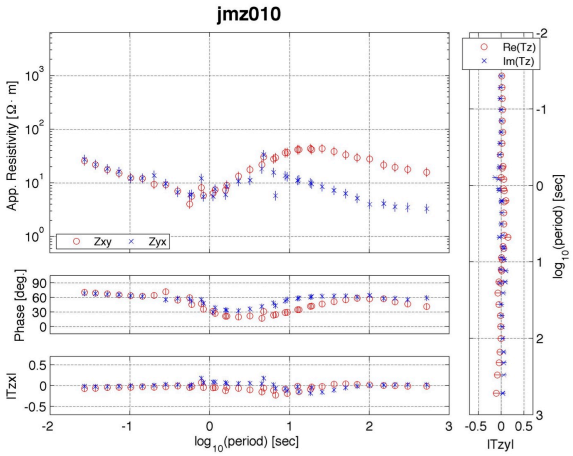
jmz010
App. Resistivity [Ω · m]
Zxy
Zyx
Phase [deg.]
ITzxI
log10(period) [sec]
Re(Tz)
Im(Tz)
ITzyI
log10(period) [sec]

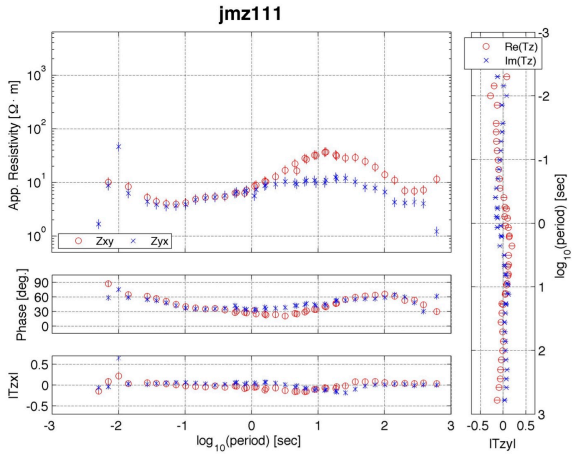
jmz111
App. Resistivity [Ω · m]
Zxy
Zyx
Phase [deg.]
ITzxI
log10(period) [sec]
Re(Tz)
Im(Tz)
ITzyI
log10(period) [sec]

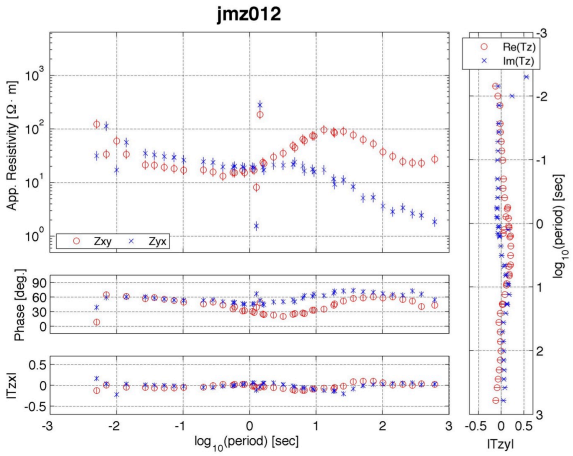
jmz012
App. Resistivity [Ω · m]
Zxy
Zyx
Phase [deg.]
ITzxI
log10(period) [sec]
Re(Tz)
Im(Tz)
ITzyI
log10(period) [sec]

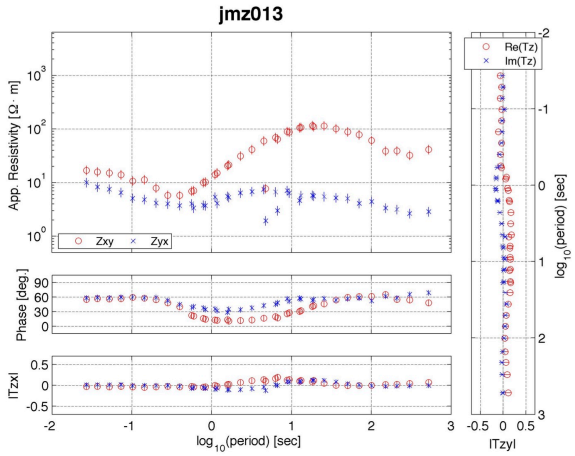
jmz013
App. Resistivity [Ω · m]
Zxy
Zyx
Phase [deg.]
ITzxI
log10(period) [sec]
Re(Tz)
Im(Tz)
ITzyI
log10(period) [sec]

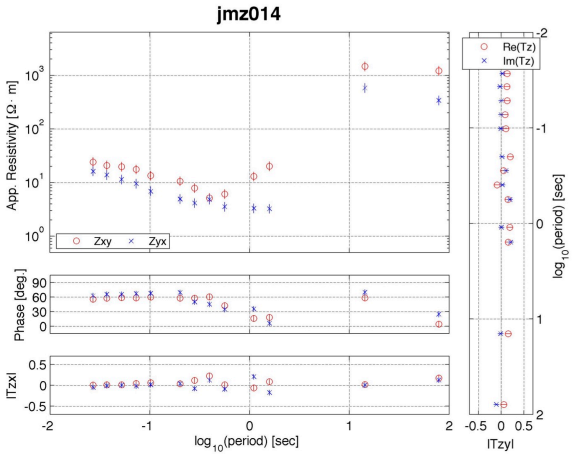
jmz014
App. Resistivity [Ω· m]
Zxy
Zyx
Phase [deg.]
ITzxI
log10(period) [sec]
Re(Tz)
Im(Tz)
ITzyI
log10(period) [sec]

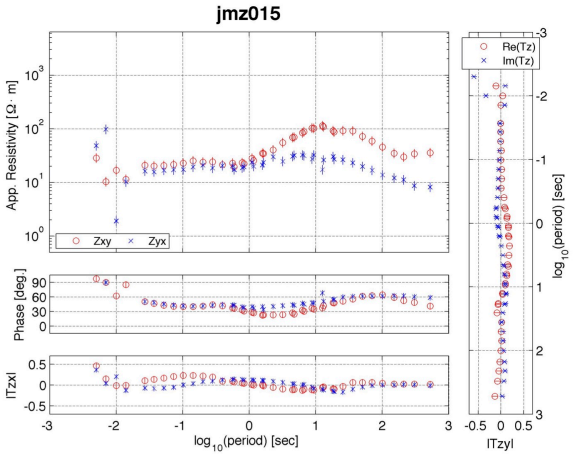
jmz015
App. Resistivity [Ω· m]
Zxy
Zyx
Phase [deg.]
ITzxI
log10(period) [sec]
Re(Tz)
Im(Tz)
ITzyI
log10(period) [sec]

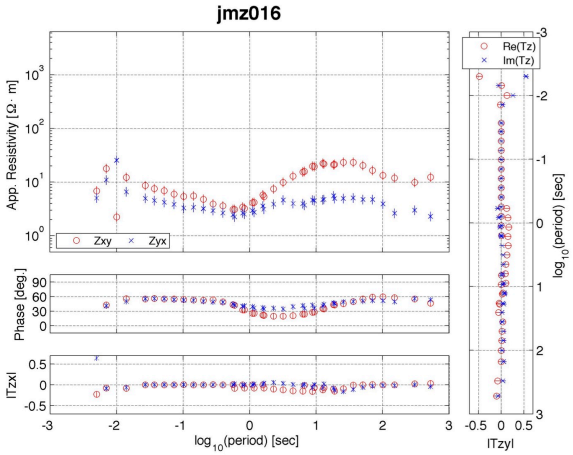
jmz016
App. Resistivity [Ω· m]
Zxy
Zyx
Phase [deg.]
ITzxI
log10(period) [sec]
Re(Tz)
Im(Tz)
ITzyI
log10(period) [sec]

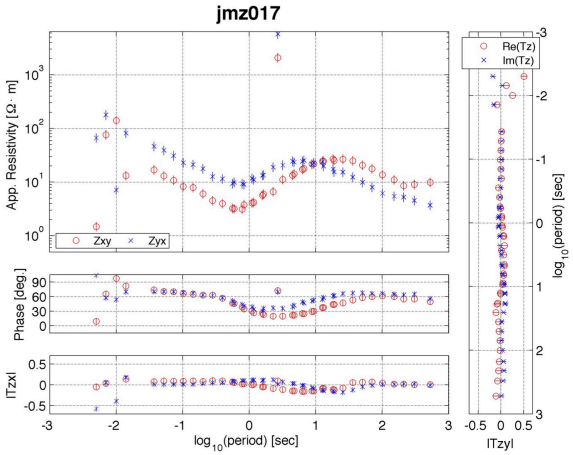
jmz017
App. Resistivity [Ω· m]
Zxy
Zyx
Phase [deg.]
ITzxI
log10(period) [sec]
Re(Tz)
Im(Tz)
ITzyI
log10(period) [sec]

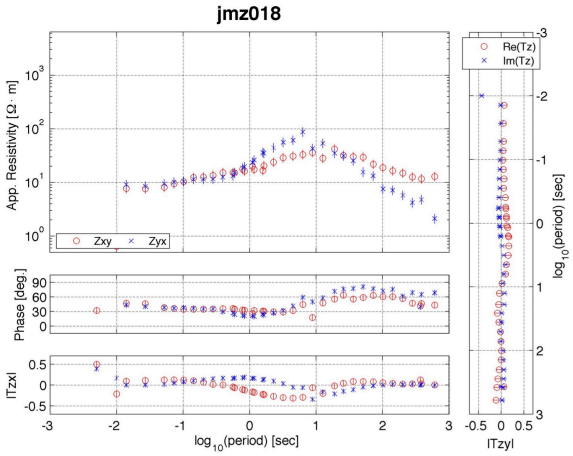
jmz018
App. Resistivity [Ω· m]
Zxy
Zyx
Phase [deg.]
|Tzx|
log10(period) [sec]
Re(Tz)
Im(Tz)
|Tzy|
log10(period) [sec]

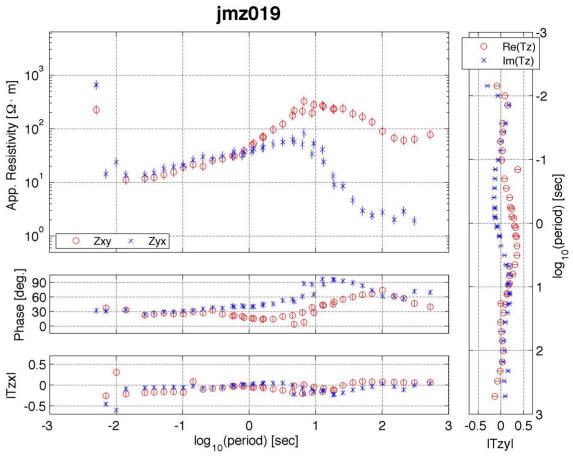
jmz019
App. Resistivity [Ω· m]
Zxy
Zyx
Phase [deg.]
|Tzx|
log10(period) [sec]
Re(Tz)
Im(Tz)
|Tzy|
log10(period) [sec]

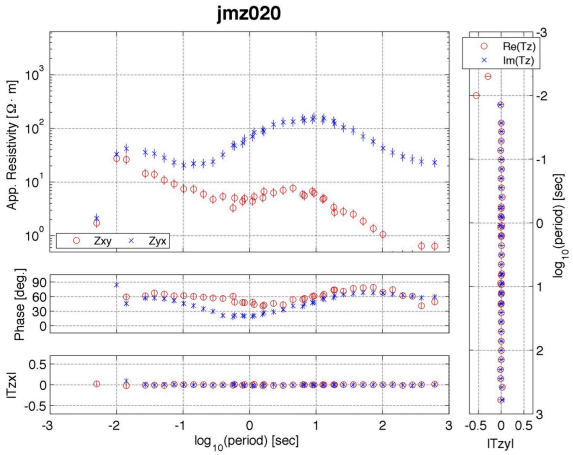
jmz020
App. Resistivity [Ω· m]
Zxy
Zyx
Phase [deg.]
|Tzx|
log10(period) [sec]
Re(Tz)
Im(Tz)
|Tzy|
log10(period) [sec]

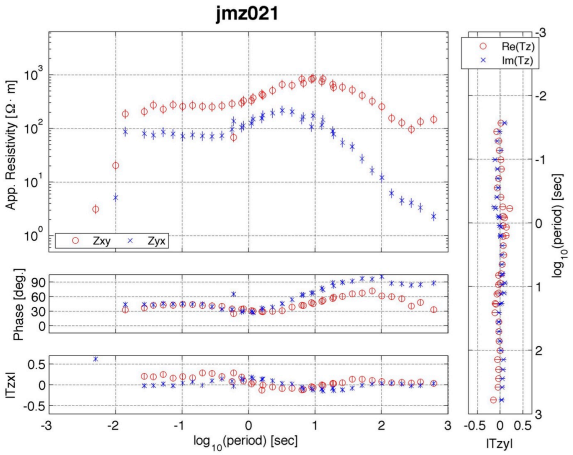
jmz021
App. Resistivity [Ω· m]
Zxy
Zyx
Phase [deg.]
|Tzx|
log10(period) [sec]
Re(Tz)
Im(Tz)
|Tzy|
log10(period) [sec]

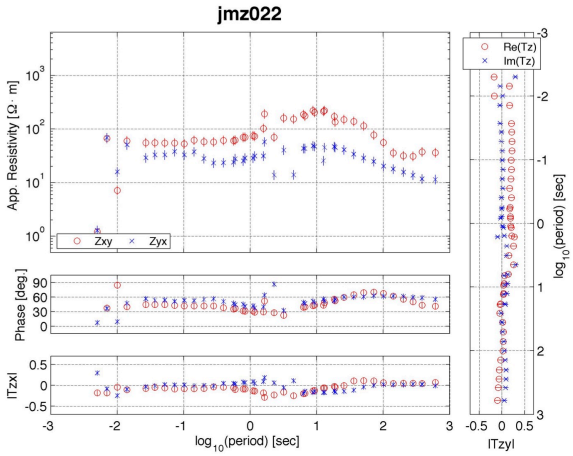
jmz022
App. Resistivity [Ω· m]
Zxy
Zyx
Phase [deg.]
|Tzx|
log10(period) [sec]
Re(Tz)
Im(Tz)
|Tzy|
log10(period) [sec]

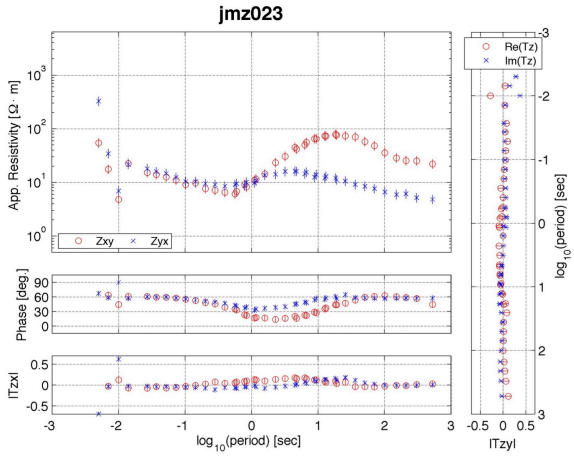
jmz023
App. Resistivity [Ω· m]
Zxy
Zyx
Phase [deg.]
|Tzx|
log10(period) [sec]
Re(Tz)
Im(Tz)
|Tzy|
log10(period) [sec]

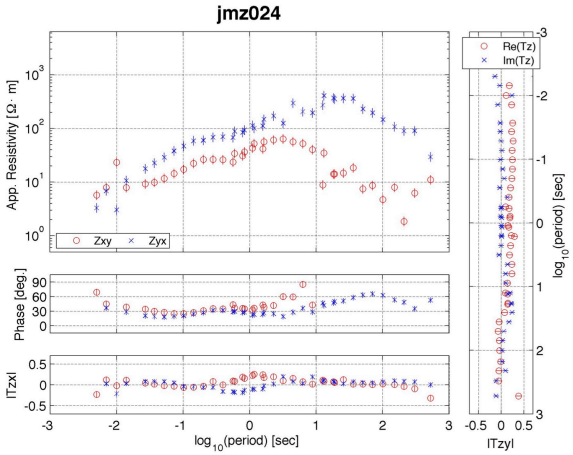
jmz024
App. Resistivity [Ω· m]
Zxy
Zyx
Phase [deg.]
|Tzx|
log10(period) [sec]
Re(Tz)
Im(Tz)
|Tzy|
log10(period) [sec]

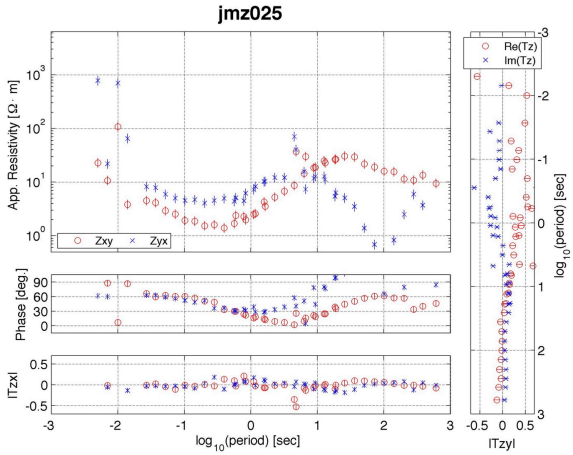
jmz025
App. Resistivity [Ω· m]
Zxy
Zyx
Phase [deg.]
|Tzx|
log10(period) [sec]
Re(Tz)
Im(Tz)
|Tzy|
log10(period) [sec]

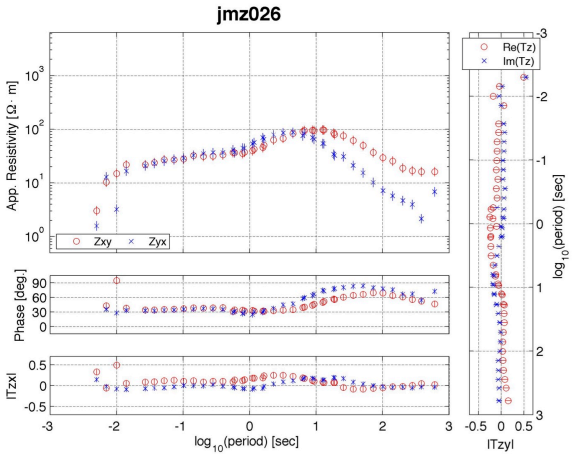
jmz026
App. Resistivity [Ω · m]
Zxy
Zyx
Phase [deg.]
|Tzx|
log10(period) [sec]
Re(Tz)
Im(Tz)
|Tzy|
log10(period) [sec]

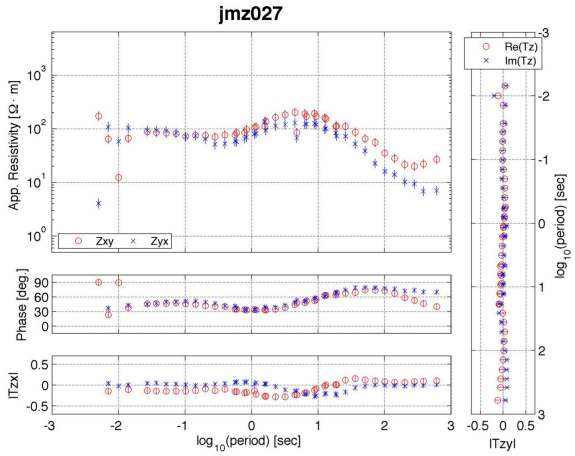
jmz027
App. Resistivity [Ω · m]
Zxy
Zyx
Phase [deg.]
|Tzx|
log10(period) [sec]
Re(Tz)
Im(Tz)
|Tzy|
log10(period) [sec]

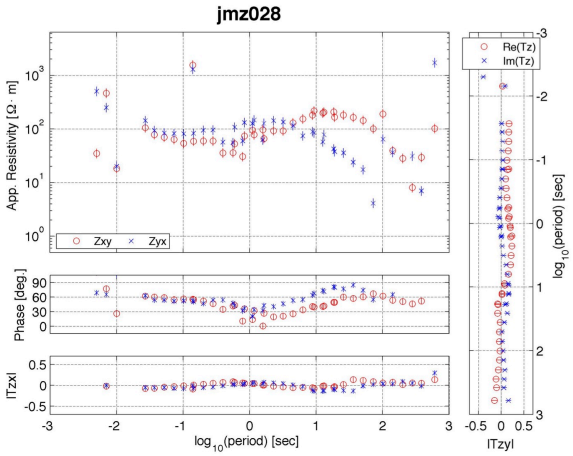
jmz028
App. Resistivity [Ω · m]
Zxy
Zyx
Phase [deg.]
|Tzx|
log10(period) [sec]
Re(Tz)
Im(Tz)
|Tzy|
log10(period) [sec]

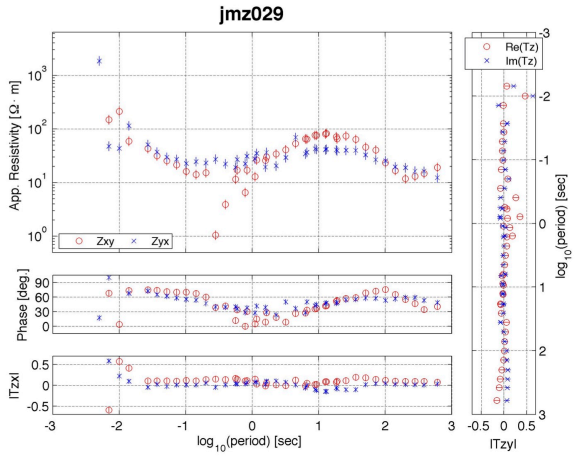
jmz029
App. Resistivity [Ω · m]
Zxy
Zyx
Phase [deg.]
|Tzx|
log10(period) [sec]
Re(Tz)
Im(Tz)
|Tzy|
log10(period) [sec]

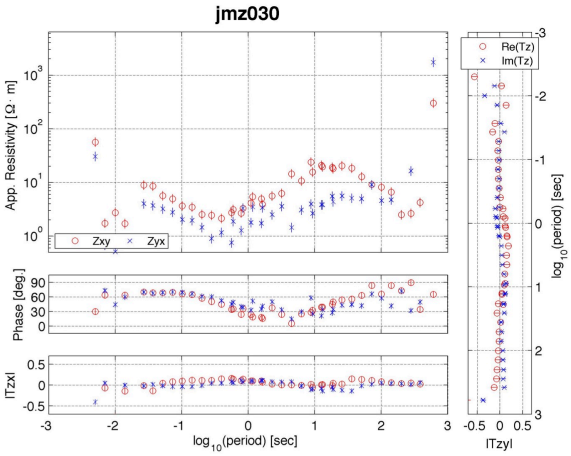
jmz030
App. Resistivity [Ω · m]
Zxy
Zyx
Phase [deg.]
|Tzx|
log10(period) [sec]
Re(Tz)
Im(Tz)
|Tzy|
log10(period) [sec]

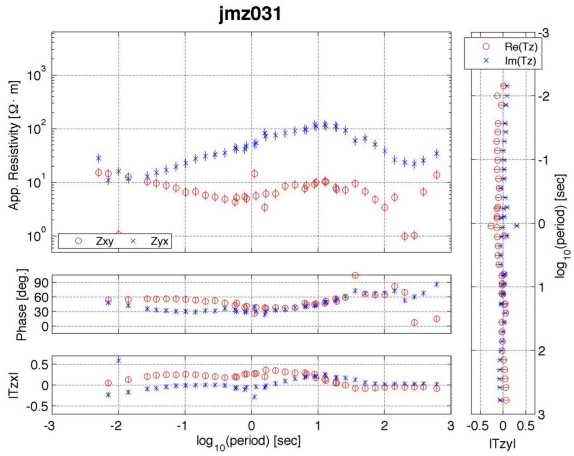
jmz031
App. Resistivity [Ω · m]
Zxy
Zyx
Phase [deg.]
|Tzx|
log10(period) [sec]
Re(Tz)
Im(Tz)
|Tzy|
log10(period) [sec]